Pair production of Higgs bosons in the final state with bottom quarks and τ leptons in the ATLAS experiment

Search results using LHC Run 2 data and prospect studies at the HL-LHC

Dissertation

zur Erlangung des mathematisch-naturwissenschaftlichen
Doktorgrades "Doctor of Philosophy" (Ph.D.)
der Georg-August-Universität Göttingen

im Promotionsprogramm Physik
der Georg-August University School of Science (GAUSS)

vorgelegt von
Petar Bokan
aus Drvar, Bosnia and Herzegovina

Göttingen, 2020

Supervision committee:

Prof. Dr. Stan Lai
II. Institute of Physics, Georg-August-Universität Göttingen

Prof. Dr. Arnaud Ferrari
Department of Physics and Astronomy, Uppsala University (Sweden)

Members of the Examination Board:

Reviewer:
Prof. Dr. Stan Lai
II. Institute of Physics, Georg-August-Universität Göttingen

Second reviewer:
Prof. Dr. Arnaud Ferrari
Department of Physics and Astronomy, Uppsala University (Sweden)

Additional reviewer:
Prof. Dr. Markus Klute
Department of Physics, Massachusetts Institute of Technology – MIT (USA)

Further members of the Examination Board:

Prof. Dr. Ariane Frey
II. Institute of Physics, Georg-August-Universität Göttingen

Prof. Dr. Lisa Freyhult
Department of Physics and Astronomy, Uppsala University (Sweden)

Prof. Dr. Sven Heinemeyer
Universidad Autónoma de Madrid, Instituto de Física Teórica – UAM - CSIC (Spain)

Prof. Dr. Jonas Strandberg
Department of Physics, Royal Institute of Technology – KTH (Sweden)

Date of the oral examination: October 30, 2020

Reference: II.Physik-UniGö-Diss-2020/04

Abstract

After the discovery of the Higgs boson, the ultimate test of the electroweak symmetry breaking and the Standard Model (SM) of particle physics is to establish evidence of Higgs boson self-coupling, which can be achieved by searching for pair production of Higgs bosons. In addition, many theories beyond the SM predict heavy resonances that could decay into pairs of Higgs bosons. A search for non-resonant and resonant pair production of Higgs bosons in the final state with two bottom quarks and two τ leptons ($b\bar{b}\tau^+\tau^-$) is presented for 36.1 fb^{-1} of proton-proton collision data at a centre-of-mass energy of 13 TeV recorded by the ATLAS experiment at the Large Hadron Collider (LHC). The observed (expected) 95% confidence level (CL) upper limit on the non-resonant Higgs boson pair production cross-section times the $b\bar{b}\tau^+\tau^-$ branching ratio corresponds to 12.7 (14.8) times the SM prediction. The ratio of the Higgs boson self-coupling to its SM expectation, κ_λ, is observed (expected) to be constrained to $\kappa_\lambda \in [-7.4, 15.7]$ ($[-8.9, 16.8]$) at 95% CL. The sensitivity is extrapolated to a search with 14 TeV centre-of-mass energy and 3000 fb^{-1}, which is the target integrated luminosity of the High-Luminosity LHC (HL-LHC). Various extrapolation assumptions are taken into account. The estimated expected signal significance for the SM Higgs boson pair production in the $b\bar{b}\tau^+\tau^-$ final state at the HL-LHC reaches 2.1 standard deviations, while the expected allowed κ_λ interval is $\kappa_\lambda \in [-0.8, 8.8]$ at 95% CL, assuming the SM Higgs boson couplings. Furthermore, potential improvements of the analysis techniques are discussed in the context of searches for pair production of Higgs bosons with the full Run 2 ATLAS data.

To my family and friends.
It doesn't matter that this is the only page you will read.

Mojoj porodici i prijateljima.
Nema veze što ćete pročitati samo ovu stranu.

Contents

Introduction

In 2012, the ATLAS and CMS experiments at CERN's Large Hadron Collider (LHC) announced the discovery of the Higgs boson [1,2], a particle whose existence was assumed nearly a half century earlier. The existence of the Higgs field, and consequently the Higgs boson, was postulated in order to formulate a theoretical concept meant to explain the origin of mass of fundamental particles – the Higgs mechanism [3–6]. The Higgs mechanism is incorporated into the Standard Model (SM) of particle physics [3–5, 7–10] in order to explain the generation of masses for the weak gauge bosons through electroweak symmetry breaking.

The observed Higgs boson is found to interact and decay in many of the ways predicted by the SM; however, some of its predicted fundamental characteristics have not yet been directly tested. The SM predicts a specific feature of the Higgs boson, namely that it can couple to itself. The strength of this coupling is directly related to the shape of the Higgs potential, and therefore it is essential for probing the exact nature of electroweak symmetry breaking. Although Higgs boson self-coupling has not been experimentally established, it is expected that it can be observed by searching for pair production of Higgs bosons, which is discussed in this thesis in the context of the ATLAS experiment at the LHC.

Based on the SM predictions, production of pairs of Higgs bosons (HH) at the LHC is mostly determined by the strength of the Higgs boson self-coupling and the top-quark Yukawa coupling. The predicted HH production cross-section is very low – three orders of magnitude lower than for the single Higgs boson production – and thus it is unlikely that this process can be observed with the amount of LHC data currently available. On the other hand, modifications to the Higgs boson self-coupling or top-quark Yukawa coupling could significantly increase the cross-section, in which case the observation of HH production would already be possible.

Furthermore, numerous theories beyond the SM have been developed in order to solve some of the SM shortcomings. Some of these theories, such as two-Higgs-doublet models [11] and the Randall-Sundrum model [12–14], predict heavy resonances that could decay into pairs of Higgs bosons. Hence, an observation of resonant pair production of Higgs bosons would be a direct link to physics beyond the SM.

This thesis describes searches for non-resonant and resonant pair production of Higgs bosons in the final state with two bottom quarks and two τ leptons ($b\bar{b}\tau^+\tau^-$ final state). The results are obtained based on proton-proton

(pp) collision data recorded between 2015 and 2018 at a centre-of-mass energy ($\sqrt{s}$) of 13 TeV by the ATLAS detector at the LHC. Non-resonant pair production of Higgs bosons is searched for assuming the SM Higgs boson couplings, as well as in the context of the anomalous Higgs boson self-coupling. In addition, resonant pair production of Higgs bosons is searched for in the context of a generic narrow-width spin-0 resonance and spin-2 Kaluza-Klein excitations of the graviton in the bulk Randall-Sundrum model.

An overview of the theoretical concepts relevant for the scope of this thesis is given in Chapters 1 and 2. The main characteristics of the LHC and the ATLAS detector are described in Chapter 3. In addition, a short outline of the usage of Monte Carlo simulations in collider physics experiments is given in the same chapter. Chapter 4 describes algorithms used to reconstruct and identify different physics objects – proxies for particles travelling through the ATLAS detector – that are used for data analysis.

Chapters 5 and 6 describe searches for non-resonant and resonant pair production of Higgs bosons in the $b\bar{b}\tau^+\tau^-$ final state using 36.1 fb^{-1} of 13 TeV pp collision data recorded by the ATLAS detector during 2015 and 2016, for which the results were published in Refs. [15] and [16].

In Chapter 7, results from Chapters 5 and 6 are extrapolated to estimate the sensitivity to pair production of Higgs bosons and the (anomalous) Higgs boson self-coupling at the High-Luminosity Large Hadron Collider (HL-LHC)[1], for which the results were published in Ref. [17].

Chapter 8 outlines proposals for revising several of the background estimation techniques presented in Chapter 5 in the context of the ongoing searches for pair production of Higgs bosons in the $b\bar{b}\tau^+\tau^-$ final state with the full ATLAS dataset recorded between 2015 and 2018, corresponding to 139 fb^{-1} of 13 TeV pp collision data.

Finally, one of the major challenges when searching for signal processes in final states with hadronically-decaying τ leptons is to correctly estimate contributions from background processes in which detector objects identified as hadronically-decaying τ leptons actually come from misidentified quark- or gluon-initiated jets. The methods used for this purpose are discussed in detail in Chapters 5 and 8.

Author's contribution

The work presented in this thesis was performed within the ATLAS collaboration which comprises more than 3000 members. Given the complexity of the experiment and the efforts needed to successfully operate the detector and the supporting infrastructure, any output from the collaboration is the product of a

[1]The High-Luminosity Large Hadron Collider (HL-LHC) project is a planned upgrade of the LHC and its experiments, with an objective to collect $\sim$ 10 times more data than originally planned for the LHC project and thus increase the potential for new discoveries.

joint work of many people. The author's personal contributions to the studies and results presented in this thesis are summarised in the following.

The thesis describes searches for pair production of Higgs bosons in the $b\bar{b}\tau^+\tau^-$ channel to which the author has significantly contributed over the last four years. For the results presented in Chapter 5, the author simulated and validated some of the signal samples listed in Section 5.1, derived the theoretical uncertainties on signal predictions, as outlined in Section 5.5.2, designed the $Z \to \mu\mu + bb$ control region described in Section 5.3.5, investigated the background modelling in the fully hadronic final state, and participated in cross-checking and validating the final results.

For the results presented in Chapter 6, the author implemented and validated the linear combination method and κ_λ re-weighting described in Section 6.1, and furthermore he was one of the leading contributors to developing the analysis strategy presented in Section 6.2 and deriving the final results presented in Section 6.3. Additionally, the author contributed to the statistical combination of the results obtained in the $b\bar{b}\tau^+\tau^-$ channel with those obtained from $b\bar{b}b\bar{b}$ and $b\bar{b}\gamma\gamma$ channels.

The author was also the leading contributor to the estimation of the sensitivity to pair production of Higgs bosons in the $b\bar{b}\tau^+\tau^-$ final state at the HL-LHC presented in Chapter 7, as well as one of the contributors to the statistical combination of the sensitivities estimated in the $b\bar{b}\tau^+\tau^-$, $b\bar{b}b\bar{b}$ and $b\bar{b}\gamma\gamma$ channels. Additionally, the author was one of the editors of the ATLAS public note [17], in which the complete results are summarised.

Since early 2019, the author is one of the contributors to ongoing searches for pair production of Higgs bosons with the full ATLAS dataset recorded between 2015 and 2018, for which much of the author's work is discussed in Chapter 8. The author also was an active member of the ATLAS taskforce formed to develop a unified method for estimating background contributions from processes where quark- or gluon-initiated jets are misidentified as hadronically-decaying τ leptons. While these efforts are still ongoing, some of the results obtained are incorporated into the author's work presented in Chapter 8.

Beyond the scope of this thesis, the author participated in the search for boosted[2] resonant pair production of Higgs bosons in the $b\bar{b}\tau^+\tau^-$ final state, recently published in Ref. [18]. For this analysis, the author participated in developing the analysis framework and he implemented a data-driven technique used to estimate the QCD-induced multijet background. As a service task for the ATLAS collaboration, the author occasionally took part in the central trigger software validation.

[2]The term boosted here indicates that the Higgs bosons (produced in the decay of a hypothetical heavy resonance) have large transverse momenta and that their decay products are therefore collimated and difficult to reconstruct as resolved detector objects. In such cases, dedicated reconstruction and identification techniques are used.

1. The Standard Model and the Higgs boson

An overview of the theoretical foundations of elementary particle physics is given in this chapter [19–22]. The Standard Model (SM) of particle physics [3–5, 7–10] describes the building blocks of the visible universe and three out of the four known fundamental interactions. The SM incorporates quantum electrodynamics (QED), the Glashow-Weinberg-Salam theory of electroweak interactions and quantum chromodynamics (QCD). Gravity is not part of this list, which is not a significant shortcoming in describing physics at energy scales typical for particle physics experiments given that the gravitational force is astonishingly weak compared to the other fundamental interactions.

Furthermore, the motivation for incorporating the Higgs mechanism into the unified electroweak theory is briefly explained. The Higgs mechanism postulated the existence of the Higgs boson, which was the last particle of the SM to be discovered by the ATLAS and CMS collaborations at the LHC [1,2]. Important properties of the Higgs boson relevant for this thesis are reviewed. Finally, the pair production of Higgs bosons within the SM is discussed in the context of the LHC.

1.1 Particles in the Standard Model

All the particles predicted by the SM have been experimentally observed. The particle content of the SM consists of: spin-$1/2$ fermions – the matter particles; spin-1 gauge bosons – the force mediators; and the spin-0 Higgs boson. The matter particles can be further split into *leptons* (electron, electron neutrino, muon, muon neutrino, tau lepton and tau neutrino: e^-, ν_e, μ^-, ν_μ, τ^- and ν_τ, respectively) and *quarks* (down, up, strange, charm, bottom and top: d, u, s, c, b and t, respectively). These two types of elementary fermions are different in many aspects, but the main difference is that quarks are subject to the *strong interaction*, while leptons are not. Both quarks and leptons appear in six *flavours*, and they are organised into three generations. A particle from one generation has the same fundamental properties as the corresponding particle from another generation, except for the mass. Each generation consists of one "up-type" and one "down-type" fermion and they are defined as follows:

$$\begin{pmatrix} \nu_e \\ e^- \end{pmatrix} \begin{pmatrix} \nu_\mu \\ \mu^- \end{pmatrix} \begin{pmatrix} \nu_\tau \\ \tau^- \end{pmatrix} \quad \begin{pmatrix} u \\ d \end{pmatrix} \begin{pmatrix} c \\ s \end{pmatrix} \begin{pmatrix} t \\ b \end{pmatrix}. \tag{1.1}$$

Neutrinos are up-type fermions and they are electrically neutral particles. In the SM, neutrinos are massless, although this contradicts experimental evidence of their oscillation [23, 24], which requires non-zero masses. The charged leptons ($Q = -1$)[1] are classified as down-type fermions. All quarks carry a fractional elementary electric charge (up-type quarks: $Q = 2/3$, down-type quarks: $Q = -1/3$). Quarks carry an additional quantum number, *colour*, which can take three values: red (R), blue (B) and green (G). Each fermion has an antiparticle[2] with identical mass and opposite quantum numbers. All the elementary particles in the SM, their spin, charge and approximate mass, based on Ref. [25], are shown in Figure 1.1.

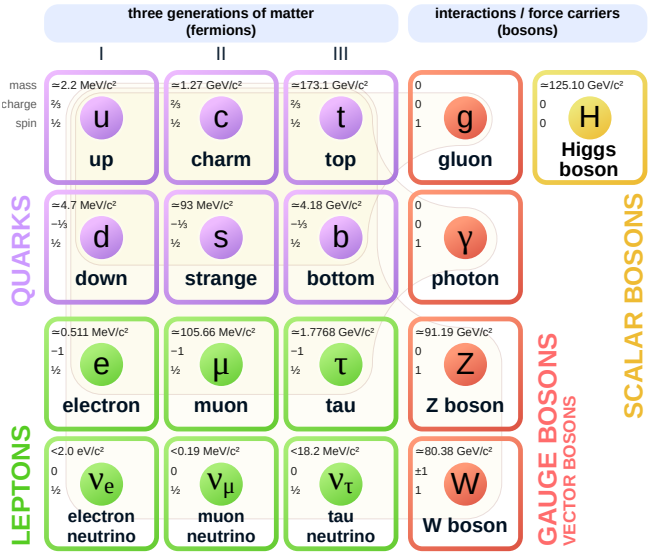

Figure 1.1. Elementary particles in the Standard Model [25].

All visible stable matter in the Universe is made of first generation fermions, i.e. the lightest matter-particles. When produced, the particles of the second and third generation, except for neutrinos, directly or indirectly decay into the particles of the first generation. As already mentioned, the SM describes three fundamental interactions. The *electromagnetic interaction* is mediated by the photon and it occurs between all electrically charged particles. The *strong interaction* is mediated by the gluons and it occurs between all the particles

[1] In this thesis, natural units ($c = \hbar = 1$, where c is the speed of light and $\hbar$ is the reduced Planck constant) are used unless stated otherwise. Electric charge is expressed in terms of the elementary charge, $e \approx 1.602 \times 10^{-19}$ C, and energy, mass and momentum are given in electronvolts, 1 eV$\approx 1.602 \times 10^{-19}$ J.

[2] It is still not clear whether neutrinos are Dirac (particle $\neq$ antiparticle, $\nu \neq \bar{\nu}$), or Majorana ($\nu \equiv \bar{\nu}$) fermions.

that carry the colour charge, namely the quarks and gluons. Finally, the *weak interaction* is mediated by the $W^{\pm}$ and Z bosons. All elementary fermions carry the charge of the weak interaction – the *weak isospin*, and therefore are subject to it. The electromagnetic and strong interactions conserve the parity symmetry ($\vec{x} \to -\vec{x}$), while the weak interaction violates it, which was first shown experimentally in nuclear β-decays of polarised cobalt-60 [26].

1.2 Symmetries in elementary particle physics

The concept of symmetries in elementary particle physics is widely used. The symmetry group of space-time in quantum relativistic physics, i.e. the group of Minkowski space-time isometries, is the Poincaré group. Particles transform under irreducible unitary representations of this group. Some of these representations are the scalar fields $\phi(x)$, vector fields $V_\mu(x)$, spinor fields $\psi(x)$, etc., classified according to the mass and spin, which are the properties of a particle that are related to the space-time symmetry.

Another group of symmetry transformations are discrete transformations. The parity symmetry (P) and its violation in the weak interaction was already mentioned. Two other important discrete symmetries are time reversal (T) and charge conjugation (C). The latter can be thought of as exchanging particle and antiparticle. The CPT-symmetry is the sole combination of C, P and T that is considered to be an exact symmetry of the Universe, while other combinations may or may not be conserved, depending on the type of interaction.

In quantum field theory it is important to also consider the *internal symmetries*, which are discussed in this section. Based on *Noether's theorem* [27], every differentiable symmetry of the action of a physical system corresponds to some conservation law. The symmetries of the space-time yield the conservation laws of linear momentum and energy, angular momentum, etc. Similarly, conservation laws of flavour, charge, colour and some other particle properties are the consequences of certain internal symmetries.

An important concept in the SM is that a free theory of N complex fields is invariant under the $\mathrm{U}(1)\times\mathrm{SU}(N)$ symmetry, where $\mathrm{U}(1)$ is a unitary group of one degree, while $\mathrm{SU}(N)$ is a special unitary group of degree N. These are examples of Lie groups[3]. Any Lie-group element can be written as

$$U = e^{i\theta^a T^a}, \tag{1.2}$$

where θ^a are real parameters of the group and T^a are the *group generators*. In contrast to *global* symmetries, local (*gauge*) symmetries are parameterised by a function that depends on space-time coordinates: $\theta \to \theta(x)$, and they are essential for defining the three fundamental interactions of the SM.

[3]Lie groups are a class of groups with a finite number of group generators, but infinite number of group elements that are organised continuously and smoothly.

1.2.1 Quantum electrodynamics

Quantum electrodynamics describes interactions involving electrically charged particles that are mediated by the photon. Its precision has been rigorously tested and it represents one of the most accurate theories ever developed.

The Dirac Lagrangian[4] describes a free massive fermion

$$\mathscr{L}_{Dirac} = \bar{\psi}(x)(i\gamma^{\mu}\partial_{\mu} - m)\psi(x), \tag{1.3}$$

where $\psi(x)$ is the fermionic field, γ_{μ} are the gamma matrices, $\partial_{\mu} = \partial/\partial x^{\mu}$ is the derivative with respect to x^{μ} and m is the fermion mass. The Dirac Lagrangian is invariant under global U(1) transformations

$$\psi(x) \xrightarrow{\mathrm{U(1)}} \psi'^{\mu}(x) = e^{i\alpha}\psi(x), \tag{1.4}$$

where α is a constant phase; however, it is not invariant under local U(1) transformations: $\alpha \to \alpha(x)$. Gauge invariance itself is not physical, although it implies a global symmetry that has physical consequences. On the other hand, gauge invariance is needed to introduce a local description of massless spin-1 particles, in this case the photon.

To achieve the U(1) gauge invariance, the derivative ∂_{μ} is replaced by the corresponding covariant derivative D_{μ},

$$D_{\mu} = \partial_{\mu} - ieA_{\mu}, \tag{1.5}$$

where the gauge field A_{μ} is now introduced. The covariant derivative has to transform in the same way as the fermionic field transforms under the U(1) gauge transformations: $D_{\mu}\psi \to D'_{\mu}\psi' = e^{i\alpha(x)}D_{\mu}\psi$. For this particular definition of the covariant derivative, the following transformation rule is obtained for the gauge field:

$$A_{\mu} \xrightarrow{\mathrm{U(1)}} A'_{\mu} = A_{\mu} + \frac{1}{e}\partial_{\mu}\alpha(x). \tag{1.6}$$

The kinetic term for the gauge field A_{μ},

$$-\frac{1}{4}F_{\mu\nu}F^{\mu\nu}, \tag{1.7}$$

is added to the Lagrangian, where $F_{\mu\nu} = \partial_{\mu}A_{\nu} - \partial_{\nu}A_{\mu}$ is the electromagnetic field strength. The QED Lagrangian is then written as

$$\begin{aligned}\mathscr{L}_{QED} &= \bar{\psi}(i\gamma^{\mu}\partial_{\mu} - m)\psi + \underbrace{e\bar{\psi}\gamma^{\mu}\psi A_{\mu}}_{\mathscr{L}_{Int}} - \frac{1}{4}F_{\mu\nu}F^{\mu\nu} = \\ &= \bar{\psi}(i\gamma^{\mu}D_{\mu} - m)\psi - \frac{1}{4}F_{\mu\nu}F^{\mu\nu}.\end{aligned} \tag{1.8}$$

[4] In this thesis the Lagrangian density is always used, even when only the term "Lagrangian" is mentioned.

The interaction term, $\mathscr{L}_{Int}$, describes the coupling of the gauge field to fermionic fields. The gauge boson is required to be massless, since a mass term of the form $m_\gamma^2 A_\mu A^\mu$ would break the gauge invariance. After deriving equations of motion and fixing the Lorentz gauge condition ($\partial_\mu A^\mu = 0$), the theory yields the QED version of the classical Maxwell equations.

1.2.2 Quantum chromodynamics and colour confinement

Quantum chromodynamics describes the strong interaction, which is mediated by the gluons. As already mentioned, quarks exist in different flavours, but also in different colours. The Lagrangian for a free quark field can be written as

$$\mathscr{L}_{Dirac} = \bar{q}_f(x)(i\gamma^\mu \partial_\mu - m)q_f(x), \tag{1.9}$$

where q_f is a quark field of flavour f. The q_f field is a colour triplet of the SU(3) group,

$$q_f = \begin{pmatrix} q_f^R \\ q_f^G \\ q_f^B \end{pmatrix}. \tag{1.10}$$

Similar to QED, the localisation of symmetry introduces interactions. A quark field transforms as

$$q_f(x) \xrightarrow{\text{SU(3)}} q'_f(x) = e^{i\alpha^a(x)T^a} q_f(x), \tag{1.11}$$

where $T^a = \frac{\lambda^a}{2}$ are the generators of the SU(3) group, $a = \{1, 2, \cdots, 8\}$. The λ^a are the Gell-Mann matrices. Since SU(3) is a non-Abelian group, the group algebra is defined by the commutation relation $[T^a, T^b] = if^{abc}T^c$, where f^{abc} is the group structure constant. The covariant derivative is defined as

$$D_\mu = \partial_\mu - i\alpha_s \frac{\lambda^a}{2} G_\mu^a, \tag{1.12}$$

where 8 gauge (gluon) fields, G_μ^a, are introduced. The coupling constant of the strong interaction is labelled as α_s. After adding the kinetic term for the gauge fields, the QCD Lagrangian is

$$\mathscr{L}_{QCD} = \sum_f \bar{q}_f(i\gamma^\mu D_\mu - m)q_f - \frac{1}{4} G_{\mu\nu}^a G^{a\mu\nu}, \tag{1.13}$$

where $G_{\mu\nu}^a = \partial_\mu G_\nu^a - \partial_\nu G_\mu^a + \alpha_s f^{abc} G_\mu^b G_\nu^c$ is the gluon field tensor. The last term is required as a consequence of the non-Abelian nature of the SU(3) group, and it implies the existence of triple and quartic gluon self-interactions.

Much experimental evidence confirms the existence of quarks and gluons, although these particles have never been directly detected. This is explained

by the hypothesis that a colour-charged particle cannot be free due to the phenomenon called *colour confinement*. Only colour-neutral particles can be observed: if quarks or gluons are created, they quickly undergo a process called *hadronisation*. A qualitative description [21] of the process of hadronisation is such that if, for instance, two quarks are created and if they start separating at high velocities, the potential of the confined colour field between them becomes stronger[5]. With enough distance between the quarks, there is enough energy to create another quark-antiquark ($q\bar{q}$) pair, which breaks the colour field into two strings. The process continues until the produced quarks reach sufficiently low energy to form colourless hadron states – *mesons* ($q\bar{q}$ states) and *baryons* (qqq states)[6]. Due to its short lifetime, only the top quark decays before there is enough time for it to hadronise.

Another characteristic of the strong interaction is that, within a hadron, the *partonic constituents* – the valence quarks that determine the properties of a hadron, as well as any virtual quarks and gluons – are relatively free to move. This phenomenon is called *asymptotic freedom*. Both concepts, colour confinement and asymptotic freedom, can be understood in terms of a running coupling constant. At low energy scales (large distances), the strong coupling, α_s, is large and the theory describing this regime is non-perturbative [29]. At high scales (small distances), α_s is small and the theory is perturbative [30,31]. The electromagnetic coupling constant depends on the scale as well, but it exhibits an opposite trend [32], and QED remains perturbative at all probed scales.

1.2.3 Electroweak interactions

The weak interactions are related to the SU(2) gauge symmetry. If ψ is a doublet of two Dirac spinors, the Dirac Lagrangian from Equation (1.3) is invariant under global SU(2) transformations. The SU(2) group has three group generators, $T^a = \frac{\sigma^a}{2}$, $a = \{1,2,3\}$, where σ^a are the Pauli matrices. Similar to SU(3), the group is non-Abelian, with a group algebra defined by the commutation relation $[T^a, T^b] = if^{abc}T^c$.

In order to account for the observed parity violation in the weak interactions, Dirac spinors are decomposed into "left-" (L) and "right-handed" (R) *chiral* components,

$$\psi_L = \frac{1}{2}(1-\gamma^5)\psi; \;\; \psi_R = \frac{1}{2}(1+\gamma^5)\psi; \;\; \psi = \psi_L + \psi_R, \tag{1.14}$$

where $\gamma^5 = i\gamma^0\gamma^1\gamma^2\gamma^3$ is the product of γ-matrices. The left-handed chiral states of quarks and leptons are organised into SU(2) doublets, similarly to

[5]The energy stored in the field is proportional the separation of the quarks, r, contributing to the potential with a $V(r) \sim \kappa r$ term, where $\kappa \sim 1$ GeV/fm has been experimentally determined.
[6]Hadrons containing 5 quarks, *pentaquarks*, have also been detected in recent years [28].

those defined in Equation (1.1),

$$L = \left\{ \begin{pmatrix} \nu_e \\ e^- \end{pmatrix}_L, \begin{pmatrix} \nu_\mu \\ \mu^- \end{pmatrix}_L, \begin{pmatrix} \nu_\tau \\ \tau^- \end{pmatrix}_L \right\} \quad Q = \left\{ \begin{pmatrix} u \\ d \end{pmatrix}_L, \begin{pmatrix} c \\ s \end{pmatrix}_L, \begin{pmatrix} t \\ b \end{pmatrix}_L \right\}. \tag{1.15}$$

The right-handed chiral states of charged fermions are SU(2) singlets,

$$l_R = \left\{ e_R^-, \mu_R^-, \tau_R^- \right\}, \; q_R^u = \{u_R, c_R, t_R\}, \text{ and } q_R^d = \{d_R, s_R, b_R\}. \tag{1.16}$$

In the SM, neutrinos and antineutrinos exist only in left-handed and right-handed chiral states, respectively. The grouping of different states in Equations (1.15) and (1.16) is based on the weak isospin, or more precisely the third component of the weak isospin, T_3, that each particle carries. The up-type and down-type fermions of left-handed chirality have $T_3 = \frac{1}{2}$ and $T_3 = -\frac{1}{2}$, respectively. The right-handed chiral states do not carry weak isospin, and thus do not interact with the weak gauge fields, W_μ^a ($a = \{1,2,3\}$), which are introduced as part of the localisation of the SU(2) symmetry. This is in agreement with experimental observations for the weak charged-currents; however, it is not in agreement with observations that the physical Z boson couples to both left- and right-handed chiral states. This apparent inconsistency is resolved in the formalism of the unified electromagnetic and weak interactions.

The electromagnetic and weak interactions are combined into the electroweak interaction, described by the $\mathrm{U}(1)_Y \times \mathrm{SU}(2)_L$ gauge symmetry, where $\mathrm{U}(1)_Y$ is referred to as the high-energy U(1) symmetry, which gives rise to a gauge field B_μ that couples to a new charge Y called *weak hypercharge*. The SU(2) symmetry is labelled with the index L to indicate that only the left-handed chiral states carry weak isospin. The weak isospin and hypercharge are related to each other, namely

$$Q = T_3 + \frac{Y}{2}, \tag{1.17}$$

where Q is electric charge. Both up- and down-components of the L and Q doublets carry the same weak hypercharge, denoted as Y_L and Y_Q, respectively. The part of the Lagrangian containing the kinetic terms for the leptons and the interaction of leptons with the four gauge fields, B_μ and W_μ^a, with coupling constants g_1 and g_2, can be written as

$$\begin{aligned} \mathscr{L}_l = {} & i\bar{L}_j \gamma^\mu (\partial_\mu - ig_1 \frac{Y_L}{2} B_\mu - ig_2 \frac{\sigma^a}{2} W_\mu^a) L_j \\ & + i\bar{l}_{Rj} \gamma^\mu (\partial_\mu - ig_1 \frac{Y_{l_R}}{2} B_\mu) l_{Rj}, \end{aligned} \tag{1.18}$$

where all generations are included after summing over j. Similarly, the part of the Lagrangian that includes the kinetic terms for quarks and the interaction

of quarks with the electroweak gauge fields is defined by

$$\begin{aligned}\mathscr{L}_q = & i\bar{Q}_j\gamma^\mu(\partial_\mu - ig_1\frac{Y_Q}{2}B_\mu - ig_2\frac{\sigma^a}{2}W^a_\mu)Q_j \\ & + i\bar{q}^u_{Rj}\gamma^\mu(\partial_\mu - ig_1\frac{Y_{q^u_R}}{2}B_\mu)q^u_{Rj} + i\bar{q}^d_{Rj}\gamma^\mu(\partial_\mu - ig_1\frac{Y_{q^d_R}}{2}B_\mu)q^d_{Rj}. \end{aligned} \tag{1.19}$$

The kinetic terms of the gauge fields and the self-interaction of the weak gauge bosons are written as

$$\mathscr{L}_{gauge} = -\frac{1}{4}W^a_{\mu\nu}W^{a\mu\nu} - \frac{1}{4}F_{\mu\nu}F^{\mu\nu}, \tag{1.20}$$

where $W^a_{\mu\nu} = \partial_\mu W^a_\nu - \partial_\nu W^a_\mu + g_2 f^{abc}W^b_\mu W^c_\nu$ and $F_{\mu\nu} = \partial_\mu B_\nu - \partial_\nu B_\mu$ are the field tensors for the W^a_μ and B_μ gauge fields.

The physical manifestations of the carriers of the electroweak force are superpositions of the introduced gauge fields,

$$\begin{aligned} W^\pm_\mu &= \frac{1}{\sqrt{2}}(W^1_\mu \mp W^2_\mu) \\ Z^\mu &= \frac{1}{\sqrt{g_1^2+g_2^2}}(g_2W^3_\mu - g_1B_\mu) \\ A^\mu &= \frac{1}{\sqrt{g_1^2+g_2^2}}(g_1W^3_\mu + g_2B_\mu), \end{aligned} \tag{1.21}$$

which is a consequence of the electroweak symmetry breaking, as it will be explained shortly. The mixing of the W^3_μ and B_μ gauge fields is parameterised by the *weak mixing angle*, $\theta_W = \tan(g_1/g_2)$, which has been experimentally measured as $\sin^2\theta_W = 0.23122(15)$ [25,33]. The electric charge can be expressed as $e = g_1\cos\theta_W = g_2\sin\theta_W$, at leading order. The fields Z^μ and A^μ represent the physical Z boson and the photon, respectively. The Lagrangian consisting of $\mathscr{L}_l + \mathscr{L}_q + \mathscr{L}_{gauge}$ describes *massless* fermions and gauge bosons, which contradicts experimental observations. This inconsistency is resolved by introducing the symmetry breaking mechanism into the theory of electroweak interactions.

1.3 Electroweak symmetry breaking

A mechanism able to account for the mass generation of the weak gauge bosons, without "breaking" the gauge theory, was proposed by several theorists in 1964 [3–6]. Since then, this mechanism, today known as the *Higgs mechanism*, has become an essential part of the SM.

1.3.1 The Higgs mechanism

The lowest-energy (vacuum) state of a theory is not necessarily invariant under the full symmetry of the corresponding Lagrangian. The symmetry is spontaneously broken when the system goes to such a vacuum state. To show that the $\mathrm{U}(1)_Y \times \mathrm{SU}(2)_L$ symmetry of the electroweak interaction is spontaneously broken, a $\mathrm{SU}(2)$ doublet of complex scalar fields,

$$\Phi = \begin{pmatrix} \phi^+ \\ \phi^0 \end{pmatrix} = \frac{1}{\sqrt{2}} \begin{pmatrix} \phi_1 + i\phi_2 \\ \phi_3 + i\phi_4 \end{pmatrix}, \tag{1.22}$$

with weak hypercharge $Y_\Phi = 1$, is considered. The Lagrangian, written as

$$\mathscr{L}_{Higgs} = (D_\mu \Phi)^\dagger (D^\mu \Phi) - V(\Phi), \tag{1.23}$$

is invariant under the $\mathrm{U}(1)_Y \times \mathrm{SU}(2)_L$ symmetry if the covariant derivative is constructed as

$$D_\mu = \partial_\mu - i g_1 \frac{Y_\Phi}{2} B_\mu - i g_2 \frac{\sigma^a}{2} W_\mu^a, \tag{1.24}$$

and if the Higgs potential if defined as

$$V(\Phi) = \mu^2 \Phi^\dagger \Phi + \lambda (\Phi^\dagger \Phi)^2. \tag{1.25}$$

Two parameters determine the shape of the potential, μ^2 and λ. In order to have a stable theory with a defined vacuum state, the potential has to be bounded from below, which is possible only if $\lambda > 0$. The second parameter, μ^2, can take either positive or negative values. If $\mu^2 \geq 0$, the potential has a global minimum at $\phi_i = 0$, $i = \{1,2,3,4\}$, and thus the $\mathrm{U}(1)_Y \times \mathrm{SU}(2)_L$ symmetry remains unbroken. On the other hand, if $\mu^2 < 0$, all states that satisfy

$$\sum_i \phi_i^2 = -\frac{\mu^2}{\lambda} \equiv v^2 \tag{1.26}$$

are vacuum states. Here, v denotes the vacuum expectation value of the Higgs field. Due to reasons discussed in the following, a vacuum state

$$\langle \Phi \rangle = \frac{1}{\sqrt{2}} \begin{pmatrix} 0 \\ v \end{pmatrix} \tag{1.27}$$

is chosen. When acting on this vacuum, all the generators of the $\mathrm{U}(1)_Y \times \mathrm{SU}(2)_L$ symmetry group yield non-zero results from which it follows that the vacuum is not invariant under the symmetry of the electroweak interactions. However, one linear combination of these generators,

$$\hat{Q} = T^3 + \frac{Y_\Phi}{2}, \tag{1.28}$$

preserves the symmetry of the vacuum, which is thus defined by the $\mathrm{U}(1)$ group, for which the generator is $\hat{Q}$. As a consequence, based on Equation (1.17), the electric charge is conserved, which is why this symmetry group

is referred to as $U(1)_{EM}$. Electroweak symmetry breaking (EWSB) is thus specified as:

$$U(1)_Y \times SU(2)_L \xrightarrow{\text{EWSB}} U(1)_{EM}. \tag{1.29}$$

The shape of the Higgs potential is shown in Figure 1.2 together with an illustration of the Higgs mechanism.

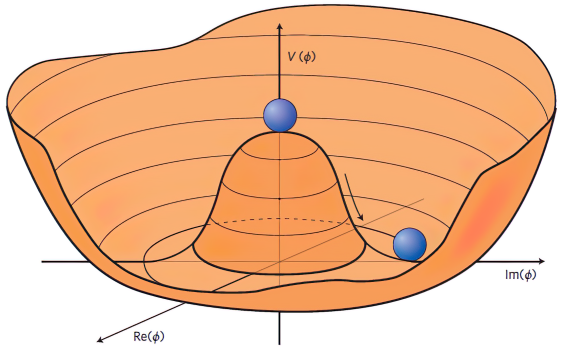

Figure 1.2. The Higgs potential is shown. The vacuum state is degenerate, represented by a circle at the bottom. The symmetry of the electroweak interaction is spontaneously broken when the system chooses one particular vacuum state. The Higgs boson corresponds to radial quantum fluctuations around the vacuum [34].

After the symmetry breaking, the photon is required to be massless, and thus the vacuum for which only the down-component of the Higgs doublet acquires non-zero vacuum expectation value is chosen. The fields can be expanded about this vacuum and for a doublet of complex scalar fields, there are four degrees of freedom. After the spontaneous symmetry breaking, one massive (Higgs) field and three massless bosonic (*Goldstone*) fields appear in the Lagrangian. These Goldstone fields are not physical and are ultimately absorbed to give the longitudinal degrees of freedom of the $W^{\pm}$ and Z bosons. Thus, the Lagrangian given by Equation (1.23) can be rewritten in the unitary gauge[7], $\phi^+ = 0$ and $\phi^0(x) \to v + H(x)$, where $H(x)$ denotes the physical Higgs field, as

$$\mathscr{L}_{Higgs} = \partial_\mu H \partial^\mu H + \left(m_W^2 W_\mu^+ W^{\mu-} + m_Z^2 Z_\mu Z^\mu\right)\left(1 + \frac{H}{v}\right)^2 + \underbrace{-\lambda v^2 H^2}_{\text{Higgs boson mass term}} \underbrace{-\lambda v H^3 - \frac{1}{4}\lambda H^4}_{\text{Higgs boson self-interaction}}, \tag{1.30}$$

[7]The unitary gauge here refers to choosing the complex scalar field ϕ^0 to be entirely real and ϕ^+ to be zero. This choice does not change the physical predictions; however, it ensures that the fields appearing in the Lagrangian correspond to the physical particles.

where the masses of the Higgs and weak gauge bosons are defined as:

$$m_H = \sqrt{-2\mu^2} = \sqrt{2\lambda v^2}; \quad m_W = \frac{1}{2} g_2 v; \quad m_Z = \frac{1}{2} v \sqrt{g_1^2 + g_2^2}. \tag{1.31}$$

The Lagrangian given by Equation (1.30) has been transformed by way of diagonalising the "mass matrix" that connects the terms quadratic in the neutral W_μ^3 and B_μ fields, which defines the transformations given by Equation (1.21). This Lagrangian includes the kinetic term of the Higgs boson, the mass terms for the Higgs, W and Z bosons, as well as terms describing the interaction of the Higgs boson with the W and Z bosons and terms corresponding to the trilinear and quartic Higgs boson self-couplings.

The Higgs boson was the last particle of the SM to be discovered, almost 50 years after the Higgs mechanism was proposed. Its discovery was announced by the ATLAS and CMS collaborations in 2012 [1,2]. Since then, the mass of the Higgs boson has been measured to be $m_H = 125.10 \pm 0.14$ GeV [25]. The vacuum expectation value of the Higgs field is determined [25] to be

$$v = \frac{2m_W}{g_2} = \sqrt{\frac{1}{\sqrt{2} G_F}} \approx 246.22 \text{ GeV}. \tag{1.32}$$

The first equality follows from Equation (1.31), while the second one is based on the definition of the Fermi constant, G_F[8]. Thus, the SM unambiguously predicts the shape of the Higgs potential. The trilinear and quartic Higgs boson self-coupling constants are defined as

$$\lambda_{HHH} = \lambda v = \frac{m_H^2}{2v} \text{ and } \lambda_{HHHH} = \frac{\lambda}{4} = \frac{m_H^2}{8v^2}, \tag{1.33}$$

while the corresponding Feynman vertices are shown in Figure 1.3. Although λ_{HHH} and λ_{HHHH} are determined in the SM, thus far there is no experimental evidence of the occurrence of these interactions in nature. An important part of the results presented in this thesis refers to searches for pair production of Higgs bosons. Their (negative) outcome allows to set experimental constraints on the strength of the trilinear Higgs boson self-coupling. Furthermore, prospects for observing the Higgs boson self-interactions at the HL-LHC are discussed in Chapter 7.

1.3.2 Fermion masses and Yukawa coupling

In the Dirac Lagrangian, which is given by Equation (1.3), the fermion mass term, $-m\bar{\psi}\psi = -m(\bar{\psi}_R \psi_R + \bar{\psi}_L \psi_L)$, is not invariant under the $\mathrm{SU}(2)_L \times \mathrm{U}(1)_Y$

[8]The Fermi constant, $G_F = 1.166\ 378\ 7(6) \times 10^{-5}$ GeV^{-2} [25], is determined by measuring the lifetime of antimuons with extremely high precision [35].

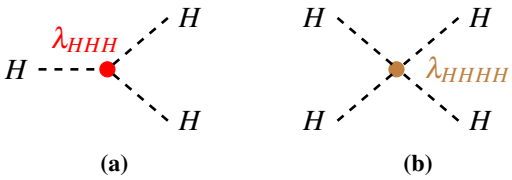

Figure 1.3. Feynman vertices corresponding to (**a**) the trilinear Higgs boson self-interaction and (**b**) the quartic Higgs boson self-interaction.

symmetry as a result of the different transformations for left- and right-handed chiral states. The following terms:

$$\mathscr{L}_{Yukawa-l} = -y_l \left(\bar{L}\Phi l_R + \bar{l}_R \Phi^\dagger L\right), \tag{1.34}$$

where y_l is the *Yukawa coupling constant*, are however invariant under the gauge symmetry of the electroweak interactions. After the spontaneous symmetry breaking and writing the Higgs doublet in the unitary gauge, the Lagrangian written above is transformed into

$$\begin{aligned}\mathscr{L}_{Yukawa-l} = & \underbrace{-\frac{y_l v}{\sqrt{2}}\left(\bar{l}_L l_R + \bar{l}_R l_L\right)}_{\text{Charged-lepton mass term}} \underbrace{-\frac{y_l}{\sqrt{2}} H \left(\bar{l}_L l_R + \bar{l}_R l_L\right)}_{\text{Lepton Yukawa interaction}} \\ & = m_l \bar{l} l - \frac{y_l}{\sqrt{2}} H \bar{l} l,\end{aligned} \tag{1.35}$$

where l is the Dirac spinor describing a charged lepton. From the first term it follows that $m_l = y_l v/\sqrt{2}$.

The masses of the down-type quarks are generated equivalently; however, in order to include mass generation for the up-type quarks, additional terms containing $\tilde{\Phi} = i\sigma^2 \Phi^*$ are added:

$$\mathscr{L}_{Yukawa-q} = -y^{ij}_{q^d}\left(\bar{Q}_i \Phi q^d_{Rj} + \bar{q}^d_{Rj}\Phi^\dagger Q_i\right) - y^{ij}_{q^u}\left(\bar{Q}_i \tilde{\Phi} q^u_{Rj} + \bar{q}^u_{Rj}\tilde{\Phi}^\dagger Q_i\right). \tag{1.36}$$

The corresponding Yukawa couplings for the up- and down-type quarks are introduced and all three generations of quarks are included, $i, j = \{1,2,3\}$, to account for the experimentally-observed *quark mixing*[9]. After writing the

[9]Several experimental observations, for example the measured decay rate of $K^-(u\bar{s}) \to \mu^- \bar{\nu}_\mu$ being around 20 times smaller than the $\pi^-(u\bar{d}) \to \mu^- \bar{\nu}_\mu$ decay rate, suggest different weak couplings for different quark flavours. This is explained by the Cabibbo hypothesis for the first two generations. This hypothesis states that the quarks couple weakly with the same strength as leptons, but that the flavour eigenstates of quarks differ from the mass eigenstates. The mixing is introduced for the down-type quarks and it is parameterised by the Cabibbo angle, $\theta_C \approx 13°$ [21].

Higgs doublet in the unitary gauge, the Lagrangian is given by

$$\mathscr{L}_{Yukawa-q} = -\frac{y^{ij}_{q^d} v}{\sqrt{2}} \left(\bar{q}^d_{Li} q^d_{Rj} + \bar{q}^d_{Rj} q^d_{Li} \right) - \frac{y^{ij}_{q^u} v}{\sqrt{2}} \left(\bar{q}^u_{Li} q^u_{Rj} + \bar{q}^u_{Rj} q^u_{Li} \right) - \frac{y^{ij}_{q^d}}{\sqrt{2}} H \left(\bar{q}^d_{Li} q^d_{Rj} + \bar{q}^d_{Rj} q^d_{Li} \right) - \frac{y^{ij}_{q^u}}{\sqrt{2}} H \left(\bar{q}^u_{Li} q^u_{Rj} + \bar{q}^u_{Rj} q^u_{Li} \right). \quad (1.37)$$

Diagonalising the masses requires changing the basis, i.e. moving from the currently used "flavour basis" to the "mass basis". The Lagrangian is finally written as

$$\mathscr{L}_{Yukawa-q} = -m^d_j \bar{q}^d_j q^d_j - m^u_j \bar{q}^u_j q^u_j - \frac{y^j_{q^d}}{\sqrt{2}} H \bar{q}^d_j q^d_j - \frac{y^j_{q^u}}{\sqrt{2}} H \bar{q}^u_j q^u_j, \quad (1.38)$$

where q^u_j and q^d_j are up- and down-type quark Dirac spinors of generation j in the mass basis. All massive fermions, as shown, couple to the Higgs boson. The strength of this coupling is proportional to the fermion mass, $y = \sqrt{2}m/v$. The neutrinos in the SM, are treated as massless particles, although it is possible to extend the SM to account for their non-zero masses.

1.3.3 The CKM and PMNS matrices

Moving to the mass basis for the quark fields, i.e. going from Equation (1.37) to Equation (1.38), requires performing unitary transformations: $q^u_{Li} \to U^u_{ij} q^u_{Lj}$, $q^d_{Li} \to U^d_{ij} q^d_{Lj}$, and similar transformations for the right-handed chiral states. These transformations also affect the kinetic terms. As a consequence, gauge interactions that mix up- and down-type quarks, i.e. interactions involving the W boson, allow for mixing of the quark generations. This mixing, which is a generalisation of the Cabibbo hypothesis to all three quark generations, is parameterised by the *Cabibbo-Kobayashi-Maskawa* (CKM) *matrix*,

$$\begin{pmatrix} d \\ s \\ b \end{pmatrix} \to \underbrace{\begin{pmatrix} V_{ud} & V_{us} & V_{ub} \\ V_{cd} & V_{cs} & V_{cb} \\ V_{td} & V_{ts} & V_{tb} \end{pmatrix}}_{\text{CKM matrix, } V \equiv \bar{U}^{u\dagger} U^d} \begin{pmatrix} d \\ s \\ b \end{pmatrix}. \quad (1.39)$$

The relative strength of the qqW interaction is defined by the relevant element of the CKM matrix, which is a complex unitary matrix parameterised by three angles and one complex phase. The complex phase is related to the CP-symmetry violation in the electroweak interactions of quarks.

As mentioned previously, neutrino oscillations [23,24] imply non-zero neutrino masses. The most widely accepted model of neutrino oscillations relies

on introducing neutrino mixing, equivalent to the mixing in the quark sector, parameterised by the *Pontecorvo-Maki-Nakagawa-Sakata* (PMNS) *matrix*. The PMNS matrix is, similar to the CKM matrix, a unitary transformation between the mass and flavour eigenstates, described by three angles and one or three complex phases, depending on whether neutrinos are considered Dirac or Majorana particles [19, 36].

1.4 The Higgs boson

The Higgs boson is the only scalar elementary particle in the SM. It is electrically neutral and colourless, with positive parity. It couples to the W and Z bosons with coupling strengths that are proportional to m_W^2 and m_Z^2, respectively. Furthermore, the Higgs boson couples to fermions with a coupling strength that is proportional to the fermion mass, as discussed in Section 1.3.2.

1.4.1 Production and decay modes

The Higgs boson can be produced through a number of different processes. The dominant production modes in pp collisions are gluon-gluon fusion (ggF), vector boson fusion (VBF), Higgs-strahlung (production in association with a W or Z boson) and in association with a pair of top quarks ($t\bar{t}H$). The leading-order (LO) Feynman diagrams corresponding to these processes are shown in Figure 1.4. The leading production mechanism at the LHC is ggF production via a loop of virtual top quarks; however, other processes, such as VBF production, are important as well since the signal extraction is somewhat easier due to a more distinguishable event topology.

The cross-section for producing the Higgs boson in pp collisions as a function of the centre-of-mass energy, $\sqrt{s}$, for the different production mechanisms, is shown in Figure 1.5. The best theoretical prediction for the inclusive ggF production cross-section at $\sqrt{s} = 13$ TeV, currently available, is around $\sigma_H^{gg\text{F}} = 48.58$ pb [37] at next-to-next-to-next-to-leading order (N3LO) in QCD and next-to-leading order (NLO) in the electroweak theory, for $m_H = 125$ GeV.

Due to the nature of its couplings to the other SM particles, the Higgs boson decays preferentially into heavier fermions and into W or Z bosons. The corresponding Feynman diagrams are shown in the top row of Figure 1.6. The largest branching ratio is for the decay $H \to b\bar{b}$, for $m_H = 125$ GeV, since the decay into a pair of top quarks is not kinematically allowed given that the top quark is heavier than the Higgs boson. Although the Higgs boson mass is less than twice the W boson mass, the second largest branching ratio is for the $H \to WW^*$ decay. The star indicates that one of the W bosons is produced off-mass-shell. The Higgs boson can also indirectly decay into massless particles, such as photons and gluons, via a loop of top quarks or W bosons, as shown in

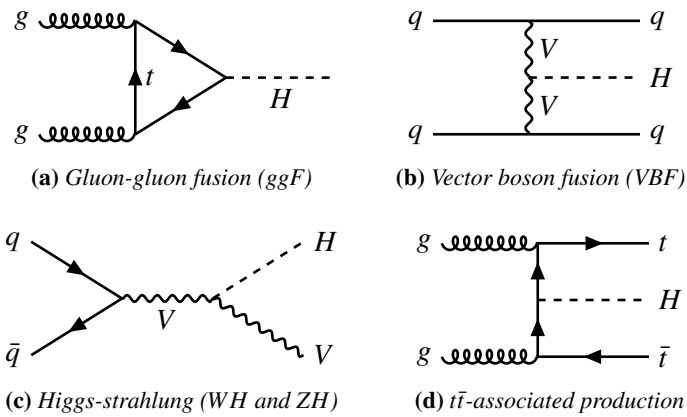

(a) *Gluon-gluon fusion (ggF)* **(b)** *Vector boson fusion (VBF)*

(c) *Higgs-strahlung (WH and ZH)* **(d)** *$t\bar{t}$-associated production*

Figure 1.4. Examples of leading-order Feynman diagrams corresponding to the dominant mechanisms for producing the Higgs boson at the LHC. The lines labelled as V refer to either the W or Z boson.

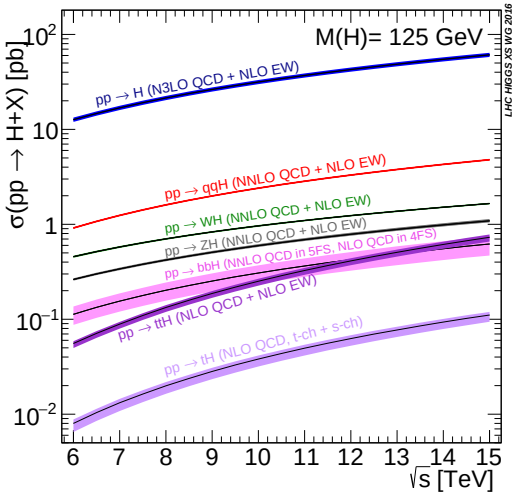

Figure 1.5. Higgs boson production cross-sections as a function of the centre-of-mass energy, $\sqrt{s}$, for pp collisions [38]. For each of the shown results, it is indicated at which order in perturbation theory they are obtained. For $pp \to H$, the results are obtained at N3LO in QCD and at NLO in the electroweak (EW) theory.

the bottom row of Figure 1.6. A list of the experimentally most relevant decay modes and their corresponding branching ratios is given in Table 1.1.

The Higgs boson was discovered at the LHC in 2012. The ATLAS and CMS collaborations announced that a new particle, consistent with the SM Higgs boson, with a mass of approximately 125 GeV, had been observed with a significance of 5.9 and 5.0 standard deviations, respectively [1, 2]. In each

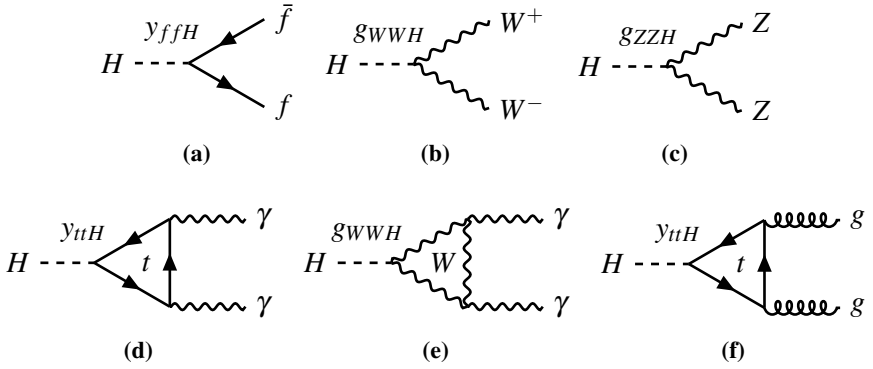

Figure 1.6. Examples of leading-order Feynman diagrams for the decays of the Higgs boson into massive fermions (excluding the top quark), W and Z bosons, photons and gluons.

Table 1.1. *Branching ratios for a SM Higgs boson with $m_H = 125$ GeV [37].*

Decay mode	Branching ratio
$H \to b\bar{b}$	0.582
$H \to WW^*$	0.214
$H \to \tau^+\tau^-$	0.0627
$H \to c\bar{c}$	0.0289
$H \to ZZ^*$	0.0262
$H \to \gamma\gamma$	0.00227

case, the discovery was a result of the combination of searches performed in several channels using 10.6 (10.4) fb^{-1} of 7 and 8 TeV ATLAS (CMS) data. The four-lepton invariant mass distributions corresponding to the searches for $H \to ZZ^* \to 4\ell$, where 4ℓ refers to $e^+e^-e^+e^-$, $\mu^+\mu^-\mu^+\mu^-$ and $e^+e^-\mu^+\mu^-$ final states, in the two experiments are shown in Figure 1.7. The observed particle is consistent with the even-parity and zero-spin hypotheses [39, 40]. Additionally, the particle has been shown to behave, interact and decay in many of the ways predicted by the SM [41, 42].

For further testing of the EWSB mechanism, a measurement of the shape of the Higgs potential is necessary. As already discussed in Section 1.3.1, the shape of the Higgs potential can be studied through the trilinear Higgs boson self-interaction. A direct way to probe the strength of this interaction is to measure the rate of pair production of Higgs bosons. Results of searches for pair production of Higgs bosons in the $b\bar{b}\tau^+\tau^-$ final state with the ATLAS detector and consequential constraints on the Higgs boson self-coupling are presented in this thesis.

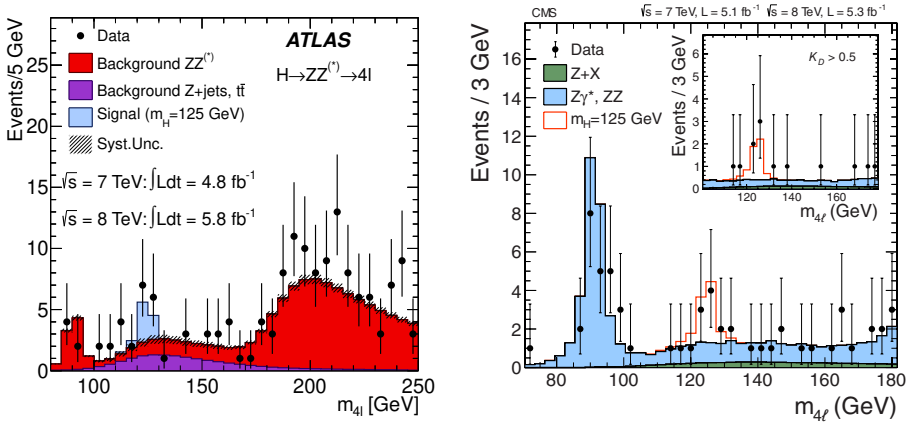

(a) **(b)**

Figure 1.7. Four-lepton invariant mass for the selected $H \to ZZ^* \to 4\ell$ candidates for the combination of 7 TeV and 8 TeV pp collision data recorded by (**a**) the ATLAS experiment [1] and (**b**) the CMS experiment [2]. The points represent the observed data, which is compared to the background expectation. The signal expectation for the SM Higgs boson with $m_H = 125$ GeV is also shown, added to the backgrounds. The inset in the plot on the right shows the four-lepton invariant mass distribution after selection of events with $K_D > 0.5$, where K_D is a kinematic discriminant based on the probability ratio of the signal and background hypotheses [2].

1.4.2 Pair production of Higgs bosons

At the LHC, based on the SM predictions, pairs of Higgs bosons (HH) are dominantly produced in ggF processes, namely via a loop of heavy quarks and via the Higgs boson self-coupling. In the latter case, a Higgs boson produced off-mass-shell decays into two Higgs bosons. The LO Feynman diagrams corresponding to these processes are shown in Figure 1.8.

Given that the interference between the amplitudes corresponding to the two processes shown in Figure 1.8 is destructive, the predicted inclusive cross-section for the ggF pair production of Higgs bosons is $\sigma_{HH} = 31.05$ fb [43–50], at $\sqrt{s} = 13$ TeV, which is more than three orders of magnitude less than the cross-section for single Higgs boson production quoted in Section 1.4.1. The cross-section predictions for $\sqrt{s} = 13$, 14 and 27 TeV, and the corresponding uncertainties, are summarised in Table 1.2.

Similar to the mechanisms for the single Higgs boson production at the LHC, in addition to the ggF mode, a pair of Higgs bosons can be produced in a VBF process, double Higgs-strahlung and in association with a pair of top quarks. The LO Feynman diagrams corresponding to the VBF HH production are shown in Figure 1.9. The VBF HH production is, for instance, essential for probing the $VVHH$ coupling (usually referred to as c_{2V}) [51], for which

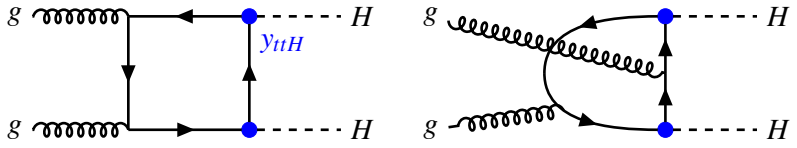

(a) *HH production via the top-quark Yukawa coupling*

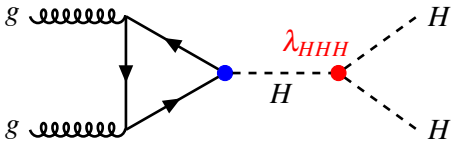

(b) *HH production via the Higgs boson self-coupling*

Figure 1.8. Examples of leading-order Feynman diagrams for the *gg*F pair production of Higgs bosons in the SM. The vertices represented by the blue dots correspond to quark Yukawa interactions, with the largest contribution from the top quarks, hence labelled y_{ttH}. The vertex represented by the red dot corresponds to the trilinear Higgs boson self-coupling, with the coupling constant λ_{HHH}.

Table 1.2. *Inclusive cross-section for the ggF pair production of Higgs bosons in pp collisions at* $\sqrt{s} = 13,14$ *and 27 TeV [43–50]. The quoted uncertainties correspond to: the choice of the factorisation and renormalisation scales, the choice of Parton Density Functions (PDF), value of strong coupling constant,* α_s*, and the mass of the top quark.*

$\sqrt{s}$	13 TeV	14 TeV	27 TeV
$\sigma_{\text{NNLO FTapprox}}$ [fb]	31.05	36.69	139.9
Scale unc. [fb]	$^{+0.68}_{-1.6}$	$^{+0.77}_{-1.8}$	$^{+1.8}_{-5.5}$
PDF + α_s unc. [fb]	± 0.93	± 1.1	± 3.5
m_t unc. [fb]	± 0.81	± 0.97	± 4.8

the LO Feynman diagram is shown in Figure 1.9c. Nonetheless, all these additional processes have significantly smaller cross-sections [52] and are less interesting in terms of probing the Higgs boson self-coupling, thus only the *gg*F *HH* production is considered in the studies presented in this thesis.

The list of possible decay channels for a pair of Higgs bosons, with the corresponding branching fractions, is given in Table 1.3. The final state with the largest branching fraction is $b\bar{b}b\bar{b}$; however, this channel suffers from a large QCD-induced multijet background. Although the $b\bar{b}\gamma\gamma$ final state has a significantly lower branching fraction, it benefits from an excellent detector resolution in reconstructing the di-photon invariant mass. The $b\bar{b}\tau^+\tau^-$ final state has a branching fraction of around 7.3% and it represents one of the most attractive channels to search for pair production of Higgs bosons due to its relatively high branching ratio and moderate background rates.

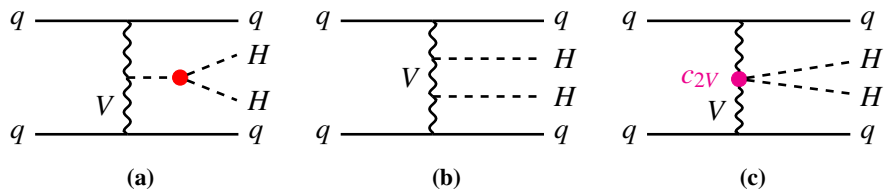

Figure 1.9. Examples of Feynman diagrams corresponding to the VBF pair production of Higgs bosons via: (**a**) Higgs boson self-coupling; (**b**) VVH couplings; and (**c**) $VVHH$ (c_{2V}) couplings.

Table 1.3. *Branching fractions corresponding to different decay channels of a pair of Higgs bosons, assuming* $m_H = 125.09$ *GeV [37].*

	$b\bar{b}$	WW^*	$\tau^+\tau^-$	ZZ^*	$\gamma\gamma$
$b\bar{b}$	34%				
WW^*	25%	4.6%			
$\tau^+\tau^-$	7.3%	2.5%	0.39%		
ZZ^*	3.1%	1.2%	0.34%	0.076%	
$\gamma\gamma$	0.26%	0.10%	0.029%	0.013%	0.0005%

1.5 Shortcomings of the Standard Model

The Standard Model achieved enormous success over the past decades, predicting several new elementary particles, including the Higgs boson. However, there are numerous observed phenomena that the SM cannot explain. Therefore, it is believed that the SM is only an effective manifestation of a more fundamental theory at currently accessible energies.

One, already mentioned, deficiency of the SM is that it does not include gravity. Below the *Planck length*[10], the SM and the theory of general relativity are no longer reconcilable and quantum effects of gravity are expected to dominate.

There are many Grand Unified Theory (GUT) models that hypothesise unification of the electromagnetic, weak and strong forces into a single force at high energies, close to the Planck scale. Such theories are appealing since they often have a more elegant structure than the SM, which is defined by 19,

[10]The Planck length is defined as $l_p = \sqrt{\hbar G_N/c^3} = 1.616\ 229(38) \times 10^{-35}$ m, where G_N is the Newtonian constant of gravitation, which corresponds to the Planck mass $M_{\text{pl}} = 1.220890(14) \times 10^{19}$ GeV [25] and the reduced Planck mass $\bar{M}_{\text{pl}} \approx 2.4 \times 10^{18}$ GeV. These values are referred to as the Planck scale.

somewhat ad hoc, independent parameters[11] (without considering neutrinos as massive particles). The SM can be extended to treat neutrinos as massive particles, but it cannot predict their masses. In addition, although the SM is a renormalisable theory, and thus finite results are obtained for higher-order corrections, the loop corrections to the Higgs boson mass need to be fine-tuned to explain its value, which is many orders of magnitude below the Planck energy scale. This is known as the SM fine-tuning problem.

Another long standing puzzle in the SM is the discrepancy between the theory predictions and experimental measurements of the anomalous magnetic moment of the muon, which is both predicted and measured with an extremely high precision [53].

The SM is not able to explain the predominance of matter over antimatter in the Universe. The violation of the CP symmetry in the quark and neutrino sectors in the SM is not sufficient to account for the observed asymmetry. If large regions of antimatter existed, electromagnetic radiation would be created by matter-antimatter annihilation, which has not been observed. The measured imbalance is assumed to be a consequence of a hypothetical process called baryogenesis; however, it is unlikely that such a process is compatible with the SM.

In the SM, the lepton flavour universality holds. However, over the last decade there have been indications of the violation of the lepton flavour universality reported by the BaBar [54, 55], Belle [56, 57] and LHCb [58–60] collaborations. All these results show anomalies in the B-meson decay and persistent deviations from the SM predictions.

Probably the most striking limitation of the SM and general relativity is their insufficiency when it comes to explaining astrophysical and cosmological observations that indicate the existence of *dark matter* and *dark energy*. Numerous observations, such as the nature of rotational curves of nearby galaxies, infer that there is much more gravitational matter than it is observed. Studies suggest that the visible matter accounts only for around 5% of the total energy density of the Universe. Dark matter accounts for another 27%, while the rest of the Universe consists of dark energy. There are no good particle candidates within the SM to explain the observed properties of the dark matter, and thus new physics is necessary to describe these phenomena. Dark energy is even a bigger mystery. It is believed to be uniformly distributed over the whole Universe, causing its accelerating expansion [61].

Several beyond the SM (BSM) theories, each aiming to solve one or more of the shortcomings of the SM listed above, predict heavy resonances that could decay into a pair of Higgs bosons, e.g. scalar resonances predicted by two-Higgs-doublet models [11], or spin-2 Kaluza-Klein excitations of the graviton

[11] The parameters of the SM are: the 9 masses of quarks and charged leptons; the 4 parameters of the CKM matrix; the g_1, g_2 and α_s coupling constants; the Higgs boson mass and the vacuum expectation value of the Higgs field; and the QCD vacuum angle.

in the bulk Randall-Sundrum model [12–14]. The generic Feynman diagram corresponding to such a process is shown in Figure 1.10. The motivation for searching for resonant pair production of Higgs boson is discussed in more details in Chapter 2 and the results of such searches in the $b\bar{b}\tau^+\tau^-$ channel are presented in this thesis.

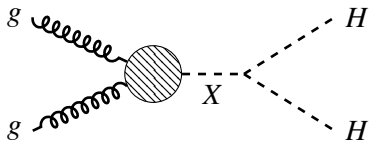

Figure 1.10. Example of a Feynman diagram corresponding to BSM *gg*F resonant pair production of Higgs bosons. The hypothetical resonance is labelled as X. The patterned-background circle indicates an effective coupling of the resonance X to gluons.

2. Beyond the Standard Model

An overwhelming number of extensions of the SM have been developed over the last decades. Such theories aim to provide more satisfactory solutions to one or more open questions in contemporary particle physics. A non-exhaustive list of problems and controversies related to the SM, arising from different observations in particle physics, astrophysics and cosmology, is given in Section 1.5. Several BSM hypotheses relevant for the scope of the research presented in this thesis are briefly summarised in this chapter.

2.1 Resonant pair production of Higgs bosons

In this thesis, two resonance hypotheses are considered: a CP-even scalar particle predicted by two-Higgs-doublet models [11], X, and spin-2 Kaluza-Klein (KK) excitations of the graviton, G_{KK}, in the bulk Randall-Sundrum model [12–14].

2.1.1 Two-Higgs-doublet models

The Higgs mechanism plays a crucial role in the SM, as explained in Section 1.3.1. The electroweak gauge symmetry is spontaneously broken when the system goes to a vacuum state that is not invariant under the $\mathrm{SU}(2)_L \times \mathrm{U}(1)_Y$ symmetry. This is achieved by introducing the doublet of complex scalar fields, Φ, with a non-zero vacuum expectation value, v, into the theory. This principle can be extended by considering two doublets of complex scalar fields, Φ_1 and Φ_2, with weak hypercharges $Y_{\Phi_1} = Y_{\Phi_2} = 1$. Such extensions of the SM are called *Two-Higgs-doublet models* (2HDMs) [11]. The most general scalar potential in such models contains 14 parameters and it includes CP-conserving, CP-violating, and charge-violating vacuum states. These new sources of CP violation make 2HDMs an appealing extension of the SM. Another attractive feature of these models is that they provide a more natural solution to the fine-tuning problem. Furthermore, 2HDMs can allow for tree-level flavour-changing neutral currents (FCNCs), which are not allowed in the SM, nor observed in nature. However, 2HDMs are usually simplified by assuming that the CP symmetry is not spontaneously broken, and that quartic terms odd in either of the doublets are not allowed due to discrete symmetries.

The resulting scalar potential depends on 8 real parameters and its minimisation gives

$$\langle \Phi_1 \rangle = \frac{1}{\sqrt{2}} \begin{pmatrix} 0 \\ v_1 \end{pmatrix} \text{ and } \langle \Phi_2 \rangle = \frac{1}{\sqrt{2}} \begin{pmatrix} 0 \\ v_2 \end{pmatrix}, \tag{2.1}$$

where v_1 and v_2 are the vacuum expectation values corresponding to the two doublets, respectively. The fields can be expanded about the vacuum and for Φ_1 and Φ_2 there are 8 degrees of freedom. After the spontaneous symmetry breaking, five massive (Higgs) fields and three Goldstone bosons are obtained. The Goldstone bosons are absorbed to give the longitudinal degrees of freedom of the $W^{\pm}$ and Z bosons. Two of the five Higgs bosons are charged ($H^{\pm}$), two are neutral and CP-even (scalars H_1 and H_2) and one is neutral and CP-odd (pseudoscalar A). The observed Higgs boson is measured to be CP-even [39, 40], therefore either of the two neutral scalar particles can be associated with it.

One of the most popular extensions of the SM that can be an example of a 2HDM is *supersymmetry* (SUSY) [62]. Other than for its mathematical elegance, SUSY is recognised for offering solutions to several of the open questions in particle physics. In SUSY, each SM particle has a "supersymmetric" partner – "sparticle". Relative to the SM particle, a supersymmetric partner differs by half a unit of spin[1]. If SUSY was an exact symmetry of nature, sparticles would have the same mass as particles, and thus would already have been discovered. Therefore, if SUSY exists, it is a broken symmetry and the mass scale of the supersymmetric partners is not predicted. Some theoretical arguments favour a relatively low mass scale of ~ 1 TeV [21]. A minimum of two Higgs doublets are required in SUSY theories since scalar fields and their complex conjugates belong to different chiral multiplets and cannot couple together in the Lagrangian. For that reason, one Higgs doublet is not sufficient to generate mass terms for both charge 2/3 and charge -1/3 quarks in SUSY. Additionally, renormalisability cannot be achieved in the case of only one Higgs doublet. The SUSY theory with two Higgs doublets and the minimum number of new particle states is called the *Minimal Supersymmetric Standard Model* (MSSM)[2] [63]. A model in which the lighter neutral scalar Higgs boson corresponds to the observed Higgs boson is called *habemus* MSSM (hMSSM) [64]. A kinematically interesting scenario in the context of pair production of the SM Higgs bosons occurs when the heavier neutral scalar particle has a mass

[1] Partners corresponding to the SM fermions and spin-1 gauge bosons are spin-0 sfermions and spin-1/2 gauginos, respectively.

[2] The MSSM includes sfermions and gauginos, but also *higgsinos*, which are the spin-1/2 supersymmetric partners of the Higgs field. In the MSSM, charged higgsinos mix with the supersymmetric partners of the $W^{\pm}$ fields (charged winos) and form physical states that are called *charginos*. Similarly, neutral higgsinos mix with the supersymmetric partners of the W^3 and B fields (neutral wino and bino) and form physical states that are called *neutralinos*. In many SUSY models, the lightest neutralino is a weakly interacting stable particle, which is a possible candidate for the dark matter.

larger than twice the measured Higgs boson mass. A search for a scalar resonance, X, decaying into a pair of Higgs bosons in the $b\bar{b}\tau^+\tau^-$ final state is performed in the context of hMSSM based on 36.1 fb^{-1} of 13 TeV data recorded by the ATLAS experiment, and the results of that search are presented in this thesis. In this case X refers to the heavier of the H_1 and H_2 scalars, while the remaining one corresponds to the measured Higgs boson.

If the SUSY-breaking scale, M_S, is assumed to be high, $M_S >> m_Z$, additional approximations can be made within the hMSSM framework, given that the measured Higgs boson mass is incorporated into the theory. These approximations constrain the dominant radiative corrections and several leading SUSY parameters. The Higgs sector of the hMSSM is then effectively parameterised by only two free parameters at leading order: the mass of the pseudoscalar Higgs boson, m_A; and the ratio of the two vacuum expectation values, defined as $\tan\beta = v_1/v_2$. In this regime, a low $\tan\beta$ region, $\tan\beta \lesssim 2-5$, becomes phenomenologically interesting since it is not experimentally excluded [65]. For HH searches in particular, the resonance-mass region below the $t\bar{t}$-production threshold is more interesting due to the high branching fraction for the $X \to HH$ decay.

2.1.2 Kaluza-Klein gravitons in the bulk Randall-Sundrum model

One of the first proposals for introducing extra spatial dimensions (EDs) in physics came from attempts of unifying the electromagnetic and gravitational fields [66]. Several scenarios regarding the nature of EDs have been studied over the past decades. An important group of theories are those where the ED is required to be *compactified*, i.e. of a finite length, or potentially periodic. In the KK theory, three-dimensional space is homogeneous and infinite, while the fourth spatial dimension is a compact circle with a radius R_{ED}. Gravitation here is a classical extension of general relativity to five dimensions, while the four-dimensional electromagnetism and gravity are obtained by dimensional reduction.

In ED theories, the (reduced) Planck scale, $\bar{M}_{\text{pl}}$, that was discussed in Chapter 1, is interpreted only as an effective scale of a more fundamental $(4+n)$-dimensional scale, M_{4+n}, to which it can be related by

$$\bar{M}_{\text{pl}}^2 = (M_{4+n})^{n+2} V_n, \tag{2.2}$$

where V_n is the volume of the compact space [12]. Depending on the nature of the compact space, e.g. how large it is, ED theories can offer a new perspective regarding the fine-tuning problem. A large enough ED solves the large hierarchy difference between the weak scale (defined by the vacuum expectation value of the Higgs field, v) and the Planck scale, but introduces a new hierar-

chy problem between v and the ED-compactification scale, which is defined as $\mu_c \sim 1/V_n^{1/n}$.

In order to avoid this new hierarchy problem, alternative types of EDs have been proposed. In the Randall-Sundrum model, the ED is a "warp" factor, i.e. a rapidly changing function. In such a theory, the most general solution of the classical Einstein motion equations yields a non-factorisable metric [67]

$$ds^2 = e^{-2\sigma(\phi)} g_{\mu\nu} dx^\mu dx^\nu + r_c^2 d\phi^2. \tag{2.3}$$

Here, x^μ are coordinates in the Minkowski space, ϕ is the coordinate for the ED and it belongs to a finite interval $\phi \in [0, \pi]$, r_c sets the size of the ED, while σ is a function of ϕ.

Given that there are no experimental signs of EDs, it is assumed that the SM particles and forces are confined to a four-dimensional space, referred to as a "brane". Two boundaries of the five-dimensional space defined by Equation (2.3), corresponding to $\phi = 0$ and $\phi = \pi$, are specified and they represent two Poincaré-invariant branes, the TeV-brane and Planck-brane, respectively. The classical action describing the full theory can be written as

$$S = S_{\text{Bulk}} + S_{\text{TeV}} + S_{\text{Planck}} + S_{\text{Matter}}, \tag{2.4}$$

where S_{Bulk} is the action of gravity in the bulk of the five-dimensional space, S_{TeV} and S_{Planck} are actions describing the gravity on the two branes, while S_{Matter} is the action describing the matter fields. Taking the vacuum energy density in the bulk and on the two branes to be $\Lambda_{\text{Bulk}} = \Lambda_{\text{Planck}} = -\Lambda_{\text{TeV}} = \Lambda$, a solution for $\sigma(\phi)$ is obtained[3]

$$\sigma(\phi) = r_c|\phi| \sqrt{\frac{-\Lambda}{24M_5^2}} \equiv r_c|\phi|k. \tag{2.5}$$

Here, k is called the curvature factor and it is of the order of the Planck scale, while M_5 is the fundamental scale of the five-dimensional space. Integrating out the ED, a relation between $\bar{M}_{\text{pl}}$ and M_5 is obtained,

$$\bar{M}_{\text{pl}}^2 = \frac{M_5^3}{k} \left(1 - e^{-2\pi k r_c}\right). \tag{2.6}$$

The SM Higgs mechanism can be added to the theory without any obstacles. If the Higgs doublet is allowed to propagate only on the TeV-brane, its SM vacuum expectation value, v, is related to a more fundamental vacuum expectation value v_5 as $v = e^{-2\pi k r_c} v_5$. Given that v_5 is of the order of M_5, and that both are the fundamental parameters of the theory, the Randall-Sundrum model provides an elegant solution for the fine-tuning problem.

[3]This assumption is necessary in order for the three vacuum energy densities to be related in terms of a single scale [12].

Gravitational fluctuations about the classical solution from Equation (2.3) introduce new physical particles. Tensor fluctuations correspond to physical KK gravitons[4]. The zero mode in expansion corresponds to the massless KK graviton, while higher modes are massive. The Lagrangian describing the coupling of the excited graviton to matter is given by

$$\mathscr{L}_{G_{\mathrm{KK}}-matter} = -\frac{1}{\bar{M}_{\mathrm{pl}} e^{-kr_c\pi}} T^{\mu\nu} \sum_{n=1}^{\infty} h_{\mu\nu}^{(n)}, \tag{2.7}$$

where $T^{\mu\nu}$ is the energy-momentum tensor of the matter field and $h_{\mu\nu}^{(n)}$ is the n^{th} excitation of the graviton [68]. The mass of the n^{th} excitation is given by

$$m_{G_{\mathrm{KK}}}^{(n)} = k x_n e^{-kr_c\pi}, \tag{2.8}$$

where x_n is the n^{th} root of the Bessel function. Some of these masses are expected to be of order of a TeV, and thus KK graviton excitations could potentially be detected as massive resonances at the LHC.

The theory is determined by two parameters, the mass of the first KK graviton excitation, $m_{G_{\mathrm{KK}}}$, and the ratio of $k/\bar{M}_{\mathrm{pl}}$. A search for $G_{\mathrm{KK}} \to HH \to b\bar{b}\tau^+\tau^-$ using 36.1 fb^{-1} of 13 TeV data recorded by the ATLAS experiment is presented in this thesis in two scenarios, for $k/\bar{M}_{\mathrm{pl}} = 1$ and $k/\bar{M}_{\mathrm{pl}} = 2$.

2.2 Non-resonant pair production of Higgs bosons

In this section, the phenomenology of pair production of Higgs bosons is discussed in the context of an anomalous trilinear Higgs boson self-coupling. As already stated in Section 1.4.2, the ggF HH production in the SM consists of the two production modes shown in Figure 1.8: one realised through the top-quark Yukawa coupling, proportional to y_{ttH}^2; and the other one realised through the Higgs boson self-coupling, proportional to $y_{ttH}\lambda_{HHH}$. In the following, these two production mechanisms are referred to as the "box" and "triangle" diagrams, respectively. The HH production cross-section and event kinematics are sensitive to the interference between the two production modes, and thus any deviation of the two couplings from the SM prediction would affect the overall HH production.

Although y_{ttH} and λ_{HHH} are predicted by the SM, deviations from their expected values are possible in different BSM scenarios [69]. Furthermore, even if the two couplings have the predicted values, in searches for HH production they could appear effectively anomalous. This can happen if some BSM processes responsible for a HH production are not taken into account in the theory predictions. For example, if some new heavy resonances exist beyond

[4]Similarly, scalar fluctuations correspond to hypothetical particles called radions.

the energy reach of the LHC, their on-mass-shell production would not be possible, but they could potentially affect HH production through quantum-loop contributions. Non-resonant pair production of Higgs bosons could also be sensitive to four-point vertices involving fermions, which are not predicted by the SM, e.g. $t\bar{t}HH$ coupling, or to deviations in the effective $ggHH$ coupling.

Any observation of anomalous λ_{HHH} or y_{ttH} couplings would indicate the existence of BSM physics. Experimental constraints on these couplings are useful since they discriminate between different BSM models.

Probing the anomalous Higgs boson self-coupling

The Feynman amplitudes corresponding to the triangle and box HH production modes can be labelled as T and B, respectively. To probe deviations of λ_{HHH} and y_{ttH} from their SM expectations ($\lambda_{HHH}^{\text{SM}}$ and y_{ttH}^{SM}), the two couplings can be treated as free parameters of the theory. The total amplitude, A, in that case can be parameterised as

$$A = \kappa_t \kappa_\lambda T + \kappa_t^2 B, \tag{2.9}$$

by using real-valued coupling modifiers

$$\kappa_\lambda = \lambda_{HHH}/\lambda_{HHH}^{\text{SM}} \text{ and } \kappa_t = y_{ttH}/y_{ttH}^{\text{SM}}. \tag{2.10}$$

This parameterisation holds beyond considering only the LO production, since higher-order QCD corrections do not introduce additional $t\bar{t}H$ and HHH vertices. Both T and B account for all diagrams proportional to $y_{ttH}\lambda_{HHH}$ and y_{ttH}^2, respectively. The total HH production cross-section is proportional to the square of the amplitude given by Equation (2.9),

$$\sigma(pp \to HH) \sim \kappa_t^4 \left[|B|^2 + \frac{\kappa_\lambda}{\kappa_t}(BT^* + TB^*) + \left(\frac{\kappa_\lambda}{\kappa_t}\right)^2 |T|^2 \right]. \tag{2.11}$$

This expression shows that kinematic distributions depend on the relative contributions from $|T|^2$, $|B|^2$ and the interference term $BT^* + TB^*$, thus this dependence can be parameterised with the ratio κ_λ/κ_t. The κ_t^4 factor affects only the normalisation of the total expected cross-section. The invariant mass of the Higgs boson pair, m_{HH}, has been identified as the variable with the largest shape variations with respect to κ_λ/κ_t. This is a consequence of different contributions of the two HH production modes to the m_{HH} spectrum. Pairs of Higgs bosons produced via self-coupling tend to populate regions of m_{HH} above the $2m_H$ threshold, while those produced via $t\bar{t}H$ couplings populate regions of m_{HH} above twice the mass of the top quark, $2m_t$. The SM case corresponds to $\kappa_\lambda = 1$ and $\kappa_t = 1$, a scenario in which the Higgs boson does not couple to itself corresponds to $\kappa_\lambda = 0$, while the interference between the triangle and the box diagrams is maximised for $\kappa_\lambda/\kappa_t \approx 2.4$. A set of m_{HH} distributions for various κ_λ hypotheses, and with fixed $\kappa_t = 1$, are shown in

Figure 2.1. Already at $\kappa_\lambda = 2$, a double-peak m_{HH} structure is noticeable due to the strong interference.

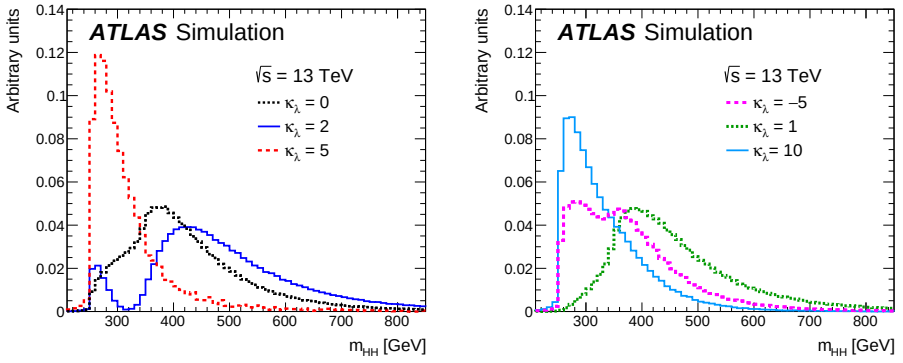

(a) **(b)**

Figure 2.1. Generator-level m_{HH} distributions for various κ_λ values: (**a**) $\kappa_\lambda = \{0, 2, 5\}$; and (**b**) $\kappa_\lambda = \{-5, 1, 10\}$. All distributions are shown for $\kappa_t = 1$ [16].

To avoid simulating non-resonant HH signal samples for every κ_λ hypothesis, which usually requires much computational time, alternative methods for obtaining signal predictions are considered and discussed in Chapter 6. For that reason, it is important to notice that instead of expressing $|A(\kappa_t, \kappa_\lambda)|^2$ as a function of $|T|^2$, $|B|^2$ and the interference term, a basis of three amplitudes for three fixed combinations of κ_λ and κ_t values can be used. If κ_λ and κ_t values are chosen as

$$(\kappa_t, \kappa_\lambda) = \{(1,0), (1,1), (1,2)\}, \tag{2.12}$$

the basis of three amplitudes is defined as

$$\begin{aligned} A(1,0) &= B \\ A(1,1) &= B + T \\ A(1,2) &= B + 2T. \end{aligned} \tag{2.13}$$

Solving the system of these three equations for $|T|^2$, $|B|^2$ and the interference term and using the results to express $|A(\kappa_t, \kappa_\lambda)|^2$ in terms of $|A(1,0)|^2$,

$|A(1,1)|^2$ and $|A(1,2)|^2$ yields

$$|A(\kappa_t,\kappa_\lambda)|^2 = \kappa_t^2\Bigg[\left(\kappa_t^2+\frac{\kappa_\lambda^2}{2}-\frac{3}{2}\kappa_t\kappa_\lambda\right)|A(1,0)|^2 + \left(2\kappa_t\kappa_\lambda-\kappa_\lambda^2\right)|A(1,1)|^2 + \left(\frac{\kappa_\lambda^2-\kappa_t\kappa_\lambda}{2}\right)|A(1,2)|^2\Bigg]. \tag{2.14}$$

Similarly, if the $(\kappa_t,\kappa_\lambda)=\{(1,0),(1,1),(1,20)\}$ basis is chosen, the obtained solution is

$$|A(\kappa_t,\kappa_\lambda)|^2 = \kappa_t^2\Bigg[\left(\kappa_t^2+\frac{\kappa_\lambda^2}{20}-\frac{399}{380}\kappa_t\kappa_\lambda\right)|A(1,0)|^2 + \left(\frac{20}{19}\kappa_t\kappa_\lambda-\frac{1}{19}\kappa_\lambda^2\right)|A(1,1)|^2 + \left(\frac{\kappa_\lambda^2-\kappa_t\kappa_\lambda}{380}\right)|A(1,20)|^2\Bigg]. \tag{2.15}$$

As discussed later in Chapter 6, Equations (2.14) and (2.15) are used to obtain expected kinematic distributions for a fine grid of κ_λ values based on only a few simulated samples. A fine grid is important for setting upper limits on the non-resonant HH production cross-section as a function of κ_λ, which are presented in this thesis based on 36.1 fb^{-1} of 13 TeV data recorded by the ATLAS experiment. These results provide useful experimental constraints on the Higgs boson self-coupling strength.

In the work presented in this thesis, only κ_λ is considered as a free parameter of the theory. As already discussed, considering κ_t as a free parameter would affect only the total cross-section, but would not introduce additional kinematical variations. Further generalisation of parameterising the phenomenology of Higgs boson pair production can be achieved in the framework of the *effective field theory* (EFT) [70]. In the SM, all Lagrangian terms are dimension-four or less. The EFT framework introduces higher-dimension operators to account for effective contributions from potential new physics that might exist at energies that are not accessible at the LHC. These higher-dimension terms can be parameterised using several effective Higgs boson couplings, typically: λ_{HHH}, y_{ttH}, c_2, c_{2g} and c_g, where the latter three correspond to $t\bar{t}HH$, $ggHH$ and ggH contact interactions, respectively. This is an interesting possibility for future experimental efforts in constraining the Higgs boson self-coupling strength.

3. The ATLAS experiment at the Large Hadron Collider

The European Organisation for Nuclear Research (CERN) is one of the world's largest and most important research centres in particle physics. Since it was founded in 1954, CERN has been a host to various international experiments responsible for numerous important discoveries, such as: the observation of weak neutral currents [71] and the subsequent discovery of the W and Z bosons in 1983 by the UA1 and UA2 experiments [72–75]; the determination of the number of light neutrino families from studying the Z boson properties at the Large Electron-Positron Collider (LEP); the direct observation of CP violation in the decay of a neutral kaon [76, 77]; the first creation and isolation of antihydrogen atoms; and the discovery of the Higgs boson in 2012 [1, 2].

3.1 The Large Hadron Collider

The largest project hosted by CERN at present is the Large Hadron Collider (LHC) [78], which is the largest high-energy particle collider in the world. The LHC consists of a number of superconducting magnets and accelerating structures put together in a 27-kilometre ring formation inside an underground tunnel. The LHC accelerates two counter-rotating beams of hadrons through separate ultra-high vacuum pipes using a 400 MHz superconducting cavity system. The dipole magnets are operated at the temperature of 1.9 K and they create a magnetic field of up to 8.33 T that guides the beams along the ring. Additional magnets are used to keep the beams focused and to apply corrections to the beam geometry. In order to guide both beams along the ring, two oppositely oriented magnetic fields are needed and for that purpose the concept of the twin-bore magnet is applied to be able to place both beam channels within the same magnetic and mechanical structure in a single cryostat.

Proton beams are obtained by stripping electrons from hydrogen atoms. They are injected into the LHC only after reaching an energy of 450 GeV, to which they are boosted using a system of several smaller accelerators. The LHC was designed to produce an instantaneous luminosity of 10^{34} cm^{-2}s^{-1} and for the maximum centre-of-mass energy of $\sqrt{s} = 14$ TeV for pp collisions[1]. The design luminosity was obtained and even surpassed during the

[1]The LHC is primarily designed for pp collisions, but lead-lead (Pb-Pb) collisions and proton-lead (p-Pb) collisions are also possible and usually done for one month per year of operation.

Run 2 data-taking[2]. For most of Run 1, the LHC was operated to provide pp collisions at $\sqrt{s} = 7$ TeV, in 2012 this was raised to 8 TeV and in Run 2 to 13 TeV. The design centre-of-mass energy of 14 TeV is planned to be reached during data-taking in Run 3.

The LHC has four beam-crossing points, around which are located seven[3] experiments. The four largest projects are the ATLAS, CMS, ALICE and LHCb experiments. The first two, ATLAS and CMS [80, 81], are often referred to as general-purpose particle detectors. Their physics goal is to probe the validity of the SM through performing precision measurements of its parameters and to search for signs of new physics. The discovery of the Higgs boson is probably the greatest achievement of the two experiments thus far, but in many other ways they represent the world's leading projects in studying particle physics at the TeV scale. The ALICE experiment [82] specialises in researching the strong-interaction sector of the SM by studying a primordial form of matter called quark-gluon plasma at extreme values of energy density and temperature in Pb-Pb collisions. The LHCb experiment [83] specialises in precision measurements of CP violation and rare decays of B-hadrons, testing the lepton universality and studying flavour physics in general. The remaining three LHC experiments are significantly smaller. The TOTEM experiment [84] measures the total pp cross-section, and elastic and diffractive scattering processes. The LHCf experiment [85] studies properties of neutral particles emitted in the very forward region of LHC collisions. Finally, the MoEDAL experiment [86] is designed to search for the magnetic monopole, which is predicted by some GUT and superstring theories.

3.1.1 Luminosity and pileup

In order to maximise the rate of pp collisions at the LHC, and to have discrete collision intervals, proton beams are organised into *bunches*, with approximately 1.1×10^{11} protons per bunch. The spacing between two bunches is 25 ns. Typically, 72 equidistant bunches form a "train", after which come 12 bunch-slot gaps. Two bunches, one from each of the two counter-rotating beams, meet at a beam-crossing (interaction) point, providing a peak bunch collision rate of approximately 40 MHz.

The event production rate at the LHC for a certain process is given by

$$\frac{dN}{dt} = L\sigma, \tag{3.1}$$

[2]The first operational period of the LHC (2009–2013) is called Run 1; the second (2015–2018) is called Run 2; the next operational period, Run 3, is planned to start in 2021.

[3]Additionally, the FASER experiment was approved in 2019, and is planned to become operational in 2021. The experiment is designed to search for new light and weakly-coupled particles, as well as to study the interactions of high-energy neutrinos [79].

where L is the instantaneous luminosity and σ is the production cross-section of that process. The instantaneous luminosity is defined as [78]:

$$L = \frac{N_1 N_2 n_b f_{\text{rev}}}{\pi \sqrt{\sigma_{x,1}^2 + \sigma_{x,2}^2} \sqrt{\sigma_{y,1}^2 + \sigma_{y,2}^2}} R, \tag{3.2}$$

where:

- N_1 and N_2 are the numbers of particles in the colliding bunches;
- n_b is the number of bunches per beam;
- f_{rev} is the revolution frequency;
- $\sigma_{x,1,2}$ and $\sigma_{y,1,2}$ are the horizontal and vertical beam sizes;
- R is the luminosity reduction factor accounting for the geometrical effects due to the crossing angle at the interaction point and to the size of the bunches.

Another important parameter, which is related to the instantaneous luminosity, is the *pileup parameter*. Any interesting process happening in a collision is "contaminated" with particles coming from inelastic pp collisions occurring in the same or nearby bunch crossings. This poses a challenge in the event reconstruction. The pileup parameter, μ, is calculated at any given time as the mean number of inelastic pp interactions per bunch crossing. This quantity, averaged over all colliding bunch pairs, is denoted by $\langle\mu\rangle$. The average or peak values for several selected LHC parameters during the Run 2 data-taking [87] are summarised in Table 3.1.

Table 3.1. *Selected LHC parameters for pp collisions at $\sqrt{s} = 13$ TeV during the Run 2 data-taking [87]. In 2017, the LHC was run in two modes: standard 25 ns bunch train operation with long trains, and "8b4e" mode, denoting a pattern of eight bunches separated by 25 ns followed by a four bunch-slot gap.*

Parameter	2015	2016	2017	2018
Max. number of colliding bunch pairs	2232	2208	2544/1909	2544
Bunch spacing (ns)	25	25	25/"8b4e"	25
Typical bunch population (10^{11} protons)	1.1	1.1	1.1/1.2	1.1
Peak luminosity (10^{33} cm^{-2}s^{-1})	5	13	16	19
Peak $\langle\mu\rangle$	~ 16	~ 41	$\sim 45/60$	~ 55

The integrated luminosity, $L_{\text{int}} = \int L dt$, is used to quantify the amount of data collected in a certain period of time. During Run 2, the LHC delivered 156 fb^{-1} of data, of which 147 fb^{-1} were recorded by ATLAS, while 139 fb^{-1} of the recorded data satisfies necessary data-quality requirements [88]. Results presented in Chapters 5–7 are based only on the data recorded in 2015 and 2016, corresponding to 36.1 fb^{-1}, while the results presented in Chapter 8 are based on the full Run 2 dataset. The dynamics of data-taking during Run 2 by the ATLAS experiment is shown in Figure 3.1. Additionally, a

luminosity-weighted distribution of the mean number of pp interactions per bunch crossing during the Run 2 ATLAS data-taking is shown in Figure 3.2.

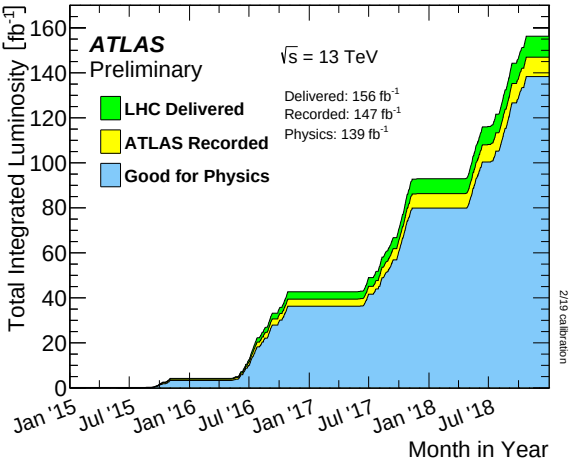

Figure 3.1. Cumulative integrated luminosity delivered by the LHC to the ATLAS detector (green), recorded by ATLAS (yellow), and certified to fulfil certain data-quality criteria (blue) [88]. The plot refers only to the Run 2 data-taking, and only to the pp collisions coming from stable proton beams.

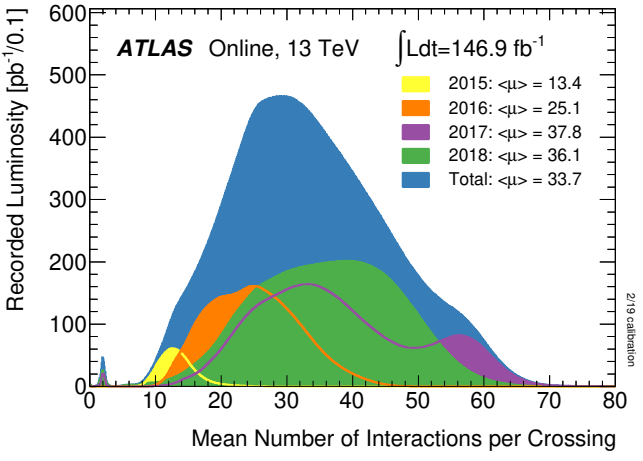

Figure 3.2. Luminosity-weighted distribution of the mean number of pp interactions per bunch crossing, $\langle\mu\rangle$, during the Run 2 ATLAS data-taking [88]. The distribution of $\langle\mu\rangle$ is shown separately for each year of the Run 2 data-taking and for Run 2 as a whole. All data recorded by the ATLAS detector during stable beams is included.

3.1.2 High-Luminosity Large Hadron Collider

The gain from running the LHC beyond Run 2 and Run 3 becomes limited. With the amount of data recorded between 2009 and 2018 it would take more than 10 years of running the LHC with its full potential to reduce the statistical uncertainty by a factor of 2 in the measurements performed in the ATLAS and CMS experiments. Additionally, the sensitivity for observing statistically limited processes predicted by the SM, e.g. pair production of Higgs bosons, would probably not be reached, while the discovery potential from a phenomenological point of view would be too weak. For those reasons, a luminosity upgrade of the LHC is planned. With this upgrade it will be possible to collect $\sim$10 times more data than originally planned for the LHC project. This new phase of the LHC, which is currently planned to start in 2026, is called High-Luminosity LHC (HL-LHC). The schedule of the (HL-)LHC installation and operation is shown in Figure 3.3.

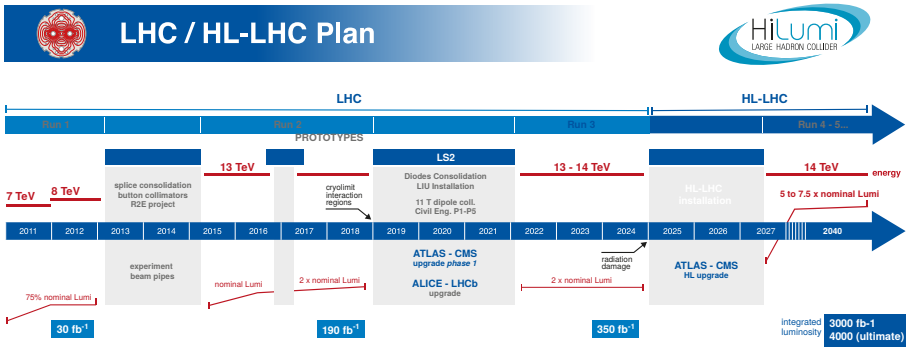

Figure 3.3. The LHC operations in the past and the schedule of future activities. The diagram shows the data-taking (Run) and technical-long-shutdown (LS) periods. After the planned upgrade, the HL-LHC is expected to become operational in 2026 [89].

The main ingredient of the planned upgrade consists of replacing the magnets responsible for squeezing the beams at the collision points. Most hardware upgrades will happen during the third long-shutdown (LS 3) period. Ultimately, the HL-LHC will produce seven times the luminosity for which the ATLAS and CMS detectors have been designed. The average pileup parameter is expected to be at around 200 pp collisions per bunch crossing. Thus, major detector upgrades are necessary to increase the radiation-hardness of sensitive elements, and to achieve finer granularity and faster readout for electronics.

One of the primary physics goals of the HL-LHC is to allow for measuring the strength of the Higgs boson trilinear self-coupling, λ_{HHH}, in order to test the electroweak symmetry breaking mechanism. The $b\bar{b}\tau^+\tau^-$ final state, as it will be shown, appears to be one of the most sensitive channels to search for non-resonant pair production of Higgs bosons. The expected sensitivity to this process is estimated in the context of the HL-LHC and the results of this study

are presented in Chapter 7. Sensitivity estimations are important in the sense of identifying analysis limitations and contributing to better detector upgrade designs, e.g. more optimal design of the triggers relevant for the $b\bar{b}\tau^+\tau^-$ final state.

3.1.3 Proton-proton collisions: parton model

Given that protons are not elementary particles, knowledge about their structure is necessary for studying pp collisions. Protons are composite particles consisting of three valence quarks, uud. The mass of the proton, m_p, is around 1 GeV, which is significantly higher than the sum of the masses of the valence quarks. The reason for this is the binding energy of the strong force that keeps the valence quarks together, which is realised through an exchange of virtual quarks and gluons. The asymptotic freedom of quarks and gluons inside the proton allows to define the assumption of the *parton model* [19, 90]. Partons are all quarks and gluons inside the proton and they are essentially free due to asymptotic freedom, in the relativistic limit.

The parton content of protons during pp collisions at the LHC is stable since two protons pass through each other in $\sim 1/13$ TeV $\sim 10^{-28}$ seconds, while the characteristic time of the strong interaction inside the proton is $\sim 1/m_p \sim 10^{-24}$ seconds. This makes it possible to consider classical probabilities $f_i(x)dx$ that a parton of species i which has a fraction x of the proton momentum will interact with a constituent of another proton. These $f_i(x)$ are known as *Parton Distribution Functions* (PDFs) and they depend on the square of the energy scale, Q^2, at which the proton is probed. Example PDFs are shown in Figure 3.4 for different values of Q^2.

The statement that a proton consists of uud valence quarks can be rewritten as

$$\int_0^1 (f_u(x) - f_{\bar{u}}(x)) = 2, \ \int_0^1 (f_d(x) - f_{\bar{d}}(x)) = 1, \ \int_0^1 (f_q(x) - f_{\bar{q}}(x)) = 0, \tag{3.3}$$

together with the momentum sum rule

$$\int_0^1 x\left[(f_u(x) - f_{\bar{u}}(x)) + (f_d(x) - f_{\bar{d}}(x)) + (f_q(x) - f_{\bar{q}}(x)) + f_g(x)\right] dx = 1, \tag{3.4}$$

where $q = \{s, c, b, t\}$. It has been measured that approximately only around 38% of the proton consists of up and down quarks. The gluon content accounts for 35% to 50% of the proton, depending on Q^2 [19]. Experimentally, the PDFs are measured in $e^- p \to e^- p$, pp, $p\bar{p}$, and other scattering processes. The PDF is approximately independent of Q^2 at fixed x, which is known as Bjorken scaling [91], but for more precise cross-section calculations at hadron colliders, associated perturbative corrections need to be taken into account. The energy dependence for a fixed x is described by the DGLAP splitting

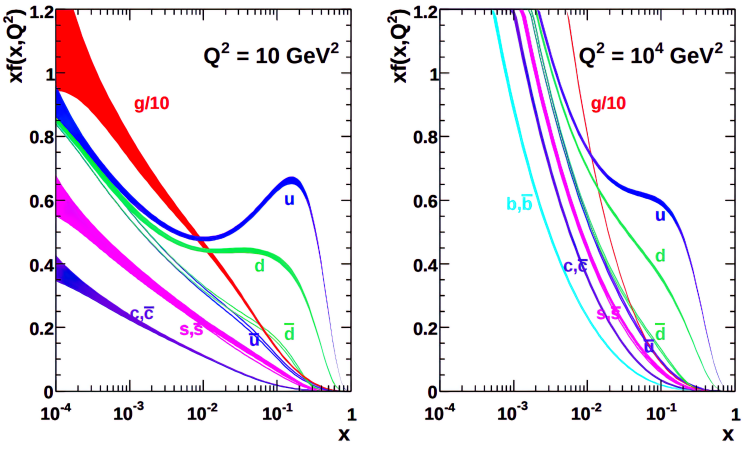

Figure 3.4. Parton distribution functions for the LHC ("MSTW 2008") calculated at NLO (68% CL) as a function of the momentum fraction x, for $Q^2 = 10$ GeV^2 and $Q^2 = 10^4$ GeV^2, where Q^2 represents the energy scale at which the proton is probed [90]. The gluon PDFs are scaled by $1/10$.

functions [92–94] that include probabilities for a parton to split or radiate an additional parton. For energetic partons this leads to a process called the *parton shower* that occurs before hadronisation. In the parton model, the hadron shower typically proceeds until the mean energy of particles in the shower reaches ~ 1 GeV, after which partons hadronise, as described in Section 1.2.2.

3.2 The ATLAS detector

The ATLAS (A Toroidal LHC ApparatuS) detector [80] is a general-purpose particle detector built around one of the LHC beam-crossing points. It has a cylindrical geometry and nearly a 4π coverage in solid angle. To describe the detector and physics processes of interest, a right-handed coordinate system with its origin at the nominal interaction point is used by convention[4]. A cut-away view of the ATLAS detector is shown in Figure 3.5.

The ATLAS detector is designed for studying particles produced in pp and Pb-Pb collisions. In order to provide shielding from cosmic rays, it is placed approximately 100 m below ground. Similar to other particle detectors, AT-

[4]The z-axis is defined by the beam direction; the positive x-axis points from the interaction point to the centre of the LHC ring; and the positive y-axis points from the interaction point upwards. The azimuthal angle ϕ is measured in the x-y (transverse) plane, around the z-axis. The polar angle θ is the angle from the z-axis. Instead of θ, the pseudorapidity or sometimes the rapidity, defined as $\eta = -\ln\tan\left(\frac{\theta}{2}\right)$ and $Y = \frac{1}{2}\ln\left(\frac{E+p_z}{E-p_z}\right)$, respectively, are used. The transverse momentum p_T, the transverse energy E_T and the missing transverse energy E_T^{miss} are defined in the transverse plane. The distance in η-ϕ space is defined as $\Delta R = \sqrt{\Delta\eta^2 + \Delta\phi^2}$.

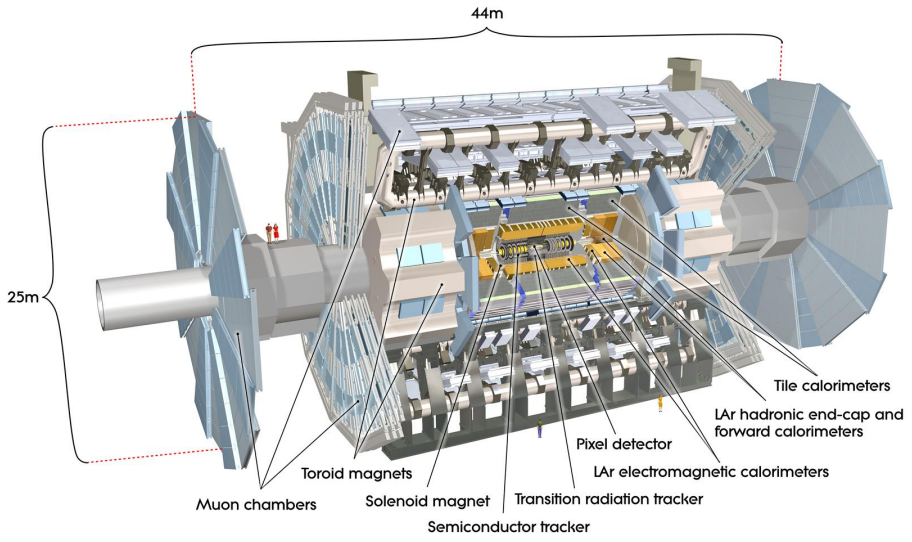

Figure 3.5. An illustration of the ATLAS detector [80]. The detector is 44 m long and it spans 25 m in height. It consists of many components, which can be grouped into several detector sub-systems: the inner detector, electromagnetic and hadronic calorimeters, and the muon spectrometer. The approximate weight of the whole detector is 7000 tonnes.

LAS exploits how different particles interact with matter in order to identify them. To allow for different interaction processes to occur, ATLAS consists of many different components. These components can be grouped into several detector sub-systems: the inner detector (ID), responsible for reconstructing trajectories of charged particles travelling through the detector; electromagnetic calorimeters (ECal) and hadronic calorimeters (HCal), responsible for measuring the energy and direction of photons, electrons and hadrons; and a muon spectrometer (MS), which is used to identify muons. To enable measuring the momentum and charge of particles, ATLAS includes a specially-designed magnet system. The detector is continuously operated and developed by the ATLAS collaboration, which consists of nearly 180 institutions from 38 countries.

All detector sub-systems are required to fulfil certain performance requirements defined by the adopted physics goals of the experiment [80]. The energy/momentum resolution and η coverage of the most important detector elements are given in Table 3.2. In the following, the design and purpose of the main ATLAS components listed above are briefly described.

Table 3.2. *Performance goals of the different ATLAS sub-detector systems [80]. The units for E and p_T are GeV. For high-p_T muons, the performance of the muon spectrometer is given independently of the inner detector. The denotation "L1" refers to the Level 1 trigger system that will be described shortly.*

Detector component	Required resolution	η coverage	
		Nominal	L1 Trigger
Inner detector	$\sigma_{p_T}/p_T = 0.05\% \cdot p_T \oplus 1\%$	± 2.5	
ECal	$\sigma_E/E = 10\%/\sqrt{E} \oplus 0.7\%$	± 3.2	± 2.5
HCal			
Barrel and end-cap	$\sigma_E/E = 50\%/\sqrt{E} \oplus 3\%$	± 3.2	
Forward	$\sigma_E/E = 100\%/\sqrt{E} \oplus 10\%$	$3.1 < \lvert\eta\rvert < 4.9$	
Muon spectrometer	$\sigma_{p_T}/p_T = 10\%$ at $p_T = 1$ TeV	± 2.7	± 2.4

3.2.1 Magnet system

A system of magnets is used to bend the trajectory of charged particles travelling through the detector in order to measure the ratio of their momentum and charge. Usually, the elementary charge is assumed since known particles with electric charge $\pm 2e$ are too short-lived and decay before reaching the inner detector. Under that assumption, the momentum is proportional to the radius of the trajectory curvature[5], while the sign of particle's electric charge is determined from the bending direction. Two large superconducting magnets are used: a solenoid to provide the magnetic field in the inner detector, and a toroid consisting of three sets of eight coils, one for the barrel and two for the two end-caps, used to provide the magnetic field in the muon spectrometer. The geometry of the ATLAS magnet system is shown in Figure 3.6.

The solenoid magnet is aligned on the beam-axis and it provides a 2 T axial magnetic field inside the inner detector. The magnet is 5.8 m long in the beam-axis direction, and it is designed to have a minimal thickness, of around 10 cm, to enable the optimal performance of the electromagnetic calorimeter. The toroid is placed between the hadronic calorimeter and the muon spectrometer. It generates a non-uniform magnetic field of up to 4 T. Both magnets are operated at a similar temperature, around 4.5 K.

3.2.2 Inner detector

The innermost sub-system of ATLAS is a tracking detector (tracker) that is responsible for measuring points along the trajectory of any charged particle, within the acceptance of $|\eta| < 2.5$. The inner detector consists of small cells organised into layers. A charged particle travelling through one of these

[5]From equality relation between the Lorentz magnetic force and the product of particle's mass and central acceleration, it follows $p_T[\text{GeV}] \approx 0.3B[\text{T}]R[\text{m}]$, where B is the magnetic flux density in Tesla, while R is the radius of the measured trajectory curvature in meters.

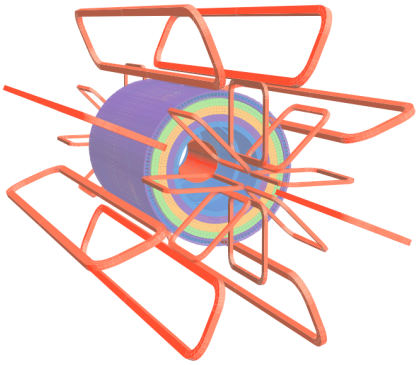

Figure 3.6. Geometry of the ATLAS magnet system (red structure) shown together with the tile calorimeter [80]. The central cylinder, inside the volume of the calorimeter, corresponds to the solenoid magnet, while the outer parts correspond to the toroid magnets.

cells causes ionisation of the sensitive material of the detector, producing a signal ("hit"). Hits from different layers are joined to reconstruct tracks. As already mentioned, the tracker is embedded into a magnetic field created by the solenoid magnet in order to force particles onto helical trajectories and to exploit this for measuring their momenta and charge. Given the busy LHC environment, the ATLAS tracker has been designed to provide robust pattern recognition and excellent momentum resolution. This further provides an excellent resolution for the primary and secondary vertex reconstruction. The momentum resolution is worse for high-p_T tracks due to smaller track-curvatures.

The ID consists of three separate, but complementary systems: the Pixel detector, the Semiconductor Tracker (SCT) and the Transition Radiation Tracker (TRT). A cut-away view of the ID and the radial layout of the mentioned subsystems are shown in Figure 3.7.

Pixel detector

Closest to the beam pipe is the Pixel detector, which is based on the silicon sensor technology. The innermost layer of the Pixel detector, called the Insertable B-Layer (IBL) [95], was installed between Runs 1 and 2 to improve the resolution for the primary- and secondary-vertex reconstruction. The IBL pixels are 50 μm $\times$ 250 μm, in $(r-\phi)\times z$ coordinates[6]. The Pixel detector consists of additional three layers. In the barrel, pixels are arranged axially around the beam-axis, while in the end-cap regions they are arranged radially into discs that are positioned perpendicularly to the beam-axis. The nominal

[6]The $(r-\phi)$ direction refers to the tangential direction defined by the circle of radius r that is centred around the beam-axis in the transverse plane.

pixel size beyond IBL is 50 μm $\times$ 400 μm. The total number of pixels is more than 90 million.

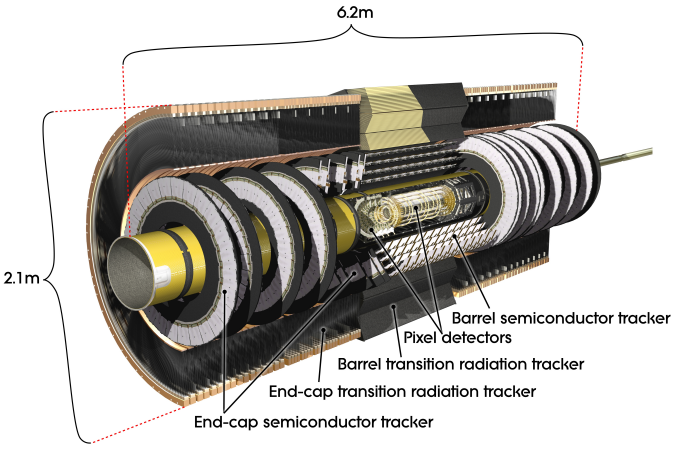

(a)

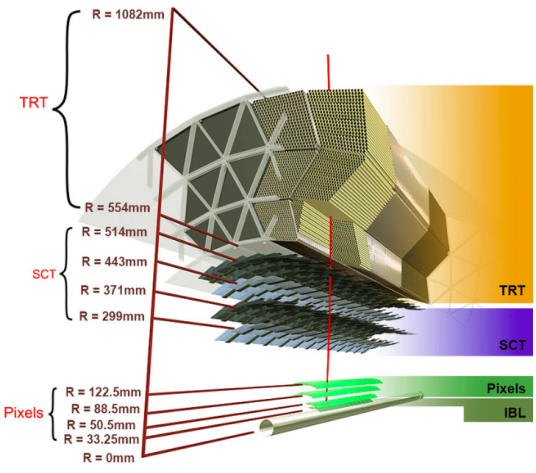

(b)

Figure 3.7. Illustrations of the ATLAS inner detector [96]: (**a**) a cut-away view and (**b**) the radial layout of the different components.

Semiconductor Tracker

The SCT consists of 4 (9) layers of silicon microstrips in the barrel (end-caps). Each SCT module has two sensors that are rotated by $\pm$20 mrad with respect to each other in order to achieve better resolution in the z (r) direction in the barrel (end-caps). The resolution in the $(r-\phi)$ direction is around 20 μm,

while the resolution in the z (r) direction is around 600 μm in the barrel (end-caps).

Transition Radiation Tracker
The outermost part of the ID, the TRT, is filled with 2 mm radius straw drift tubes. In the barrel (end-caps) the straws are positioned parallel (radially) to the beam-axis. The tubes are filled with a mixture of several gases, while the region around the tubes is filled with a material that increases radiation of the transitioning charged particles. The transition radiation is sensitive to the relativistic γ factor of the transitioning particle. In order to exploit this characteristic, the signal produced in the drift tubes is shaped and discriminated against two adjustable thresholds, a low-threshold and a high-threshold. The probability for high-threshold hits is significantly higher for electrons, and thus the fraction of these hits is an important information for discriminating between electrons and hadrons, e.g. pions. The TRT measures position only in the $(r-\phi)$ direction, with a resolution of 130 μm, but it provides a large number of hits, typically 36 per track (although this number depends on the $|\eta|$ region).

3.2.3 Electromagnetic and hadronic calorimeters

The ATLAS calorimeter system consists of the electromagnetic calorimeter (ECal) with an acceptance of $|\eta| < 3.2$, and hadronic calorimeter (HCal) with an acceptance of $|\eta| < 4.9$. An illustration of the calorimeter design is shown in Figure 3.8.

The main purpose of the calorimeters is to measure the energy and direction of motion of electrons, photons and sufficiently-long-lived hadrons. For electrons, the energy loss at high energy is dominated by Bremsstrahlung, while energetic photons undergo e^+e^- pair production. The characteristic radiation length, X_0, depends on the type of medium through which the particles are travelling. In a suitable medium, an incoming energetic electron or photon causes a cascade of interactions – an *electromagnetic (EM) shower*. After particles in the shower reach sufficiently low energy, they are stopped and absorbed. This creates a cluster of measurable signals that is later calibrated to measure the energy of the initial particle.

Energetic hadrons develop *hadronic showers* through a succession of inelastic hadronic interactions. The interaction length, λ, is significantly larger than X_0 for the same medium. The HCal is thus positioned further away from the interaction point compared to the ECal. In addition, hadronic showers spread more in the transverse direction compared to EM showers since the opening angle of the cascade scales with the interaction length. Pions, being the lightest mesons, dominate hadronic showers. Approximately one third of the produced pions are neutral, π^0, and, as a result of $\pi^0 \to \gamma\gamma$ decays, their energy is dissipated in the form of EM showers.

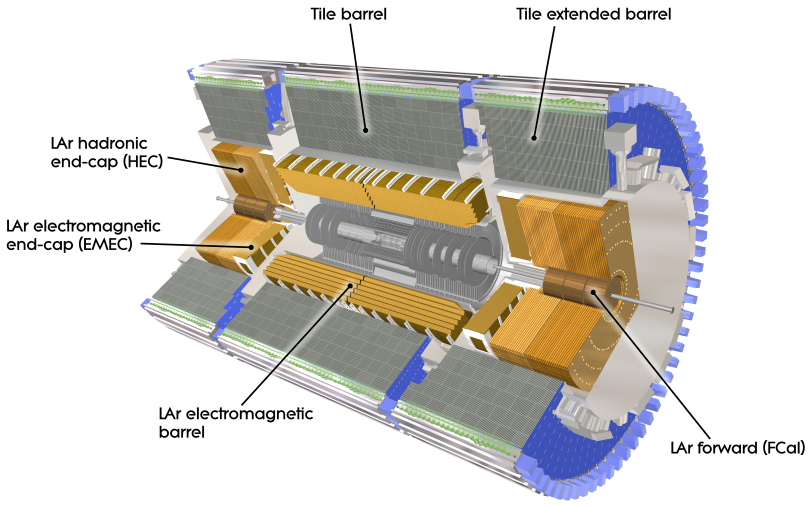

Figure 3.8. Cut-away view of the ATLAS calorimeter system [80].

Both the ECal and HCal are sampling calorimeters, in which the (passive) material that produces the particle shower and the (active) material used to measure the deposited energy are arranged to form alternating layers. The shower depth, measured in radiation or interaction lengths, is proportional to the logarithm of the energy of the initial particle. For that reason, it is possible to measure a wide range of energies with a calorimeter of finite depth.

Electromagnetic calorimeter

The pseudorapidity coverage of ECal is $|\eta| < 3.2$. Passive layers are made of lead, while liquid argon (LAr) is used to form active layers. The ECal is split into two barrels (EMB), with an acceptance of $|\eta| < 1.475$, and two end-cap regions (EMEC), covering the region of $1.357 < |\eta| < 3.2$. The region between $1.37 \leq |\eta| \leq 1.52$ ("crack region"), which corresponds to the transition region between the barrel and end-cap cryostats, suffers from a significantly reduced resolution compared to the rest of the ECal. The thickness of the ECal corresponds to around 23 X_0 and it consists of 3 layers. The bulk of the energy of a typical ECal EM shower is deposited in the middle layer, which spans a depth of about 17 X_0, and has a $\Delta\eta \times \Delta\phi$ resolution of 0.025×0.025.

A thin LAr presampler layer is placed in front of the ECal, covering the $|\eta| < 1.8$ region. The purpose of this 11-mm layer is to provide sampling for particles that start showering in front of the ECal.

Hadronic calorimeter

The central part of the HCal is the tile calorimeter, where iron and scintillating tiles are used to form passive and active layers, respectively. The pseudorapid-

ity coverage of the tile calorimeter is $|\eta| < 1.7$, with a $\Delta\eta \times \Delta\phi$ granularity of 0.1×0.1. Two additional HCal-end-caps (HEC), made of copper and LAr, are placed on both sides of the tile calorimeter, covering the $1.5 < |\eta| < 3.2$ range. The granularity of HEC is $\Delta\eta \times \Delta\phi = 0.1 \times 0.1$ and 0.2×0.2, depending on η. The thickness of the HCal is around 11 λ.

Forward calorimeter
Additionally, the Forward calorimeter (FCal) covers the $3.1 < |\eta| < 4.9$ region. It is split into one electromagnetic- and two hadronic-calorimeter layers. The electromagnetic layer uses copper (LAr) as its passive (active) medium. For the hadronic components of FCal, tungsten is used instead of copper.

3.2.4 Muon spectrometer

The Muon Spectrometer (MS) is designed to detect muons. Muons mainly travel through the ATLAS detector without decaying, given that their lifetime is ~ 2.2 μs. In addition, muons are mostly minimum ionising particles, i.e. they lose only a small fraction of energy in the ID and the calorimeter systems. This is typically not sufficient for a proper identification, thus an additional detector is needed. The MS is the outermost part of the ATLAS detector, with an acceptance of $|\eta| < 2.7$, and it spans the largest volume, as shown in Figure 3.9. The magnetic field created by the toroid magnets bends muons in the $(r-z)$ plane. Muons are then reconstructed by combining the track-information from the ID and MS.

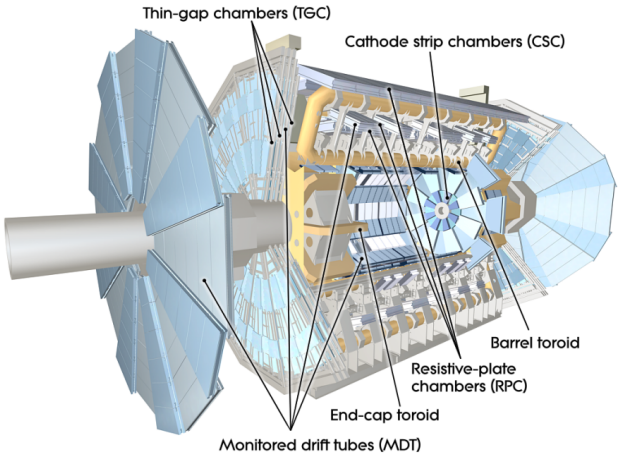

Figure 3.9. The ATLAS Muon Spectrometer [80].

The MS uses different detection technologies. The Monitored Drift Tubes (MDTs) cover the central η region. Together with the Cathode Strip Chambers

(CSCs), covering $2 < |\eta| < 2.7$, they provide precision tracking. The MDTs have a 35 μm resolution in z, while CSCs have a 40 μm $\times$ 5 mm resolution in $z \times r$. The long response time of MDTs makes it impossible to use them as a part of the trigger system. For that reason, two additional faster components, the Resistive Plate Chambers (RPCs) and the Thin Gap Chambers (TGCs) are used, with an pseudorapidity coverage of $|\eta| < 1.05$ and up to $|\eta| < 2.4$, respectively, to provide tracking information to the trigger system.

3.2.5 Trigger system

As previously mentioned, the nominal bunch collision rate at the LHC is approximately 40 MHz. This rate is far beyond what is feasible to record in terms of the necessary recording speed and the available storage space. For those reasons, a specialised trigger system has been developed to identify events of interest.

In Run 2, ATLAS used a two-level trigger system: the hardware-based Level 1 (L1) trigger, built from custom electronics, and the software-based High Level Trigger (HLT) [97]. A schematic of the ATLAS Trigger and Data Acquisition system is shown in Figure 3.10. An event is saved only if it passes both the L1 and HLT selection requirements.

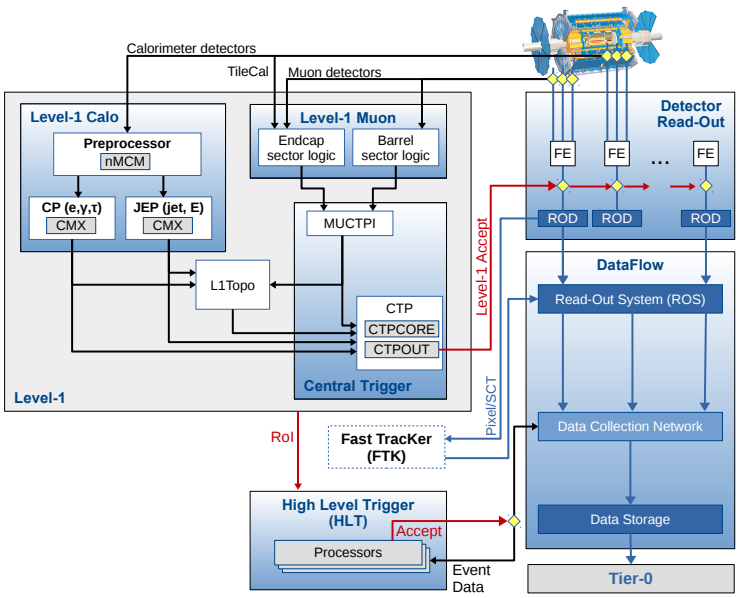

Figure 3.10. Schematic view of the ATLAS Trigger and Data Acquisition system in Run 2 [98].

The L1 trigger reduces the event rate from 40 MHz to around 100 kHz. It takes approximately 2.5 μs to process an event. To achieve such latency, the

L1 trigger uses significantly reduced detector granularity and applies rough approximations to the object reconstruction. This leads to a significantly worse energy and momentum resolution. In addition to making a decision if an event should be passed to the HLT, the L1 system identifies Regions of Interest (RoIs) in the calorimeters and the MS.

The HLT further reduces the event rate down to approximately 1 kHz. It uses information from the ID, the calorimeters and the MS, focusing on the RoIs identified at L1. The algorithms used to identify physics objects at the HLT are as similar as possible to those used in the later (offline) event reconstruction. However, the performance of these algorithms is limited by the required latency.

The trigger system is based on identifying events containing electrons, photons, jets, E_T^{miss}, or muons with a sufficiently high energy/momentum[7]. An event can fire multiple "trigger chains", but firing one chain is enough to record the event. Additionally, a set of "pre-scaled" triggers is used for calibration purposes, for studying characteristics of an average event produced in collisions (minimum bias events), for measuring specific properties of physics objects at low energies, etc. These triggers select randomly only a defined fraction of events that pass the trigger requirements.

3.3 Monte Carlo simulation

Modelling different stochastic physics processes is necessary in order to interpret the data recorded at a collider physics experiment. This modelling is based on *Monte Carlo* (MC) simulations, which rely on sampling many times over values of a random variable in a way consistent with its underlying probability distributions, and building a representative sample of events in that way. It takes many steps to go from first-principles theoretical calculations to simulated complex detector signatures that provide a satisfactory description of the experimental data [99]. These steps are to a large extent independent from each other since they occur at different energies, i.e. the simulation chain can be *factorised*.

Matrix element and parton shower

As already discussed in Section 3.1.3, a set of PDFs is used to describe the content of the colliding protons, which is taken into account when simulating a hard-scatter process of interest. The first steps in the event simulation are calculating the *Matrix Element* (ME) at some fixed order in α_s, and simulating the parton shower (PS). Different techniques can then be employed to *merge* the ME and PS [100].

[7]The trigger system also uses identification algorithms to select events containing b-jet or hadronically-decaying τ leptons, but also events with some specific properties, e.g. events with high H_T (scalar sum of energy of all objects in the event).

In renormalisable quantum field theory, ultraviolet divergences that appear in ME calculations can be regularised in terms of some energy scale, referred to as *the renormalisation scale*[8], μ_r. Similarly, the role of a PS is to describe the evolution of the outgoing energetic partons until they start hadronising. A cutoff energy scale between the perturbative and non-perturbative regime is introduced and it is called *the factorisation scale*, μ_f. These two energy scales are not physical, but their choice can have a non-negligible effect on the results of the simulation.

The ME calculations for signal and background predictions used in this thesis are obtained using MADGRAPH5_aMC@NLO [101], POWHEG-BOX [102], SHERPA [103] and PYTHIA [104–106]. Except for PYTHIA, these generators are able to provide ME calculations at NLO in QCD. On the other hand, PYTHIA and SHERPA are multipurpose generators, also able to simulate PS and hadronisation processes.

The most commonly used PS generators are HERWIG [107–109], which is based on an angular-ordered shower evolution, and PYTHIA [104–106, 110], which is based on a p_T-ordered shower evolution. Additionally, SHERPA [111] is also commonly used and its PS and hadronisation methods are similar to the HERWIG approach.

Hadronisation and the underlying events

The hadronisation, which is the next step in the simulation chain, is based on different phenomenological models, since there is no well-established underlying hadronisation theory. The two most common approaches are the *String model* [112] used by PYTHIA and the *Cluster model* [113] used by HERWIG. Additional radiation coming from the same pp collision as the hard parton-parton interaction – *the underlying event*, is also simulated using different phenomenological models [114, 115]. A set of *tunes* [116, 117] is used to constrain a large number of parameters on which the non-perturbative phenomenological models depend, in order to obtain a satisfactory description of the experimental data.

B-hadron and τ-lepton decays

Some complicated decays, such as B-hadron and τ-lepton decays, are often simulated using dedicated packages, e.g. EVTGEN [118] and TAUOLA [119].

[8]The underlying Lagrangian of a theory, $\mathscr{L}_{\text{bare}}$, is assumed to depend on the "bare" parameters of the theory, which are not the same as the physical (observable) parameters. The theory is renormalisable if this Lagrangian can be written as $\mathscr{L}_{\text{bare}} = \mathscr{L}_{\text{r}} + \mathscr{L}_{\text{c.t.}}$, where $\mathscr{L}_{\text{r}}$ is the renormalised Lagrangian, written in terms of physical parameters and fields, while the counterterms Lagrangian, $\mathscr{L}_{\text{c.t.}}$, absorbs the divergences. This implies scale-dependent (running) coupling constants.

Pileup simulation
Interactions from pp interactions that happen in the same (in-time pileup) or nearby bunch-crossing (out-of-time pileup) are modelled by overlying minimum bias events over the hard-scatter events [120]. The pileup profile of the simulated events is re-weighted to match the one in data.

Detector response simulation
Up to this point, the simulated results fundamentally depend only on the centre-of-mass energy and the type of collisions. Event simulation at this stage is called the *truth-* or *generator-level* information. Although a truth-level distribution can be interpreted as something that would be measured with a perfect detector, essentially it is unphysical.

Computationally, the most extensive step in the simulation chain is the simulation of the detector response. A detailed map of the ATLAS detector, including all detector sub-systems, magnets, mechanical structures, cryostats, cables, electronics, etc., is imported into GEANT4 [121], which is then used to simulate the truth-level particles interactions with the detector material and to produce characteristic energy deposits (hits), that are subsequently transformed into analogue or digital signals using dedicated digitisation algorithms. After simulating the Read Out Driver (ROD) electronics, the simulated events are processed in the same way as the data [99]. The same trigger criteria and event reconstruction techniques, which are summarised in Chapter 4, are further applied.

4. Reconstruction and identification of physics objects

A brief description of different algorithms used to reconstruct and identify physics objects based on signals emerging in the detector, both in data and MC simulations, is given in this chapter. Low-level objects, mainly tracks, vertices and calorimeter-cell clusters, are reconstructed first. They are used to reconstruct more complex objects, which serve as candidates for electrons, photons, muons, jets, hadronically-decaying τ leptons, etc. An illustration of some typical detector signatures is shown in Figure 4.1.

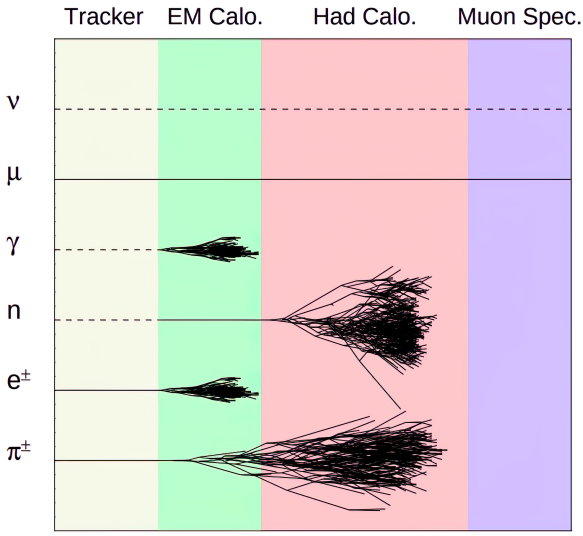

Figure 4.1. Illustration of the interaction patterns for different particles travelling through the ATLAS detector [122]. Solid lines indicate observable trajectories in the tracker and the MS for charged particles and minimal energy losses in the calorimeter for muons. Dashed lines indicate no signal being produced by the incoming particle in the respective detector sub-system. Electromagnetically- and hadronically-interacting particles produce EM and hadronic showers in the calorimeter system.

Each reconstructed (e.g. electron-like) object may represent a true candidate (real electron producing a characteristic signature in the detector), or it may be a fake candidate (e.g. quark- or gluon-initiated jet producing an

electron-like detector signature). In data, the two cases cannot be distinguished, while in MC simulation, distinguishing between real and fake candidates is possible based on the truth-level record[1]. To achieve high rejection of the fake candidates, a set of identification and isolation algorithms are applied to the reconstructed objects.

Various corrections are performed in order to calibrate the energy or momentum of the reconstructed objects. Additional corrections are applied to MC simulation to account for any difference between the reconstruction or identification efficiencies between the simulated event samples and data.

4.1 Track and vertex reconstruction

Tracks are reconstructed [124] based on hits occurring in different layers of the inner detector when charged particles travel through the sensitive material. A track is characterised by a set of parameters: transverse and longitudinal impact parameters[2], d_0 and z_0, respectively; ϕ and θ angles; and the ratio of its charge and momentum, q/p.

Raw detector measurements in the Pixel detector and SCT are clustered using a connected component analysis (CCA) [125] to create three-dimensional *space-points*, which are used directly for the track reconstruction. Given the dense LHC environment, many space-points include signals from multiple traversing particles, which are identified using dedicated algorithms. The *seed tracks* are reconstructed from three space-points after which a certain selection is performed before they are required to be compatible with additional space-points.

The selected seed tracks are passed on to a combinatorial Kalman filter [126], which further builds track candidates by considering available space-points from all Pixel and SCT layers. Each track candidate is assigned a score based on the number of included space-points, missing space-points in some layers, track p_T, χ^2, etc. This score, which describes the quality of a track, is used to decide which tracks have priority when it comes to resolving potential ambiguities. In the next step, the TRT measurements are also included [127], and a high-resolution track fit is performed.

Once the track reconstruction and selection are finalised, a dedicated vertex finder algorithm [128, 129] is employed. The starting vertex seed is found based on the global maximum in the z_0 distribution of the tracks with respect to the interaction point. All tracks are checked for compatibility with this vertex and, if an incompatibility of $d_0/\sigma(d_0) > 7$ is found, the track is left unassoci-

[1] This is usually done by geometrically matching the detector-level object to the truth-level object, or by ghost-association [123].

[2] The transverse impact parameter, d_0, is defined as the closest distance between the interaction point (IP) and the track projection onto the transverse plane, while the longitudinal impact parameter, z_0, is defined as the minimal value of $|z_{\text{track}} - z_{\text{IP}}|$.

ated. This procedure is repeated until all the tracks are associated with some vertex. The vertex with the highest sum of p_T^2 of the associated tracks is taken as the primary vertex (PV) of the event. The remaining reconstructed vertices within the bunch-crossing area are considered to be pileup interactions. Other vertices that are outside the bunch-crossing area are called secondary vertices.

4.2 Electrons

The reconstruction, identification and isolation of electrons [130] in the ATLAS experiment is based on localised clusters of energy deposited in the ECal, tracks reconstructed in the ID, and close matching in the $\eta \times \phi$ space between the two.

In ATLAS, electrons are reconstructed within the $|\eta| < 2.47$ region. The energies deposited in the three layers of ECal and the presampler are summed to form energy towers in cells of 0.025×0.025 in $\Delta\eta \times \Delta\phi$. A sliding-window algorithm [131] is used to search for clusters of towers, called seed clusters, with a minimum transverse energy of 2.5 GeV. In the next step, tracks with $p_T > 0.5$ GeV are extrapolated into the volume of the ECal and associated to the seed clusters. The track impact point and the seed-cluster barycentre are required to be within a distance of less than 0.05 in $|\Delta\eta|$ and less than 0.1 in $|\Delta\phi|$. If a seed cluster does not have any tracks associated to it, it is considered a photon candidate. If there are more tracks associated with the seed cluster, one is chosen as the primary track. If the primary candidate track can be matched to a secondary vertex and has no pixel hits, then this object is classified as a photon converted into e^+e^- pair. Thus, in order to select electron candidates, the primary candidate track is required to come from the primary vertex. In the last step, the cluster size is increased to account for the lateral spread of energy and any energy depositions beyond the ECal are added to the total cluster energy.

The electrons produced in decays of heavy resonances are called *prompt electrons*. Electrons can also be produced in semi-leptonic decays of hadrons, via photon conversions, or there can be fake electron candidates. The electron identification algorithm [130], based on a multivariate likelihood (LH) technique, is trained to select prompt electrons and reject other candidates. Three levels of identification (working points) are defined: *loose*, *medium* and *tight*. The loose working point has the highest true-prompt-electron identification efficiency, and the lowest non-prompt-electron rejection, while the opposite is true for the tight working point. The electron identification efficiencies for the three working points, as a function of the electron E_T and η, are shown in Figure 4.2.

The isolation algorithm [130] is used to further reject non-prompt electrons. An isolation cone of a fixed or p_T-dependent radius ΔR around the electron candidate is defined. Calorimeter- and track-based variables are constructed

to quantify the amount of activity in the isolation cone, excluding the electron candidate itself. These variables are used to define several electron isolation working points.

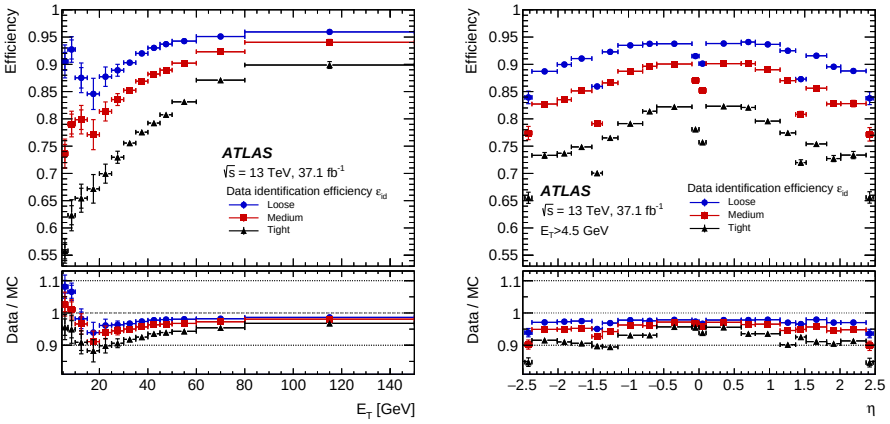

(a) **(b)**

Figure 4.2. Electron identification efficiencies calculated from a $Z \to e^+e^-$ sample for the three working points, as a function of the (**a**) electron E_T and (**b**) electron η [130]. The bottom panels show the data-to-simulation ratios, with statistical and systematic uncertainties.

The detailed electron energy calibration is performed using multivariate techniques [132, 133], based on MC simulations and data, after the final selection of the electron candidates.

4.3 Muons

Muons are reconstructed and identified based on the information from the ID, MS and calorimeter system. Tracks are reconstructed in the ID and MS independently. In the MS, local track segments are formed from hit patterns in each MS chamber. The track segments from different layers of the MS are then fitted to form a MS track [134]. In approximately 96% of cases, muons are reconstructed by performing a global refit that uses hits from both the ID and MS. The muon candidates that are reconstructed in this way are referred to as *combined muons*. Other types of muons correspond to tagged ID tracks that are matched to muon signatures in the MS, or the calorimeter.

Additional muon identification criteria [134] are applied to suppress non-prompt muons, which are mainly coming from pion and kaon decays. The non-prompt muons are often characterised by a distinctive "kink" topology in the reconstructed track, or they originate from a secondary vertex. Several variables that offer good discrimination between the prompt and non-prompt

muons are combined to define four muon identification selections (working points): *loose*, *medium*, *tight* and *high-*p_T. The muon reconstruction efficiency for the medium working point, as a function of the muon p_T and η, is shown in Figure 4.3.

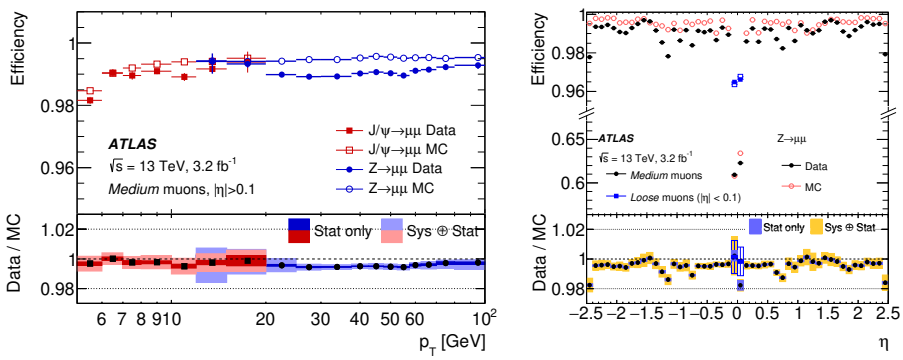

(a) **(b)**

Figure 4.3. Muon reconstruction efficiency [134] for the medium identification working point, as a function of the (**a**) muon p_T measured in $J/\psi \to \mu^+\mu^-$ and $Z \to \mu^+\mu^-$ events and (**b**) muon η measured in $Z \to \mu^+\mu^-$ events. The bottom panels show the data-to-simulation ratios, with statistical and systematic uncertainties.

Similar to the electron case, several working points of the muon isolation are defined based on different track- and calorimeter-based variables, constructed to measure the level of activity in an isolation cone around the muon candidate. The momentum scale and resolution, as well as the dimuon mass resolution, are obtained from studying $J/\psi \to \mu^+\mu^-$, $\Upsilon \to \mu^+\mu^-$ and $Z \to \mu^+\mu^-$ events [135]. These studies are used to correct the MC simulation to improve their agreement with data and to minimise the corresponding uncertainties.

4.4 Jet reconstruction

Almost immediately after being produced, a quark or gluon showers and hadronises. This creates a collimated spray of hadrons – a jet. By measuring the energy, direction, shape and different substructure variables, one can learn about the parton[3] initiating the jet. However, jets do not always correspond to a single parton. For example, a pair of quarks produced in the decay of a resonance can be reconstructed as a single jet, or even as more than two jets, depending on how collimated the two quarks and their radiation products are.

[3]The parton definition in the context of jets is ambiguous, but it usually refers to a quark or gluon produced in the hard-scatter interaction, or coming from the decay of a heavy resonance.

A jet definition includes a *jet algorithm* and a *recombination scheme* [136]. The former defines how to group some inputs into a set of jets, while the latter determines how to assign a momentum to a jet. In simulations, a jet can be defined at the parton-, hadron- (particle-), or detector-level, as illustrated in Figure 4.4. The particle-level jet is usually called *truth-jet*. A good jet algorithm provides a similar set of reconstructed jets at all levels.

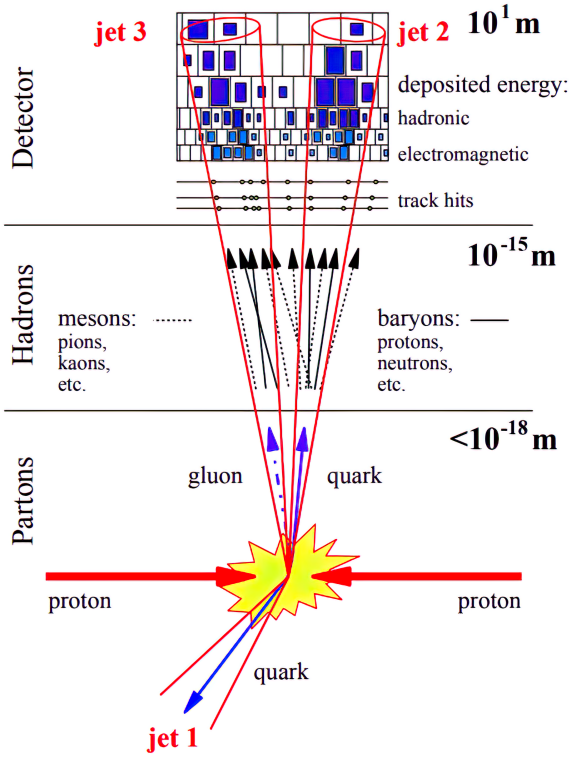

Figure 4.4. Illustration of a jet evolution [137].

A clustering algorithm [138] is used to define topologically connected calorimeter cells with energy depositions that are above the calorimeter noise, σ_{cell}. These clusters are referred to as *topo-clusters*. In ATLAS, they are seeded from calorimeter cells with an energy E_{cell} that is greater than $4\sigma_{\text{cell}}$. Additional adjacent cells are added to form a cluster if they satisfy $E_{\text{cell}} > 2\sigma_{\text{cell}}$. The formation of topo-clusters is completed by adding a single layer of adjacent cells with $E_{\text{cell}} > 0$.

The calorimeter jets used in the studies presented in this thesis are reconstructed from the topo-clusters using the anti-k_t jet algorithm [139, 140]. An important characteristic of this algorithm is that it is infrared and collinear (IRC) safe, meaning that the final set of jets is not changed if a collinear splitting of one of the constituents is introduced, or if some soft radiation occurs.

The anti-k_t algorithm starts with calculating

$$d_{ij} = \min\left(\frac{1}{p_{T,i}^2}, \frac{1}{p_{T,j}^2}\right)\frac{\Delta R_{i,j}^2}{R^2} \text{ and } d_{iB} = \frac{1}{p_{T,i}^2}, \tag{4.1}$$

where d_{ij} is the p_T-weighted "distance" between two constituents i and j, d_{iB} is defined as a threshold value of this distance for the constituent i, as explained in the following, while R is the size parameter of the algorithm. In the next step, a minimum of all d_{ij} and d_{iB} is found. If the minimum value corresponds to some d_{ij}, the constituents i and j are merged. If the minimum value corresponds to some d_{iB}, the constituent i is considered to be one of the final jets and it is removed from the list. The procedure is repeated until there are no more constituents that are not clustered into jets. In ATLAS, the jet size parameter[4] is nominally set to $R = 0.4$.

Several steps are needed to correct and calibrate the jets [141, 142]. The direction of the jet is recalculated with respect to the PV, since initially this is done with respect to the nominal interaction point. The average amount of pileup is subtracted from each jet depending on the defined jet area [143] and the number of reconstructed primary vertices. The *Absolute MC-based calibration* is applied to match the reconstructed jet energy at the EM scale to the particle-level energy scale. This calibration is derived from MC simulation and it affects the jet energy and η. In the next step, the *global sequential calibration* is applied to reduce biases on the jet flavour and to account for the energy leaked outside the hadronic calorimeter. Finally, the *in situ* jet calibration is applied only to data. Such corrections are derived by balancing the p_T of a jet against some other well-measured object. In order to reduce the number of jets reconstructed as a consequence of pileup (pileup jets), the Jet Vertex Tagger (JVT) [144] is used to identify jets associated with the hard-scatter interaction.

Particle-flow jets

The *particle-flow jets* [145] are a distinct jet collection reconstructed from inputs from the ID and the calorimeter system. The energy depositions coming from the charged particles in the calorimeter are removed from consideration. Instead, their momenta measured in the ID, together with the calorimeter energy depositions of the neutral particles, are used as inputs for reconstructing jets. The particle-flow algorithm improves the accuracy of the energy measurement of the charged hadrons. The particle-flow jet reconstruction is used for the results presented in Chapter 8.

[4] In reconstructing hadronically-decaying resonances with high momenta, where decay products are too collimated to be reconstructed as separate resolved $R = 0.4$ jets, it is more convenient to use "large-radius jets", e.g. $R = 1.0$ anti-k_t jets.

4.5 Identification of *b*-jets

The process of identifying a *b*-jet, i.e. a jet containing a *B*-hadron, is called *b*-tagging, and it is essential for studying many physics processes where *b*-jets need to be distinguished from light-flavour[5] and *c*-jets.

A *B*-hadron has a characteristic mean lifetime[6] of around 1.5 ps, a higher mass compared to mesons composed of lighter quarks, and several characteristic decay features, which can be exploited for the purpose of *b*-tagging. For $p_T > 20$ GeV, *B*-hadrons on average travel several millimetres before they decay, creating a secondary vertex within the jet, as illustrated in Figure 4.5. In addition, the charged decay products of a *B*-hadron tend to produce tracks that, with respect to the PV, have large impact parameters.

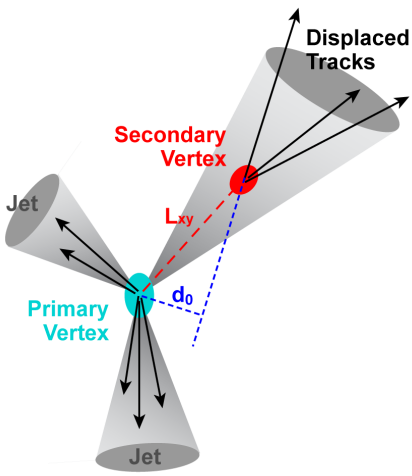

Figure 4.5. Illustration of some of the characteristics of a *b*-jet: presence of a secondary vertex within the jet and tracks with large impact parameters that originate from the secondary vertex.

The *b*-tagging algorithm used to obtain the results presented in Chapters 5–7 is referred to as the *MV2c10 tagger* [146]. It is based on a Boosted Decision Tree (BDT) classification, which combines information from several other algorithms. Dedicated impact-parameter-based algorithms – *IP2D* and *IP3D* [147, 148], are used to separate tracks associated to jets according to whether or not they are compatible with the PV. The *secondary-vertex finder* (SV1) [147, 148] method is used to reconstruct displaced secondary vertices within the jet. Additionally, the *JetFitter* [149] algorithm reconstructs multiple vertices within the jet in order to map the full *B*-hadron decay chain. Different variables obtained from these algorithms are used as inputs to the

[5]The term light-flavour jet refers to jets initiated by an up, down, or strange quark, or a gluon. Similarly, the term heavy-flavour jet is used for jets initiated by a bottom, or a charm quark.
[6]The charmed *B*-meson has a shorter mean lifetime of around 0.5 ps.

BDT. The BDT is trained to select true b-jets and reject other reconstructed jets. The training is performed against the background sample consisting of approximately 93% (7%) of light-flavour jets (c-jets). The obtained result is called the MV2c10 BDT output score, and it is used as a final discriminant for tagging a jet as a b-jet. The MV2c10 BDT output score evaluated using simulated $t\bar{t}$ events is shown in Figure!4.6a. The MV2c10 rejection factors, calculated as inverse of the background efficiencies, are shown in Figure 4.6b for light-flavour and c-jets, separately, as a function of the true-b-jet efficiency.

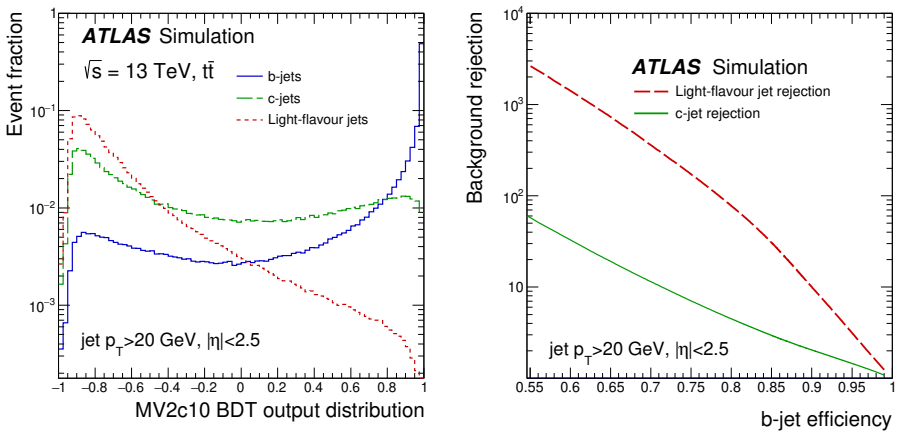

(a) **(b)**

Figure 4.6. (**a**) The MV2c10 output score for b-jets (solid line), c-jets (dashed line) and light-flavour jets (dotted line), evaluated using simulated $t\bar{t}$ events [150]. (**b**) The rejection factors for light-flavour jets (dashed line) and c-jets (solid line) as a function of the b-jet tagging efficiency of the MV2c10 b-tagging algorithm [150].

Similar to the electron and muon identification algorithms, several working points are defined for the b-jet identification. For the results presented in Chapters 5–7, the working point corresponding to a 70% efficiency for identifying true b-jets in simulated $t\bar{t}$ events is used. The efficiency is approximately constant with respect to the true-b-jet p_T. It corresponds to rejection factors of 381 for light-flavour jets, 12 for c-jets and 55 for hadronically-decaying τ leptons [146].

Deep Learning b-tagging algorithm: DL1r

Another b-tagging algorithm – the *DL1r tagger*, has been developed and tested in ATLAS [151]. Other than using the deep-learning neural network approach, an additional novelty of the DL1r algorithm, with respect to the MV2c10 tagger, is that the information obtained from the IP2D and IP3D algorithms is replaced by the impact-parameter-based algorithm developed using the recur-

rent neural network (RNN) approach – RNNIP [152]. The DL1r tagger mainly improves the b-tagging performance at high p_T, and it was used when obtaining the results in Chapter 8.

Muon-in-jet and PtReco corrections

In addition to the standard jet calibration, two additional corrections to the jet energy scale are applied in order to improve the reconstructed invariant-mass resolution of a resonance decaying into two bottom quarks. The *muon-in-jet* [153] correction is applied to account for the decays of B- and C-hadrons into muons, since muons deposit only a fraction of their energy in the calorimeter. The four-momentum of a muon found within the jet is added to the four-momentum of the jet if the muon has $p_T > 5$ GeV and if it satisfies the medium identification working point. If more such muons are found within the jet, the one closest in ΔR to the jet-axis is chosen. The calorimeter energy deposited by that muon is subtracted from the jet energy.

A second correction, denoted *PtReco* [153], is applied to account for the residual difference in simulations between the reconstructed-jet p_T and the p_T of the corresponding[7] truth-jet. The effect of the two corrections on the di-b-jet invariant mass distribution, m_{bb}, in simulated $ZH \to \ell^+\ell^- b\bar{b}$ samples, where ℓ stands for an electron or muon, is shown in Figure 4.7. In addition, the PtReco correction can be replaced by the Kinematic Likelihood Fit [153], but this method has not been used for the results presented in this thesis.

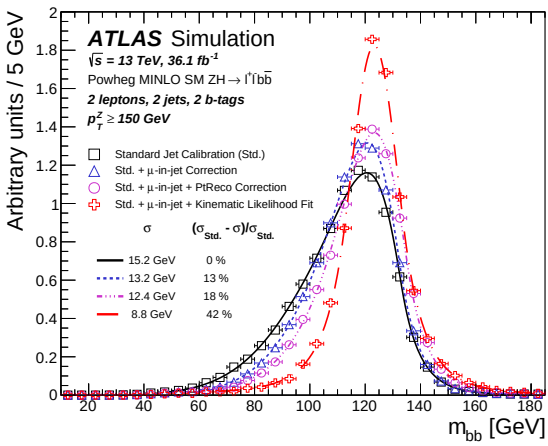

Figure 4.7. Comparison of four m_{bb} distributions as additional corrections are applied to the jet energy scale [153], evaluated on simulated $ZH \to \ell^+\ell^- b\bar{b}$ events. All distributions include the standard jet calibration. First, the muon-in-jet correction is applied (blue triangles) and then the PtReco correction is added (magenta circles). In addition, the PtReco correction is replaced by the Kinematic Likelihood Fit (red crosses).

[7] The reconstructed jet and the truth-jet are required to be geometrically matched.

4.6 Missing transverse energy

The partons colliding at the LHC have only longitudinal momentum. For this reason, the law of conservation of momentum can be applied in the transverse plane. Particles that interact only weakly, such as neutrinos, leave the volume of the detector unobserved. In the case of a perfect detector, the sum of the transverse momenta of such particles, $\vec{p}_T^{\,\text{miss}}$, can be calculated from the transverse momenta of the observed detector objects as

$$\vec{p}_T^{\,\text{miss}} = -\sum_i \vec{p}_{T,i}^{\,\text{visible}}. \tag{4.2}$$

However, due to the limited detector resolution, some physics objects may be reconstructed poorly, or not reconstructed at all, which needs to be taken into account in the calculation of $\vec{p}_T^{\,\text{miss}}$. Additionally, certain objects can be outside the detector acceptance.

All objects used for calculating the $\vec{p}_T^{\,\text{miss}}$ (namely: electrons, muons, photons, hadronically-decaying τ leptons, jets calculated from energy deposits in the calorimeter, and charged-particle tracks) are calibrated in order to improve the $\vec{p}_T^{\,\text{miss}}$ resolution. The measured momentum that is not assigned to any of the listed physics objects is called the *soft-term* [154]. It is measured from reconstructed charged-particle tracks not associated with other reconstructed objects. These tracks are matched to the PV to exclude pileup contributions. Information about the contribution from neutral particles to the track-based soft-term is not included since it is too sensitive to pileup contributions, and is anyway expected to be symmetric in ϕ. The magnitude of $\vec{p}_T^{\,\text{miss}}$ is typically referred to as *missing transverse energy*, denoted E_T^{miss}.

4.7 Reconstruction and identification of τ leptons

The mean lifetime of τ leptons is very short, approximately 0.29 ps, which means their decay occurs predominantly within the beam pipe. They decay through the emission of an off-mass-shell W boson, which then decays either leptonically or hadronically, as shown in the Feynman diagram in Figure 4.8.

4.7.1 Leptonically-decaying τ leptons

The branching ratio of τ leptons into electrons (muons) is 17.8% (17.4%) [25]. Such electrons and muons, on their own, are indistinguishable from other prompt electron and muon candidates. Furthermore, the two neutrinos produced in the leptonic τ-lepton decay cannot be identified directly, as already explained in Section 4.6. Thus, a leptonically-decaying τ lepton, referred to as τ_{lep} in this thesis, is reconstructed as a charged electron, or muon, with some contribution to E_T^{miss}.

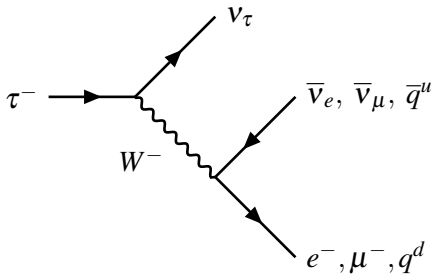

Figure 4.8. Feynman diagram of the decays of a τ lepton by emission of an off-mass-shell W boson. The q^u and q^d symbols refer to any up- (except for the top quark) and down-type quarks, respectively.

4.7.2 Hadronically-decaying τ leptons

Due to its high mass of approximately 1.777 GeV [25], τ is the only lepton heavy enough to decay into hadrons. This happens approximately 64.8% of the time. Typically, hadronically-decaying τ leptons, denoted τ_{had} in this thesis, decay into one or three charged pions or kaons and up to two neutral pions, and a ν_τ. Decay modes with one charged hadron are called *1-prong* decays, while those with three charged hadrons are referred to as *3-prong* decays. The most frequent hadronic τ-lepton decay modes and the corresponding branching ratios are listed in Table 4.1.

Table 4.1. *Approximate branching ratios for the most frequent hadronic τ-lepton decay modes [25]. The symbol h^- refers to a charged hadron (either a pion or a kaon). Some of the decays are realised through intermediate resonances, $\rho(770)$ or $a_1(1260)$ mesons.*

Decay mode	Intermediate resonance	Branching ratio [%]
$\tau^- \to h^- \nu_\tau$		11.5
$\tau^- \to h^- \pi^0 \nu_\tau$	$\rho(770)$	26.0
$\tau^- \to h^- \pi^0 \pi^0 \nu_\tau$	$a_1(1260)$	9.5
$\tau^- \to h^- h^+ h^- \nu_\tau$	$a_1(1260)$	9.8
$\tau^- \to h^- h^+ h^- \pi^0 \nu_\tau$		4.8
Other modes with hadrons		3.2
All modes with hadrons		64.8

The reconstruction of the τ_{had} candidate[8] consists of three steps that are briefly summarised below.

[8]It is more correct to distinguish between two notations: τ_{had}, which refers to a hadronically-decaying τ lepton; and $\tau_{\text{had-vis}}$, which refers to only the visible part of the τ_{had} candidate, given that the energy of neutrinos cannot be measured. For simplicity, in this thesis only the former is used, while the exact meaning should be understood from the context.

Seed jets
In the first step, the τ_{had} candidate is seeded from a jet candidate [155]. The jet collection used for this purpose, reconstructed using the anti-k_t algorithm with $R = 0.4$, is similar to the jet collection obtained from topo-clusters, for which the procedure is described in Section 4.4. The difference is that the local hadronic calibration (LC) [138] is applied to the topo-clusters before jets are formed. Only jets with $p_T > 10$ GeV within the $|\eta| < 2.5$ region are considered.

Vertex association
The τ-lepton decay vertex (TV) is usually displaced with respect to the PV, due to the τ-lepton decay length. Finding the correct vertex enables to require that the seed-jet-associated tracks are matched to the TV in order to suppress pileup contributions, without significantly reducing the τ_{had} reconstruction efficiency. All tracks within a cone of 0.2 in ΔR around the seed-jet-axis (core region) are used to choose the TV from the PV candidates. The direction of the τ_{had} candidate is then corrected with respect to the TV and the impact parameters are recalculated [155].

Track selection
The selection of tracks in the core region of the τ_{had} candidate is optimised to maximise the efficiency for reconstructing 1- and 3-prong τ_{had} candidates with the correct charged particle multiplicity [155].

Energy calibration
Other than forming seed-jets from topo-clusters calibrated to the LC scale, two additional energy corrections are applied to the τ_{had} candidates [155]. First, the energy contribution from pileup interactions is estimated and subtracted. Second, corrections accounting for contributions from emissions that are not energetic enough to reach the calorimeter or to form the topo-clusters, and corrections accounting for emissions that are not contained within the core region of the τ_{had} candidate, are derived and applied.

Identification
The reconstruction of τ_{had} candidates does not provide much discrimination against quark- and gluon-initiated jets. Hence, an additional τ_{had} identification algorithm (τ_{had}-ID) is crucial. For obtaining the results presented in Chapters 5–7, a BDT-based τ_{had}-ID [155, 156] was used, while for obtaining the results in Chapter 8, a more advanced RNN-based τ_{had}-ID [157] was adopted. Both algorithms use track- and calorimeter-based variables as inputs. The track information from the core region and the remaining region of the seed jet (isolation region) is considered separately. The HCal provides information about the shape of the hadronic shower, while the ECal is sensitive to the π^0 components of the hadronic τ-lepton decay. Both the BDT and RNN

τ_{had}-IDs are trained separately for 1- and 3-prong decays. They are trained to select true-τ_{had} candidates from $Z/\gamma^* \to \tau\tau$ events, and to reject quark- and gluon-initiated τ_{had} candidates from di-jet events. Only τ_{had} candidates with $p_T > 20$ GeV and outside the crack region ($1.37 < |\eta| < 1.52$) are considered for the results presented in this thesis.

The τ_{had}-ID BDT output scores for 1- and 3-prong τ_{had} candidates in $Z/\gamma^* \to \tau_{\text{had}}\tau_{\text{had}}$ (Signal) and di-jet (Background) events are shown in Figure 4.9. The rejection of fake-τ_{had} candidates as a function of the true-τ_{had} selection efficiency is shown separately for the 1- and 3-prong BDT (RNN) algorithms in Figure 4.10 (4.11).

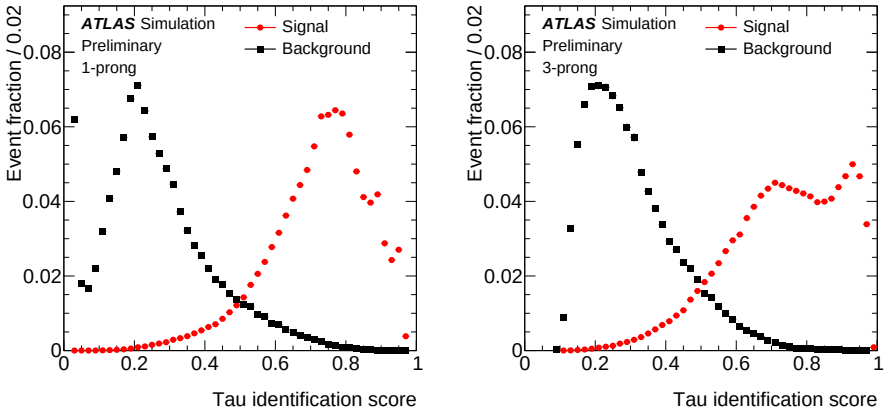

Figure 4.9. The τ_{had}-ID BDT output score for the true-τ_{had} candidates (red circles) and simulated quark- and gluon-initiated jets reconstructed as τ_{had} candidates (black squares) for (**a**) 1-prong and (**b**) 3-prong τ_{had} candidates [155].

4.7.3 The Missing Mass Calculator

Each τ-lepton decay involves one or two neutrinos, which makes it difficult to reconstruct the invariant mass of a resonance decaying into a pair of τ leptons, $m_{\tau\tau}$. The invariant mass of the visible decay products in this final state has a broad spectrum and does not offer a good discrimination against background processes. Even if a perfect detector response is assumed, and if there are no other neutrinos in the event, $m_{\tau\tau}$ cannot be calculated analytically since there are more unknown variables than constraints. There are at least 6 unknown quantities, p_x, p_y and p_z of the invisible part of each of the two τ leptons. In addition, for each τ_{lep} object, the invariant mass of the invisible part is unknown, given that there are two neutrinos present in such a leptonic decay. That accounts for 6 to 8 unknown quantities for a pair of τ leptons, while only

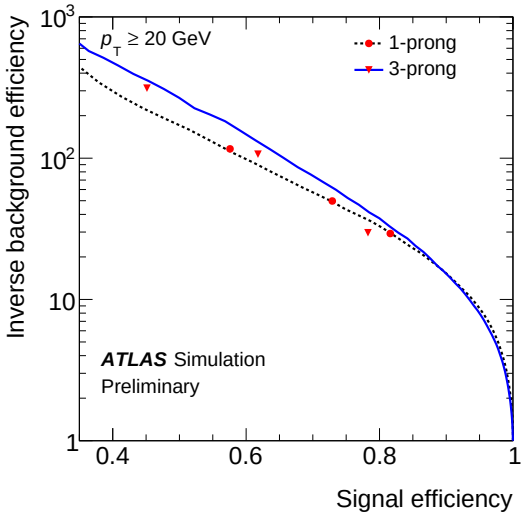

Figure 4.10. BDT τ_{had}-ID: Inverse of the selection efficiency (rejection factors) for quark- and gluon-initiated jets reconstructed as τ_{had}, as a function of the true-τ_{had} selection efficiency, separately for 1- and 3-prong candidates [155]. Different markers indicate the three defined working points: tight, medium and loose, with increasing true-τ_{had} selection efficiencies. The working points do not correspond exactly to the curve because they implement variable cuts to achieve a reduced p_T-dependency of the efficiency.

4 independent constraints can be imposed between them. However, not all solutions are equally probable, which can be exploited.

The Missing Mass Calculator (MMC) algorithm [158] is designed to search for the most probable solution based on different probability density functions that are provided as inputs. These probability density functions include, for example, the expected angular distance between the visible and invisible parts of the τ-lepton decay for a particular value of the τ-lepton p_T. In this way, a global event likelihood is defined and used to obtain the most probable $m_{\tau\tau}$ value. Two examples of the $m_{\tau\tau}$ distributions obtained using the MMC algorithm, $m_{\tau\tau}^{\text{MMC}}$, are shown in Figure 4.12: the $m_{\tau\tau}^{\text{MMC}}$ distribution in simulated SM $HH \to b\bar{b}\tau_{\text{had}}^{+}\tau_{\text{had}}^{-}$ (signal) events, where the τ_{had} pair is produced in the Higgs boson decay; and the $m_{\tau\tau}^{\text{MMC}}$ distribution in simulated $t\bar{t}$ events with two τ_{had} in the final state. In the latter case, the two τ leptons do not come from the same mother particle and there are additional neutrinos from the W boson decay in the event. The MMC algorithm significantly improves the $m_{\tau\tau}$ reconstruction for the signal process, while also increasing the separation between the signal and $t\bar{t}$ events.

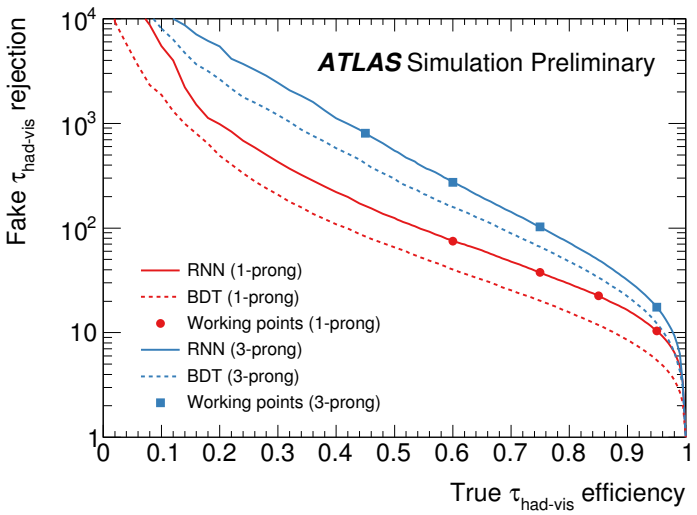

Figure 4.11. RNN τ_{had}-ID: Rejection factors for quark- and gluon-initiated jets reconstructed as τ_{had}, as a function of the true-τ_{had} selection efficiency, separately for 1- and 3-prong candidates [157]. Solid (dashed) lines refer to the RNN (BDT) τ_{had}-ID, for comparison. Differences between the performance of the BDT τ_{had}-ID here and in Figure 4.10 are a consequence of re-tuning the BDT algorithm and re-optimising the reconstruction of τ_{had} candidates for studying the full Run 2 ATLAS dataset. Different markers indicate the four defined working points for the RNN τ_{had}-ID: tight, medium, loose and very-loose, with increasing true-τ_{had} selection efficiencies.

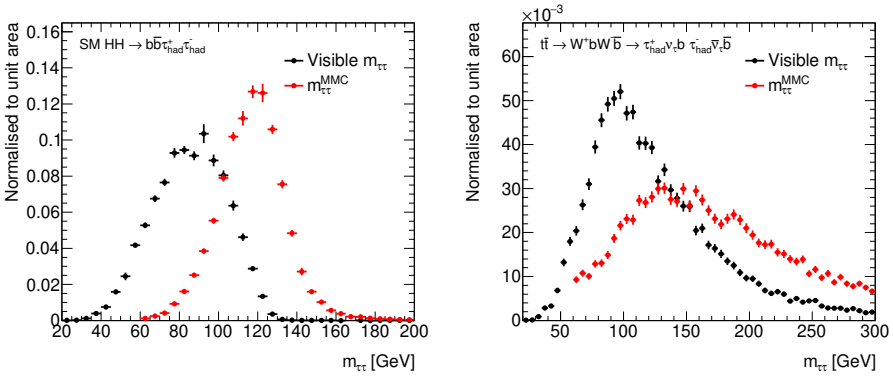

Figure 4.12. Comparison between the visible $m_{\tau\tau}$ and $m_{\tau\tau}^{\text{MMC}}$ distributions for (**a**) the SM $HH \to b\bar{b}\tau_{\text{had}}^{+}\tau_{\text{had}}^{-}$ signal events and (**b**) $t\bar{t}$ events with two τ_{had} in the final state.

5. Searches for pair production of Higgs bosons in the $b\bar{b}\tau^+\tau^-$ final state with 36.1 fb^{-1} of 13 TeV pp collision data in ATLAS

In this chapter, a search for the resonant and non-resonant pair productions of Higgs bosons in the $b\bar{b}\tau^+\tau^-$ final state with 36.1 fb^{-1} of 13 TeV pp collision data recorded by the ATLAS detector in 2015 and 2016 is presented. The results of the analysis are published in Ref. [15]. As already mentioned in Section 1.4.2, only the dominant ggF non-resonant (SM)[1] pair production of Higgs bosons is considered. Additionally, a scalar resonance decaying into a pair of Higgs bosons is searched for in the context of hMSSM, as explained in Section 2.1.1, and the results are interpreted for $\tan\beta = 2$. The spin-2 KK excitations of the graviton, G_{KK}, in the bulk Randall-Sundrum model, decaying into pairs of Higgs bosons, are searched for using two benchmarks with $k/\bar{M}_{\text{pl}} = 1$ and $k/\bar{M}_{\text{pl}} = 2$, as discussed in Section 2.1.2.

The analysis presented in this chapter is re-interpreted in order to probe anomalous trilinear Higgs boson self-couplings, but those results are presented in Chapter 6. Furthermore, the results presented in this chapter and in Chapter 6 are extrapolated to estimate the sensitivity to the non-resonant HH production in the $b\bar{b}\tau^+\tau^-$ final state at the HL-LHC, as will be described in Chapter 7.

Two final states are considered in the analysis: the final state with one leptonically- and one hadronically-decaying τ lepton, referred to as the $\tau_{\text{lep}}\tau_{\text{had}}$ final state in this thesis; and the final state with two hadronically-decaying τ leptons, which is referred to as the $\tau_{\text{had}}\tau_{\text{had}}$ final state. The $\tau_{\text{lep}}\tau_{\text{had}}$ ($\tau_{\text{had}}\tau_{\text{had}}$) decay channel has a branching ratio of 45.7% (42.0%) with respect to all $H \to \tau\tau$ decays. The final state with two leptonically-decaying τ leptons, $\tau_{\text{lep}}\tau_{\text{lep}}$, with a branching ratio of 12.4%, was not considered in the analysis. Both $\tau_{\text{lep}}\tau_{\text{had}}$ and $\tau_{\text{had}}\tau_{\text{had}}$ channels are described in this chapter, with emphasis on the $\tau_{\text{had}}\tau_{\text{had}}$ channel.

[1] In order to distinguish between discussing non-resonant pair production of Higgs bosons for $\kappa_\lambda \neq 1$ and for $\kappa_\lambda = 1$ (SM) throughout this thesis, the latter is referred to as the SM pair production of Higgs bosons, even though this terminology only refers to the assumed signal kinematics. It does not always refer to the assumed cross-section, given that higher or lower normalisation values are probed when setting upper limits on the production cross-section.

5.1 Simulation of signal and background processes

A typical event simulation chain in the ATLAS experiment is described in Section 3.3. In this section, the complete set of simulated signal and background samples used in the analysis is described. The list of processes, generators used for the ME calculations, PS and hadronisation simulations, PDFs and tunes is summarised at the end of this section. The assumed production cross-section values used for normalising the simulated samples to the integrated luminosity of the dataset are specified in the following.

SM pair production of Higgs bosons
The MADGRAPH5_aMC@NLO (MG5_aMC@NLO) v2.2.3 [101] framework is used to simulate the SM pair production of Higgs bosons at NLO using the method called FTApprox [159]. This method includes finite top-quark mass effects only for the real-radiation NLO corrections, while the virtual-loop corrections are realised with the Higgs effective field theory (HEFT) framework [160], assuming an infinite top-quark mass. To account for the finite top-quark mass effect in the virtual-loop corrections, the simulated events are re-weighted to reproduce the truth-level m_{HH} spectrum obtained in Refs. [45, 161], which is shown in Figure 5.1. Parton showers and hadronisation are simulated with HERWIG++ [107].

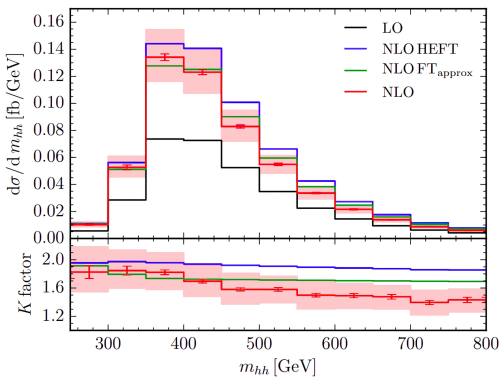

Figure 5.1. Comparison of truth-level Higgs boson pair invariant mass distributions, denoted here m_{hh}, between the full NLO prediction (red) and the FTApprox approach (green) [45].

The predicted cross-section for the SM ggF pair production of Higgs bosons is evaluated at NNLO in QCD [44–47, 161], matched to the next-to-next-to-leading logarithm (NNLL) resummation in the heavy top-quark limit [48, 49]. The obtained cross-section [43] of

$$\sigma_{HH}^{\mathrm{SM}} = 33.41^{+1.45}_{-2.00}(\text{scale}) \pm 1.67(\text{theory}) \pm 0.77(\alpha_s) \pm 0.70(\text{PDF})\ \text{fb} \quad (5.1)$$

is then used to normalise the simulated signal. The results presented in this chapter were published before the latest cross-section calculations quoted in

Table 1.2 ($\sigma_{HH}^{\mathrm{SM}} = 31.05$ fb for m_H=125 GeV at 13 TeV) became available, hence the difference. The branching ratios of the Higgs boson are assumed to be equal to the SM predictions, which is also the case for all other results presented in this thesis.

Non-resonant pair production of Higgs bosons with varied λ_{HHH}
Events with non-resonant pair production of Higgs bosons are generated for $\kappa_\lambda = \{0, 1, 2, 20\}$ with $\kappa_t = 1$ at LO using MG5_aMC@NLO v2.3.3, while the PS and hadronisation processes are simulated using PYTHIA 8.2 [105, 106]. These samples are used to obtain results in Chapter 6, and thus more details will follow.

Resonant pair production of Higgs bosons
Events with a generic narrow-width scalar, X, or a spin-2 KK graviton, G_{KK}, in the bulk Randall-Sundrum model, both decaying into two Higgs bosons, are generated at LO using MG5_aMC@NLO v2.3.3, while PYTHIA 8.2 is used for simulating the PS and hadronisation processes. The narrow-width approximation for the scalar resonance implies that the results obtained from testing this signal hypothesis can be interpreted only in the context of models in which the width of the resonance is smaller than the experimental resolution. The cross-section for $pp \to X \to HH$ is taken from Ref. [37], while the production cross-section and width of G_{KK} are taken from Ref. [67]. In both cases, samples are generated for different resonance-mass hypotheses, which are listed in Table 5.1.

Table 5.1. *The set of mass hypotheses for which the resonant signal samples are generated.*

Resonance	Mass hypotheses [GeV]
X, $\tan\beta = 2$	260, 275, 300, 325, 350, 400, 450, 500, 550, 600, 700, 1000
G_{KK}, $k/\bar{M}_{\mathrm{pl}} = 1$	260, 300, 400, 500, 600, 700, 800, 900, 1000
G_{KK}, $k/\bar{M}_{\mathrm{pl}} = 2$	260, 275, 300, 325, 350, 400, 450, 500, 550, 600, 700, 1000

Simulation of $t\bar{t}$ and single-top-quark events
Events with pair production of top quarks ($t\bar{t}$) and events with singly-produced top quarks (single top) are generated using POWHEG-BOX [102] v2 (v1 for the t-channel single-top production) and MADSPIN [162], while PYTHIA 6.4 [104] is used for simulating the PS and hadronisation processes. The $t\bar{t}$ events are produced with the h_{damp} parameter[2] set to the top-quark mass and they are normalised to the production cross-section calculated at NNLO in QCD including

[2]The h_{damp} parameter is a resummation damping factor, also used to control the matching of POWHEG ME to the PS and to effectively regulate the high-p_T radiation against which the $t\bar{t}$ system recoils.

the resummation of NNLL soft gluon terms [163]. The single-top events are normalised to the production cross-section calculated at NLO [164, 165] (approximate NNLO [166]) in QCD for the t- and s-channel (Wt production).

Simulation of Z+jets and W+jets events
Events with Z or W bosons produced in association with jets are simulated using SHERPA 2.2.1 [103, 111, 167–169]. The simulated samples are normalised to match the cross-sections calculated at NNLO in QCD [170].

Simulation of Drell-Yan and diboson events
Drell-Yan, ZZ, WZ and WW events are simulated using SHERPA 2.2.1. The obtained samples are normalised to the generator cross-section prediction. The quark-induced ZH events are simulated with PYTHIA 8.1 and normalised to the cross-sections calculated at NNLO for QCD processes and at NLO for electroweak processes [171–177]. The gluon-induced ZH events [178] are generated using POWHEG-BOX v2, and PYTHIA 8.1 for simulating the PS and hadronisation processes. These samples are normalised to the cross-sections calculated at NLO+NLL [179–183].

Simulation of $t\bar{t}H$ events
Events with a Higgs boson produced in association with a pair of top quarks are generated using MG5_aMC@NLO v2.2.3, while PYTHIA 8.2 is used to simulate the PS and hadronisation processes. The obtained samples are normalised to the cross-section obtained from Ref. [37], which includes NLO electroweak and QCD corrections.

All other background processes are found to have negligible contributions, except for the QCD-induced multijet background. Given that simulating multijet events is subject to large uncertainties, data-driven methods are used to estimate their contribution, as will be discussed in Section 5.3.

Other steps of the simulation chain are performed as described in Section 3.3. Properties of B- and C-hadron decays in the event simulation are modelled with EVTGEN 1.2.0 for all processes except those simulated with SHERPA. The list of MC generators used to simulate the relevant signal and background samples, together with the PDF sets and tunes used, is provided in Table 5.2.

5.2 Object and event selections

In this section, the online and offline selection of events corresponding to the final state of interest, i.e. $b\bar{b}\tau^+\tau^-$ final state, is described. The online (trigger) event selection is described in Section 5.2.1. The general overview of the offline reconstruction and identification of different physics objects in events

Table 5.2. *List of generated MC samples that are used to model different signal (upper part of the table) and SM-background processes (bottom part of the table) contributing to the $b\bar{b}\tau^+\tau^-$ final state. The list of generated samples is common for the $\tau_{\text{lep}}\tau_{\text{had}}$ and $\tau_{\text{had}}\tau_{\text{had}}$ channels. For each generated sample, the generator and the PDF used for calculating the ME are listed, as well as the generator and the tune used for simulating the PS and hadronisation processes. For processes where the PS generator is not specified, the same generator is used to calculate the ME and to simulate the PS and hadronisation processes. The second column specifies at which order of perturbation theory in QCD the ME are calculated.*

Process	ME Order	Generator	Parton Shower	PDF	Tune
		Signal processes:			
SM HH	NLO	MG5_aMC@NLO v2.2.3 [101]	HERWIG++ [107]	CT10 [184]	UEEE5 [185]
Non-resonant HH (varied κ_λ)	LO	MG5_aMC@NLO v2.3.3	PYTHIA 8.2 [105, 106]	NNPDF23LO [186]	A14 [187]
$X \to HH$	LO	MG5_aMC@NLO v2.3.3	PYTHIA 8.2	NNPDF23LO	A14
$G_{\text{KK}} \to HH$	LO	MG5_aMC@NLO v2.3.3	PYTHIA 8.2	NNPDF23LO	A14
		Background processes:			
Single top and $t\bar{t}$	NLO	POWHEG-BOX v2 t-channel: v1 [102]	PYTHIA 6.4 [104]	CT10	Perugia 2012 [117]
Z+jets, W+jets	NLO	SHERPA 2.2.1 [103, 111, 167–169]		NNPDF30NNLO [188]	
Drell-Yan	NLO	SHERPA 2.2.1		CT10NLO	
ZZ, WZ, WW	NLO	SHERPA 2.2.1		CT10NLO	
Quark-induced ZH	NLO	PYTHIA 8.1		NNPDF23LO	A14
Gluon-induced ZH	NLO	POWHEG-BOX v2 [178]	PYTHIA 8.1	CT10	AZNLO [189]
$t\bar{t}H$	NLO	MG5_aMC@NLO v2.2.3	PYTHIA 8.2	NNPDF23LO	A14

recorded by the ATLAS detector, or simulated events, is already described in Chapter 4. The exact identification techniques and working points used to select the $b\bar{b}\tau^+\tau^-$ final state for the results presented in this chapter are specified throughout this section. Given that the different identification techniques are applied independently from each other, it is possible that one detector object is reconstructed and identified as multiple physics objects. For that reason, an *overlap removal* procedure is performed, as described below. Finally, the baseline event selection, referred to as the *preselection*, is defined for the $\tau_{\text{lep}}\tau_{\text{had}}$ and $\tau_{\text{had}}\tau_{\text{had}}$ channels.

5.2.1 Online event selection

The ATLAS trigger system is briefly described in Section 3.2.5. An event is required to pass two levels of the ATLAS trigger system, L1 and HLT, in order to be recorded. At both stages, a set of online-level objects are reconstructed and certain online-identification algorithms are applied. The online-level objects have worse resolution compared to the fully reconstructed objects used later in the analysis, and thus the offline kinematic requirements usually must be tighter than those applied online to reach the full trigger efficiency. In addition, the online-identification requirements are usually looser compared to those applied offline to maximise the total identification efficiency. For simulated events, the online-level event reconstruction is performed and the trigger decision is emulated, such that the simulated events are treated in the same way as the data events.

Triggers used to select the $\tau_{\text{lep}}\tau_{\text{had}}$-like final states are based on requiring the presence of a single lepton (electron or muon), or a lepton plus a τ_{had} candidate, at trigger level. To select the $\tau_{\text{had}}\tau_{\text{had}}$-like final states, the presence of one or two τ_{had} candidates at trigger level is required. In all cases, the required objects must satisfy certain kinematic and identification criteria. In the following, the four trigger categories used in the $b\bar{b}\tau^+\tau^-$ analysis are described. It is implied that all considered objects are at trigger level and that all identification and isolation algorithms are designed for the online-object selection.

Single-lepton trigger

In the $\tau_{\text{lep}}\tau_{\text{had}}$ channel, events are first tested if they pass a logical OR of single-lepton triggers (SLT). The single-electron triggers [190] require the presence of at least one electron with $p_T > 24$ GeV that satisfies the medium identification (raised to 26 GeV and changed to the tight identification criteria for the 2016 data-taking) and the loose isolation criteria; or at least one electron with $p_T > 60$ GeV with the same identification, but without any isolation requirement; or at least one electron with $p_T > 120 - 140$ GeV that satisfies the loose identification criteria. Similarly, the single-muon triggers [191] require the presence of at least one muon with $p_T > 24 - 26$ GeV (depending on the

data-taking period) that satisfies the loose identification and isolation criteria; or at least one reconstructed muon with $p_T > 50$ GeV without any additional identification and isolation requirements.

Lepton plus τ_{had} trigger
The second trigger category used in the $\tau_{\text{lep}}\tau_{\text{had}}$ channel consists of triggers that require the presence of one lepton (electron or muon) and one τ_{had} candidate – lepton plus τ_{had} triggers (LTT). All events are checked if they pass the LTT requirements. The electron (muon) plus τ_{had} trigger requires the presence of at least one electron (muon) with $p_T > 17$ GeV ($p_T > 14$ GeV) and at least one τ_{had} candidate with $p_T > 25$ GeV. The electron/muon and the τ_{had} candidate are required to satisfy their respective medium identification criteria. For the events that correspond to the 2016 data-taking, electrons and muons are also required to satisfy the loose isolation criteria. Additionally, for the events that correspond to the 2016 data-taking, the LTT also requires the presence of an additional jet at L1 with $p_T > 25$ GeV.

Single-τ_{had} trigger
In the $\tau_{\text{had}}\tau_{\text{had}}$ channel, events are tested if they pass the single-τ_{had} trigger (STT) [192]. In this case, an event is required to have at least one τ_{had} candidate with $p_T > 80 - 160$ GeV (depending on the data-taking period) that satisfies the medium identification criteria.

Di-τ_{had} trigger
Events that do not pass the STT are checked if they pass the di-τ_{had} trigger (DTT) [192], which requires the presence of two τ_{had} candidates with $p_T > 35\ (25)$ GeV for the leading (sub-leading) candidate. Both candidates are required to satisfy the medium identification criteria. For the events that correspond to the 2016 data-taking, the DTT also requires the presence of an additional jet at L1 with $p_T > 25$ GeV.

The trigger efficiencies in simulations are corrected to match those in data, and the corresponding uncertainties are considered. These universal corrections in some cases are not valid for misidentified physics objects (e.g. fake-τ_{had} objects) since they can be final-state-dependent. Hence, this needs to be taken into account when the corresponding background processes are estimated.

5.2.2 Object selection

All events that pass the online selection are required to have a reconstructed primary vertex. Electrons, muons, jets and τ_{had} candidates are fully reconstructed and calibrated as defined in Chapter 4. In the next step, some of these physics objects are required to fulfil certain offline identification and isolation

criteria, to be within characteristic η-acceptance regions and to have some minimum p_T. These requirements are listed in Table 5.3.

Table 5.3. *Optimised selection of physics objects that correspond to the $b\bar{b}\tau^+\tau^-$ final state, including the p_T and $|\eta|$ requirements that they must fulfil. The crack region, $1.37 < |\eta| < 1.52$, is excluded ("!cr") for electrons and τ_{had} candidates. The identification (isolation) working points are specified for electrons, muons, τ_{had} candidates and b-jets (electrons and muons).*

Object		Identification	Isolation	p_T [GeV]	$\lvert\eta\rvert$
Central jet				> 20	< 2.5
Electron	[130]	loose	loose	> 7	< 2.47, !cr
Muon	[134]	loose	loose	> 7	< 2.7
τ_{had}	[155, 156]	BDT > 0.35		> 20	< 2.5, !cr
b-jet	[146, 150]	MV2c10: 70%		> 20	< 2.5

Jets are reconstructed from topo-clusters using the anti-k_t algorithm with $R = 0.4$. Only central jets ($|\eta| < 2.5$) with $p_T > 20$ GeV are considered in the analysis. Pileup jets are suppressed by applying the JVT algorithm [144] to all jets within the $|\eta| < 2.4$ region that have $p_T < 60$ GeV. The MV2c10 algorithm with a 70% efficiency for the true b-jets is used to perform b-tagging.

Electrons (muons) with $p_T > 7$ GeV are identified using the loose working point of the identification algorithm described in Section 4.2 (4.3). The loose working point is used when performing the overlap removal procedure; however, tighter identification working points are used in the event selection, as will be explained. Electrons and muons are also required to be isolated by checking that there are no nearby tracks or energy deposits in the calorimeter within a variable-size cone around them. The loose isolation working point is used, targeting a fixed value of the isolation efficiency for the true electrons (muons) of around 99%, uniform in p_T and $|\eta|$ of the electron (muon). This isolation criteria is inverted in order to define a control region for estimating the multijet background in the $\tau_{\text{lep}}\tau_{\text{had}}$ channel, as will be explained.

The τ_{had} candidates with $p_T > 20$ GeV are required to have unit charge and exactly one or three charged tracks in the core region. The candidates with one core track are rejected if they overlap with an identified electron candidate that has $p_T > 5$ GeV within $\Delta R < 0.4$. The BDT-based τ_{had}-ID is later applied using the medium working point to define the $\tau_{\text{lep}}\tau_{\text{had}}$- and $\tau_{\text{had}}\tau_{\text{had}}$-channel sensitive regions.

Fail-τ_{had} candidates

The medium τ_{had}-ID criterion is inverted for the purpose of defining control regions that are later used for estimating contributions from background processes where one or two quark- or gluon-initiated jets are misidentified as τ_{had} candidates. The τ_{had} candidates that fail the BDT identification for the medium

working point and in addition still have a τ_{had}-ID BDT score above 0.35 are referred to as fail-τ_{had} candidates. The distribution of the τ_{had}-ID BDT score is shown in Figure 4.9.

Parameterised truth-tagging
In final states requiring two b-jets, the substantial b-tagging rejection factors can lead to a significant statistical uncertainty on simulated processes containing only light-flavour and c-jets. In order to increase the number of simulated events for such processes in analysis-sensitive regions, the b-tagging selection is not used directly. Instead, all non-true b-jets are kept, and each event is weighted by the measured probabilities that some light-flavour/c-jet is misidentified as a b-jet. This procedure is called *parameterised truth-tagging* [153] and it is used for all simulated background events except those that correspond to dominant background processes contributing to the $b\bar{b}\tau^+\tau^-$ final state, i.e. production of $t\bar{t}$ and $Z+bb$ events.

5.2.3 Overlap removal

Most physics objects are reconstructed and identified independently from each other. Therefore, it can occur that one detector object is reconstructed or identified as multiple physics objects. For example, the reconstruction of τ_{had} candidates is seeded from jets. Thus, it is expected that the detector object corresponding to a τ_{had} candidate is reconstructed as both a τ_{had} candidate and as a jet[3]. In most cases, if a τ_{had} candidate satisfies the defined τ_{had}-ID requirements, the jet matched to it must be removed from the list of physics objects to prevent double counting.

The overlap removal procedure is optimised to maximise the efficiency of selecting the simulated signal events, while trying to keep the background rejection as high as possible. This procedure is to some extent standardised since it depends on how the identification efficiencies and misidentification rates compare between different physics objects in the ATLAS experiment. Certain modifications are usually made to improve the performance for a defined final state, or to allow for defining some specific control regions.

The overlap removal procedure in the $b\bar{b}\tau^+\tau^-$ analysis is applied in two steps. In the first step (Step 1), the overlap removal is performed for electrons, muons, jets and τ_{had} candidates, based on their definitions in Table 5.3, but taking into account all jets, regardless of whether they are b-tagged or not. Step 1 of the overlap removal procedure is summarised in Table 5.4. If after this step an event contains an electron or muon, it is assigned to the $\tau_{\text{lep}}\tau_{\text{had}}$ channel. Conversely, if an event does not contain any electrons or muons, it

[3]The two objects are usually not matched perfectly since there is a difference between the jet collection used for seeding the τ_{had} reconstruction and the nominal jet collection. In addition, the two objects are calibrated separately.

is assigned to the $\tau_{\text{had}}\tau_{\text{had}}$ channel. The second part (Step 2) of the overlap removal will be discussed in Section 5.2.4.

Table 5.4. *Overlap removal – Step 1: In the first step of the overlap removal applied in the $b\bar{b}\tau^+\tau^-$ analysis, electrons, muons, τ_{had} candidates and jets are checked for geometrical overlaps. These objects are defined in Table 5.3; however, all jets are considered, regardless of whether they are b-tagged or not. The last column specifies which object is kept if an overlap is found. Step 2 of the overlap removal is discussed in Section 5.2.4.*

	Objects	Overlap defined as	Priority
1.	electron – jet	$\Delta R < 0.2$	electron
2.	electron – jet	$0.2 \leq \Delta R < 0.4$	jet
3.	muon – jet	$\Delta R < 0.4$ and < 3 tracks with $p_T > 500$ MeV	muon
4.	muon – jet	$\Delta R < 0.4$ and ≥ 3 tracks with $p_T > 500$ MeV	jet
5.	electron – muon	$\Delta R < 0.2$ and sharing an inner-detector track	muon
6.	muon – τ_{had}	$\Delta R < 0.2$	muon
7.	electron – τ_{had}	$\Delta R < 0.2$	electron

5.2.4 Event categorisation

The $\tau_{\text{lep}}\tau_{\text{had}}$ channel is split into SLT and LTT categories[4], based on the applied trigger selection. Similarly, the $\tau_{\text{had}}\tau_{\text{had}}$ channel is split into STT and DTT categories. Events are categorised as described below.

Trigger requirements and selection of electrons, muons and τ_{had} candidates

- **SLT category:** In the SLT category, an event is required to pass the SLT and to have exactly one tight electron or one medium muon with a p_T at least 1 GeV higher than the trigger threshold. This electron or muon is required to be "trigger-matched", i.e. geometrically matched to the corresponding trigger-level object, using $\Delta R < 0.07$ and $\Delta R < 0.1$ matching criteria, respectively. If the event contains more electrons or muons, based on how they are defined in Table 5.3, it is rejected. The event is also checked for medium τ_{had} candidates and it is immediately accepted if only one such candidate is found. If more than one medium τ_{had} candidate is found, the event is rejected. If no medium τ_{had} candidates are found, the event is checked for the presence of fail-τ_{had} candidates (defined in Section 5.2.2) with the purpose of defining control regions that are used for data-driven background estimations, as will be discussed

[4]The categories here refer to different event selection criteria that depend on the trigger, and thus the same abbreviation is used. The exact meaning, e.g. if SLT refers to the single-lepton trigger or to the category of events that pass one of the single-lepton triggers and dedicated offline selection, should be understood from the context.

in Section 5.3. If more than one fail-τ_{had} candidates are found, one is chosen randomly; if none are found, the event is rejected.

- **LTT category:** The SLT and LTT cannot be applied as a logical OR[5], and thus events are considered for the LTT category only if the identified electron or muon is below the SLT offline p_T-threshold (trigger threshold $+1$ GeV). The identified electron (muon) is further required to be trigger-matched, with a p_T at least 1 GeV higher than the trigger threshold, and to satisfy the tight (medium) identification criteria. Events with additional electrons or muons, as defined in Table 5.3, are rejected. Events are also required to contain a trigger-matched τ_{had} candidate (medium or fail-τ_{had}), using a $\Delta R < 0.2$ matching criterion, with $p_T > 30$ GeV (5 GeV above the trigger threshold). An event is rejected if it contains additional medium τ_{had} candidates.
- **STT category:** In the $\tau_{\text{had}}\tau_{\text{had}}$ channel, events are first checked if they pass the STT. If that is the case, they are required to contain a trigger-matched τ_{had} candidate (medium or fail-τ_{had}) with a p_T at least 20 GeV above the trigger threshold. Given that two τ_{had} candidates are required in the $\tau_{\text{had}}\tau_{\text{had}}$ channel, events are checked for additional medium τ_{had} objects. An event is rejected if there is more than one additional medium τ_{had} candidate, accepted if there is exactly one, or checked for fail-τ_{had} candidates if there are no additional medium τ_{had} candidates. Similar to the SLT case, one fail-τ_{had} candidate is selected randomly if several such objects are found, while the event is rejected if no fail-τ_{had} candidates are found.
- **DTT category:** Events failing the STT are tested if they pass the DTT requirements[6]. The event must have two trigger-matched τ_{had} candidates (each can be either medium or fail-τ_{had}) with $p_T > 40\,(30)$ GeV for the leading (sub-leading) candidate. The event is rejected if it contains additional medium τ_{had} candidates.

Overlap removal – Step 2

The overlap removal is split into two steps since the τ_{had} selection includes a random selection of non-trigger-matched fail-τ_{had} candidates, as explained above. In this step, all b-jets, non-b-tagged jets, medium τ_{had} candidates and fail-τ_{had} candidates are checked if they geometrically overlap within $\Delta R < 0.4$. If two objects are found to overlap they are kept with the following priority:

$$\text{medium } \tau_{\text{had}} > b\text{-jet} > \text{fail-}\tau_{\text{had}} > \text{non-}b\text{-tagged jet}. \tag{5.2}$$

[5]This is because the trigger-efficiency corrections are measured independently, and not for a logical OR of the two triggers.

[6]In this case, the logical OR is applied between the STT and DTT, but only because the overlap between the events that pass both triggers is found to be at a $\sim 1\%$ level.

The defined priority maximises the signal selection efficiency and the number of events in control regions with 2 b-tagged jets. The $\tau_{\text{lep}}\tau_{\text{had}}$ events are rejected if they do not contain exactly one selected electron or muon and one τ_{had} candidate that satisfies the medium or fail-τ_{had} identification criteria. Similarly, the $\tau_{\text{had}}\tau_{\text{had}}$ events are rejected if they do not contain exactly two selected τ_{had} candidates that satisfy the medium or fail-τ_{had} identification criteria.

Jet selection
All events are required to have at least 2 central jets with $p_T > 45$ (20) GeV for the leading (sub-leading) jet. The 45 GeV cut is motivated by the event topology. In addition, given that the LTT and DTT both require an additional jet with $p_T > 25$ GeV at L1, the leading offline jet in those two trigger categories is required to have a minimum p_T of 80 GeV. The full trigger efficiency is reached only above that value, due to a poor jet-p_T resolution at L1. Events are split into different regions based on the number of b-tagged jets: 0-, 1- and 2-b-tag regions. Events are rejected if they contain more than 2 b-tagged jets.

All events are also required to have $m_{\tau\tau}^{\text{MMC}} > 60$ GeV to reject the low-mass Drell-Yan background. A summary of the event selection for the $\tau_{\text{lep}}\tau_{\text{had}}$ and $\tau_{\text{had}}\tau_{\text{had}}$ channels and for the different trigger categories is provided in two complementary tables. The required objects are defined in Table 5.5, while the event selection is shown in Table 5.6.

Table 5.5. *Definitions of different selected final-state objects and their required multiplicities for the $\tau_{\text{lep}}\tau_{\text{had}}$ and $\tau_{\text{had}}\tau_{\text{had}}$ channels (upper part of the table). If any additional objects are found, as defined in the bottom part of the table, the event is vetoed.*

Object	Multiplicity $\tau_{\text{lep}}\tau_{\text{had}}$ ($\tau_{\text{had}}\tau_{\text{had}}$)	Identification	Isolation	p_T [GeV]	$\lvert\eta\rvert$
Central jet	≥ 2			Specified in Table 5.6	< 2.5
Electron	$= 1$ ($= 0$)	tight	loose		< 2.47, !cr
Muon		medium	loose		< 2.5
τ_{had}	$= 1$ ($= 2$)	BDT: medium			< 2.5, !cr
Fail-τ_{had}		BDT: !medium and BDT > 0.35			< 2.5, !cr
b-jet	≤ 2	MV2c10: 70%		> 20	< 2.5
An event is rejected if it contains any additional:					
Electron		loose	loose	> 7	< 2.47, !cr
Muon		loose	loose	> 7	< 2.7
τ_{had}		BDT: medium		> 20	< 2.5, !cr
b-jet		MV2c10: 70%		> 20	< 2.5

Table 5.6. *Summary of the event selection shown separately for the four trigger categories. One electron or muon (ℓ) and one τ_{had} candidate are required in the $\tau_{\text{lep}}\tau_{\text{had}}$ channel. In the $\tau_{\text{had}}\tau_{\text{had}}$ channel, two τ_{had} candidates are required. In both channels, at least two central jets must be present. The definitions of the required objects are listed in Table 5.5. In cases when more than one object is required, the respective p_T threshold for the leading (sub-leading) object is given outside (within) the parentheses. For the SLT and STT categories, the p_T requirements depend on the data-taking period, therefore several thresholds are listed, separated by commas. The defined selection is almost entirely driven by the trigger requirements, except for the leading-jet p_T cut in the SLT and STT categories, and the cut on $m_{\tau\tau}^{\text{MMC}}$ in all four trigger categories.*

$\tau_{\text{lep}}\tau_{\text{had}}$ channel		$\tau_{\text{had}}\tau_{\text{had}}$ channel	
Trigger selection:			
Single-ℓ trigger SLT	$\ell+\tau_{\text{had}}$ trigger LTT	Single-τ_{had} trigger STT	Di-τ_{had} trigger DTT
Lepton and τ_{had} selection:			
$e/\mu+\tau_{\text{had}}$		$\tau_{\text{had}}+\tau_{\text{had}}$	
$p_T^{\ell} > 25, 27$ GeV	18 GeV $< p_T^e <$ SLT cut 15 GeV$< p_T^{\mu} <$ SLT cut		
$p_T^{\tau} > 20$ GeV	$p_T^{\tau} > 30$ GeV	$p_T > 100, 140, 180$ (20) GeV	$p_T > 40$ (30) GeV
Jet selection: (≥ 2 central jets)			
$p_T > 45$ (20) GeV	$p_T > 80$ (20) GeV	$p_T > 45$ (20) GeV	$p_T > 80$ (20) GeV
Additional selection:			
$m_{\tau\tau}^{\text{MMC}} > 60$ GeV			

As already mentioned, the selected events are split into 3 regions based on the number of *b*-tagged jets. Furthermore, the selected events are split into opposite-sign (OS) and same-sign (SS) categories, based on whether the visible τ-lepton decay products (electron/muon and τ_{had}) have opposite-sign, or same-sign electric charges. Finally, only events where all selected τ_{had} candidates satisfy the medium identification working point are considered (this is referred to as the *preselection*), while events where at least one of the selected τ_{had} candidates fails the medium identification working point are used to construct fail-τ_{had}-ID control regions (CRs) for estimating backgrounds with fake-τ_{had} candidates.

Three separate signal regions (SRs) are defined: $\tau_{\text{lep}}\tau_{\text{had}}$ SLT, $\tau_{\text{lep}}\tau_{\text{had}}$ LTT and $\tau_{\text{had}}\tau_{\text{had}}$ SR, each corresponding to the OS 2-*b*-tag region with respect to the preselection in the corresponding category. Several validation regions (VRs) are defined to check background modelling, as discussed later.

5.3 Background estimation

Several processes contribute to the $b\bar{b}\tau^+\tau^-$ final state, or more specifically to the $bb\tau_{\text{had}}\tau_{\text{had}}$ and $bb\tau_{\text{lep}}\tau_{\text{had}}$ (i.e. $bb\ell\tau_{\text{had}}$) final states[7]. These processes have significantly larger production cross-sections than what is expected for pair production of Higgs bosons, making it a great challenge for the analysis to develop techniques that are efficient in extracting the signal.

The $t\bar{t}$ production process is by far the dominant background in the $\tau_{\text{lep}}\tau_{\text{had}}$ channel, and one of the most important backgrounds in the $\tau_{\text{had}}\tau_{\text{had}}$ channel. The top quark decays almost exclusively into a W boson and a bottom quark. In 11.4% of the cases [25], the W boson decays into a τ lepton and the corresponding neutrino. The significantly larger branching ratio for the $t\bar{t}$ decay into the $bb\ell\tau_{\text{had}}$ final state, compared to the $bb\tau_{\text{had}}\tau_{\text{had}}$ final state, makes the background rates in the $\tau_{\text{lep}}\tau_{\text{had}}$ channel larger by almost an order of magnitude compared to the background rates in the $\tau_{\text{had}}\tau_{\text{had}}$ channel. The expected sensitivity to the signal in the $\tau_{\text{lep}}\tau_{\text{had}}$ channel is thus somewhat lower. The $t\bar{t}$ background consists of events with one (two) true-τ_{had} objects[8] for the $\tau_{\text{lep}}\tau_{\text{had}}$ ($\tau_{\text{had}}\tau_{\text{had}}$) channel, but also events where (at least) one τ_{had} candidate is misidentified, mostly coming from a quark-initiated jet. The corresponding Feynman diagrams are shown in Figure 5.2. The proper modelling of the τ_{had}-ID applied to the fake-τ_{had} candidates in simulation is challenging and the jet$\rightarrow\tau_{\text{had}}$ misidentification probabilities are observed to differ between the simulation and data. For that reason, backgrounds that contribute with a significant amount of events with fake-τ_{had} candidates are estimated using data-driven or semi-data-driven techniques, as will be explained.

Other than $t\bar{t}$, important background processes are multijet events with quark- or gluon-initiated jets misidentified as τ_{had} objects, which contribute more to the $\tau_{\text{had}}\tau_{\text{had}}$ channel, and $Z(\rightarrow\tau\tau)$+jets events. It is extremely challenging to simulate accurately multijet processes, and thus these contributions are estimated using data-driven methods. The Z+jets events are split into three categories: $Z+(bb,bc,cc)$ (Z+heavy flavour jets, in short Z+hf), $Z+(bq_{\text{lf}},cq_{\text{lf}})$, where $q_{\text{lf}}=\{u,d,s\}$; and $Z+q_{\text{lf}}q_{\text{lf}}$ (Z+light flavour jets, in short Z+lf) events. All the other processes listed in Section 5.1 are considered as well.

Backgrounds for which the selected τ_{had} candidates are expected to be correctly identified are all estimated using simulation and for some of them ($t\bar{t}$ and Z+hf) the overall normalisation is freely floated in the final fit, as will be discussed in Sections 5.3.1 and 5.3.5. Major backgrounds for which the selected τ_{had} candidates are expected to be fake are estimated using data- or semi-data-

[7]The bar-sign which indicates a presence of an antiparticle, as well as the plus and minus signs that indicate an electric charge of a particle are sometimes omitted for simplicity.

[8]If the reconstructed τ_{had} candidate is matched geometrically ($\Delta R<0.2$) to a generator-level hadronically-decaying τ lepton, the reconstructed τ_{had} object is considered to be correctly identified.

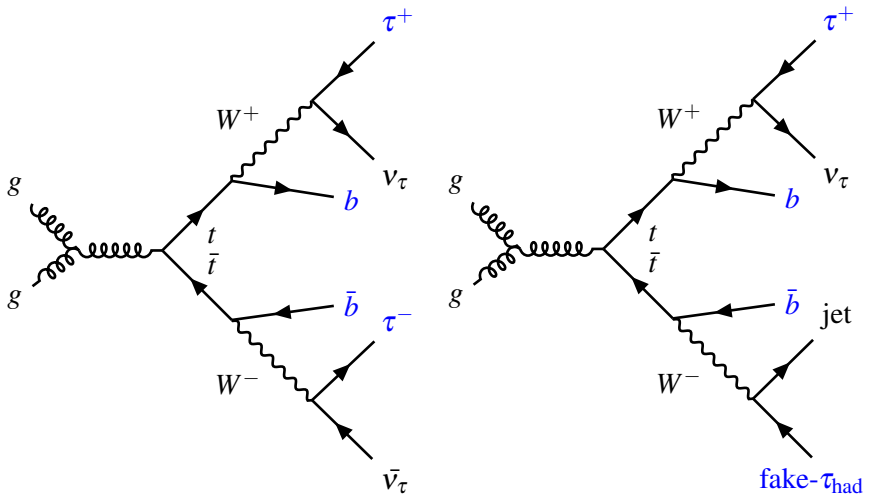

Figure 5.2. An example of the *s*-channel $t\bar{t}$ production, with a subsequent decay into the (**a**) $bb\tau\tau$ final state and (**b**) $bb\tau$+fake-τ_{had} final state.

driven methods, as discussed below. Other (minor) such backgrounds are estimated using simulation.

5.3.1 Estimation of the $t\bar{t}$ background with true-τ_{had} candidates

In both channels, MC simulation is used to estimate the $t\bar{t}$ background containing true-τ_{had} candidates. The normalisation of this background is treated as a free parameter in the final fit, and thus it is determined from data. The $t\bar{t}$ normalisation factor is correlated between the three SRs and the $Z \to \mu\mu$+hf CR that is defined in Section 5.3.5. The post-fit normalisation is mostly driven by the $\tau_{\text{lep}}\tau_{\text{had}}$ SRs due to a significantly larger number of selected $t\bar{t}$ events and thus lower relative statistical uncertainties. In addition, the fraction of the $t\bar{t}$ background with respect to the total background is higher in the $\tau_{\text{lep}}\tau_{\text{had}}$ channel than in the $\tau_{\text{had}}\tau_{\text{had}}$ channel. In the $\tau_{\text{had}}\tau_{\text{had}}$ SR and the $Z \to \mu\mu$+hf CR, the $t\bar{t}$ post-fit normalisation is allowed to differ with respect to the normalisation in the $\tau_{\text{lep}}\tau_{\text{had}}$ SRs if the difference is within the uncertainty on the ratio of acceptance $\times$ efficiency for the $t\bar{t}$ events between the respective region and the $\tau_{\text{lep}}\tau_{\text{had}}$ SRs, as will be discussed in Section 5.5.2.

5.3.2 Processes with fake-τ_{had} candidates in the $\tau_{\text{lep}}\tau_{\text{had}}$ channel

In the $\tau_{\text{lep}}\tau_{\text{had}}$ channel, a combined Fake Factor method is used to estimate contributions from several processes where the reconstructed τ_{had} candidate

is a misidentified quark- or gluon-initiated jet. A fake factor, FF, is calculated in a dedicated control region, as the ratio of the number of data events containing a medium fake-τ_{had} candidate to the number of data events where the selected τ_{had} object is fake and identified as a fail-τ_{had} candidate. To estimate the number of events with a fake-τ_{had} candidate in data, in the fake factor control region, the number of events containing the true-τ_{had} candidate is estimated from simulation and subtracted from the total number of data events. Fake factors usually depend strongly on the p_T of the τ_{had} candidate, and thus they are binned in this variable. The fake factor in some bin i is then defined as

$$FF_i = \frac{N_{\text{data},i}(\text{medium } \tau_{\text{had}}) - N_{\text{MC},i}(\text{medium true-}\tau_{\text{had}})}{N_{\text{data},i}(\text{fail-}\tau_{\text{had}}) - N_{\text{MC},i}(\text{fail-true-}\tau_{\text{had}})}, \tag{5.3}$$

where N_{data} (N_{MC}) is the number of data (simulated) events containing a medium or fail-τ_{had} candidate.

The probability for a jet to fake a τ_{had} candidate depends on the origin of the jet. Thus, the fake factors calculated for two processes, e.g. $t\bar{t}$ and multijet events, would be different because the jet composition in terms of the seed particle is not the same between the two samples. Fake factors in the $\tau_{\text{lep}}\tau_{\text{had}}$ channel are measured for three different processes: $t\bar{t}$, multijet (QCD) and W+jets events. For each of these processes, a dedicated control region is defined in Table 5.7.

Table 5.7. *Definition of the three control regions used to derive τ_{had}-ID FFs in the $\tau_{\text{lep}}\tau_{\text{had}}$ channel, each one enriched in $t\bar{t}$, multijet, or W+jets events. The selection in this table is applied on top of the $\tau_{\text{lep}}\tau_{\text{had}}$-channel selections listed in Tables 5.5 and 5.6, separately for the SLT and LTT trigger categories. The transverse mass between the lepton ℓ and the E_T^{miss} is $m_T^W = \sqrt{p_T^{\ell} E_T^{\text{miss}}(1 - cos\Delta\phi)}$, where $\Delta\phi$ is the angle between the p_T of the lepton and the direction of the E_T^{miss} ($\vec{p}_T^{\,\text{miss}}$). The m_T^W variable tends to have high values for the $t\bar{t}$ events and low values for the signal events.*

Control Region	Selection		
$t\bar{t}$	$m_T^W > 40$ GeV	OS	2 b-tags
multijet	Inverted electron/muon isolation	OS	0 b-tags /1 b-tag
W+jets	$m_T^W > 40$ GeV	OS	0 b-tags

In the $\tau_{\text{lep}}\tau_{\text{had}}$ channel, fake factors are measured in the three CRs as a function of the τ_{had}-candidate p_T, separately for the SLT and LTT categories, and separately for 1- and 3-prong candidates. Fake factors for the same process are expected to differ between the two trigger categories since the selected τ_{had} candidates in the LTT category are required to pass the online τ_{had}-ID as a part

of the event selection. The fake factors in the SLT category are shown in Figure 5.3.

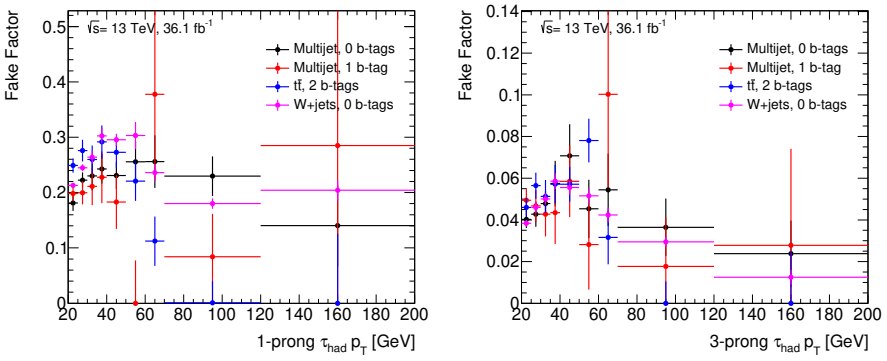

(a) *1-prong* **(b)** *3-prong*

Figure 5.3. Fake factors as a function of the τ_{had}-candidate p_T measured in the $\tau_{\text{lep}}\tau_{\text{had}}$ SLT CRs that are defined in Table 5.7, separately for 1- and 3-prong τ_{had} candidates. The vertical error bars show statistical uncertainties.

The combined fake factor in some p_T range (bin i) is calculated as

$$FF_{\text{comb},i} = FF_{\text{QCD},i} \times r_{\text{QCD},i} + FF_{W+\text{jets}/t\bar{t},i} \times (1 - r_{\text{QCD},i}), \tag{5.4}$$

where FF_{QCD}, $FF_{W+\text{jets}}$ and $FF_{t\bar{t}}$ are measured in the respective CRs. In addition, r_{QCD} is the fraction of multijet events in the fail-τ_{had}-ID region after the subtraction of events containing a true-τ_{had} candidate, defined as

$$r_{\text{QCD},i} = \frac{N_{\text{data},i}(\text{fail-}\tau_{\text{had}}) - N_{\text{MC},i}(\text{fail-fake-}\tau_{\text{had}}) - N_{\text{MC},i}(\text{fail-true-}\tau_{\text{had}})}{N_{\text{data},i}(\text{fail-}\tau_{\text{had}}) - N_{\text{MC},i}(\text{fail-true-}\tau_{\text{had}})}. \tag{5.5}$$

In multijet events, selected electrons and muons are misidentified quark- or gluon-initiated jets. Given that the electron and muon misidentification rates are expected to differ, the r_{QCD} factors are measured separately for the electron and muon channels, as shown in Figure 5.4.

Since the 0- (2-)b-tag region is completely dominated by W+jets ($t\bar{t}$) events, the contribution from $t\bar{t}$ (W+jets) events is not taken into account when the combined fake factors are calculated. In the 1-b-tag region, the fake factors corresponding to $t\bar{t}$ and W+jets events are combined based on the relative contributions of these processes, estimated using MC simulation. The multijet FFs measured in the 1-b-tag region are used to obtain the combined FFs in the 2-b-tag region due to low statistics in the 2-b-tag multijet CR. The combined fake factors in the 2-b-tag region are applied to all events in the fail-τ_{had}-ID OS 2-b-tag CR to obtain the background prediction corresponding to the multijet and $t\bar{t}$ events with fake-τ_{had} candidates in the $\tau_{\text{lep}}\tau_{\text{had}}$ SRs. Contributions from

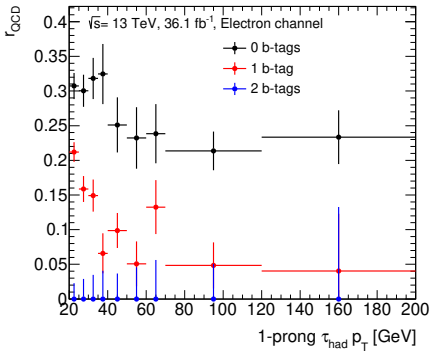

(a) *Electron channel, 1-prong*

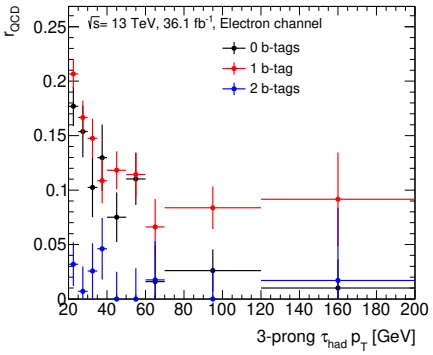

(b) *Electron channel, 3-prong*

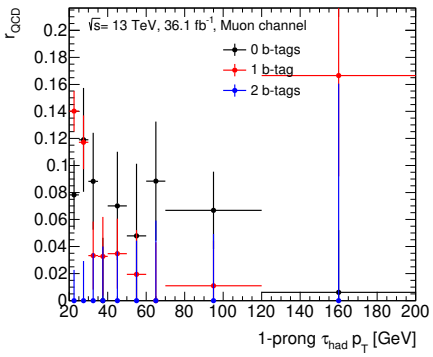

(c) *Muon channel, 1-prong*

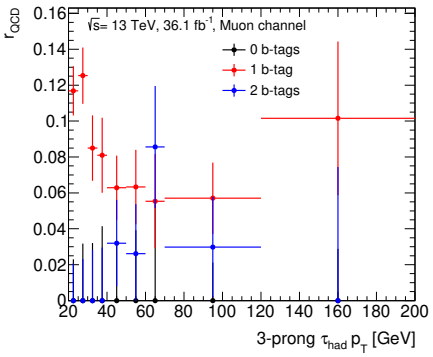

(d) *Muon channel, 3-prong*

Figure 5.4. Measured r_{QCD} factors as a function of the τ_{had}-candidate p_T in the $\tau_{\text{lep}}\tau_{\text{had}}$ SLT category, separately for the electron and muon channels and for 1- and 3-prong τ_{had} candidates. The vertical error bars show statistical uncertainties.

other processes containing fake-τ_{had} candidates are estimated from MC simulation. The method is found to provide a good prediction-to-data agreement in the 0- and 1-*b*-tag CRs, the SS validation regions, as well as in the $\tau_{\text{lep}}\tau_{\text{had}}$ SRs, for which the figures can be found in Ref. [15].

5.3.3 Multijet estimation in the $\tau_{\text{had}}\tau_{\text{had}}$ channel

The multijet background in the $\tau_{\text{had}}\tau_{\text{had}}$ channel is also estimated using a data-driven FF method. Event-level fake factors are derived in the SS region and applied to the OS-region events where at least one of the τ_{had} candidates fails the medium identification working point. The fake factors for the DTT category are binned in p_T of both the leading and sub-leading τ_{had} candidates, while the fake factors for the STT category are inclusive in p_T due to low

statistics. The fake factor in some bin i is defined as

$$FF_i = \frac{N^{SS}_{\text{data}-\text{MC(non-multijet)},i}\,(2 \text{ medium } \tau_{\text{had}})}{N^{SS}_{\text{data}-\text{MC(non-multijet)},i}\,(\geq 1 \text{ fail-}\tau_{\text{had}})}, \tag{5.6}$$

where "SS" indicates that only the SS-region events are used. In this case, the number of all non-multijet simulated events is subtracted from the total number of data events, regardless of whether the selected τ_{had} candidates are true or fake. A separate set of fake factors is derived for the each b-tag category, and for the different combinations of the τ_{had} prongness: $(1,1)$, $(1,3)$, $(3,1)$, and $(3,3)$, for the leading and sub-leading τ_{had} candidates, respectively. However, a set of fake factors calculated in the 1-b-tag category is used for the multijet estimation in the 2-b-tag region due to low statistics in the 2-b-tag SS CR, as illustrated in Figure 5.5. For that reason, a set of transfer factors (TFs) are derived for correcting the normalisation of the multijet prediction in the 2-b-tag region.

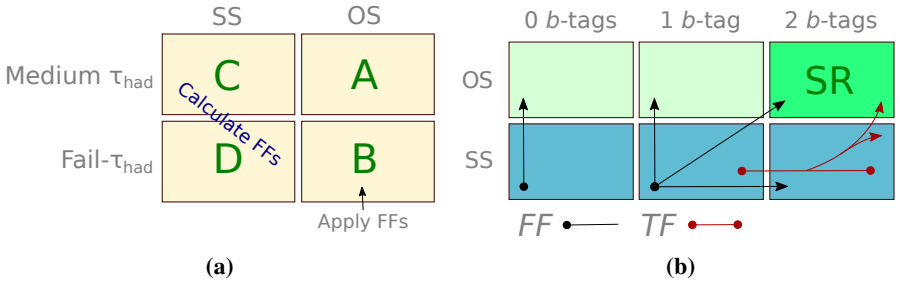

Figure 5.5. Graphical illustration of the Fake Factor method used to estimate the multijet background in the $\tau_{\text{had}}\tau_{\text{had}}$ channel. (**a**) A set of fake factors, FF, is calculated in the "SS" region as C/D, after subtracting the number of non-multijet simulated events from the number of data events in all regions. These fake factors are then applied to the OS-region events that contain at least one fail-τ_{had} candidate, region B, to obtain a multijet estimation in the OS region where 2 medium τ_{had} candidates are required, region A. (**b**) A separate set of fake factors is measured for the each b-tag region, but fake factors measured in the 1-b-tag region are applied in the 2-b-tag region. A set of transfer factors, TF, between the 1- and 2-b-tag regions is derived and applied as a correction for the multijet background estimation in the 2-b-tag region.

Transfer factors are derived as ratios of fake factors that are calculated inclusively in p_T of the τ_{had} candidates and together for the DTT- and STT-category events, between the 2-b-tag SS and 1-b-tag SS regions. The obtained fake factors and transfer factors are applied to the OS-region events where at least one τ_{had} candidate fails the medium identification working point. The fake factors measured for the DTT-category events in the 1-b-tag SS region are shown in Figure 5.6, while the p_T-inclusive fake factors that correspond to the STT-category events in the 1-b-tag region are listed in Table 5.8. The

transfer factors from the 1-*b*-tag region to the 2-*b*-tag region are given in the same table.

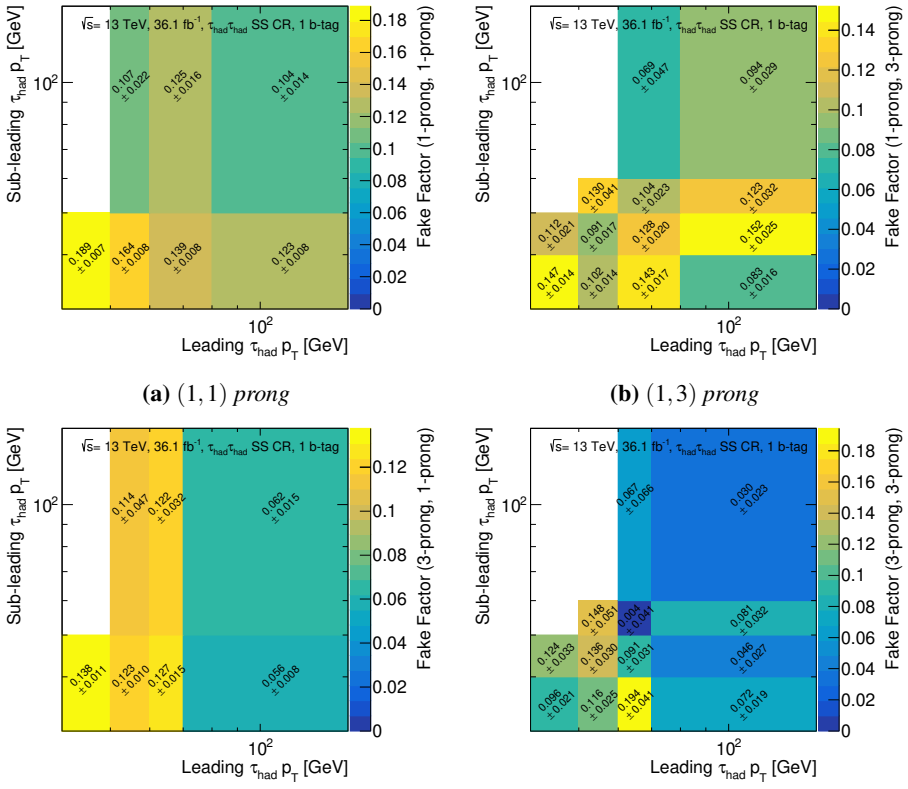

(a) $(1,1)$ *prong* **(b)** $(1,3)$ *prong*

(c) $(3,1)$ *prong* **(d)** $(3,3)$ *prong*

Figure 5.6. Event-level fake factors corresponding to the DTT category derived in the 1-*b*-tag SS region, separately for the different combinations of the τ_{had} prongness.

Table 5.8. *Fake factors corresponding to the STT category derived in the 1-b-tag SS region (middle column), and the DTT+STT* $1 \to 2$*-b-tag transfer factors (last column), with statistical uncertainties.*

Prong category	1-*b*-tag SS STT FF	$1 \to 2$-*b*-tag SS DTT+STT TF
$(1,1)$	0.080 ± 0.007	0.936 ± 0.099
$(1,3)$	0.024 ± 0.003	1.09 ± 0.21
$(3,1)$	0.038 ± 0.009	1.12 ± 0.22
$(3,3)$	0.015 ± 0.005	1.17 ± 0.44

The method is validated in the 0- and 1-*b*-tag OS validation regions, as well as the 2-*b*-tag SS validation region. A good modelling of the p_T of the leading

and sub-leading τ_{had} candidates is shown for some of the validation regions in Figure 5.7. Additional plots are shown in Appendix A: Figures A.1 and A.2.

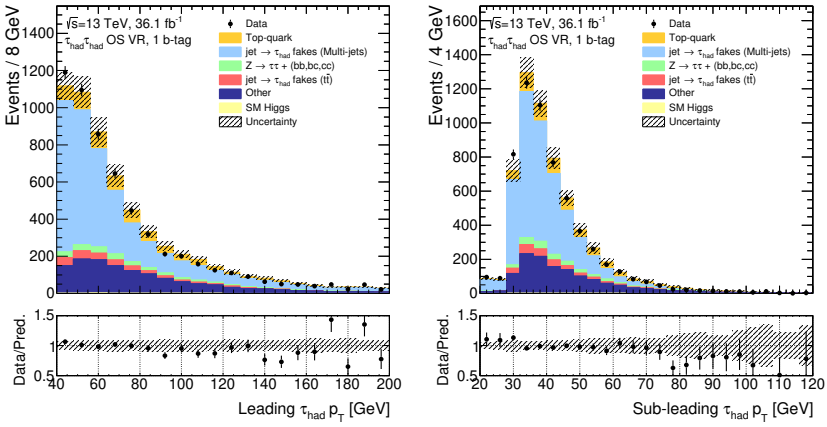

(a) *OS 1-b-tag validation region*

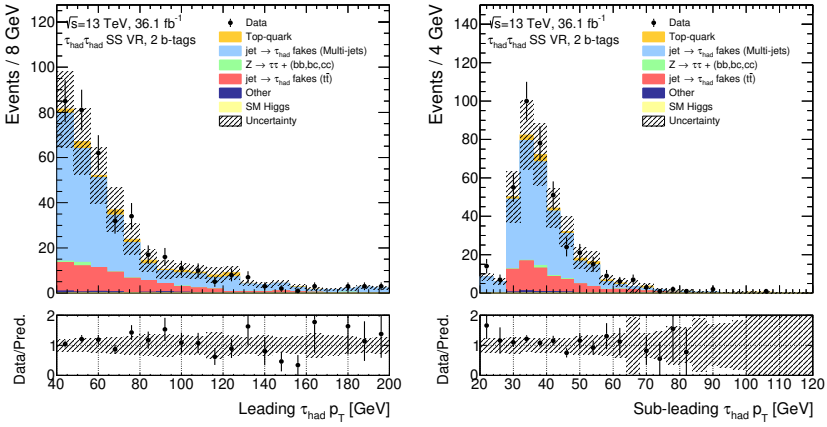

(b) *SS 2-b-tag validation region*

Figure 5.7. Distributions of the leading (sub-leading) τ_{had}-candidate p_T are shown on the left-hand (right-hand) side in two different regions used to validate the multijet background estimation. The pre-fit statistical and systematic uncertainties are displayed.

5.3.4 Estimation of the $t\bar{t}$ background with fake-τ_{had} candidates in the $\tau_{\text{had}}\tau_{\text{had}}$ channel

In the $\tau_{\text{had}}\tau_{\text{had}}$ channel, the $t\bar{t}$ background with one or two fake-τ_{had} candidates is estimated using a semi-data-driven Fake Rate (FR) method. The FR method

is chosen in this case due to difficulties in defining a $t\bar{t}$-dominated CR with enough statistics that would allow to develop a fully data-driven FF method. Fake rates are measured in data, but applied to a MC $t\bar{t}$ template that is defined below.

The fake rates are measured in the $\tau_{\text{lep}}\tau_{\text{had}}$-channel $t\bar{t}$ control region that is defined in Table 5.7, with the m_T^W cut raised to be greater than 80 GeV to remove any signal contribution. In that region, the (quark- or gluon-initiated) jet $\rightarrow \tau_{\text{had}}$ candidate fake rate in some bin i is calculated as

$$FR_i = \frac{N_{\text{data}-\text{MC(all except } t\bar{t} \text{ with fake-}\tau_{\text{had}}),i} \text{ (medium trigger-matched } \tau_{\text{had}})}{N_{\text{data}-\text{MC(all except } t\bar{t} \text{ with fake-}\tau_{\text{had}}),i} \text{ (all } \tau_{\text{had}})}. \tag{5.7}$$

The number (N) of simulated non-$t\bar{t}$ events plus the number of simulated $t\bar{t}$ events with a true-τ_{had} candidate is subtracted from the total number of data events. The fake rate is then calculated as the ratio of the number of events with a medium τ_{had} candidate to the total number of events remaining after the subtraction. Given that the selected τ_{had} candidates in the $\tau_{\text{had}}\tau_{\text{had}}$ channel are required to pass the online τ_{had}-ID in addition to the offline medium τ_{had}-ID as a part of the event selection[9], the identical (emulated) online τ_{had}-ID requirement is applied to the τ_{had} candidate for those events that are accounted for in the numerator of the FR calculation. The fake rates defined in this way account for the probability that a fake-τ_{had} candidate passes both the online and the medium offline identification working point[10]. Due to very low statistics after emulating the online τ_{had}-ID in the dedicated CR, and the lack of dependence on the τ_{had}-candidate p_T, fake rates are derived in bins of the τ_{had}-candidate $|\eta|$, separately for 1- and 3-prong objects, as shown in Figure 5.8.

MC template for the $t\bar{t}$ background with fake-τ_{had} candidates

Given that the defined fake rates account for both online and offline τ_{had}-ID, they need to be applied to all events that pass the $\tau_{\text{had}}\tau_{\text{had}}$-channel selection, but without requiring the events to pass the DTT and STT. Thus, an equivalent selection to the one presented in Tables 5.5 and 5.6 for the DTT category[11], but without requiring events to pass the trigger and without requiring the τ_{had} candidates to be matched to the trigger-level objects, is applied to the MC $t\bar{t}$

[9] Except for the sub-leading τ_{had} candidate in STT-category events.

[10] This is not completely true for two reasons. The first caveat is that a lower cut is applied on the τ_{had}-ID BDT score when τ_{had} candidates are selected. This changes the definition of the fake rate, but also introduces a bias in the estimation due to differences in the data and simulated efficiencies for the τ_{had}-ID BDT score > 0.35 identification requirement. Another caveat is that the medium and non-medium τ_{had} candidates are not treated in the same way in the overlap removal (Equation (5.2)). These two sources of potential discrepancy are covered by systematic uncertainties that will be discussed in Section 5.5.3.

[11] The selection for the DTT category is applied to all events, and a systematic uncertainty is applied to account for the fraction of events that would fall into the STT category, as discussed in Section 5.5.3.

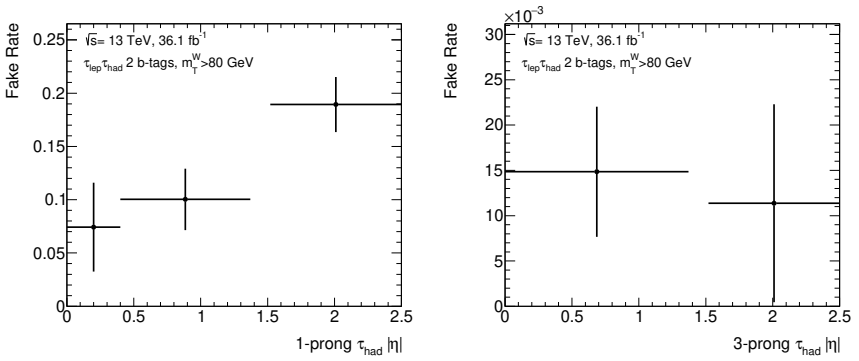

(a) *1-prong* **(b)** *3-prong*

Figure 5.8. Fake rates as a function of the τ_{had}-candidate $|\eta|$, measured in the $\tau_{\text{lep}}\tau_{\text{had}}$-channel $t\bar{t}$ CR with $m_T^W > 80$ GeV, separately for 1- and 3-prong τ_{had} candidates. The vertical error bars show statistical uncertainties.

events to obtain the template to which the fake rates are applied. In this way, a prediction for the $t\bar{t}$ background with fake-τ_{had} candidates is obtained. A good pre-fit modelling of the p_T of the leading and sub-leading τ_{had} candidates in the $\tau_{\text{had}}\tau_{\text{had}}$ OS $t\bar{t}$ validation region ($\tau_{\text{had}}\tau_{\text{had}}$ SR + 140 GeV$<m_{bb}<$300 GeV, where m_{bb} is the invariant mass of the di-b-jet system[12]) is shown in Figure 5.9. Additional plots are shown in Appendix A: Figure A.3.

5.3.5 Normalisation of the background events with $Z \to \tau\tau$+heavy flavour jets

The $Z \to \tau\tau$+jets background is estimated from simulation, using the SHERPA MC generator, as specified in Section 5.1. It has been observed that the normalisation of this background is underestimated for simulated events with a non-zero multiplicity of heavy-flavour jets. For that reason, an attempt to define a $Z + bb$ CR and to derive the normalisation correction from data was made. In the $\tau_{\text{lep}}\tau_{\text{had}}$ channel, the relative fraction of the $Z + bb$ background is too low to define a CR, while in the $\tau_{\text{had}}\tau_{\text{had}}$ channel, any attempted selection suffered from significant contamination from other processes. Given that it is the production cross-section that is expected not to be well modelled for these particular events, it can be assumed that the predicted Z+hf normalisation factor does not depend on the Z boson decay mode. Considering that, a $Z \to \mu\mu$+hf CR with a high purity is defined.

[12]The $m_{bb}>$140 GeV cut is implemented in order to remove the expected signal and to reduce the amount of the non-$t\bar{t}$ backgrounds in the validation region. Above 300 GeV the amount of the $t\bar{t}$ background with fake-τ_{had} candidates is very small, and thus this region is also removed when defining the validation region.

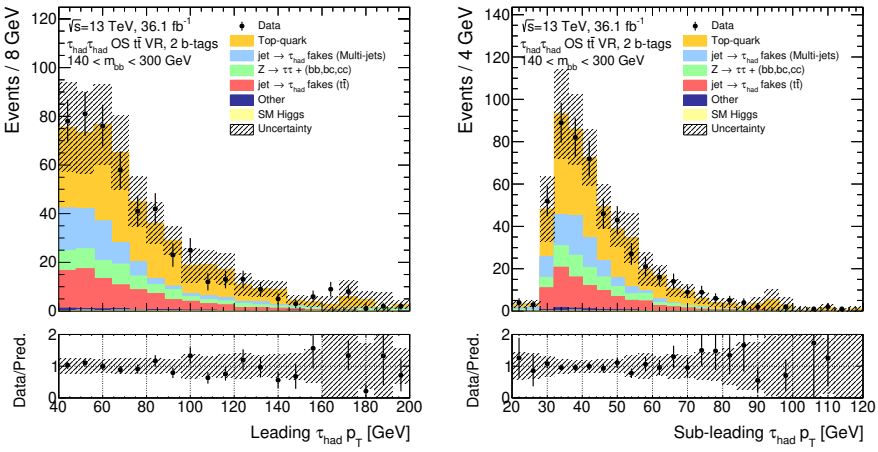

(a) **(b)**

Figure 5.9. Distributions of the (**a**) leading and (**b**) sub-leading τ_{had}-candidate p_T in the $\tau_{\text{had}}\tau_{\text{had}}$-channel OS $t\bar{t}$ validation region ($\tau_{\text{had}}\tau_{\text{had}}$-channel SR selection with 140 GeV$<m_{bb}<$300 GeV). The pre-fit statistical and systematic uncertainties are displayed.

Events in the $Z \to \mu\mu$+hf CR are required to:

- pass the single-muon trigger, as defined in Section 5.2.1;
- have exactly two muons with $p_T > 27$ GeV, defined as in Table 5.5, and one of these muons matched to the trigger-level object;
- have at least two central jets with $p_T > 45\ (20)$ GeV for the leading (sub-leading) jet, and exactly 2 b-tagged jets, defined as in Table 5.5.
- In addition: the invariant dimuon mass is required to be between 81 GeV and 101 GeV, in order to select events around the Z mass peak;
- the invariant mass of the two b-jets is required to be less than 80 GeV, or more than 140 GeV, to veto SM ZH events.

The event yields of the $Z \to \mu\mu$+hf CR are included in the final fit, in addition to the three SRs. The normalisation of the Z+hf events in the fit is treated as a free parameter, and it is correlated between the SRs and the CR. The post-fit normalisation is mostly driven by the CR due to a significantly larger number of selected Z+hf events and thus lower relative statistical uncertainties. In addition, the fraction of the Z+hf background with respect to the total background is significantly higher in the CR than in any of the SRs. In the SRs, the post-fit normalisation is allowed to differ if the difference is within the uncertainty on the ratio of acceptance $\times$ efficiency between the respective SR and the CR, as will be discussed in Section 5.5.2. The Z+hf normalisation factor obtained from the background-only-hypothesis fit to data in the search for the SM HH signal is 1.34 ± 0.16.

The modelling of the dimuon mass distribution in the $Z \to \mu\mu$+hf CR is shown in Figure 5.10a; however, the shape is not taken into account in the final fit. The post-fit normalisation factor is applied to the pre-fit Z+hf yield and the resulting background prediction in the $Z \to \mu\mu$+hf CR is shown in Figure 5.10b, where good agreement between the background prediction and the data is obtained.

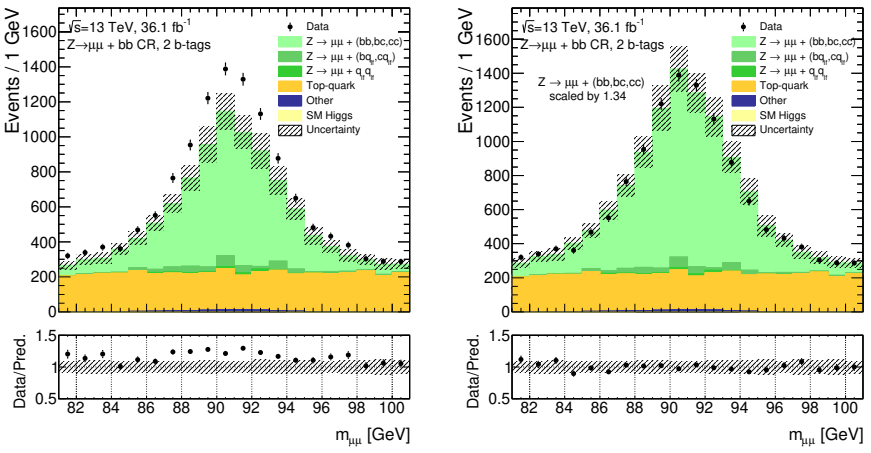

(a) *No scaling applied* **(b)** *Scaling applied*

Figure 5.10. Dimuon invariant mass in the $Z \to \mu\mu$+hf CR. (**a**) The distribution is pre-fit and it includes statistical and experimental systematic uncertainties. (**b**) The post-fit normalisation factor of 1.34 is applied to the pre-fit Z+hf background yield.

5.4 Multivariate analysis

The event preselection presented in Tables 5.5 and 5.6 is not optimised in terms of sensitivity to pair production of Higgs bosons. The main goal of the preselection is to maximise the acceptance $\times$ efficiency for the signal processes, considering the trigger limitations, and to make it possible to define optimal control regions for background estimation. The acceptance $\times$ efficiency for the SM Higgs boson pair production in the SR (already defined as the OS 2-b-tag region with respect to the preselection) is around 3.2% (1.9%) for the $\tau_{\text{lep}}\tau_{\text{had}}$ ($\tau_{\text{had}}\tau_{\text{had}}$) channel. Given that only around 40 SM $HH \to b\bar{b}\tau^+\tau^-$ events are expected to be produced in the $\tau_{\text{lep}}\tau_{\text{had}}$ ($\tau_{\text{had}}\tau_{\text{had}}$) final states for 36.1 fb^{-1} of pp collision data, the number of expected events after the SR selection is only around 1.2 (0.7). The number of expected background events is more than 4 (3) orders of magnitude larger.

A set of *Boosted Decision Trees* (BDTs) [193, 194] is used to maximise the sensitivity of the analysis to the signal processes. Separate BDTs are trained for every signal hypothesis and for every resonance-mass hypothesis, as described below. A set of input variables that offer good separation between signal and background events are used in the training process. Compared to a cut-based analysis that takes into account only the signal-to-background separation that each individual input variable provides, BDTs also account for correlations between different variables, and thus they perform better.

5.4.1 Boosted Decision Trees

A simple decision tree is a classifier that performs subsequent binary splits of data into different classes. The classifier is trained on a dataset for which it is known to which class each data entry belongs to. A set of variables describing this dataset, and offering a high level of discrimination power between data entries that belong to different classes, is used to construct the decision tree.

In the use case presented here, decision trees are trained on simulated samples to separate signal and background events. The tree starts from a *root node* that contains all events used in the training. The root node is split into two child nodes based on a simple cut on one of the input variables. The optimal cut is determined based on the weighted sum of *Gini indices* corresponding to the two child nodes. The Gini index for one node is defined as $p(1-p)$, where p is the *purity*, which is calculated from the number of signal (s) and background (b) events as $p = s/(s+b)$. The two Gini indices are each weighted by the number of events $(s+b)$ in the respective node and added together. The optimal cut is then defined as the one that gives two nodes with the highest separation power with respect to the parent node, based on the calculation above.

This procedure is repeated for each obtained node until some stopping criterion is fulfilled. The final nodes (leaves) are labelled as signal-like or background-like, depending on the fraction of signal and background events they contain. In this way, if N input variables are used, the total N-dimensional phase space is split into rectangular regions that are labelled as signal or background regions.

A decision tree is defined by several parameters, such as its maximum depth, minimum leaf-node size and the number of cuts. The maximum depth refers to the maximum number of nodes between the root node and the final leaf node. The minimum leaf-node size refers to the minimum percentage of training events that a leaf node is required to contain. The number of cuts determines the number of grid points in the range of an input variable that is scanned to determine the optimal splitting cut.

The decision tree obtained as described above is not a very powerful classifier. It usually suffers from either a poor separation power, or from *over-*

training. The latter usually occurs when parameters that define the properties of a decision tree allow it to treat statistical fluctuations as data features. To improve the performance and stability of decision trees, a procedure called *boosting* is applied. The most popular boosting algorithm, also used for the results presented in this thesis, is *the adaptive boost* (AdaBoost). A series of decision trees are trained and events that are misclassified by one tree are given a higher event weight in the training of the following tree. The boost weight, α, is derived from the misclassification rate, ε_{err}, of the previous tree, as $\alpha = (1-\varepsilon_{\text{err}})/\varepsilon_{\text{err}}$. The weights of the entire sample are then renormalised to the initial sum of weights.

For every individual decision tree, the result of the classification of a given event, described by $\mathbf{x}$, where $\mathbf{x}$ is a vector containing the obtained values of the BDT input variables in this event, is labelled as $h(\mathbf{x})$. It is equal to $+1$ if the event falls into one of the signal leaf nodes, and -1 otherwise. The final BDT score of the event described by $\mathbf{x}$ is then calculated as

$$\text{BDT score } (\mathbf{x}) = \frac{1}{N_{\text{trees}}} \sum_{i=1}^{N_{\text{trees}}} \ln(\alpha_i) h_i(\mathbf{x}). \tag{5.8}$$

The BDT score takes values[13] between -1 and 1 and it can be used as a discriminant between signal and background processes. In the case of good separation, high BDT scores are on average assigned to signal events and low BDT scores to background events. The important parameters that define the AdaBoost algorithm are the number of trained decision trees, N_{trees}, and the learning rate, β. The learning rate controls the boost step of the algorithm and it is applied as an exponent to the boost weight, α.

Estimated signal and background events that pass the SR selection are used in constructing the BDTs in the analysis. The events are equally split into training and testing samples. The BDTs are checked for overtraining by making sure the BDT score distributions from the training and testing samples are compatible.

Additionally, in order to use all available simulated events, the training and testing samples are swapped and another classifier is trained. Each classifier is always applied only to the events that were not used to train it. The two classifiers are applied randomly, in equal portions, to the data events. A high performance and stability of the BDTs are obtained by tuning the BDT parameters to the values listed in Table 5.9.

5.4.2 Training of BDTs in the analysis

A number of BDTs are trained independently in each of the three SRs: $\tau_{\text{lep}}\tau_{\text{had}}$ SLT, $\tau_{\text{lep}}\tau_{\text{had}}$ LTT and $\tau_{\text{had}}\tau_{\text{had}}$. All variables used for training the BDTs are

[13] Ranges are arbitrary and can differ between different software packages.

Table 5.9. *Optimised values of the BDT parameters.*

BDT Parameter	Value
Boost algorithm	AdaBoost
Number of trees, N_{trees}	200
Maximum depth of a tree	4
Minimum leaf-node size	5%
Number of cuts	100
Learning rate, β	0.15

summarised below. The choice of input variables differs between the SRs and signal models, as summarised in Table 5.10.

List of variables used for training the BDTs:

- $m_{\tau\tau}^{\text{MMC}}$: The invariant mass of the $\tau\tau$ system obtained from the MMC.
- m_{bb}: The invariant mass of the system of two b-jets.
- m_{HH}: The scaled invariant mass of the reconstructed $bb\tau\tau$ system. The four-vectors corresponding to the di-b-jet and $\tau\tau$ systems, where the latter is obtained using the MMC algorithm, are scaled by 125 GeV$/m_{bb}$ and 125 GeV$/m_{\tau\tau}^{\text{MMC}}$, respectively, and then combined together into a four-vector corresponding to the $bb\tau\tau$ system. This scaling is performed in order to improve the m_{HH} resolution for the signal processes.
- $\Delta R(b,b)$: The angular distance between the two b-jet four-vectors.
- $\Delta R(\tau,\tau)$: The angular distance between the four-vectors of the visible τ-lepton decay products.
- E_T^{miss}: The missing transverse energy, as defined in Section 4.6.
- E_T^{miss} ϕ centrality: The variable describing the E_T^{miss} ($\vec{p}_T^{\,\text{miss}}$) ϕ direction, $\phi_{E_T^{\text{miss}}}$, with respect to the ϕ coordinates of the visible τ-lepton decay products, ϕ_{τ_1} and ϕ_{τ_2}. The variable[14] is calculated as

$$E_T^{\text{miss}}\ \phi \text{ centrality} = \frac{A+B}{\sqrt{A^2+B^2}}, \tag{5.9}$$

  where A and B are defined as

$$A = \frac{\sin(\phi_{E_T^{\text{miss}}} - \phi_{\tau_2})}{\sin(\phi_{\tau_1} - \phi_{\tau_2})}, B = \frac{\sin(\phi_{\tau_1} - \phi_{E_T^{\text{miss}}})}{\sin(\phi_{\tau_1} - \phi_{\tau_2})}. \tag{5.10}$$

- m_T^W: The transverse mass between the lepton ℓ and the E_T^{miss}, defined as

$$m_T^W = \sqrt{p_T^\ell E_T^{\text{miss}}(1-\cos\Delta\phi)}, \tag{5.11}$$

[14]The E_T^{miss} ϕ centrality is equal to $\sqrt{2}$ (1) if the E_T^{miss} direction lies exactly between (is exactly aligned with one of) the visible τ-lepton decay products. If the E_T^{miss} lies outside the ϕ angle spanned by the visible τ-lepton decay products, the E_T^{miss} ϕ centrality is smaller than 1.

where $\Delta\phi$ is the azimuthal angle between the $\vec{p}_T$ of the lepton and the direction of the E_T^{miss} ($\vec{p}_T^{\,\text{miss}}$).

- $\Delta\phi(H,H)$: The azimuthal angle $\Delta\phi$ between the four-vectors of the di-b-jet system and the four-vector of the $\tau\tau$ system, where the latter is obtained from the MMC.
- $\Delta p_T(\ell, \tau_{\text{had}})$: The difference in p_T between the electron or muon and the visible τ_{had} object.
- The sub-leading b-jet p_T.

Table 5.10. *Variables used as inputs for training the BDTs for the different channels and signal models.*

Variable	$\tau_{\text{lep}}\tau_{\text{had}}$ channel		$\tau_{\text{had}}\tau_{\text{had}}$ channel
	SLT resonant	SLT non-resonant and LTT	
m_{HH}	✓	✓	✓
$m_{\tau\tau}^{\text{MMC}}$	✓	✓	✓
m_{bb}	✓	✓	✓
$\Delta R(\tau,\tau)$	✓	✓	✓
$\Delta R(b,b)$	✓	✓	✓
E_T^{miss}	✓		
E_T^{miss} ϕ centrality	✓		✓
m_T^W	✓	✓	
$\Delta\phi(H,H)$	✓		
$\Delta p_T(\ell, \tau_{\text{had}})$	✓		
Sub-leading b-jet p_T	✓		

One BDT classifier per SR is trained to select the SM Higgs boson pair production. In the searches for resonant signals, separate BDTs are trained for the scalar resonance, G_{KK} with $k/\bar{M}_{\text{pl}} = 1$, and G_{KK} with $k/\bar{M}_{\text{pl}} = 2$. The BDTs are trained for each resonance-mass hypothesis listed in Table 5.1. Given that m_{HH} is one of the BDT input variables, it cannot be guaranteed that the results of the search can be interpolated between the simulated samples if only the signal corresponding to the target resonance mass is used in the training. For that reason, the BDTs for one resonance mass point are trained on the signal model that includes the sample corresponding to that mass point and samples corresponding to the two neighbouring mass points[15].

The main difference between the three resonance models, for the same mass hypothesis, is the resonance width, which impacts the event kinematics, as can be seen in Figure 5.11. Different widths also lead to different values of the signal acceptance $\times$ efficiency, especially for the mass points close to the threshold for the on-mass-shell HH production. The input variables used for

[15] Only one neighbouring mass point is added to the training for the lowest and highest resonance-mass hypotheses.

training the BDTs in the $\tau_{\text{had}}\tau_{\text{had}}$-channel SR are shown in Figure 5.12. The corresponding variables used for training the BDTs in the $\tau_{\text{lep}}\tau_{\text{had}}$ SRs can be found in Ref. [15].

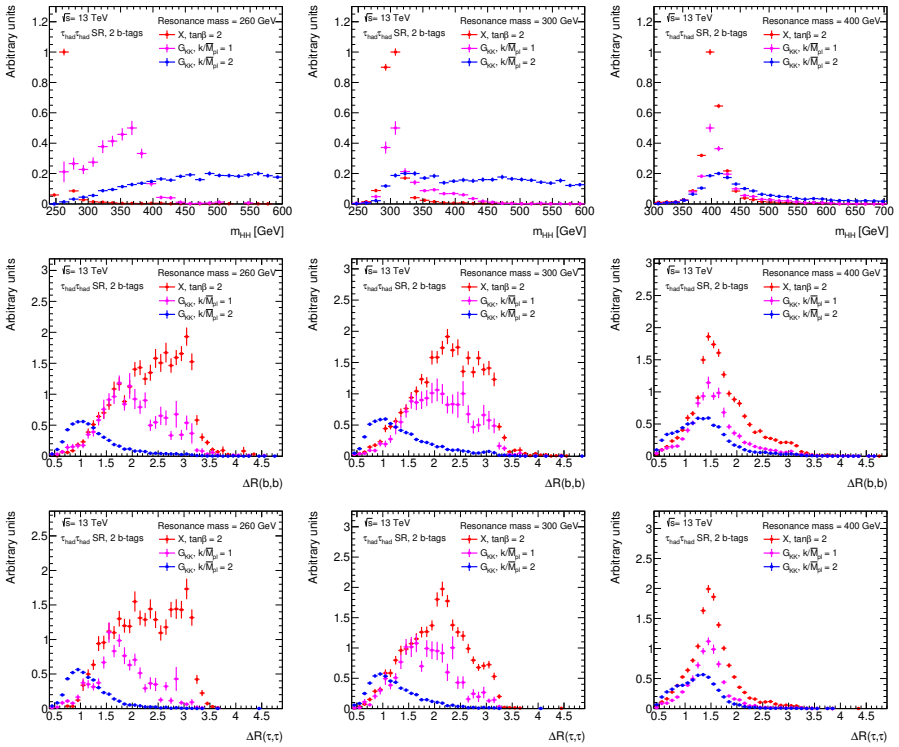

Figure 5.11. Distributions of reconstructed m_{HH}, $\Delta R(b,b)$ and $\Delta R(\tau,\tau)$ in the $\tau_{\text{had}}\tau_{\text{had}}$-channel SR for the resonance masses of 260 GeV (left), 300 GeV (middle) and 400 GeV (right) for the narrow-width scalar resonance X (red), G_{KK} with $k/\bar{M}_{\text{pl}} = 1$ (magenta) and G_{KK} with $k/\bar{M}_{\text{pl}} = 2$ (blue).

In the $\tau_{\text{had}}\tau_{\text{had}}$ channel, the BDTs are trained against three major background processes: $t\bar{t}$, $Z \to \tau\tau$+jets and multijet events, weighted by their expected cross-sections in order to reproduce the expected background composition. In the $\tau_{\text{lep}}\tau_{\text{had}}$ channel, the BDTs are trained against $t\bar{t}$ events. The obtained BDT scores are fitted using the profile likelihood fit to obtain the final results, which will be discussed in Section 5.6. The pre-fit BDT score for the BDT trained on the SM Higgs boson pair production signal sample in the $\tau_{\text{had}}\tau_{\text{had}}$ channel is shown in Figure 5.13. The BDT scores corresponding to the resonant signals in the $\tau_{\text{had}}\tau_{\text{had}}$ channel, as well as the BDT scores corresponding to the classifiers used to extract signals in the $\tau_{\text{lep}}\tau_{\text{had}}$-channel SRs are shown in Section 5.6, and they can also be found in Ref. [15].

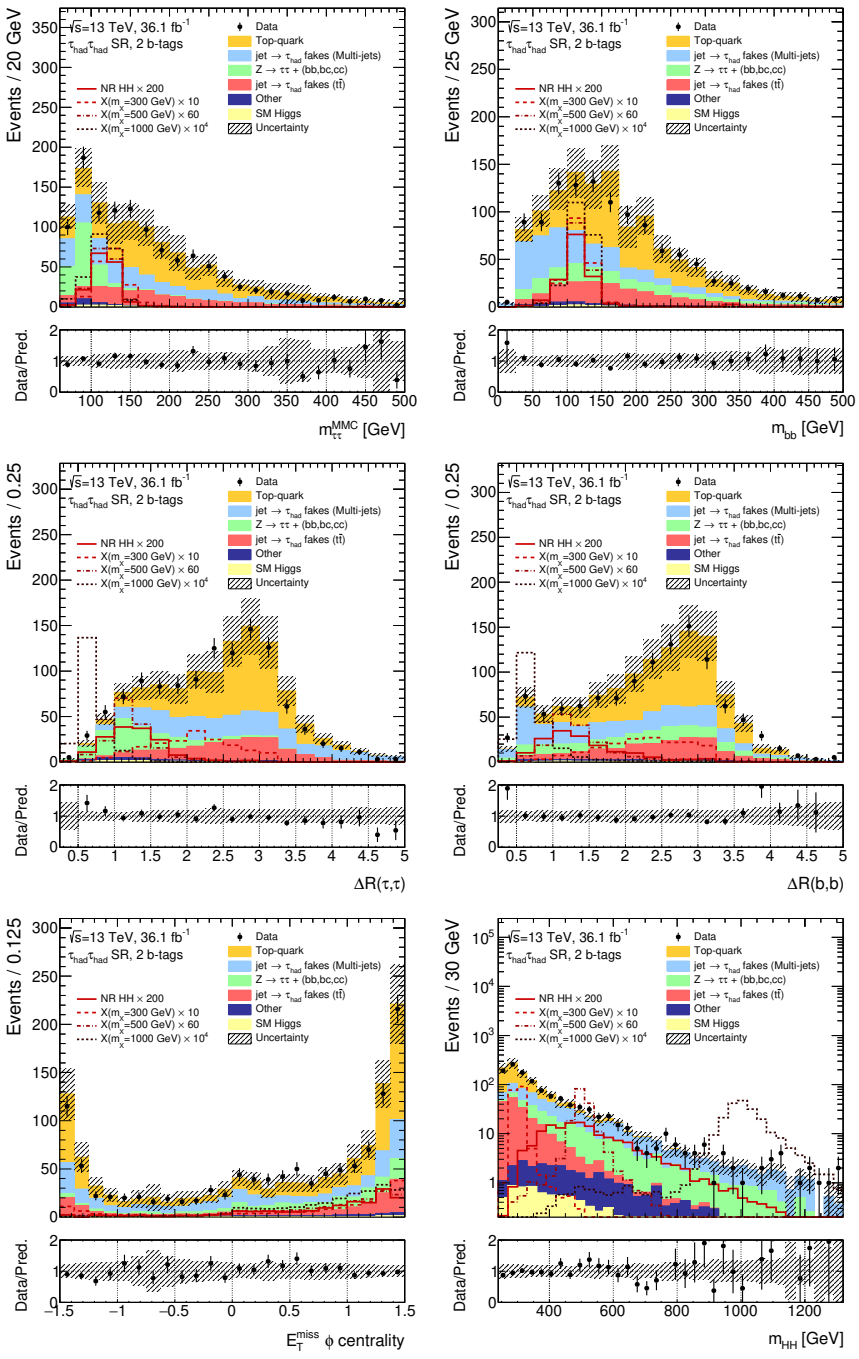

Figure 5.12. Pre-fit distributions of the input variables used for training the BDTs in the $\tau_{\text{had}}\tau_{\text{had}}$-channel SR. The distributions include statistical and systematic uncertainties in the background estimation. The non-resonant SM HH signal (NR HH) and the signal corresponding to the scalar resonance ($X \to HH$, for $m_X = \{300, 500, 1000\}$ GeV) are overlaid and scaled by arbitrary normalisation factors for better visualisation.

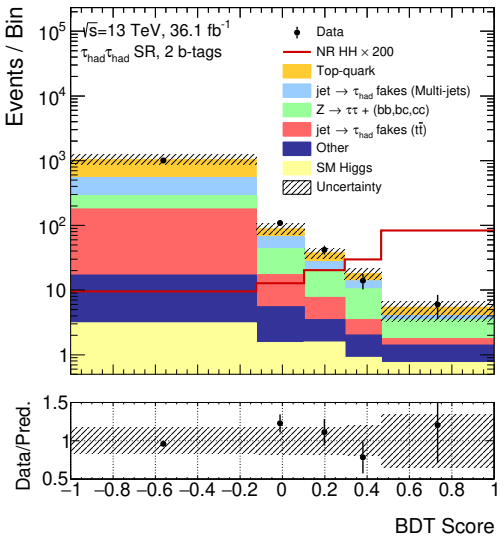

Figure 5.13. Pre-fit distribution of the BDT score for the non-resonant SM HH signal (NR HH) in the $\tau_{\text{had}}\tau_{\text{had}}$-channel SR. The statistical and systematic uncertainties in the background estimation are included. The signal is overlaid after being scaled by a factor of 200 for better visualisation. The choice of binning is discussed in Section 5.7.

5.5 Systematic uncertainties

Systematic uncertainties related to the background and signal estimation in the $\tau_{\text{lep}}\tau_{\text{had}}$ and $\tau_{\text{had}}\tau_{\text{had}}$ SRs are evaluated and propagated to the final fit. They include experimental and theoretical modelling uncertainties, as summarised below.

5.5.1 Experimental uncertainties

Experimental uncertainties include those arising from the measured integrated luminosity, the modelling of pileup, as well as those related to the reconstruction and identification of different physics objects. These uncertainties are mostly analysis-independent and they have been reported in different publications by the ATLAS collaboration, as cited below.

Integrated luminosity and pileup

The uncertainty on the measured integrated luminosity of the dataset used to obtain the results presented in this chapter is 2.1% [87]. This normalisation uncertainty is applied to all simulated signal and background samples for which the normalisation is not treated as a free parameter in the fit. The luminosity uncertainty is correlated between all processes to which it is applied. The pileup profile of the simulated events is re-weighted to match the one in data,

as discussed in Section 3.3, and thus the associated uncertainties are propagated to the final results [195].

Trigger requirements
To account for any differences between the simulated and data events when applying trigger requirements, trigger efficiencies with respect to the offline physics objects are measured in data and simulation, and they are used to calculate trigger scale factors[16] that are applied to the simulated events in the analysis [190–192]. Uncertainties on these scale factors are propagated as systematic uncertainties in signal and background estimation.

Reconstruction and identification of physics objects
Uncertainties related to the reconstruction (namely those associated to the momentum/energy scale and resolution), identification and isolation of electrons [130], muons [134], τ_{had} candidates [156] and jets [141, 142] are accounted for and propagated to the final results. Different sources contributing to these uncertainties in an uncorrelated manner are treated separately in the profile likelihood fit. The main sources of uncertainties related to different physics objects, and the number of degrees of freedom (nuisance parameters) with which they contribute in the fit, are listed in Table 5.11. These uncertainties are propagated to the calculation of E_T^{miss} [154]. Additionally, the uncertainties in E_T^{miss} include those from the calculation of the soft-term.

5.5.2 Modelling uncertainties: simulated signal and background processes

The modelling uncertainties for the simulated signal and background processes are discussed in this section and summarised in Table 5.12. The uncertainties in the modelling of the data- and semi-data-driven backgrounds are discussed in Section 5.5.3.

Signal processes
The theoretical uncertainties on the signal acceptance $\times$ efficiency ($A \times \varepsilon$) are evaluated by performing the analysis selection on specially-generated, particle-level signal samples. The generation of these samples follows the configuration of the baseline samples, but with modifications to probe the following sources of theoretical uncertainties: the calculation of matrix elements; the modelling of the parton shower and hadronisation processes, which includes the modelling of the initial and final state radiation; and the parton density

[16]The trigger scale factors are derived for events with correctly identified electrons, muons and τ_{had} objects that are matched to trigger-level objects. The fraction of events with fake electrons and muons in the $\tau_{\text{lep}}\tau_{\text{had}}$ channel is estimated to be small, while the majority of events with fake-τ_{had} objects in both channels are estimated using data- or semi-data-driven techniques.

Table 5.11. *List of systematic uncertainties related to the reconstruction, identification and isolation of different physics objects, as well as the calculation of E_T^{miss}. Different sources of uncertainties are listed for each physics object, while the number of nuisance parameters with which they contribute in the profile likelihood fit is stated in the column titled "Components". All these represent the uncertainties in the normalisation and shape of the final discriminant (BDT score), hence labelled as type "NS".*

Object	Sources of systematic uncertainties	Components	Type
Electrons	Energy scale and resolution, identification, isolation, trigger	5	NS
Muons	p_T scaling and resolution smearing, identification, isolation, trigger	18	NS
τ_{had} candidates	Energy scale, identification, τ_{had} – electron overlap removal, trigger	14	NS
Jets	Jet energy scale and resolution	4	NS
b-tagging	Identification of b-jets and misidentification of c- and light-jets	14	NS
E_T^{miss}	Objects, soft-term	3	NS

functions. The analysis selection is mimicked at truth-level, without taking into account the efficiencies of the trigger selection or the reconstruction and identification of relevant physics objects.

To evaluate the uncertainties in the calculation of matrix elements and the potential effects of missing higher order terms, the renormalisation and factorisation scales used to generate the SM HH signal samples are varied together as well as independently up and down by a factor of 2, which gives 6 variations in total. For the resonant signals, a simplified approach is followed in order to reduce the number of samples needed[17], where both the renormalisation and factorisation scales are varied coherently up or down by a factor of 2. None of these variations are found to affect the shape of the BDT input variables calculated using truth-level information. The ratio of the overall $A \times \varepsilon$ between the largest up and down variations and the nominal prediction for the SM HH signal are found to be 1.02 ± 0.03 and 0.98 ± 0.03 (1.02 ± 0.04 and 0.99 ± 0.04) for the $\tau_{\text{lep}}\tau_{\text{had}}$ ($\tau_{\text{had}}\tau_{\text{had}}$) channel, i.e. statistically consistent with 1. The effect of the scale variations on $A \times \varepsilon$ for the different resonant samples in the $\tau_{\text{had}}\tau_{\text{had}}$ channel is shown in Figure 5.14.

[17] The two approaches are compared when evaluating these uncertainties for the SM sample and they are found to give results that are compatible within statistical uncertainties.

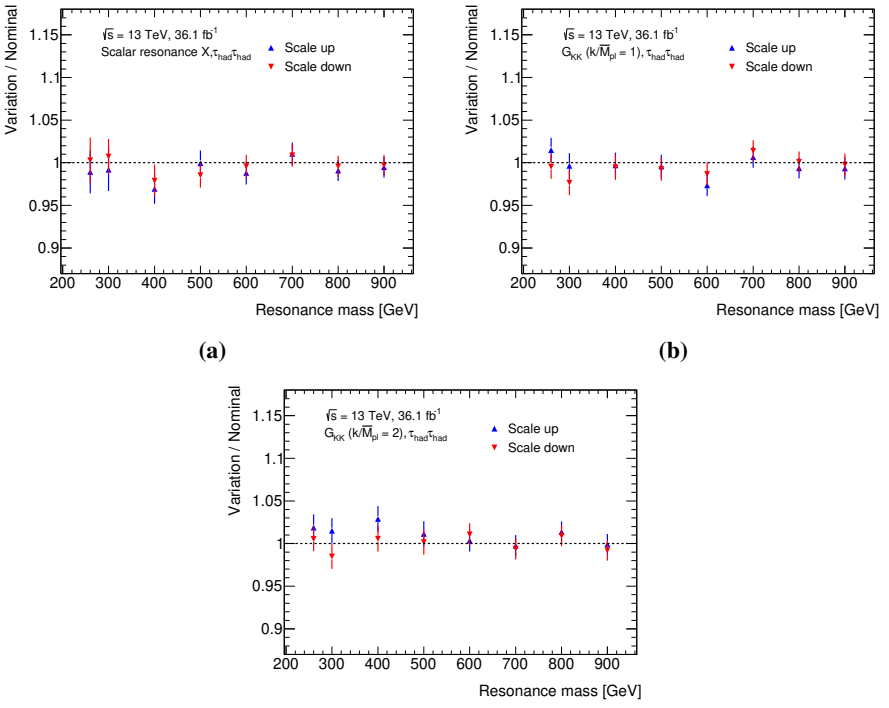

Figure 5.14. Ratio of $A \times \varepsilon$ measured in the scale-varied samples over the baseline sample in the $\tau_{\text{had}}\tau_{\text{had}}$ channel for: (**a**) the scalar resonance; (**b**) G_{KK} with $k/\bar{M}_{\text{pl}} = 1$; and (**c**) G_{KK} with $k/\bar{M}_{\text{pl}} = 2$. The upward-pointing triangles correspond to doubling both the renormalisation and factorisation scales, while the downward-pointing triangles correspond to halving them.

Uncertainties due to modelling of the parton shower and hadronisation processes and the modelling of underlying events are evaluated by comparing samples obtained using different generators. In particular, for the SM HH signal, PYTHIA 8.2 is used instead of HERWIG++, while for the resonant signals HERWIG++ is used as an alternative sample instead of (nominally used) PYTHIA 8.2. Although small shape differences are found in some of the BDT input variables, no shape effect on the BDT score is found when these differences are parameterised and propagated. The ratio of the overall $A \times \varepsilon$ between the alternative and nominal SM HH samples is found to be 1.05 ± 0.03 (1.09 ± 0.04) in the $\tau_{\text{lep}}\tau_{\text{had}}$ ($\tau_{\text{had}}\tau_{\text{had}}$) channel. The ratios in the $A \times \varepsilon$ between the alternative and nominal resonant signal samples in the $\tau_{\text{had}}\tau_{\text{had}}$ channel are shown in Figure 5.15, while similar results are obtained for the $\tau_{\text{lep}}\tau_{\text{had}}$ channel. The 12% normalisation uncertainty is applied to all resonant signals in the $\tau_{\text{lep}}\tau_{\text{had}}$ and $\tau_{\text{had}}\tau_{\text{had}}$ SRs.

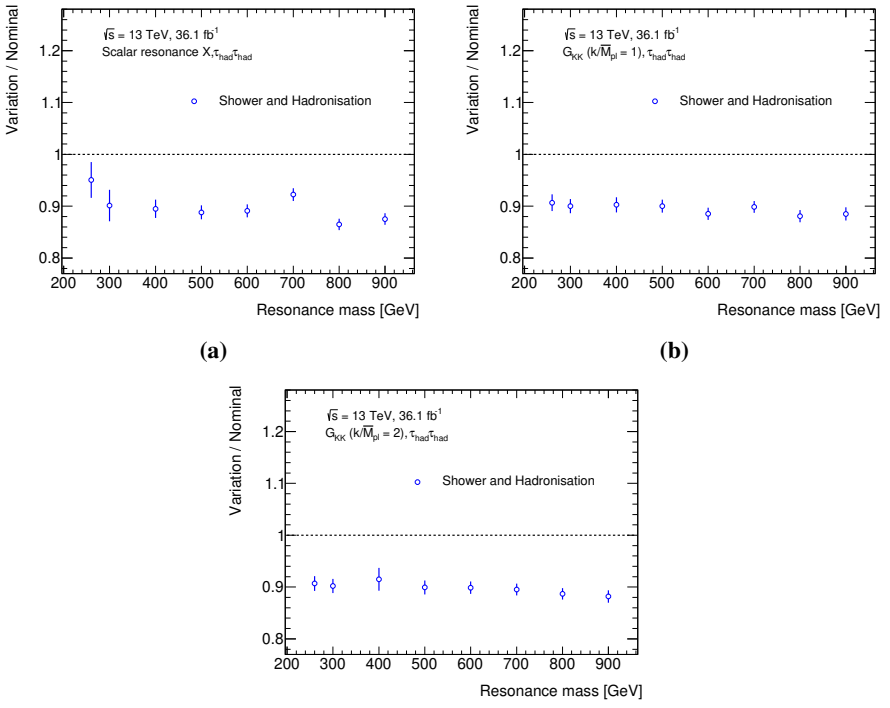

Figure 5.15. Ratio of $A \times \varepsilon$ measured in the sample with the alternative parton shower and hadronisation model over the baseline sample in the $\tau_{\text{had}}\tau_{\text{had}}$ channel for: (**a**) the scalar resonance; (**b**) G_{KK} with $k/\bar{M}_{\text{pl}} = 1$; and (**c**) G_{KK} with $k/\bar{M}_{\text{pl}} = 2$.

The PDF uncertainties are evaluated using PDF4LHC15 sets [196], which combine CT14, MMHT14 and NNPDF30 PDFs. The uncertainty is evaluated by calculating $A \times \varepsilon$ for each PDF variation. The standard deviation of these values divided by $A \times \varepsilon$ of the nominal sample is taken as the signal PDF uncertainty. The PDF uncertainty is found to be negligible for all signals in all SRs.

The theoretical uncertainties on the cross-section for the SM HH signal, given by Equation (5.1), are added in quadrature and applied as a 8% normalisation uncertainty in the fit.

Modelling of $t\bar{t}$ events that do not contain fake-τ_{had} candidates

In the $\tau_{\text{had}}\tau_{\text{had}}$ and $\tau_{\text{lep}}\tau_{\text{had}}$ SRs, as well as in the $Z \to \mu\mu$+hf CR, the $t\bar{t}$ background that does not contain any fake-τ_{had} candidates is estimated using simulation. Several uncertainties in $A \times \varepsilon$ are probed by generating alternative samples with modified configurations with respect to those defined in Section 5.1. The factorisation and renormalisation scales are varied coherently by factors of

0.5 and 2. The uncertainty on the parton shower and hadronisation model, and the uncertainty in modelling the underlying events, are estimated by switching the MC generator between PYTHIA 6.4 and HERWIG. Additional uncertainties related to the hard scatter processes and the merging of the matrix element and parton shower are estimated by comparing the nominal sample with an alternative sample generated using MG5_aMC@NLO for the matrix element and HERWIG++ for the modelling of the parton shower and hadronisation processes. The effects on the shape and normalisation are treated separately. The largest shape differences between the nominal and alternative samples in the SRs are parameterised in m_{bb} and the transverse momentum of the di-b-jet system, p_T^{bb}, and they are propagated as shape uncertainties on the final discriminant, i.e. the respective BDT score. The total up and down systematic variations of the $t\bar{t}$ background in the $\tau_{\text{had}}\tau_{\text{had}}$-channel SR, after summing all experimental and modelling uncertainties in quadrature, are shown in Figure 5.16a. All individual uncertainties are considered separately in the final fit.

The normalisation of the $t\bar{t}$ background is freely floated in the final fit and it is correlated between the SRs and the $Z \to \mu\mu$+hf CR. Given that the post-fit normalisation is mostly driven by the $\tau_{\text{lep}}\tau_{\text{had}}$ SRs, the $t\bar{t}$ normalisation in the $\tau_{\text{had}}\tau_{\text{had}}$ SR is allowed to differ from the best post-fit value if the difference is within the uncertainty on the ratio of $A \times \varepsilon$ between the $\tau_{\text{had}}\tau_{\text{had}}$ and $\tau_{\text{lep}}\tau_{\text{had}}$ SRs. This is referred to as the $\tau_{\text{lep}}\tau_{\text{had}} \to \tau_{\text{had}}\tau_{\text{had}}$ extrapolation uncertainty, and it is calculated as

$$\sigma_{A\times\varepsilon}^{\tau_{\text{lep}}\tau_{\text{had}}\to\tau_{\text{had}}\tau_{\text{had}}} = \frac{(N_{\tau_{\text{had}}\tau_{\text{had}}}/N_{\tau_{\text{lep}}\tau_{\text{had}}})_{\text{nominal}} - (N_{\tau_{\text{had}}\tau_{\text{had}}}/N_{\tau_{\text{lep}}\tau_{\text{had}}})_{\text{variation}}}{(N_{\tau_{\text{had}}\tau_{\text{had}}}/N_{\tau_{\text{lep}}\tau_{\text{had}}})_{\text{nominal}}}, \tag{5.12}$$

where N is the number of $t\bar{t}$ events in the respective SR. Similarly, an extrapolation uncertainty between the $\tau_{\text{lep}}\tau_{\text{had}}$ SR and the $Z \to \mu\mu$+hf CR is calculated as well. The up and down variations, with respect to the expected number of events in the nominal sample, are treated separately and added in quadrature. The extrapolation uncertainty from the $\tau_{\text{lep}}\tau_{\text{had}}$ SR to the $\tau_{\text{had}}\tau_{\text{had}}$ SR ($Z \to \mu\mu$+hf CR) is $^{+30\%}_{-32\%}$ $\left(^{+8.1\%}_{-9.3\%}\right)$.

Modelling of Z+heavy-flavour jets events

Similar to the $t\bar{t}$ background, uncertainties in the modelling of the Z+hf background are evaluated by generating alternative MC samples with specific variations in their configuration. The renormalisation and factorisation scales are varied together and independently up and down by a factor of 2 and the largest up and down variations are taken as scale uncertainties. The uncertainty in the parton shower and hadronisation model is evaluated by generating an alternative sample using MG5_aMC@NLO at LO with the NNPDF23LO PDF set for the matrix element and PYTHIA 8.2 with the A14 tune for the parton shower and hadronisation processes. The PDF uncertainties are evaluated by

calculating the standard deviation of NNPDF30 PDF replicas and taking an envelope of these variations with those obtained from comparing the nominal PDF with MMHT2014nnlo68cl and CT14nnlo sets [196]. The shape differences are parameterised either in m_{bb} or p_T^{bb}, since one of these variables is always the one showing the largest shape variations with respect to the nominal, and they are propagated as shape uncertainties on the respective BDT score. The total up and down systematic variations of the $Z \to \tau\tau$+hf background in the $\tau_{\text{had}}\tau_{\text{had}}$-channel SR, after summing all experimental and modelling uncertainties in quadrature, are shown in Figure 5.16b. All individual uncertainties are considered separately in the final fit.

The normalisation of the Z+hf background is freely floated in the final fit and it is correlated between the SRs and the CR. The post-fit normalisation is mostly driven by the $Z \to \mu\mu$+hf CR. The normalisation in the SRs is allowed to differ within the extrapolation uncertainties derived similarly to Equation (5.12), but in this case with respect to the $Z \to \mu\mu$+hf CR. The obtained extrapolation uncertainty from the $Z \to \mu\mu$+hf CR to the $\tau_{\text{had}}\tau_{\text{had}}$ ($\tau_{\text{lep}}\tau_{\text{had}}$) SR is $\pm 35\%$ ($\pm 29\%$).

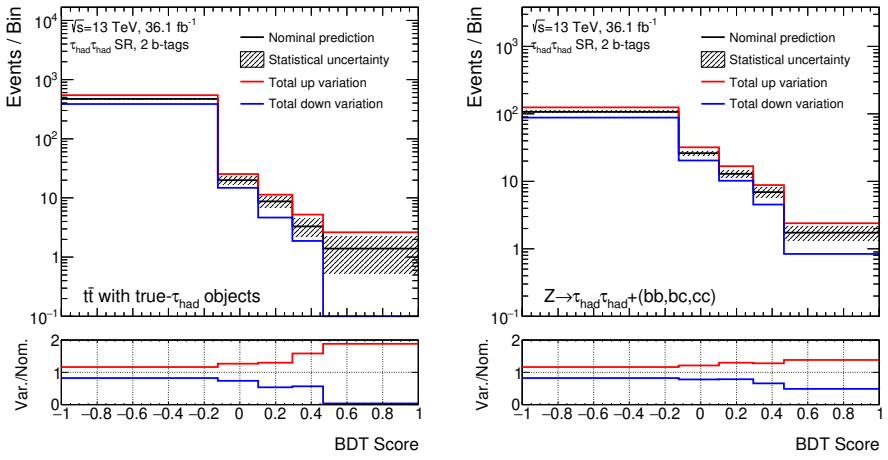

(a) **(b)**

Figure 5.16. Distribution of the BDT score for the classifier trained on the SM HH signal for the (**a**) $t\bar{t}$ background with true-τ_{had} candidates and (**b**) $Z \to \tau\tau$+hf background in the $\tau_{\text{had}}\tau_{\text{had}}$-channel SR. The nominal prediction is shown as a histogram in black with the corresponding statistical uncertainties. The total up (down) systematic variation, after summing individual experimental and modelling uncertainties in quadrature, is shown as a histogram in red (blue). Ratios of the total up and down systematic variations to the nominal prediction are shown in the bottom panels.

Other MC-based background estimates

The cross-section uncertainties for the background processes where the normalisation is determined from simulation, as summarised in Section 5.1, are added in quadrature and applied as process-specific normalisation uncertainties in the fit. The uncertainty on the production cross-section of events with $Z+(q_{\text{lf}}q_{\text{lf}}, bq_{\text{lf}}, cq_{\text{lf}})$, in short $Z+qq_{\text{lf}}$, is 5%. An additional normalisation uncertainty of 20% is applied to $Z \to ee$+jets events, based on the normalisation discrepancy observed between the dedicated $Z \to ee$+jets 0-b-tag and 1-b-tag $\tau_{\text{lep}}\tau_{\text{had}}$ preselection CRs. The normalisation uncertainty of 30% (50%) is applied to events with W+heavy-flavour jets in the $\tau_{\text{lep}}\tau_{\text{had}}$ ($\tau_{\text{had}}\tau_{\text{had}}$) channel. This is a minor background in both channels, but a large uncertainty is motivated by the normalisation mismodelling observed for Z+hf events, as discussed in Section 5.3.5. In the $\tau_{\text{had}}\tau_{\text{had}}$ channel, the 30% uncertainty is inflated to 50% to account for an additional fake-τ_{had} candidate that must be present in the event.

Cross-section uncertainties of 3.7%, 4.2% and 5.4% are applied to the single-top-quark events produced in s, t and Wt channels, respectively, while a cross-section uncertainty of 6% is applied to ZZ, WZ and WW (VV) events. The $t\bar{t}H$ and ZH processes are kinematically very similar to the signal processes, and thus conservative normalisation uncertainties of 30% and 28% are applied for these background components, respectively. These uncertainties are motivated by the corresponding $t\bar{t}H$ and ZH experimental measurements [153,197] performed by the ATLAS experiment.

5.5.3 Modelling uncertainties: data-driven background estimates

The last set of systematic uncertainties refers to the modelling of the background processes that contain fake-τ_{had} candidates, which are estimated using data- and semi-data-driven techniques.

Processes with fake-τ_{had} candidates in the $\tau_{\text{lep}}\tau_{\text{had}}$ channel

Several systematic uncertainties are assigned to the prediction of background processes with fake-τ_{had} candidates in the $\tau_{\text{lep}}\tau_{\text{had}}$ channel, which is described in Section 5.3.2.

The FFs are varied up and down by their statistical uncertainty. The subtraction of the $t\bar{t}$ background with true-τ_{had} candidates in the calculation of FFs is separately varied up and down by the corresponding experimental uncertainties, modelling uncertainties, and cross-section uncertainty of 6%. A set of normalisation and shape uncertainties is obtained in this way with normalisation uncertainties on the total prediction of $\pm$15%, $\pm$19% and $\pm$12% for the three sets of variations, respectively. The subtraction of the single-top-quark, VV, $t\bar{t}H$ and ZH processes is conservatively varied up and down by 50% given that these variations lead to small variations in FFs. The uncer-

Table 5.12. *List of systematic uncertainties related to the modelling of backgrounds that are estimated using simulation. Different sources of uncertainties are listed for every process and it is indicated to which of the fit regions they refer to. Each individual uncertainty is labelled as "S" if it refers to the shape of the final discriminant, or "N " if it refers to the normalisation of the sample.*

Process	Sources of systematic uncertainty	Applied in	Type
SM HH	Cross-section: 8%	SRs	N
	$(A \times \varepsilon)$: 9%	$\tau_{\text{had}}\tau_{\text{had}}$	N
	$(A \times \varepsilon)$: 5%	$\tau_{\text{lep}}\tau_{\text{had}}$	N
X, G_{KK}	$(A \times \varepsilon)$: 12%	SRs	N
$t\bar{t}$	Freely floated (mostly driven by the $\tau_{\text{lep}}\tau_{\text{had}}$ SR)	all regions	N
	$(A \times \varepsilon)_{\tau_{\text{had}}\tau_{\text{had}}}/(A \times \varepsilon)_{\tau_{\text{lep}}\tau_{\text{had}}}$: -32%, $+30\%$	$\tau_{\text{had}}\tau_{\text{had}}$	N
	$(A \times \varepsilon)_{Z+\text{hf CR}}/(A \times \varepsilon)_{\tau_{\text{lep}}\tau_{\text{had}}}$: -9.3%, $+8.1\%$	Z+hf CR	N
	m_{bb} shape $\rightarrow$ BDT score shape	SRs	S
	p_T^{bb} shape $\rightarrow$ BDT score shape	SRs	S
Z+hf	Freely floated (mostly driven by the Z+hf CR)	all regions	N
	$(A \times \varepsilon)_{\tau_{\text{had}}\tau_{\text{had}}}/(A \times \varepsilon)_{Z+\text{hf CR}}$: $\pm 35\%$	$\tau_{\text{had}}\tau_{\text{had}}$	N
	$(A \times \varepsilon)_{\tau_{\text{lep}}\tau_{\text{had}}}/(A \times \varepsilon)_{Z+\text{hf CR}}$: $\pm 29\%$	$\tau_{\text{lep}}\tau_{\text{had}}$	N
	m_{bb} shape $\rightarrow$ BDT score shape	SRs	S
	p_T^{bb} shape $\rightarrow$ BDT score shape	SRs	S
$Z + qq_{\text{lf}}$	Cross-section: 5%	all regions	N
$Z \rightarrow ee$	Normalisation: 20%	all regions	N
W+hf	Normalisation: 50%	$\tau_{\text{had}}\tau_{\text{had}}$	N
	Normalisation: 30%	$\tau_{\text{lep}}\tau_{\text{had}}$	N
Single top	Cross-section ($s/t/Wt$): 3.7%/4.2%/5.4%	all regions	N
VV	Cross-section: 6%	all regions	N
ZH	ATLAS measurement [153]: 28%	all regions	N
$t\bar{t}H$	ATLAS measurement [197]: 30%	all regions	N

tainties in r_{QCD} coming from the subtraction of simulated events are estimated in the same way.

Equivalently to the OS-region estimate, the combined FF method is applied to estimate the contribution from processes with fake-τ_{had} candidates in the SS region. The ratio between the background prediction and data in the 2-b-tag SS preselection region is found to show the largest variations as a function of m_{HH}, and thus it is parameterised in this variable. This closure un-

certainty, i.e. the deviations of the obtained ratio away from 1, is symmetrised and propagated as a normalisation ($\pm 1\%$) and shape uncertainty on the final discriminant in the SR.

An additional uncertainty on the FFs measured in the $t\bar{t}$ CR is estimated by comparing the FFs calculated directly from the simulated $t\bar{t}$ sample between two selections: the $t\bar{t}$-CR selection and the SR selection, in order to account for the extrapolation from the CR to the SR. No significant shape effect is found, and thus only a normalisation uncertainty of around 11% downwards is considered. Similarly, the uncertainty on the FFs measured in the multijet CR is estimated by comparing them to the FFs measured in the SS region, which also has a significant fraction of multijet events. The difference is propagated as a normalisation ($\pm 2\%$) and shape uncertainty on the final discriminant.

No additional uncertainties are assigned to events with electrons and muons that are misidentified as τ_{had} candidates, given that they contribute with less than 5% to the total number of events with fake-τ_{had} candidates.

Modelling of the $t\bar{t}$ background with fake-τ_{had} candidates in the $\tau_{\text{had}}\tau_{\text{had}}$ channel

The estimation of the $t\bar{t}$ background with fake-τ_{had} candidates in the $\tau_{\text{had}}\tau_{\text{had}}$ channel is described in Section 5.3.4. The FRs are varied up and down by their statistical uncertainty. An uncertainty accounting for applying only the DTT-category selection, as described in Section 5.3.4, is assigned as a function of the fake-τ_{had}-candidate p_T and propagated as a normalisation ($\pm 4\%$) and as a shape uncertainty on the final discriminant.

The subtraction of the $t\bar{t}$ background with true-τ_{had} candidates in the calculation of FRs is varied up and down by 10%, which corresponds to the $t\bar{t}$ normalisation uncertainty derived from the $\tau_{\text{lep}}\tau_{\text{had}}$-only fit. This has a large impact on the FRs, resulting in a $\approx \pm 100\%$ normalisation uncertainty on the prediction of the $t\bar{t}$ with fake-τ_{had} candidates in the $\tau_{\text{had}}\tau_{\text{had}}$ SR, which is then constrained by the fit. Contributions from other backgrounds are not varied since their impact is smaller than the statistical uncertainty of the measured FRs. An additional normalisation ($\pm 16\%$) and shape uncertainty is obtained by varying the m_T^W cut from 80 GeV to 65 GeV in order to bring the CR definition closer to the SR definition.

Given that the FRs are applied to simulated $t\bar{t}$ events, all modelling uncertainties that are considered for the $t\bar{t}$ background with true-τ_{had} candidates are estimated in this case as well. The uncertainties in the two components of the $t\bar{t}$ sample are found to be compatible. The uncertainties derived for the $t\bar{t}$ background with true-τ_{had} candidates are therefore applied to the estimation of the $t\bar{t}$ events with fake-τ_{had} candidates due to their significantly better statistical precision.

The total up and down systematic variations of the $t\bar{t}$ background with fake-τ_{had} candidates in the $\tau_{\text{had}}\tau_{\text{had}}$-channel SR, after summing all discussed mod-

elling uncertainties in quadrature, are shown in Figure 5.17a. All individual uncertainties are considered separately in the final fit.

Modelling of the multijet background in the $\tau_{\text{had}}\tau_{\text{had}}$ channel
The estimation of the multijet background in the $\tau_{\text{had}}\tau_{\text{had}}$ channel is described in Section 5.3.3. The FFs are varied up and down by their statistical uncertainty. The subtraction of the non-multijet processes when calculating the FFs, including the subtraction of the MC-based $t\bar{t}$ background with fake-τ_{had} candidates, is conservatively varied up and down by 50%. These variations are propagated as a normalisation ($\pm 3\%$) and shape uncertainty on the final discriminant in the $\tau_{\text{had}}\tau_{\text{had}}$ SR.

The ratio of the background prediction to data in the SS 2-b-tag region is parameterised in m_{HH}, the variable that shows the largest shape variations. This closure uncertainty, i.e. the deviations of the ratio between the background estimation and data away from 1, is symmetrised and propagated as a normalisation ($\pm 3\%$) and shape uncertainty on the final discriminant in the SR.

The transfer factors between the 1- and 2-b-tag regions, given in Table 5.8, are varied up and down by their statistical uncertainty and propagated as a normalisation ($\pm 16\%$) and shape uncertainty on the final discriminant. The extrapolation uncertainty from the SS region to the OS region is estimated by taking the ratio of FFs calculated in these two regions after selecting events with one b-tagged jet and $\Delta\phi(\tau_{\text{had}}, \tau_{\text{had}}) > 2.0$. Deviations of this ratio from 1, as a function of the leading τ_{had}-candidate p_T, are propagated as a normalisation ($\pm 10\%$) and shape uncertainty on the final discriminant.

The total up and down systematic variations of the multijet background in the $\tau_{\text{had}}\tau_{\text{had}}$-channel SR, after summing all discussed modelling uncertainties in quadrature, are shown in Figure 5.17b. All individual uncertainties are considered separately in the final fit.

5.6 Statistical analysis

Statistical data analysis in experimental particle physics is used to test different signal hypotheses and to characterise the sensitivity of an experiment to some phenomena of interest.

5.6.1 Likelihood model

Particle physics experiments are often based on counting events that pass certain selection criteria, which is also the case in the work presented in this thesis. All measurements of a variable x that exhibit good separation between signal and background events, e.g. the BDT score shown in Figure 5.13, can be written as $\{x_1, x_2, ..., x_n\}$, where n is the total number of obtained events. On

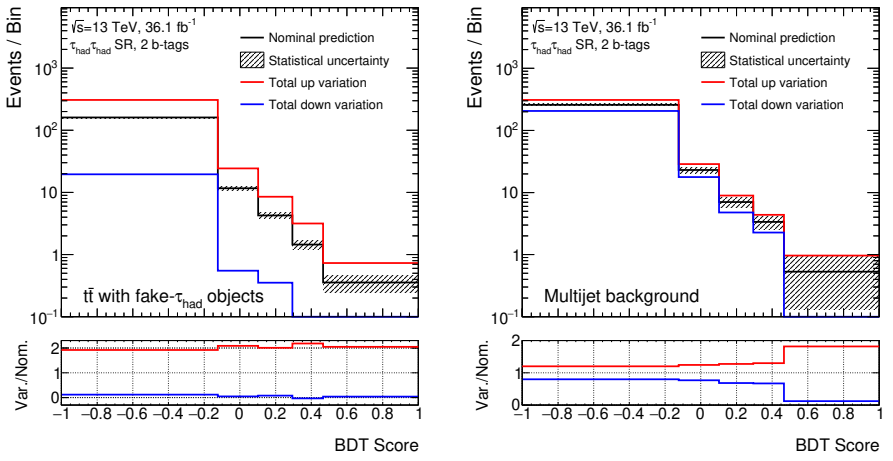

(a) **(b)**

Figure 5.17. Distribution of the BDT score for the classifier trained on the SM HH signal for the (**a**) $t\bar{t}$ background with fake-τ_{had} candidates and (**b**) multijet background in the $\tau_{\text{had}}\tau_{\text{had}}$-channel SR. The nominal prediction is shown as a histogram in black with the corresponding statistical uncertainties. The total up (down) systematic variation, after summing individual modelling uncertainties in quadrature, is shown as a histogram in red (blue). Ratios of the total up and down systematic variations to the nominal prediction are shown in the bottom panels.

the other hand, the physics model used to interpret this measurement predicts $\mu\nu_{\text{tot}}^{\text{sig}} + \nu_{\text{tot}}^{\text{bkg}}$ events, where μ is the *signal strength*, while $\nu_{\text{tot}}^{\text{sig}}$ and $\nu_{\text{tot}}^{\text{bkg}}$ are the expected numbers of signal and background events, respectively. If $\mu = 0$, the background-only scenario is assumed, while if $\mu = 1$, the nominal signal-plus-background scenario is assumed. The probability for obtaining $\{x_1, x_2, ..., x_n\}$ for a given μ [198] can be written as

$$P(\{x_1,x_2,...,x_n\}|\mu) = \text{Pois}(n|\mu\nu_{\text{tot}}^{\text{sig}} + \nu_{\text{tot}}^{\text{bkg}}) \left[\prod_{e=1}^{n} \frac{\mu\nu_{\text{tot}}^{\text{sig}} f_{\text{sig}}(x_e) + \nu_{\text{tot}}^{\text{bkg}} f_{\text{bkg}}(x_e)}{\mu\nu_{\text{tot}}^{\text{sig}} + \nu_{\text{tot}}^{\text{bkg}}}\right], \tag{5.13}$$

where $\text{Pois}(n|\mu\nu_{\text{tot}}^{\text{sig}} + \nu_{\text{tot}}^{\text{bkg}})$ is the Poisson probability for obtaining n events when $\mu\nu_{\text{tot}}^{\text{sig}} + \nu_{\text{tot}}^{\text{bkg}}$ events are expected, while $f_{\text{sig}}(x_e)$ and $f_{\text{bkg}}(x_e)$ are the signal and background probability density functions (pdfs) for obtaining an event with $x = x_e$.

In the use case presented in this thesis, a binned equivalent of the probability model presented above is used, where a bin b is expected to contain ν_b^{sig} signal and ν_b^{bkg} background events. It can be shown that the probability for observing

a data histogram $\{n_1, n_2, ..., n_{\text{last bin}}\}$ for a given μ is then

$$P(\{n_1, n_2, ..., n_{\text{last bin}}\}|\mu) = \text{const.} \cdot \prod_b \text{Pois}(n_b|\mu\nu_b^{\text{sig}} + \nu_b^{\text{bkg}}), \tag{5.14}$$

where n_b is the number of data events in a bin b. For a fixed data histogram $\{n_1, n_2, ..., n_{\text{last bin}}\}$, this probability depends on μ and it becomes the likelihood function $L(\mu)$.

The model can be generalised [198] by including multiple background samples[18]. Furthermore, a combined likelihood model can be constructed for multiple channels, or multiple SRs and CRs that have orthogonal event selections, in which case some of the parameters discussed below can be correlated between the channels/regions.

The likelihood is defined by a number of parameters that are split into three disjoint sets: $\mathbf{N}$, $\mathbf{S}$ and $\mathbf{\Gamma}$. A free (unconstrained) normalisation parameter $\phi_p \in \mathbf{N}$ can be assigned to any sample, similar to the signal strength μ that is assigned to the signal process. An externally-constrained normalisation parameter η_{cs}, such as the cross-section uncertainty, or an externally-constrained coherent shape variation in the form of a varied histogram σ_{csb}, representing for example an experimental uncertainty, can be assigned to any sample s in a channel c to allow for the normalisation or shape of this sample to vary within an assigned uncertainty. Parameters associated to these types of uncertainties are labelled as $\alpha_p \in \mathbf{S}$. The content of an individual bin can be varied by introducing bin-by-bin scale factors used for statistical uncertainties or bin-by-bin shape uncertainties, $\gamma_{csb} \in \mathbf{\Gamma}$. All the parameters defined above are split into parameters of interest, usually the signal strength μ, and nuisance parameters (NPs).

The probability for observing data histograms n_{cb} for the considered channels and obtaining a set of auxiliary measurements a_p, given ϕ_p, α_p, and γ_b, is defined as

$$P(n_{cb}, a_p|\phi_p, \alpha_p, \gamma_b) = \prod_c \prod_b \text{Pois}(n_{cb}|\nu_{cb}) \cdot G(L_0|\lambda, \Delta_L) \cdot \prod_{p \in \mathbf{S}+\mathbf{\Gamma}} f_p(a_p|\alpha_p), \tag{5.15}$$

where the expected number of events ν_{cb} in some bin b of a channel c can be written as

$$\nu_{cb}(\phi_p, \alpha_p, \gamma_b) = \lambda\gamma_{cb}\phi_{cs}(\boldsymbol{\alpha})\eta_{cs}(\boldsymbol{\alpha})\sigma_{csb}(\boldsymbol{\alpha}). \tag{5.16}$$

Here, $G(L_0|\lambda, \Delta_L)$ represents Gaussian constraint term with the luminosity parameter[19] λ and the nominal value L_0. The product of unconstrained nor-

[18] It is also possible to generalise the model by including multiple signal samples; however, this is not done for the results presented in this thesis.

[19] The luminosity parameter is correlated between all simulated samples in all channels, and thus indices on λ are omitted. Similarly, the statistical uncertainty in bin b is considered for the sum of simulated samples, and thus the index s is omitted for γ_{cb}.

malisation factors for a sample s in a channel c is defined as

$$\phi_{cs} = \prod_{p \in \mathbf{N}} \phi_p. \tag{5.17}$$

This includes the signal strength μ. Several types of constraints f_p are used when constructing the last product term of Equation (5.15), as discussed in the following.

The Gaussian constraint is a good approximation of the auxiliary measurement a_p when the likelihood of α_p given a_p has a Gaussian shape. The width of the Gaussian constraint in this case represents the size of the uncertainty. This constraint is typically used to model the majority of NPs corresponding to the experimental uncertainties. In many cases, the uncertainties in theoretical predictions, such as the cross-section uncertainties, are modelled using the log-normal distribution [198], which is a recommended method in cases where the error of a process involves many small multiplicative errors and when the normalisation parameters are required to remain positive. The NPs that are based on counting events in a control region, as well as those accounting for bin-by-bin statistical uncertainties, are modelled using Poisson (Gamma) constraints.

Monte Carlo statistical uncertainty

The model above does not consider the statistical uncertainty in simulation. As discussed before, simulating a large number of events can be computationally extensive, and thus the simulated samples used in the analysis have non-negligible statistical uncertainties. If such MC statistical uncertainties were to be considered for each sample in each bin, the model would include too many NPs. Hence, only the total MC statistical uncertainty per bin is considered, contributing one NP per bin.

Maximum likelihood estimator

As long as the likelihood function is a differentiable function of the parameters (e.g. μ) on which it depends, a maximum likelihood (ML) estimator of those parameters ($\hat{\mu}$) is obtained by finding the parameter values that maximise the likelihood function. In the asymptotic limit, i.e. if the number of measurements goes to infinity, the ML estimator is consistent ($\hat{\mu} \to \mu_{\text{true}}$) and unbiased ($E[\hat{\mu}] - \mu_{\text{true}} \to 0$), meaning that the ML is the best estimator (of μ) since no other estimator can be more efficient, i.e. have a smaller variance [194].

5.6.2 Test statistic

To test some value of the parameter of interest – the signal strength μ, the profile likelihood ratio [199] is used. As previously explained, for a set of obtained data histograms and auxiliary measurements a_p, the probability given

by Equation (5.15) becomes the likelihood function $L(\mu, \boldsymbol{\theta})$, where $\boldsymbol{\theta}$ includes all NPs but not the parameter of interest. The profile likelihood ratio is used to test a particular value of μ and it is defined as

$$\lambda(\mu) = \frac{L(\mu, \hat{\hat{\boldsymbol{\theta}}})}{L(\hat{\mu}, \hat{\boldsymbol{\theta}})}, \tag{5.18}$$

where $\hat{\hat{\boldsymbol{\theta}}}$ is the conditional ML estimator of $\boldsymbol{\theta}$ that depends on μ. The denominator, $L(\hat{\mu}, \hat{\boldsymbol{\theta}})$, is the unconditional ML with $\hat{\mu}$ and $\hat{\boldsymbol{\theta}}$ being the unconditional ML estimators of μ and $\boldsymbol{\theta}$. Given that the unconditional ML estimate must be larger than the conditional ML estimate, it follows $0 \leq \lambda(\mu) \leq 1$. Values close to 1 indicate good agreement between the data and the assumed μ.

For calculating the p-value, which is defined as a probability of measuring data of equal or greater incompatibility with the predictions of the tested hypothesis, it is convenient to use the test statistic

$$t_\mu = -2\ln\lambda(\mu). \tag{5.19}$$

The p-value is then defined as

$$p_\mu = \int_{t_{\mu,\text{obs}}}^{\infty} f(t_\mu|\mu)dt_\mu, \tag{5.20}$$

where $t_{\mu,\text{obs}}$ is the observed value of t_μ and $f(t_\mu|\mu)$ is the pdf of t_μ, both for some assumed value of μ.

In searches for new signals, one often defines the *null hypothesis*, H_0, as the background-only hypothesis, which assumes no signal being present in the observed data, i.e. $\mu = 0$. This is tested against the *alternative hypothesis*, H_1, where it is assumed that the observed data includes the signal process. The tested hypothesis is accepted or rejected with some confidence level (CL) based on the obtained p-value. Different definitions of the p-value are used depending on the aim of the statistical analysis, which is discussed in the following.

Discovery of a positive signal

For the discovery of a positive signal, a test statistic q_0 corresponding to the background-only hypothesis

$$q_0 = \begin{cases} -2\ln\lambda(0), & \hat{\mu} \geq 0 \\ 0, & \hat{\mu} < 0 \end{cases} \tag{5.21}$$

is used to calculate the p-value

$$p_0 = \int_{q_{0,\text{obs}}}^{\infty} f(q_0|0)dq_0, \tag{5.22}$$

which quantifies the level of disagreement between data and the background-only hypothesis. Here $f(q_0|0)$ is the pdf of the statistic q_0 assuming $\mu = 0$. The values $\hat{\mu} < 0$ correspond to a deficit of the observed events with respect to the prediction, and thus $q_0 = 0$ is set in this region if only positive signals are expected.

The p-value can be converted to a significance Z for a Gaussian distributed variable. If the observed value of this variable is found at Z standard deviations above its mean expectation value, then the integral of the upper tail of the Gaussian is equal to p, i.e.

$$Z = \Phi^{-1}(1-p), \tag{5.23}$$

where Φ^{-1} is the quantile, or the inverse of the cumulative distribution, of the standard Gaussian. The convention in the particle physics community is that a discovery can be claimed if the p-value p_0 is smaller than 2.87×10^{-7}, i.e. if the background-only hypotheis is rejected with a significance of $Z = 5$ or greater [199].

Upper limits

The test statistic used for establishing upper limits on the signal strength is defined as

$$q_\mu = \begin{cases} -2\ln\lambda(\mu), & \hat{\mu} \leq \mu \\ 0, & \hat{\mu} > \mu. \end{cases} \tag{5.24}$$

In this case $q_\mu = 0$ is set if the data fluctuate upward with respect to the signal-plus-background hypothesis for a given μ, and thus these cases are excluded from the rejection region of the test. The p-value representing the level of agreement between the data and hypothesised μ is defined as

$$p_\mu = \int_{q_{\mu,\text{obs}}}^{\infty} f(q_\mu|\mu) dq_\mu. \tag{5.25}$$

The 95% CL upper limit on μ can be obtained as the largest value of μ for which the p-value is not less than 0.05. However, a more conservative approach, the CL_s method [200] discussed below, is used to obtain the upper-limits results presented in this thesis. For excluding some signal hypothesis, usually a threshold of $p = 0.05$ ($Z = 1.64$) is adopted [199].

Median significance and Asimov dataset

While designing and optimising an analysis, it is useful to consider the expected (i.e. mean or median) significance for some hypothesis of interest. For this purpose, an artificial dataset, referred to as the *Asimov dataset*, is usually constructed. In practise, the Asimov dataset is constructed as the sum of the predicted event yields in all background processes and some signal process(es) with an assumed signal strength μ'. This dataset is used to evaluate the ML

estimators for all parameters in the likelihood. The obtained median significance is used as a test of how much the results vary as a result of statistical fluctuations in data. In Chapter 7, the concept of the Asimov dataset is used to obtain several predictions for the HL-LHC dataset. In this way, the expected significance for observing non-resonant Higgs boson pair production is obtained for different assumptions regarding the true nature of the Higgs boson couplings.

The CL_s method

If there is a downward fluctuation of background events, the p-value calculated using the test statistic given by Equation (5.24) can lead to strong exclusion limits even for signals to which there is no expected sensitivity. For that reason, the CL_s method [200] is used to normalise the confidence level observed for the signal-plus-background hypothesis, CL_{s+b}, to the confidence level observed for the background-only hypothesis, CL_b,

$$\mathrm{CL}_s = \frac{\mathrm{CL}_{s+b}}{\mathrm{CL}_b} = \frac{\int_{q_{\mu,\mathrm{obs}}}^{\infty} f(q_\mu|\mu)dq_\mu}{\int_{q_{\mu,\mathrm{obs}}}^{\infty} f(q_\mu|0)dq_\mu}. \tag{5.26}$$

This approach allows to obtain sensible exclusion limits on the signal strength, even when the experiment cannot distinguish between signal and background-only hypotheses, in which case CL_b becomes small and penalises the value obtained for CL_{s+b} (p_μ). In summary, instead of finding the upper limit on the signal strength as the largest value of μ for which p_μ is not less than 0.05, the upper limit on μ in the CL_s method is defined as the largest value of μ for which CL_s is not less than 0.05.

5.7 Results

The results of searches for resonant and non-resonant pair production of Higgs bosons using 36.1 fb^{-1} of 13 TeV data are presented in this section. The results are obtained by performing a simultaneous profile likelihood fit in the three SRs and the $Z \to \mu\mu$+hf CR, separately for each signal hypothesis. In each SR and for each signal hypothesis, the respective BDT score is used as a final discriminant for fitting and limit setting, as explained in Section 5.4. By construction, the BDT score in each SR has a better separation power between the signal and background processes than any of the BDT input variables[20]. The $Z \to \mu\mu$+hf CR is used as a 1-bin region in the fit. The procedure dis-

[20] An alternative approach, where m_{HH} is removed from the BDT input variables and then used for fitting and limit setting after cutting on the BDT score, was tested, but it was found to degrade the expected limits.

cussed in Section 5.6 is used to construct the combined likelihood and obtain upper limits on the signal strength[21].

Re-binning the BDT score distributions
The final-discriminant histograms are produced with 1000 bins, and the binning optimisation is performed before conducting the fit by re-binning each histogram from its last bin (high BDT score) to its first bin (low BDT score), based on the following criteria: the pre-fit relative background statistical uncertainty in each bin b of the BDT output score, $\sigma(\nu_b^{\text{bkg}})/\nu_b^{\text{bkg}}$, is required to be less than x times the fraction of signal in that bin with respect to the amount of signal in the SR, $\nu_b^{\text{sig}}/\nu_{\text{SR}}^{\text{sig}}$, plus 1% offset, i.e.

$$\frac{\sigma(\nu_b^{\text{bkg}})}{\nu_b^{\text{bkg}}} < x \times \frac{\nu_b^{\text{sig}}}{\nu_{\text{SR}}^{\text{sig}}} + 0.01, \tag{5.27}$$

where x is set to 0.5 (0.4; 0.2) for the re-binning performed in the $\tau_{\text{had}}\tau_{\text{had}}$ ($\tau_{\text{lep}}\tau_{\text{had}}$ LTT and non-resonant SLT; resonant SLT) case. Additionally, the number of expected background events in each bin is required to be greater than 5 (10) for the $\tau_{\text{had}}\tau_{\text{had}}$ ($\tau_{\text{lep}}\tau_{\text{had}}$) channel. Both these choices are based on maximising the expected limits, but also ensuring the stability of the fit. An example of a histogram binned following this procedure is shown in Figure 5.13. In some cases very narrow bins are obtained in the middle part of the BDT score range. For that reason, in order to have a better visualisation, the BDT score histograms in the following are always transformed to histograms with equidistant bins, but keeping the same bin content. Although this changes the shape of the distribution, it does not change any of the results.

5.7.1 SM pair production of Higgs bosons

The post-fit expected number of background events in the search for the SM pair production of Higgs bosons, for the background-only hypothesis, is found to be statistically compatible with the observed number of events across all bins in all fit regions. The post-fit signal and background yields in each of the SRs, obtained after performing a combined fit in the $\tau_{\text{lep}}\tau_{\text{had}}$ and $\tau_{\text{had}}\tau_{\text{had}}$ SRs, with the $Z \to \mu\mu$+hf CR included, are shown in Table 5.13, for the full SR selection and for only the two last bins of the respective BDT score histogram. The post-fit distributions of the BDT score are shown in Figure 5.18.

[21]The results of searches for resonant HH production are presented as limits on the resonance production cross-section times the resonance branching ratio to HH, times the HH branching ratio to the $b\bar{b}\tau^+\tau^-$ final state. The results presented in this form are easier to interpret because one does not need to know the initially-assumed cross-sections and branching ratios. For SM HH production, the results are presented as limits on the signal strength, i.e. limits on $\sigma_{HH}/\sigma_{HH}^{\text{SM}}$, and thus, in this case, the uncertainty on the signal cross-section is included in the fit (a reminder that "SM" here refers to the assumed signal kinematics, but not to the assumed cross-section given that higher normalisation values are probed when setting upper limits).

Table 5.13. *Post-fit expected numbers of signal and background events [15] from the search for the SM pair production of Higgs bosons, determined from a combined $\tau_{\text{lep}}\tau_{\text{had}}+\tau_{\text{had}}\tau_{\text{had}}$ background-only fit, compared to the observed number of data events in each of the three SRs separately. The upper part of the table refers to the full SR selection, while the bottom part of the table refers to the last two bins of the respective BDT score histogram (for the BDT classifiers trained on the SM signal). Due to rounding, the individual background yields do not sum to the total background yield. Additionally, due to large correlations, uncertainties on individual backgrounds can be larger than the total uncertainty.*

Process	$\tau_{\text{lep}}\tau_{\text{had}}$ channel (SLT)	$\tau_{\text{lep}}\tau_{\text{had}}$ channel (LTT)	$\tau_{\text{had}}\tau_{\text{had}}$ channel
	Full signal region		
$t\bar{t}$ with true-τ_{had}	17800 ± 1100	1475 ± 94	360 ± 100
Single top	1130 ± 110	72.9 ± 7.6	39.7 ± 5.9
$t\bar{t}$ with fake-τ_{had}	-	-	160 ± 120
Multijet	-	-	294 ± 57
Jet $\rightarrow$ fake-τ_{had}	9000 ± 1100	475 ± 76	-
$Z \rightarrow \tau\tau + (bb, bc, cc)$	416 ± 97	117 ± 28	291 ± 91
Other	197 ± 32	14.5 ± 2.3	22.9 ± 5.9
SM Higgs ($t\bar{t}H$ and ZH)	38 ± 10	4.1 ± 1.0	8.2 ± 2.1
Total background	28610 ± 180	2159 ± 46	1178 ± 40
Data	28612	2161	1180
SM HH	0.96 ± 0.13	0.219 ± 0.032	0.73 ± 0.14
	Last two bins of the BDT score		
$t\bar{t}$ with true-τ_{had}	18.2 ± 4.2	23.2 ± 1.7	4.5 ± 1.4
Single top	6.4 ± 1.3	3.7 ± 1.2	1.06 ± 0.57
$t\bar{t}$ with fake-τ_{had}	-	-	1.9 ± 1.4
Multijet	-	-	3.89 ± 0.87
Jet $\rightarrow$ fake-τ_{had}	12.0 ± 2.3	6.6 ± 1.5	-
$Z \rightarrow \tau\tau + (bb, bc, cc)$	10.2 ± 2.6	7.7 ± 3.1	12.6 ± 3.6
Other	3.89 ± 0.69	1.51 ± 0.36	1.09 ± 0.32
SM Higgs ($t\bar{t}H$ and ZH)	1.94 ± 0.43	0.58 ± 0.14	1.54 ± 0.41
Total background	52.7 ± 4.5	39.5 ± 3.0	26.7 ± 3.5
Data	45	47	20
SM HH	0.48 ± 0.07	0.16 ± 0.02	0.54 ± 0.10

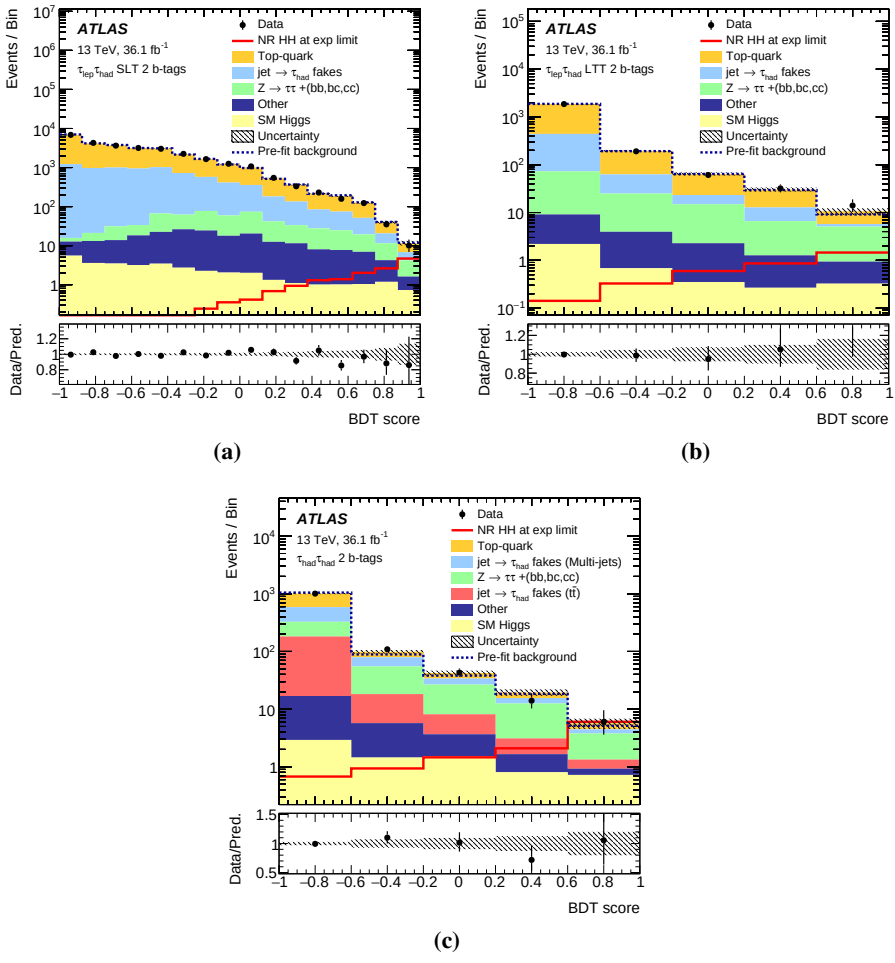

Figure 5.18. Distributions of the BDT score for the SM HH signal (NR HH) in the (**a**) $\tau_{\text{lep}}\tau_{\text{had}}$ SLT, (**b**) $\tau_{\text{lep}}\tau_{\text{had}}$ LTT, and (**c**) $\tau_{\text{had}}\tau_{\text{had}}$ SRs [15]. Distributions are shown after the combined background-only-hypothesis fit to data. The signal is overlaid after being scaled to approximately the expected limit. The hatched band indicates the combined statistical and systematic uncertainty in the background prediction. The ratio of the data to the sum of the backgrounds is shown in the lower panel.

As no significant excess over the expected background is found, the results are used to set 95% CL upper limits on $\sigma_{HH}/\sigma_{HH}^{\text{SM}}$, assuming $\sigma_{HH}^{\text{SM}} = 33.41$ fb and the SM Higgs boson branching ratios as given in Table 1.1. The results corresponding to each of the SRs individually, the combined $\tau_{\text{lep}}\tau_{\text{had}}$-channel results and the combined $\tau_{\text{lep}}\tau_{\text{had}}+\tau_{\text{had}}\tau_{\text{had}}$ results are summarised in Table 5.14. The combined observed (expected) upper limit on $\sigma_{HH}/\sigma_{HH}^{\text{SM}}$ at 95% CL is 12.7 (14.8), representing the most stringent limit on non-resonant HH production cross-section obtained from an individual channel using the

2015 and 2016 LHC data, in both the ATLAS and CMS experiments [16,201], when assuming the SM HH signal kinematics.

Table 5.14. *Upper limits on the signal strength of the SM Higgs boson pair production, $\sigma_{HH}/\sigma_{HH}^{\mathrm{SM}}$, at 95% CL [15], when considering each SR separately, the combination of the $\tau_{\mathrm{lep}}\tau_{\mathrm{had}}$ SRs, and the combination of the $\tau_{\mathrm{lep}}\tau_{\mathrm{had}}$ and $\tau_{\mathrm{had}}\tau_{\mathrm{had}}$ SRs. In all cases, the $Z\to\mu\mu$+hf CR is included. In the $\tau_{\mathrm{had}}\tau_{\mathrm{had}}$-only fit, the normalisation of the $t\bar{t}$ background with true-τ_{had} candidates is not freely floated and the $\tau_{\mathrm{lep}}\tau_{\mathrm{had}}\to\tau_{\mathrm{had}}\tau_{\mathrm{had}}$ extrapolation uncertainties related to the $t\bar{t}$ normalisation are replaced by the uncertainties in $A\times\varepsilon$ for the $t\bar{t}$ events with true-τ_{had} candidates in the $\tau_{\mathrm{had}}\tau_{\mathrm{had}}$ channel (-37% and $+34\%$). The combined observed (expected) limit on $\sigma_{HH}/\sigma_{HH}^{\mathrm{SM}}$, assuming SM Higgs boson branching ratios given in Table 1.1, is 12.7 (14.8). The 1σ and 2σ uncertainties in the expected limits are listed as well.*

Channel	Observed	-2σ	-1σ	Expected	1σ	2σ
$\tau_{\mathrm{lep}}\tau_{\mathrm{had}}$ SLT	21.3	15.7	21.1	29.3	40.8	55
$\tau_{\mathrm{lep}}\tau_{\mathrm{had}}$ LTT	134	50	68	94	131	175
$\tau_{\mathrm{lep}}\tau_{\mathrm{had}}$ combined	23.5	15.2	20.5	28.4	39.5	53
$\tau_{\mathrm{had}}\tau_{\mathrm{had}}$	16.4	9.33	12.5	17.4	24.2	32.4
Combined	12.7	7.93	10.7	14.8	20.6	27.6

The effect of the systematic uncertainties discussed in Section 5.5 is evaluated by checking their impact on the uncertainty in $\mu=\sigma_{HH}/\sigma_{HH}^{\mathrm{SM}}$ when performing a conditional signal-plus-background-hypothesis fit with μ set to the expected 95% CL upper limit of 14.8. The results are summarised in Table 5.15. The effects of individual sources of uncertainty making up the categories listed in the table are grouped in the final fit to determine their correlated combined effect on the signal strength. The statistical uncertainty of the data is the dominant uncertainty in the fit, followed by the modelling of the $t\bar{t}$ background, the reconstruction and identification of the true-τ_{had} candidates, and the statistical uncertainty of the simulated background samples.

5.7.2 Resonant pair production of Higgs bosons

Similar to the previous case, no significant excess over the expected background is found in the searches for resonant pair production of Higgs bosons. The post-fit BDT score distributions in the $\tau_{\mathrm{had}}\tau_{\mathrm{had}}$ SR corresponding to the combined $\tau_{\mathrm{lep}}\tau_{\mathrm{had}}+\tau_{\mathrm{had}}\tau_{\mathrm{had}}$ background-only-hypothesis fit results are shown in Figure 5.19 for the scalar resonance X and G_{KK} with $k/\bar{M}_{\mathrm{pl}}=1$. The corresponding BDT score distributions for the $\tau_{\mathrm{lep}}\tau_{\mathrm{had}}$ SRs can be found in Ref. [15]. The results of the searches for resonant pair production of Higgs bosons are presented as upper limits on the resonance production cross-section times the $X/G_{\mathrm{KK}}\to HH$ and $HH\to b\bar{b}\tau^+\tau^-$ branching ratios as a function of the resonance mass. These results are shown in Figure 5.20.

Table 5.15. *Percentage uncertainties on the simulated SM HH signal strength, $\Delta\mu/\mu = \Delta(\sigma_{HH}/\sigma_{HH}^{\mathrm{SM}})/(\sigma_{HH}/\sigma_{HH}^{\mathrm{SM}})$, obtained from a conditional signal-plus-background-hypothesis fit with μ set to the combined $\tau_{\mathrm{lep}}\tau_{\mathrm{had}}+\tau_{\mathrm{had}}\tau_{\mathrm{had}}$ expected 95% CL upper limit of 14.8.*

Source	Uncertainty [%]
Total	±54
Data statistics	±44
Simulation statistics	±16
Experimental uncertainties	
Integrated luminosity	±2.4
Pileup re-weighting	±1.7
τ_{had} candidates	±16
Fake-τ_{had} estimation	±8.4
b-tagging	±8.3
Jets and E_T^{miss}	±3.3
Electrons and muons	±0.5
Theoretical and modelling uncertainties	
Single top and $t\bar{t}$	±17
Signal	±9.3
Z+hf	±6.8
SM Higgs	±2.9
Other backgrounds	±0.3

The scalar resonance, if interpreted as a CP-even heavy Higgs boson in the hMSSM benchmark scenario with $\tan\beta = 2$, is excluded at 95% CL for the mass range of 305 GeV $< m_X <$ 402 GeV. The spin-2 KK excitations of the graviton, G_{KK}, in the bulk Randall-Sundrum model, for $k/\bar{M}_{\mathrm{pl}} = 1$ ($k/\bar{M}_{\mathrm{pl}} = 2$) are excluded for 325 GeV $< m_{G_{\mathrm{KK}}} <$ 885 GeV (the entire mass range of this search, 260 GeV $< m_{G_{\mathrm{KK}}} <$ 1000 GeV).

5.8 Combined ATLAS results

A statistical combination of searches for pair production of Higgs bosons using up to 36.1 fb^{-1} of 13 TeV data recorded by the ATLAS experiment was performed. The combination includes analyses searching for pair production of Higgs bosons in the: $b\bar{b}b\bar{b}$, $b\bar{b}W^+W^-$, $b\bar{b}\tau^+\tau^-$, $W^+W^-W^+W^-$, $b\bar{b}\gamma\gamma$ and $W^+W^-\gamma\gamma$ final states [16].

A simultaneous profile likelihood fit to the data is performed across all the channels. All regions used in the fit are orthogonal by construction, or found to have negligible overlap. The experimental uncertainties are correlated across

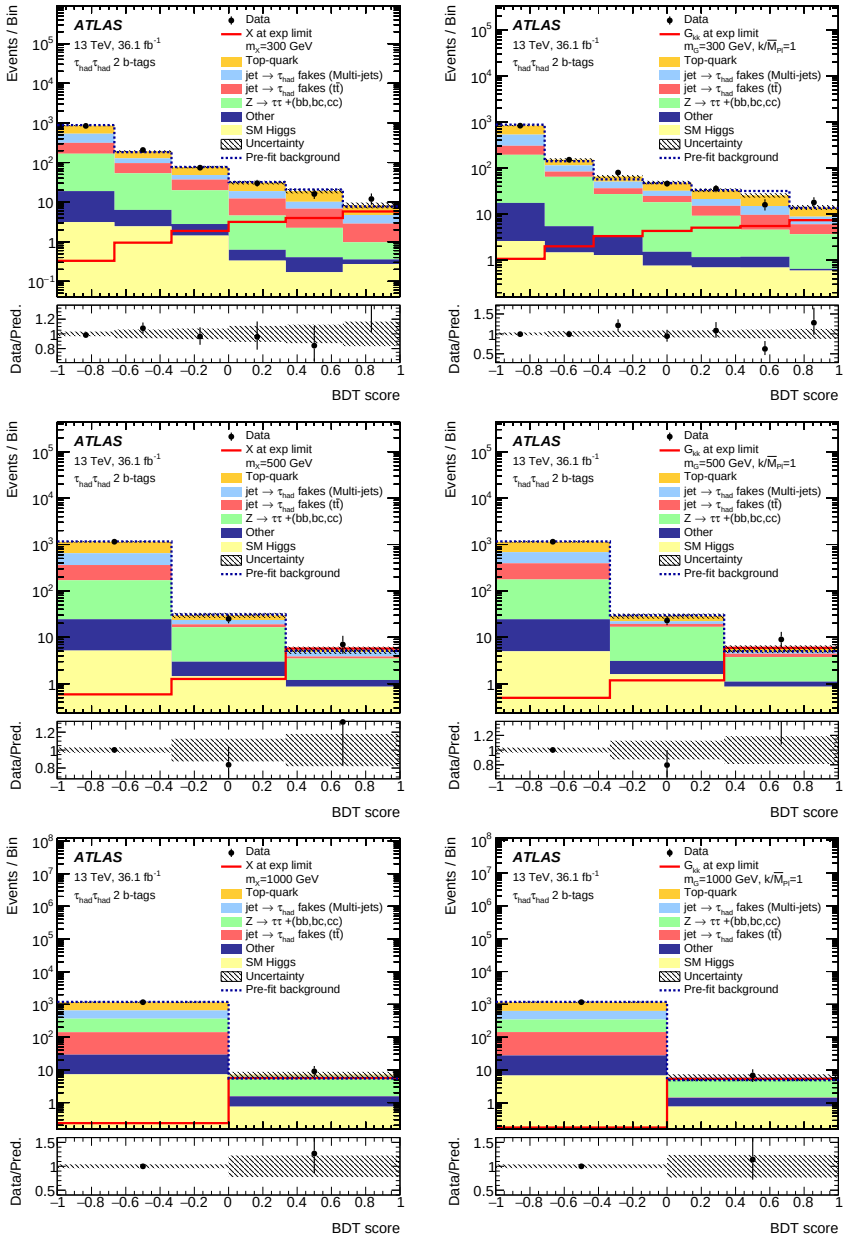

Figure 5.19. Distributions of the BDT score [15] for a narrow-width scalar resonance X (left) and G_{KK} with $k/\bar{M}_{\mathrm{pl}} = 1$ (right), for resonance masses of 300 GeV (top), 500 GeV (middle) and 1000 GeV (bottom) in the $\tau_{\mathrm{had}}\tau_{\mathrm{had}}$ channel. Distributions are shown after the combined background-only-hypothesis fit to data. The signal is overlaid after being scaled to approximately the expected limit. The hatched band indicates the combined statistical and systematic uncertainty in the background prediction. The ratio of the data to the sum of the backgrounds is shown in the lower panel.

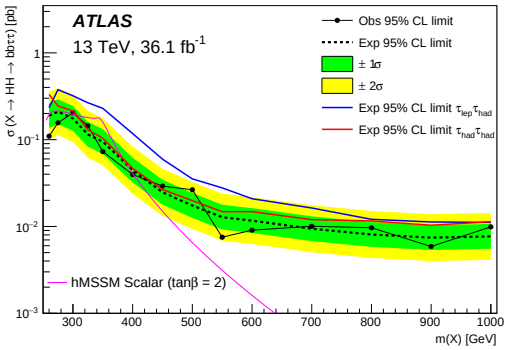

(a)

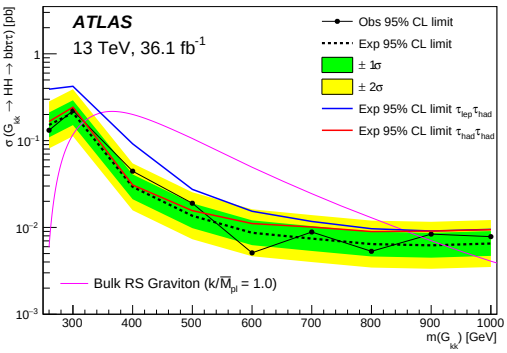

(b)

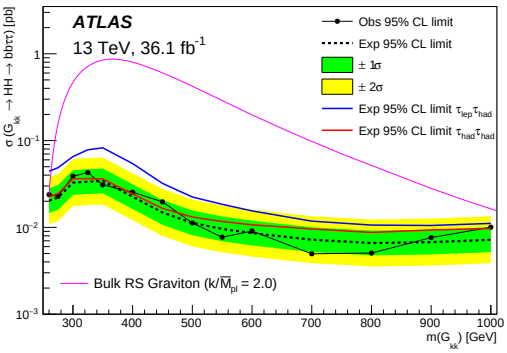

(c)

Figure 5.20. Observed (expected) combined $\tau_{\text{lep}}\tau_{\text{had}}$ and $\tau_{\text{had}}\tau_{\text{had}}$ 95% CL upper limits on the resonance production cross-section times branching ratio to the $HH \to b\bar{b}\tau^+\tau^-$ final state as a function of the resonance mass are shown as solid (dashed) lines for the (**a**) narrow-width scalar resonance X, (**b**) G_{KK} with $k/\bar{M}_{\text{pl}} = 1$, and (**c**) G_{KK} with $k/\bar{M}_{\text{pl}} = 2$ [15]. The expected limits at 95% CL in the $\tau_{\text{had}}\tau_{\text{had}}$ and $\tau_{\text{lep}}\tau_{\text{had}}$ channels are shown separately. The predicted theory cross-section times branching ratio to the $HH \to b\bar{b}\tau^+\tau^-$ final state is overlaid.

all channels, as well as the uncertainties on the signal $A \times \varepsilon$, while the uncertainties on the signal cross-section are removed from consideration. The theoretical and modelling uncertainties in the background predictions in the different channels are left uncorrelated.

The combination of searches for non-resonant HH production, assuming the SM signal kinematics, is shown in Figure 5.21. The observed (expected) combined upper limit on $\sigma_{HH}/\sigma_{HH}^{\mathrm{SM}}$ is 6.9 (10) at 95% CL. The three channels with the highest sensitivity, $b\bar{b}\tau^+\tau^-$, $b\bar{b}b\bar{b}$ and $b\bar{b}\gamma\gamma$, report a deficit of data with respect to the background-only prediction, and thus the observed combined limit is more stringent than the expected one; however, the difference is within the 2σ uncertainty band around to the expected limit.

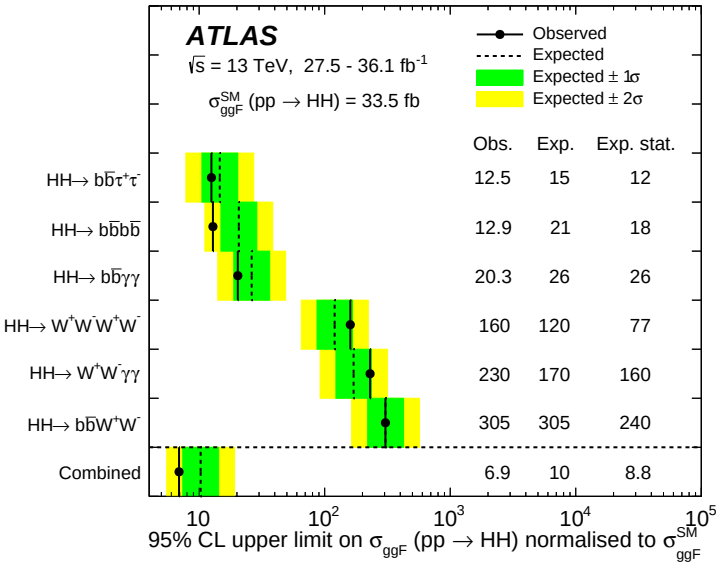

Figure 5.21. Upper limits at 95% CL on $\sigma_{HH}/\sigma_{HH}^{\mathrm{SM}}$ from the $b\bar{b}\tau^+\tau^-$, $b\bar{b}b\bar{b}$, $b\bar{b}\gamma\gamma$, $W^+W^-W^+W^-$, $W^+W^-\gamma\gamma$ and $b\bar{b}W^+W^-$ analyses and their statistical combination [16]. The column "Obs" lists the observed limits, "Exp" the expected limits with all statistical and systematic uncertainties included, and "Exp. stat." the expected limits obtained when considering only statistical uncertainties in the data.

The combination of searches for the resonant HH production is shown in Figure 5.22. The $b\bar{b}\tau^+\tau^-$ analysis contributes significantly to the combined sensitivity at lower resonance masses, while the $b\bar{b}b\bar{b}$ analysis yields the highest sensitivity at higher resonance masses. In the case of $k/\bar{M}_{\mathrm{pl}} = 1$ ($k/\bar{M}_{\mathrm{pl}} = 2$), the bulk RS model is excluded at 95% CL in the graviton mass range from 310 GeV to 1380 GeV (260 GeV, where the scan starts, to 1760 GeV).

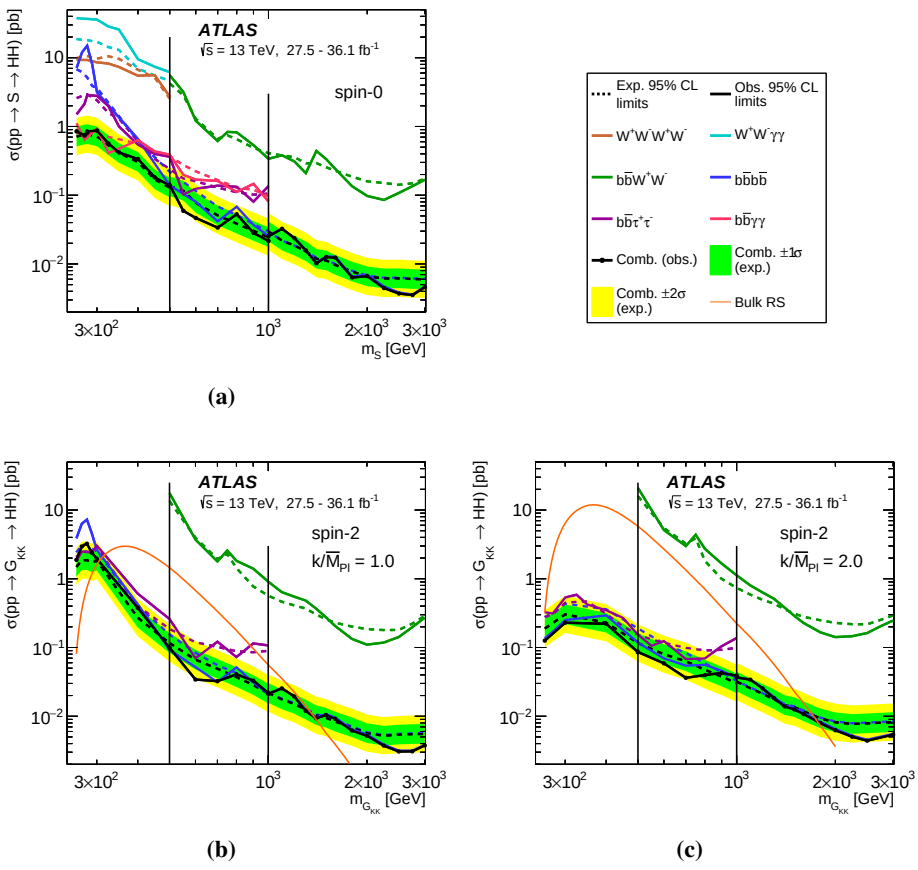

Figure 5.22. Observed (expected) combined 95% CL upper limits on the resonance production cross-section times branching ratio to a pair of Higgs bosons as a function of the resonance mass are shown as solid (dashed) lines for the (**a**) narrow-width scalar resonance X, (**b**) G_{KK} with $k/\bar{M}_{\mathrm{pl}} = 1$, and (**c**) G_{KK} with $k/\bar{M}_{\mathrm{pl}} = 2$ [16]. The observed (expected) limits corresponding to individual channels are shown as solid (dashed) lines of different colours, while the vertical black lines in each panel indicate mass intervals where different final states are combined. The combination of searches for $G_{\mathrm{KK}} \to HH$ include only the results from the $b\bar{b}b\bar{b}$, $b\bar{b}W^+W^-$ and $b\bar{b}\tau^+\tau^-$ analyses.

6. Constraints on the trilinear Higgs boson self-coupling strength

The analysis strategy presented in Chapter 5 is used to set experimental constraints on the anomalous trilinear Higgs boson self-coupling, λ_{HHH}, for which the results are published in Ref. [16]. Only the $\tau_{\text{had}}\tau_{\text{had}}$ channel and the SLT category of the $\tau_{\text{lep}}\tau_{\text{had}}$ channel are considered, while the LTT category is not included[1]. As discussed in Section 2.2, the kinematics of non-resonant ggF pair production of Higgs bosons are determined by the ratio of κ_λ/κ_t in the framework in which deviations from $\lambda_{HHH}^{\text{SM}}$ and y_{ttH}^{SM} are allowed, while all other couplings correspond to the SM predictions. Thus, simultaneous variations of κ_λ and κ_t would affect only the predicted production cross-section, i.e. the interpretation of the results, while they would not yield new signal shapes. For that reason, $\kappa_t = 1$ is assumed, or more precisely, all couplings other than λ_{HHH} are assumed to have SM values. The procedure used to obtain the signal predictions for a fine grid of κ_λ values, the strategy used for the signal extraction and limit setting, and the corresponding results are presented in the following.

6.1 Linear combination and κ_λ re-weighting

To probe variations in κ_λ, four signal samples are generated at LO in QCD, corresponding to $\kappa_\lambda = \{0, 1, 2, 20\}$, using the configuration for which the details are specified in Table 5.2. As outlined in Section 2.2, three arbitrary samples corresponding to different κ_λ values can be used to obtain a signal prediction for any κ_λ value. This procedure is referred to as the *linear combination* of the signal samples with varied κ_λ in this thesis.

In order to validate the method, samples corresponding to $\kappa_\lambda = \{0, 1, 20\}$ are linearly combined before applying any event selection, based on Equation (2.15), to obtain the signal prediction for $\kappa_\lambda = 2$. This is then compared to the generated $\kappa_\lambda = 2$ sample. The prediction obtained using the linear combination method and the generated sample are found to be compatible within statistical uncertainties for all kinematic variables of interest. Additionally, the $\kappa_\lambda = \{0, 1, 2\}$ samples are linearly combined, as defined by Equation (2.14), to obtain the signal prediction for $\kappa_\lambda = 20$, which is then found to be in good agreement with the generated $\kappa_\lambda = 20$ sample. Comparisons, i.e. closure tests of the linear combination method, are shown in Figure 6.1 for m_{HH}, the Higgs boson p_T and the $\tau_{\text{had-vis}}$ p_T. Other distributions show good agreement as well.

[1] This is due to technical reasons and time constraints.

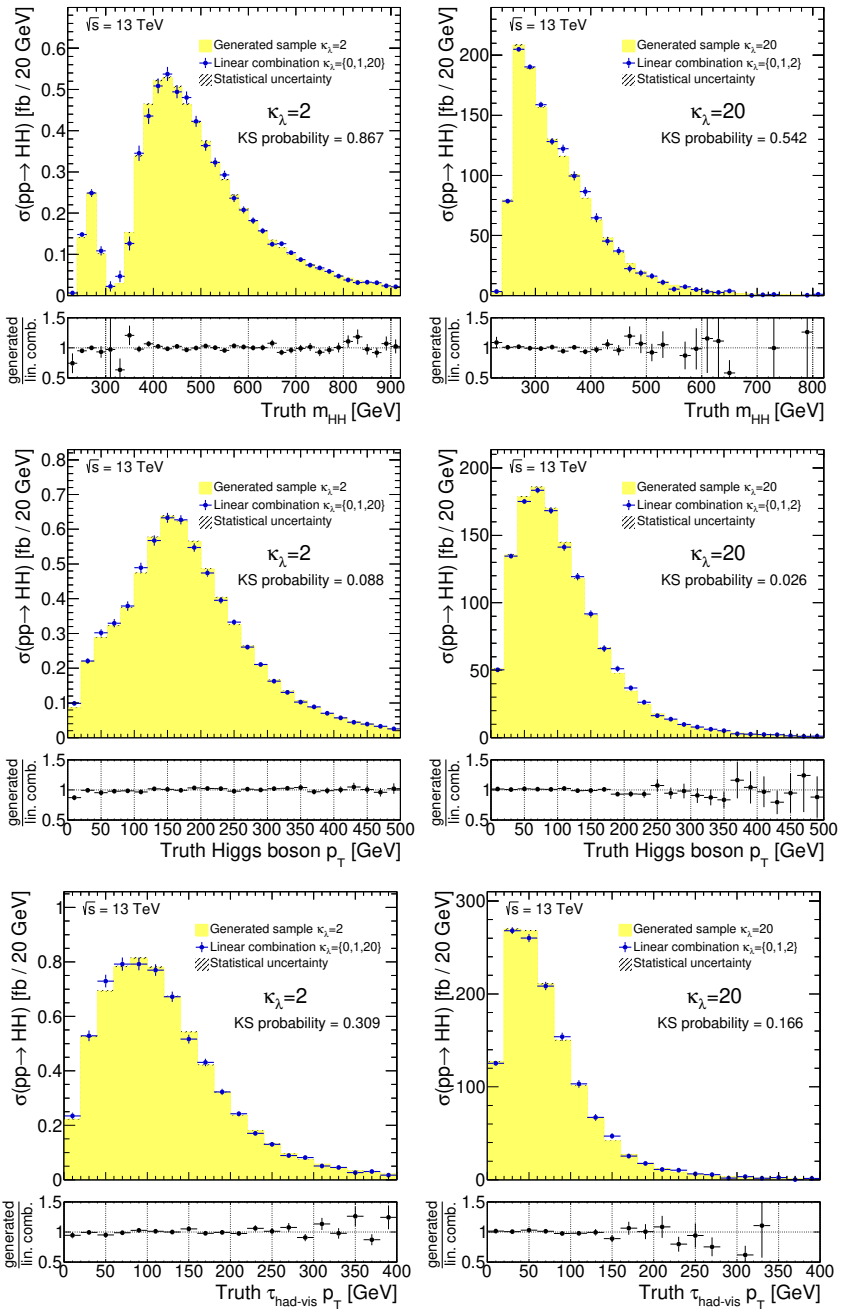

Figure 6.1. Comparison of truth-level distributions of m_{HH}, Higgs boson p_T and $\tau_{\text{had-vis}}$ p_T between the generated sample (yellow area) and the signal prediction obtained by using the linear combination method (blue markers) are shown for the $\kappa_\lambda = 2$ ($\kappa_\lambda = 20$) hypothesis on the left-hand (right-hand) side. The Kolmogorov-Smirnov test is used to obtain the KS probability that the two samples come from the same underlying probability distribution, i.e. that the two samples are compatible.

The four κ_λ values for which the signal samples are simulated were chosen for practical reasons. The $\kappa_\lambda = 0$ ($\kappa_\lambda = 1$) sample corresponds to a scenario in which the Higgs boson does not couple to itself (the Higgs boson couples to itself as predicted in the SM), and thus it is a useful benchmark. The $\kappa_\lambda = 20$ sample corresponds to a scenario in which the non-resonant HH production is dominated by the triangle diagram, and thus, in contrast to $\kappa_\lambda = \{0,1\}$ samples, it consists of events that populate the low-m_{HH} region. In this way, all parts of the m_{HH} spectrum are sufficiently populated, which lowers the statistical uncertainty on the obtained signal predictions when performing the linear combination. The $\kappa_\lambda = 2$ sample corresponds to a strong interference between the box and triangle diagrams, hence it is useful in validations of the linear combination method.

The $\kappa_\lambda = \{0,1,20\}$ basis is chosen as it is less prone to statistical fluctuations due to a higher number of events at low m_{HH}, as already explained. The second basis, $\kappa_\lambda = \{0,1,2\}$, is only used to obtain the signal prediction for $\kappa_\lambda = 2$ in order to use the generated sample itself and for $\kappa_\lambda = 3$ in order to obtain smoother kinematic distributions in a region with significant interference.

The linear combination method requires the input samples to be correctly normalised, i.e. the cross-section needs to be taken into account. Given that only the LO cross-section calculations were available for processes with $\kappa_\lambda \neq 1$ when these studies were performed, the input samples are normalised to the cross-section values given in Table 6.1.

Table 6.1. *Cross-sections for non-resonant pair production of Higgs bosons with* $\kappa_\lambda = \{0,1,2,20\}$ *calculated at LO [37].*

κ_λ	0	1	2	20
Cross-section [fb]	30.56	14.41	6.76	1323

From this table, it can be seen that the difference between the cross-section that corresponds to the $\kappa_\lambda = 1$ hypothesis and the cross-section given by Equation (5.1) (i.e. the SM HH production cross-section calculated at NNLO in QCD) is more than a factor of 2. For this reason, a scaling of the LO cross-section for varied κ_λ is introduced, as will be discussed later. The signal predictions obtained from the linear combination method are by construction normalised to the LO cross-sections shown in Figure 6.2 given that the cross-section depends quadratically on κ_λ for a fixed κ_t, as indicated by Equation (2.11). The exact dependency is obtained by fitting a second degree polynomial to the cross-section values given in Table 6.1.

The κ_λ re-weighting

To avoid having to fully simulate signal samples with a sufficient number of events, a κ_λ *re-weighting* procedure was developed. The signal predictions

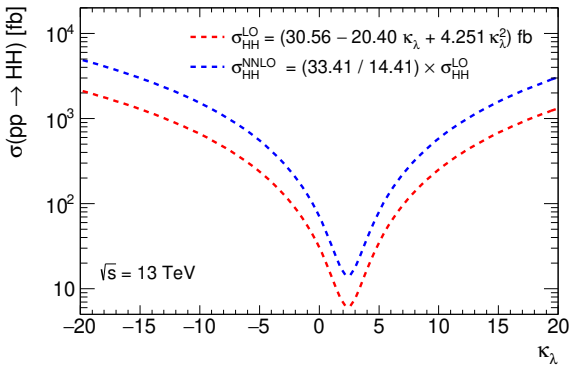

Figure 6.2. Cross-sections for the non-resonant *ggF HH* production at LO in QCD, σ^{LO}_{HH}, as a function of κ_λ (red line), obtained by fitting a second degree polynomial to the cross-section values given in Table 6.1. An approximation of the NNLO non-resonant *HH* production cross-section as a function of κ_λ (blue line) is obtained by scaling σ^{LO}_{HH} by the ratio of the NNLO to LO cross-section for $\kappa_\lambda = 1$ ($\sigma^{\text{SM, NNLO}}_{HH}/\sigma^{\text{SM, LO}}_{HH} = 33.41/14.41$), as will be explained below.

for various κ_λ hypotheses, obtained at truth-level using the linear combination method, are used to derive event weights for re-weighting the fully simulated signal sample corresponding to the SM hypothesis, $\kappa_\lambda = 1$, to any other κ_λ value ($\kappa_\lambda = 1 \rightarrow \kappa_\lambda = x$).

The m_{HH} variable is found to have the largest shape variations[2] with respect to changes in κ_λ. For that reason, a set of weights are derived as a function of m_{HH} as

$$w_{\text{bin } i}(\kappa_\lambda = 1 \rightarrow \kappa_\lambda = x) = \frac{m^{\text{LO}}_{HH,\text{bin } i}(\kappa_\lambda = x)}{m^{\text{LO}}_{HH,\text{bin } i}(\kappa_\lambda = 1)}, \tag{6.1}$$

where bins with a width of 10 GeV are used. A subset of m_{HH} distributions obtained using the linear combination method are shown in Figure 6.3. The weights derived based on Equation (6.1), using these distributions, are shown in Figure 6.4. These weights are then applied to the fully simulated signal sample corresponding to the SM pair production of Higgs bosons described in Section 5.1 (used to obtain the results presented in Chapter 5). As already explained, this sample is simulated at NLO using the FTApprox method, after which it is re-weighted to account for the finite top-quark mass effect in the virtual-loop corrections.

In the following, two assumptions are made: (1) that the higher-order QCD corrections on the differential cross-section as a function of m_{HH} are independent of κ_λ; and (2) that the finite top-quark mass corrections from Refs. [45, 161] are valid for all κ_λ. Based on the assumption (1), the LO cross-section

[2] Another variable that exhibits similar variations is the transverse momentum of the Higgs boson.

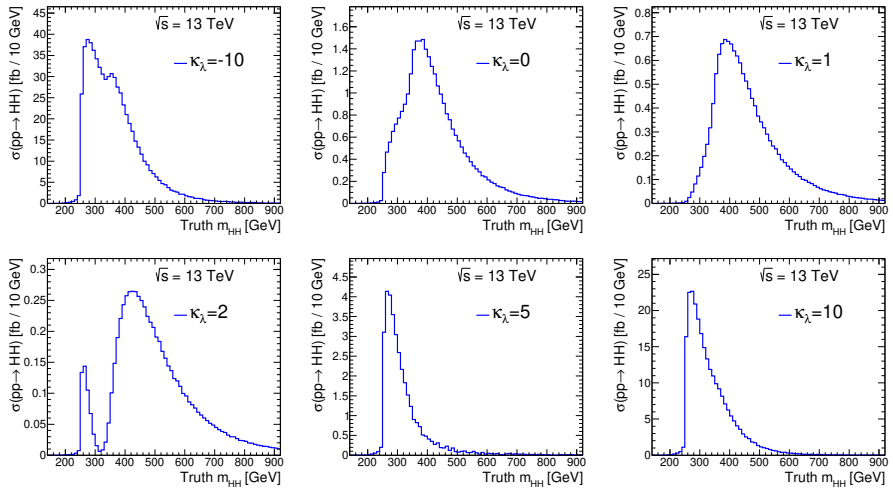

Figure 6.3. Results of the linear combination: Distributions of m_{HH} for $\kappa_\lambda = \{-10, 0, 1, 2, 5, 10\}$. The overall normalisation of the distributions corresponds to the cross-section calculated at LO in QCD that is shown in Figure 6.2.

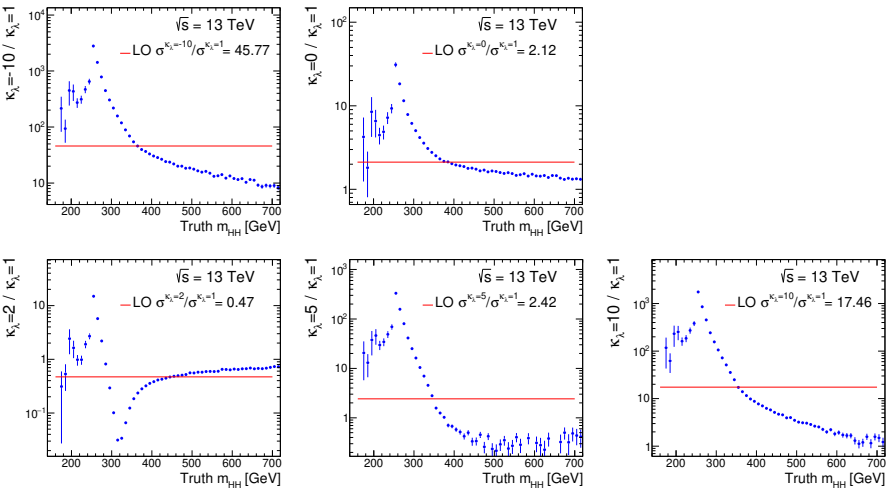

Figure 6.4. Binned ratios of the m_{HH} distributions for $\kappa_\lambda = \{-10, 0, 2, 5, 10\}$ to $\kappa_\lambda = 1$, at LO, derived based on Equation (6.1). The ratios depict differences in shape and normalisation, where the ratio of cross-sections calculated at LO is indicated by the red horizontal line.

prediction shown in Figure 6.2 (red) is scaled by the ratio of the NNLO to LO cross-sections for $\kappa_\lambda = 1$, $\sigma_{HH}^{\text{SM, NNLO}} / \sigma_{HH}^{\text{SM, LO}} = 33.41/14.41$ (blue), given that only the LO cross-section calculations for varied κ_λ were available at the time the studies presented in this chapter were performed. The obtained scaled theory prediction is used for the interpretation of the final results. To

validate the assumption (1), the comparison of truth-level m_{HH} distributions corresponding to the NLO and LO $\kappa_\lambda = 1$ samples is shown in Figure 6.5. The ratio of the two distributions is found to be approximately flat.

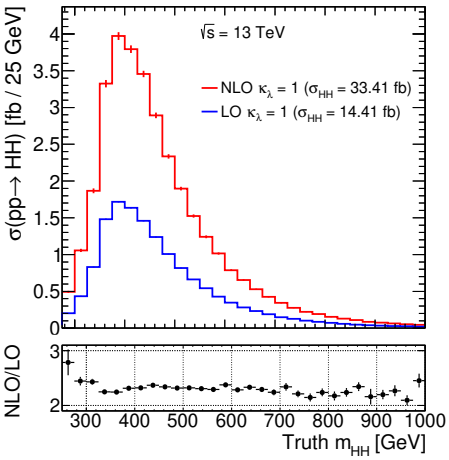

Figure 6.5. Comparison of truth-level m_{HH} distributions for the NLO (FTApprox) sample before the finite top-quark mass correction (red) and LO $\kappa_\lambda = 1$ sample (blue).

6.2 Analysis strategy

Additional closure studies are performed using the detector-level information[3], after the SR selection defined in Tables 5.5 and 5.6 is performed, and potential systematic uncertainties are evaluated. The κ_λ re-weighting is performed using the events that pass the SR selection, and it is confirmed that all kinematic distributions of interest are correctly reproduced by comparing the re-weighted sample to an independent fully simulated LO $\kappa_\lambda \neq 1$ signal sample that is run through the full analysis chain.

6.2.1 Acceptance × efficiency

To ensure that the signal acceptance × efficiency ($A \times \varepsilon$) as a function of κ_λ is correctly reproduced, $A \times \varepsilon$ is determined in bins of truth-level m_{HH} and found to be the same for different κ_λ hypotheses[4], as shown in Figure 6.6a. Given

[3]The LO non-resonant HH signal samples with a limited but sufficient number of events are fully simulated for κ_λ=$\{0, 1, 20\}$ in order to perform these studies.

[4]The $A \times \varepsilon$ as a function of m_{HH} is obtained from simulated signal samples and it is calculated per bin, i.e. the number of events that pass the SR selection in a given bin is divided by the number of events before any selection in that same bin.

that the κ_λ re-weighting is performed as a function of m_{HH}, it reproduces the overall $A \times \varepsilon$ by construction. The overall $A \times \varepsilon$ as a function of κ_λ is shown in Figure 6.6b. The large variations in $A \times \varepsilon$ are a consequence of the strong m_{HH} (Higgs boson p_T) dependence on κ_λ, as shown in Figure 2.1. Consequently, the p_T of the Higgs boson decay products tends to be lower for events with low m_{HH}, and thus these events are more likely to fail the SR selection.

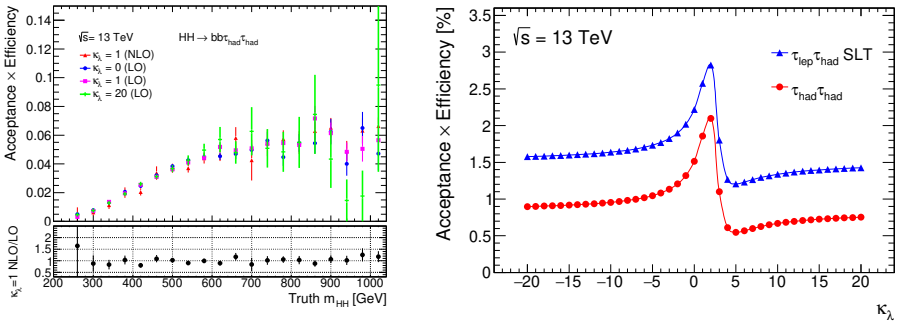

(a) **(b)**

Figure 6.6. (**a**) Acceptance × efficiency as a function of m_{HH} in the $\tau_{\text{had}}\tau_{\text{had}}$-channel SR, shown separately for the NLO (FTApprox) SM signal sample and the LO $\kappa_\lambda = \{0, 1, 20\}$ samples. The ratio of the distributions that correspond to the SM NLO (FTApprox) and LO samples is shown in the bottom panel. (**b**) Overall signal $A \times \varepsilon$ as a function of κ_λ, shown separately for the $\tau_{\text{had}}\tau_{\text{had}}$- and $\tau_{\text{lep}}\tau_{\text{had}}$-channel (only the SLT category) SRs. The $A \times \varepsilon$ changes significantly with κ_λ due to its strong impact on the p_T of the Higgs boson decay products.

6.2.2 BDT strategy

In order to maximise the sensitivity of the analysis, different BDT strategies were tested. In all cases, the input variables listed in Table 5.10 are used to train the BDTs in the $\tau_{\text{had}}\tau_{\text{had}}$ and $\tau_{\text{lep}}\tau_{\text{had}}$ (SLT) SRs. Furthermore, the parameters of the algorithm are kept the same as those specified in Table 5.9. Three BDT strategies are tested:

(1) using the nominal BDT classifier trained on the SM signal sample and applying it to all varied-κ_λ signal predictions;
(2) training a dedicated BDT classifier for each κ_λ hypothesis;
(3) training a BDT on the signal prediction that corresponds to the $\kappa_\lambda = 20$ hypothesis[5] and applying it to all varied-κ_λ signals.

[5]The $\kappa_\lambda = 20$ hypothesis is chosen due to the large contribution of the triangle diagram (populating the low-m_{HH} region), and conversely the small contribution of the box diagram, to the overall non-resonant HH production. By training a BDT classifier on the $\kappa_\lambda = 20$ hypothesis, a higher sensitivity to signals that correspond to softer m_{HH} spectra is reached.

Although Option (2) is found to give optimal performance, the sensitivity gain compared to Option (3) is found to be minimal. Thus, Option (3) is chosen for simplicity and since in that case the shape of the BDT score for the background prediction stays the same across the whole κ_λ range. Option (1) is found to give slightly worse performance than Option (3) for those κ_λ values that yield softer m_{HH} spectra. Regardless of the BDT strategy, the BDT response for different signal hypotheses varies, as indicated in Figure 6.7. Events with lower m_{HH} tend to have lower BDT scores assigned to them since the background contribution is dominant in that region.

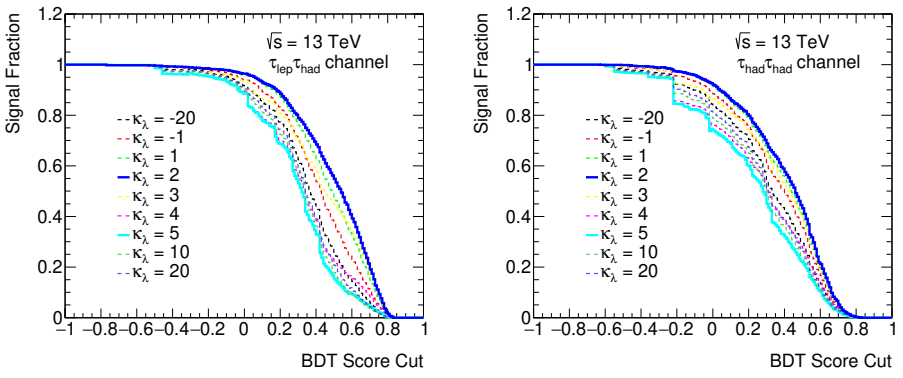

Figure 6.7. Signal fraction, i.e. ratio of the number of expected signal events above a given BDT score to the total number of expected signal events in the SR, as a function of the BDT score cut for the BDT classifier trained on the $\kappa_\lambda = 20$ signal prediction, shown separately for a set of signals with varied κ_λ in the (**a**) $\tau_{\text{lep}}\tau_{\text{had}}$ SLT and (**b**) $\tau_{\text{had}}\tau_{\text{had}}$ SRs.

6.3 Results

A profile likelihood fit is performed separately for each κ_λ signal hypothesis. The fit is performed simultaneously in the two SRs that are considered in this case and the 1-bin $Z \to \mu\mu$+hf CR. The final discriminant used in both SRs is the BDT score distribution. The binning criteria applied to the BDT score, which are defined in Section 5.7, are kept the same. The BDT score distributions corresponding to the classifier trained on the $\kappa_\lambda = 20$ signal, after the combined background-only-hypothesis fit to data, are shown in Figure 6.8.

No significant excess over the expected background is found, and thus upper limits on the cross-section are set. The results are shown in Figure 6.9 as 95% CL upper limits on the ggF non-resonant HH production cross-section times the $b\bar{b}\tau^+\tau^-$ branching ratio as a function of κ_λ. Based on the theory prediction, the observed (expected) combined allowed κ_λ interval is $[-7.4, 15.7]$ ($[-8.9, 16.8]$) at 95% CL. The shape of the limit curve is a consequence of variations in signal $A \times \varepsilon$ and variations in the signal BDT response with κ_λ.

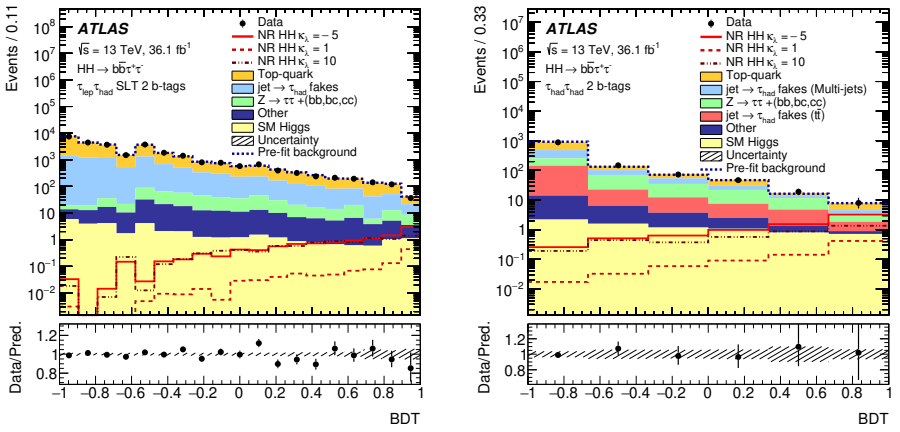

(a) **(b)**

Figure 6.8. Distributions of the BDT score for the BDT classifier trained on the $\kappa_\lambda = 20$ signal hypothesis in (**a**) the $\tau_{\text{lep}}\tau_{\text{had}}$ SLT and (**b**) $\tau_{\text{had}}\tau_{\text{had}}$ SRs [16]. Distributions are shown after the combined background-only-hypothesis fit (including the $Z \to \mu\mu$+hf CR) to data. The signal prediction for $\kappa_\lambda = \{-5, 1, 10\}$ is overlaid after being scaled to approximately the expected limit. The hatched band indicates the combined statistical and systematic uncertainty in the background. The ratio of the data to the sum of the backgrounds is shown in the lower panel.

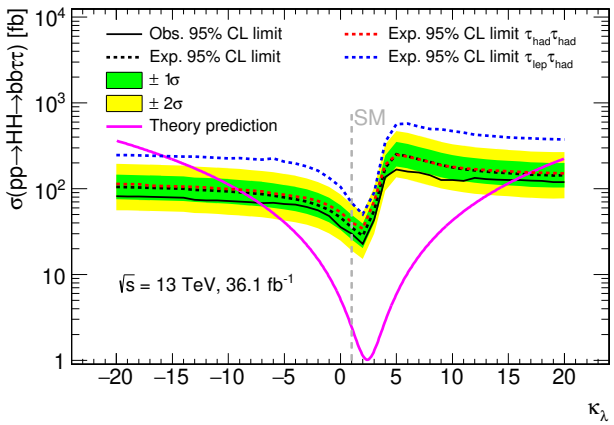

Figure 6.9. Upper limits at 95% CL on the cross-section of the ggF non-resonant HH production times the $b\bar{b}\tau^+\tau^-$ branching ratio as a function of κ_λ. The observed (expected) combined limit is shown as a solid (dashed) black line. The $\pm 1\sigma$ and $\pm 2\sigma$ uncertainty bands are shown for the combined expected limit. In addition, the expected limit for the $\tau_{\text{had}}\tau_{\text{had}}$ ($\tau_{\text{lep}}\tau_{\text{had}}$ SLT) channel is shown as a red (blue) dashed line. The theoretical prediction of the cross-section as a function of κ_λ (an approximation of the NNLO HH production cross-section in Figure 6.2) is also shown.

The fluctuations in the observed limit are a consequence of the binning strategy used. The lower edge of the last (most sensitive) bin varies with κ_λ, and thus a different number of data events in that bin is observed for different κ_λ values.

The Higgs boson branching ratio depends on κ_λ due to NLO electroweak corrections [202], but this dependence is not taken into account. The effect on the allowed κ_λ interval is however expected to be at the order of a few percent. Uncertainties on the theory cross-section prediction are also not considered.

6.4 Combined ATLAS results

A statistical combination of searches for the non-resonant pair production of Higgs bosons with varied κ_λ using up to 36.1 fb^{-1} of $\sqrt{s} = 13$ TeV data recorded by the ATLAS experiment was performed for the $b\bar{b}b\bar{b}$, $b\bar{b}\tau^+\tau^-$, and $b\bar{b}\gamma\gamma$ final-state analyses [16]. The combination strategy follows closely the approach used to obtained the combined ATLAS results presented in Section 5.8.

The signal $A \times \varepsilon$ is shown as a function of κ_λ separately for the $b\bar{b}b\bar{b}$, $b\bar{b}\tau^+\tau^-$, and $b\bar{b}\gamma\gamma$ channels in Figure 6.10. The results of the combined κ_λ scan are shown in Figure 6.11. The observed (expected) combined allowed κ_λ interval is found to be $[-5.0, 12.0]$ ($[-5.8, 12.0]$) at 95% CL.

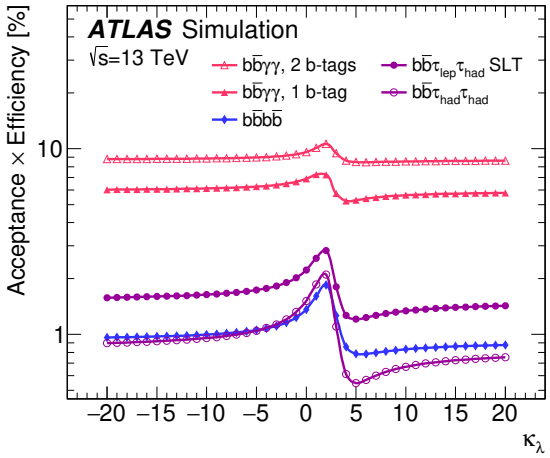

Figure 6.10. Overall signal $A \times \varepsilon$ as a function of κ_λ, shown separately for the $b\bar{b}b\bar{b}$, $b\bar{b}\tau^+\tau^-$ ($\tau_{\text{had}}\tau_{\text{had}}$ and $\tau_{\text{lep}}\tau_{\text{had}}$ SLT SRs), and $b\bar{b}\gamma\gamma$ (1- and 2-b-tag SRs) channels [16].

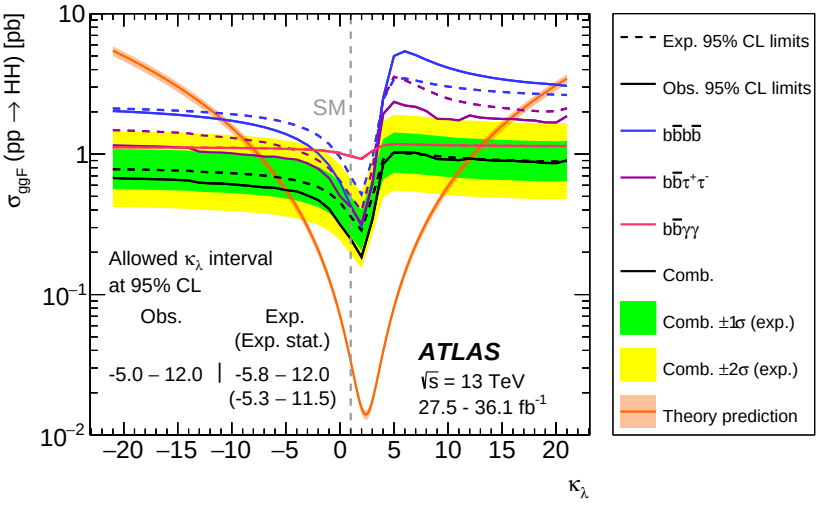

Figure 6.11. Upper limits at 95% CL on the cross-section of the *gg*F non-resonant *HH* production as a function of κ_λ [16]. The observed (expected) limits are shown as solid (dashed) lines for the $b\bar{b}b\bar{b}$, $b\bar{b}\tau^+\tau^-$, and $b\bar{b}\gamma\gamma$ channels, as well as their combination. The $\pm1\sigma$ and $\pm2\sigma$ uncertainty bands are shown for the combined expected limit. The theoretical prediction of the cross-section as a function of κ_λ (an approximation of the NNLO *HH* production cross-section in Figure 6.2) is also shown.

7. Prospects for observing the pair production and self-coupling of the Higgs boson at the HL-LHC

The expected sensitivity to the SM pair production of Higgs bosons at the HL-LHC is estimated by extrapolating the results presented in Chapter 5, which are in this chapter referred to as "the current analysis". The prospects for constraining λ_{HHH} at the HL-LHC are estimated for several assumptions regarding the true nature of the Higgs boson couplings by extrapolating the results presented in Chapter 6. In both cases, the extrapolation is performed while assuming different scenarios regarding the evolution of the systematic uncertainties listed in Section 5.5 towards the HL-LHC era. Given that the sensitivity of the analysis is limited by the trigger requirements, the impact of different trigger designs on the expected sensitivity is also estimated. Finally, the statistical combination of the projections with the results obtained from the $b\bar{b}b\bar{b}$ and $b\bar{b}\gamma\gamma$ analyses is presented, as well as the overall combination of the ATLAS and CMS projections. The ATLAS projections can be found in Ref. [17], while the combined ATLAS and CMS results can be found in Ref. [203].

As discussed in Section 3.1.2, the HL-LHC is expected to deliver between 3000 and 4000 fb^{-1} of 14 TeV pp collision data, which is almost two orders of magnitude more data than used to obtain the results presented in Chapters 5 and 6. The HL-LHC environment, with 200 expected pp collisions per bunch crossing, will be extremely challenging in terms of reconstruction and identification of physics objects. Nevertheless, the planned upgrades of the ATLAS detector, the constant improvements in the reconstruction, calibration and identification techniques, and expected smaller statistical uncertainties on the correction factors applied to MC simulations, all lead to an expected performance of the ATLAS experiment that is not very different from the performance of the current experiment.

7.1 Extrapolation strategy

The kinematic and BDT input distributions of simulated signal and backgrounds are compared at truth-level in samples of events generated at $\sqrt{s} =$ 13 TeV and $\sqrt{s} = 14$ TeV. They are found to be similar to a large extent, as shown in Appendix A: Figure A.4. Thus, the samples generated at $\sqrt{s} =$

13 TeV, which are specified in Table 5.2, are re-used and scaled to account for changes in the cross-section coming from the increase in the centre-of-mass energy, and no shape corrections are considered. Several paragraphs in the following detail the extrapolation strategy.

Cross-section
The SM signal is scaled to the cross-section of 36.69 fb, which is the SM ggF HH production cross-section at $\sqrt{s} = 14$ TeV calculated at NNLO precision in QCD, as specified in Table 1.2 and Ref. [38]. The signal predictions for varied κ_λ, which are obtained based on the procedure described in Section 6.1, are scaled to the approximate NNLO cross-section at 14 TeV, i.e. to the cross-section calculated at LO in QCD, as shown in Figure 6.2, times the factor of $\sigma_{HH}^{\text{SM, NNLO}}(14\text{ TeV})/\sigma_{HH}^{\text{SM, LO}}(13\text{ TeV}) = 36.69/14.41$. This implies re-scaling the cross-section curve to have the SM HH production cross-section matched to the NNLO prediction and re-scaling from $\sqrt{s} = 13$ TeV to 14 TeV. The ZH and $t\bar{t}H$ processes are normalised to their respective cross-section values at $\sqrt{s} = 14$ TeV, which are obtained from Ref. [38]. For all other background processes, the cross-section values specified in Section 5.1 are used, but they are scaled by a factor of 1.18 to account for the approximate cross-section increase due to the boost in the centre-of-mass energy.

Luminosity, pileup and b-tagging
The predicted event yields of signal and background processes are scaled to integrated luminosities of up to 3000 fb^{-1}. The performance of the upgraded ATLAS detector at the HL-LHC is assumed to be similar to that of the current detector, in spite of the increase in pileup. An exception is the b-tagging efficiency, which is assumed to be 8% higher per b-jet for the same c- and light-jet rejection due to the planned upgrades of the ATLAS inner detector [204]. When accounting for the higher b-tagging efficiency, a conservative approach is taken by treating all events as if they contain two true-b-jets, which is not always the case for the different background processes.

Normalisation of $t\bar{t}$ and Z+hf events
In the current analysis, the normalisations of the $t\bar{t}$ background with true-τ_{had} candidates and of the Z+hf background are determined from a profile likelihood fit to data. The obtained post-fit normalisation factor for the $t\bar{t}$ background is found to be consistent with 1, while the normalisation factor for the Z+hf background is found to be 1.34 ± 0.16, based on the background-only-hypothesis fit in the search for the SM signal[1], as explained in Section 5.3.5. In the extrapolation, the normalisations of the two background processes are not freely floated. Instead, the normalisation of the Z+hf background is scaled

[1] As a reminder, the post-fit results differ between different searches even for the background-only hypothesis since the BDT classifier and the binning of the BDT score are signal-dependent.

by 1.34 to account for the mismodelling observed in the current analysis. As a result, the $Z \to \mu\mu$+hf CR is omitted in the final fit. No corrections to the $t\bar{t}$ normalisation are applied in this case.

Binning of the final discriminant
The BDT score distributions are binned using the same criteria as in Section 5.7. Although the binning criteria are kept the same, the binning itself changes in the extrapolation due to the scaling of the number of expected background events. This leads to improvements in the expected sensitivity that are slightly beyond what is expected from naive cross-section and luminosity scaling. As will be discussed in the following, some of the statistical uncertainties on the background predictions are scaled or neglected in the extrapolation; however, the full statistical uncertainties (as in the current analysis) are conservatively taken into account when determining the binning.

7.2 Treatment of the systematic uncertainties

Four different scenarios are assumed regarding the evolution of the systematic uncertainties presented in Section 5.5 and they are defined in the following. In all these scenarios, the theoretical uncertainties on the signal cross-section are not taken into account, but they are found to have a negligible impact on the final results.

Scenario 1: Current systematic uncertainties
In the first scenario, nearly all pre-fit systematic uncertainties are set to their pre-fit values from the current analysis. Exceptions are the uncertainties related to the $t\bar{t}$ and Z+hf normalisations that are modified to account for the different treatment of these backgrounds in the final fit. The current relative post-fit uncertainties on their normalisation, which are around 12% each, are incorporated in the fit as nuisance parameters. The $t\bar{t}$ (Z+hf) normalisation extrapolation uncertainties in the $\tau_{\text{had}}\tau_{\text{had}}$ SR ($\tau_{\text{lep}}\tau_{\text{had}}$ and $\tau_{\text{had}}\tau_{\text{had}}$ SRs) are kept unchanged with respect to the current analysis.

Scenario 2: MC statistical uncertainty neglected
In this scenario, the same assumptions are made as in the first scenario; however, the MC statistical uncertainty is neglected, assuming that the size of MC samples will increase significantly beyond the data luminosity if needed.

Scenario 3: Baseline
The baseline scenario is defined as the nominal assumption on the size of the systematic uncertainties relevant for this analysis at the point in time when the ATLAS detector at the HL-LHC will have collected 3000 fb^{-1} of data. The assumed uncertainty on the integrated luminosity is 1%. Uncertainties

in the modelling of the pileup and of the detector response are assumed to stay the same as in the current analysis given that it is difficult to disentangle their statistical component from technological and methodological limitations of the experiment.

In the extrapolation, since the 12% normalisation uncertainties on the $t\bar{t}$ and Z+hf background predictions are of statistical nature, they are scaled down to account for the increase in the expected number of events[2]. The extrapolation normalisation uncertainties on the $t\bar{t}$ and Z+hf background predictions are halved assuming improvements in the theoretical modelling of these processes.

Systematic uncertainties in estimating the backgrounds with fake-τ_{had} candidates, which are in the current analysis modelled using data-driven methods, are left unchanged since it is difficult to quantify which fraction of these uncertainties is of statistical nature. However, the statistical uncertainties on these background predictions are scaled to follow the increase in the expected number of events, hence they are significantly reduced when extrapolating to the full targeted integrated luminosity.

As indicated in Table 5.12, the normalisation uncertainties assigned to the $t\bar{t}H$ and ZH processes are 30% and 28% in the current analysis, respectively. Due to the large impact of these uncertainties on the results in the baseline scenario, and in order to account for improvements in experimental measurements of these processes with an increased luminosity, they are reduced to 10% and 5%, respectively, corresponding approximately to the current theoretical uncertainties in the modelling of these processes [38].

The normalisation uncertainties assigned to other minor background processes are halved in the baseline scenario, based on the general consensus between the ATLAS and CMS collaborations on how to treat subdominant theoretical uncertainties in the HL-LHC sensitivity projections.

Scenario 4: No systematic uncertainties

In the final scenario, all systematic uncertainties, including the MC statistical uncertainties, are neglected. These results, when compared to those in the baseline scenario, indicate the impact of the overall estimated systematic uncertainty on the expected sensitivity.

[2]The uncertainty is scaled by a factor of $1/\sqrt{(L_{\text{target}}/36.1)\times 1.18\times(1.08)^2}$, where L_{target} is the assumed integrated luminosity; 36.1 fb^{-1} is the luminosity of the dataset used for the current results; the factor 1.18 accounts for the approximate increase in the cross-section due to the change in the centre-of-mass energy; while $(1.08)^2$ represents the increase in the b-tagging efficiency assuming two true-b-jets in each event.

7.3 Results

The sensitivity projections are obtained by performing the simultaneous profile likelihood fit to the BDT score distributions in the three SRs. Unless stated otherwise, the results are obtained by performing a fit to the background-only Asimov dataset. The post-fit BDT score distributions that are scaled to the assumed integrated luminosity of 3000 fb^{-1}, assuming the baseline systematic-uncertainty scenario, are shown in Figure 7.1.

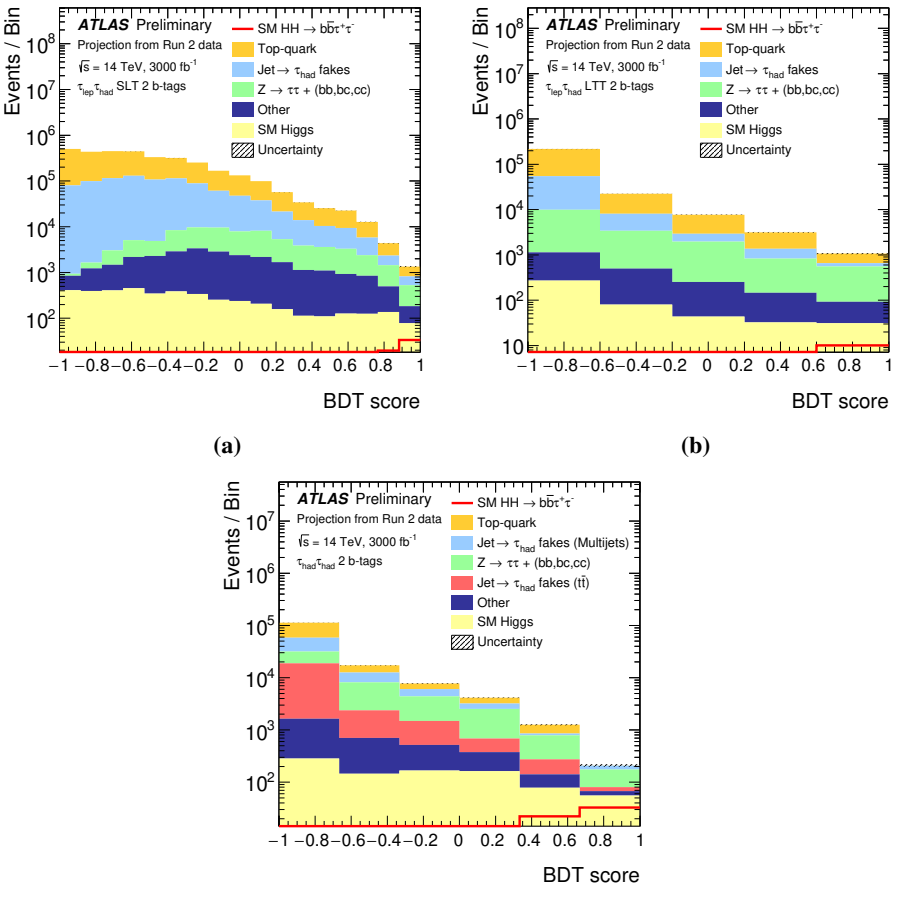

Figure 7.1. Distributions of the BDT score for the backgrounds and the SM *HH* signal in the (**a**) $\tau_{\text{lep}}\tau_{\text{had}}$ SLT, (**b**) $\tau_{\text{lep}}\tau_{\text{had}}$ LTT, and (**c**) $\tau_{\text{had}}\tau_{\text{had}}$ SR [17], scaled to 3000 fb^{-1}. Distributions are shown after the combined background-only-hypothesis fit to the background-only Asimov dataset. The signal is overlaid after being scaled to approximately the expected limit. The hatched band indicates the combined statistical and systematic uncertainty in the background prediction in the baseline systematic-uncertainty scenario.

The signal and background yields obtained are shown in Table 7.1 for the full SR selection and for only the two last bins of the BDT score distribution, in each of the SRs separately. The signal yield is estimated from the fit to the signal-plus-background Asimov dataset with $\mu'(\kappa_\lambda = 1) = 1$.

Table 7.1. *Expected event yields from the fit to the background-only Asimov dataset scaled to 3000 fb^{-1}, assuming the baseline systematic-uncertainty scenario [17]. The upper part of the table refers to the full SR selection, while the bottom part of the table refers to the last two bins of the respective BDT score histogram. Due to rounding, the individual background yields do not sum to the total background yield. Additionally, due to large correlations, uncertainties on individual backgrounds can be larger than the total uncertainty. The signal yield is estimated from the fit to the signal-plus-background Asimov dataset with $\mu'(\kappa_\lambda = 1) = 1$.*

Process	$\tau_{\text{lep}}\tau_{\text{had}}$ channel		$\tau_{\text{had}}\tau_{\text{had}}$ channel
	(SLT)	(LTT)	
$t\bar{t}$ with true-τ_{had}	2218000 ± 13000	176000 ± 2300	57600 ± 2000
Single top	129200 ± 2800	8240 ± 230	4490 ± 150
$t\bar{t}$ with fake-τ_{had}	-	-	20400 ± 2200
Multijet	-	-	33500 ± 2100
Jet $\rightarrow$ fake-τ_{had}	867000 ± 13000	51100 ± 2300	-
$Z \rightarrow \tau\tau + (bb, bc, cc)$	51800 ± 2100	14600 ± 600	23800 ± 1100
Other	24300 ± 1000	1710 ± 160	2550 ± 350
SM Higgs ($t\bar{t}H$ and ZH)	4280 ± 360	460 ± 40	900 ± 60
Total background	3295300 ± 1800	252050 ± 500	143200 ± 400
SM HH	107 ± 6	23.9 ± 1.3	81 ± 8
Last two bins of the BDT score			
$t\bar{t}$ with true-τ_{had}	1830 ± 40	1780 ± 30	370 ± 30
Single top	720 ± 20	420 ± 40	32.3 ± 2.8
$t\bar{t}$ with fake-τ_{had}	-	-	146 ± 19
Multijet	-	-	100 ± 20
Jet $\rightarrow$ fake-τ_{had}	640 ± 40	210 ± 30	-
$Z \rightarrow \tau\tau + (bb, bc, cc)$	1290 ± 70	1150 ± 70	610 ± 60
Other	460 ± 20	180 ± 20	80 ± 10
SM Higgs ($t\bar{t}H$ and ZH)	220 ± 10	64 ± 3	134 ± 8
Total background	5730 ± 90	4230 ± 90	1470 ± 90
SM HH	52 ± 3	16.2 ± 0.8	54 ± 5

The 95% CL upper limits on $\sigma_{HH}/\sigma_{HH}^{\text{SM}}$ are shown in Figure 7.2 as a function of the integrated luminosity of the search, in the range between 36.1 and 3000 fb^{-1}. The extrapolation of the limits is presented for the combination

of the $\tau_{\text{lep}}\tau_{\text{had}}$ and $\tau_{\text{had}}\tau_{\text{had}}$ channels in the four systematic-uncertainty scenarios, and also for the two channels separately in the baseline scenario. In the absence of Higgs boson pair production, i.e. when performing fits to the background-only Asimov dataset, the combined $b\bar{b}\tau^+\tau^-$ analysis is expected to be at the border of excluding the SM pair production of Higgs bosons at 95% CL. The limit on $\sigma_{HH}/\sigma_{HH}^{\text{SM}}$ is 0.99 in the baseline systematic-uncertainty scenario, for an assumed integrated luminosity of 3000 fb^{-1}. If systematic uncertainties are not considered, the expected 95% CL upper limit on $\sigma_{HH}/\sigma_{HH}^{\text{SM}}$ becomes 0.80.

Similarly, the expected p_0-value for rejecting the background-only hypothesis, when performing fits to the signal-plus-background Asimov dataset with $\mu'(\kappa_\lambda = 1) = 1$, is shown in Figure 7.3 as a function of the integrated luminosity of the search for the combination of the $\tau_{\text{lep}}\tau_{\text{had}}$ and $\tau_{\text{had}}\tau_{\text{had}}$ channels in the four systematic-uncertainty scenarios. Each obtained expected p_0-value at 3000 fb^{-1} is converted into a significance. The expected significance in the baseline scenario (when systematic uncertainties are not considered) is 2.1 (2.5) standard deviations. All these results are summarised in Table 7.2.

Table 7.2. *Expected 95% CL upper limit on $\sigma_{HH}/\sigma_{HH}^{\text{SM}}$, p_0-value and significance, for an assumed integrated luminosity of 3000 fb^{-1}, for the four systematic-uncertainty scenarios. The results correspond to the combination of the $\tau_{\text{lep}}\tau_{\text{had}}$ and $\tau_{\text{had}}\tau_{\text{had}}$ channels.*

Scenario	-1σ	Expected limit	$+1\sigma$	Expected p_0-value	Significance $[\sigma]$
No systematic uncertainties	0.58	0.80	1.12	0.00685	2.5
Baseline	0.71	0.99	1.37	0.0187	2.1
MC stat. uncert. neglected	0.8	1.2	1.6	0.0413	1.7
Current systematic uncert.	1.9	2.7	3.7	0.258	0.65

For the results extrapolated to 3000 fb^{-1} assuming the current systematic uncertainties, the MC statistical uncertainty becomes dominant, accounting for around 90% of the total uncertainty on the signal strength[3]. Due to the high impact of the MC statistical uncertainty, a significantly worse expected 95% CL upper limit on $\sigma_{HH}/\sigma_{HH}^{\text{SM}}$ of 2.7 is obtained in this systematic-uncertainty scenario. After neglecting the MC statistical uncertainty, some of the dominant uncertainties in the analysis become the normalisation uncertainties assigned to the $t\bar{t}H$ and ZH processes. These background events are very similar to the signal, often being assigned a high BDT score, and thus it is expected that their impact on the results will increase with a higher sensitivity to the signal processes. However, as already explained, the uncertainties in the modelling of the $t\bar{t}H$ and ZH backgrounds in the current analysis are conservatively driven

[3]This uncertainty is obtained from a conditional signal-plus-background-hypothesis fit to the background-only Asimov dataset, with μ set to the expected 95% CL upper limit.

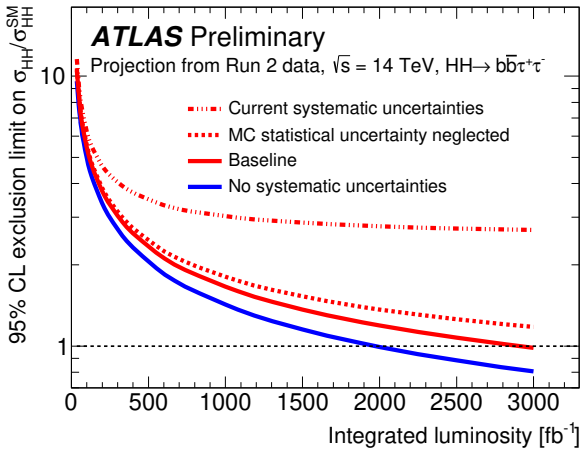

(a)

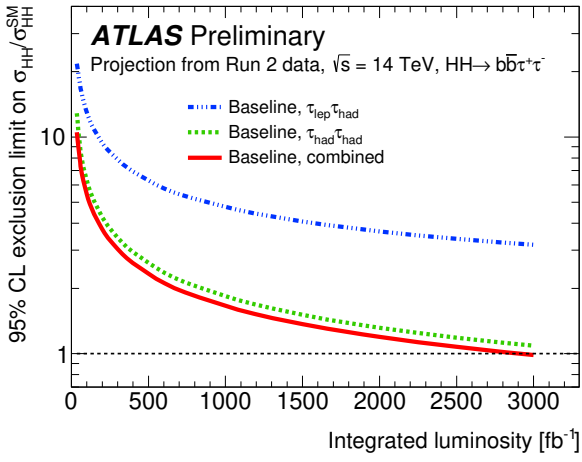

(b)

Figure 7.2. Expected 95% CL upper limit on $\sigma_{HH}/\sigma_{HH}^{\mathrm{SM}}$ as a function of the integrated luminosity of the search between 36.1 and 3000 fb^{-1} [17]. The results are shown for the (**a**) combined $\tau_{\mathrm{lep}}\tau_{\mathrm{had}}$ and $\tau_{\mathrm{had}}\tau_{\mathrm{had}}$ channels in each of the four systematic-uncertainty scenarios, and (**b**) $\tau_{\mathrm{lep}}\tau_{\mathrm{had}}$ and $\tau_{\mathrm{had}}\tau_{\mathrm{had}}$ channels separately in the baseline systematic-uncertainty scenario.

by the ATLAS measurements of these processes, hence they are expected to be significantly improved in the future.

The impact of the systematic uncertainties in the baseline scenario is evaluated by checking their contribution to the uncertainty in the signal strength, $\mu = \sigma_{HH}/\sigma_{HH}^{\mathrm{SM}}$, in a conditional signal-plus-background-hypothesis fit to the background-only Asimov dataset, with μ set to the expected 95% CL up-

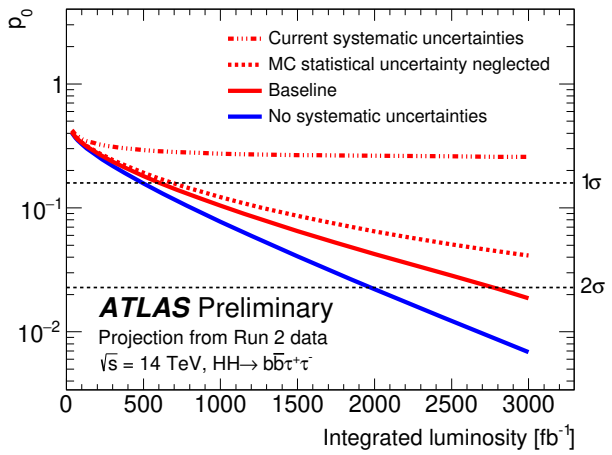

Figure 7.3. Expected p_0-value for rejecting the background-only hypothesis when performing fits to the Asimov dataset with $\mu'(\kappa_\lambda = 1) = 1$ as a function of the integrated luminosity of the search between 36.1 and 3000 fb^{-1} [17]. The results are shown for the combination of the $\tau_{\text{lep}}\tau_{\text{had}}$ and $\tau_{\text{had}}\tau_{\text{had}}$ channels in each of the four systematic-uncertainty scenarios.

per limit of 0.99. The results are summarised in Table 7.3. The uncertainty in the signal strength obtained from a conditional signal-plus-background-hypothesis fit to the signal-plus-background Asimov dataset with $\mu'(\kappa_\lambda = 1) = 1$, with μ set to 1, is 47% (42%) in the baseline (no systematic uncertainties) scenario.

7.3.1 Constraints on the trilinear Higgs boson self-coupling

The results presented in Chapter 6 are extrapolated following the same approach to estimate the sensitivity to the trilinear Higgs boson self-coupling at the HL-LHC. As a reminder, the $\tau_{\text{lep}}\tau_{\text{had}}$ LTT SR is not included when obtaining these results, while the BDT classifier used to separate the signal predictions from the expected background is trained on the $\kappa_\lambda = 20$ signal sample. One difference is that, for this sensitivity study, a fixed binning is used as a function of κ_λ. This is necessary for performing the likelihood ratio tests described below, which require the same likelihood definition as a function of κ_λ. For this reason, the binning obtained for the SM signal, based on the criteria described in Section 5.7, is used across the whole κ_λ range. This leads to an improvement of 5% to 10% in the expected limits for the signal predictions that correspond to softer m_{HH} spectra.

The expected 95% CL upper limits on the non-resonant HH production cross-section as a function of κ_λ obtained from fits to the background-only

Table 7.3. *Percentage uncertainties on the simulated SM HH signal strength, $\Delta\mu/\mu = \Delta(\sigma_{HH}/\sigma_{HH}^{\mathrm{SM}})/(\sigma_{HH}/\sigma_{HH}^{\mathrm{SM}})$, from a conditional signal-plus-background-hypothesis fit with μ set to the expected 95% CL upper limit of 0.99 [17]. The results are shown for the baseline systematic-uncertainty scenario in which the MC statistical uncertainties are neglected, hence no contribution from the limited simulation statistics to the uncertainty in μ.*

Source	Uncertainty [%]
Total	± 52
Data statistics	± 43
Simulation statistics	± 0
Total systematic uncertainty	± 30
Experimental uncertainties	
Integrated luminosity	± 4.3
Pileup re-weighting	± 7.0
τ_{had} candidates	± 13
Fake-τ_{had} estimation	± 8.3
b-tagging	± 8.1
Jets and E_T^{miss}	± 3.5
Electrons and muons	± 5.1
Total experimental uncertainties	± 18
Theoretical and modelling uncertainties	
Single top and $t\bar{t}$	± 6.6
Signal	± 8.6
Z+hf	± 11
SM Higgs	± 8.5
Other backgrounds	± 4.4
Total theoretical and modelling uncertainties	± 17

Asimov dataset are shown in Figure 7.4. Based on the theory prediction, the expected combined allowed κ_λ interval in the baseline systematic-uncertainty scenario is $\kappa_\lambda \in [1.0, 7.0]$. However, it is important to take into account several caveats when interpreting this constraint. The results are obtained from fits to the background-only Asimov dataset, i.e. $\sigma_{HH} = 0$ is assumed. On the other hand, the framework in which variations of λ_{HHH} are probed, as discussed in Section 2.2, includes the SM predictions for all couplings except the Higgs boson self-coupling. Therefore, it is implicitly assumed here that some other process cancels the box-diagram contribution in non-resonant pair production of Higgs bosons.

Expected constraints on κ_λ are obtained for another two assumptions regarding the true nature of the Higgs boson couplings. In the first case, the

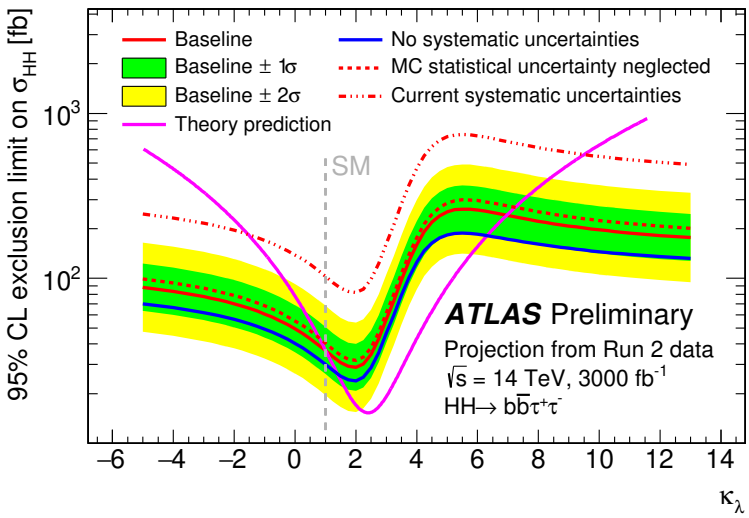

Figure 7.4. Upper limits at 95% CL on the cross-section of the *gg*F non-resonant HH production as a function of κ_λ [17]. The combined expected limits from the $\tau_{\text{lep}}\tau_{\text{had}}$ and $\tau_{\text{had}}\tau_{\text{had}}$ channels in the baseline systematic-uncertainty scenario are shown as a red solid line with the corresponding $\pm1\sigma$ and $\pm2\sigma$ uncertainty bands. For comparison, the solid blue line corresponds to the limits obtained when systematic uncertainties are not taken into account. The limits for the other two scenarios are shown as dashed lines. The theory prediction of the cross-section as a function of κ_λ (cross-section calculated at LO in QCD, as shown in Figure 6.2, times the factor of $\sigma_{HH}^{\text{SM, NNLO}}(14\text{ TeV})/\sigma_{HH}^{\text{SM, LO}}(13\text{ TeV}) = 36.69/14.41$) is also shown.

expected constraints on κ_λ are obtained after assuming the SM pair production of Higgs bosons, i.e. the fits are performed to the Asimov dataset that includes the background processes and the SM signal, with $\mu'(\kappa_\lambda = 1) = 1$. In the second case, it is assumed that the Higgs boson does not couple to itself, i.e. the fits are performed to the Asimov dataset that includes the background processes and the $\kappa_\lambda = 0$ signal, with $\mu'(\kappa_\lambda = 0) = 1$.

Conditional maximum likelihood fits are performed with different κ_λ hypotheses to both of these Asimov datasets, for an assumed integrated luminosity of 3000 fb^{-1}. The ratio of the maximum likelihood value for a given κ_λ hypothesis to the maximum likelihood value for the $\kappa_\lambda = 1$ hypothesis, when performing fits to the $\mu'(\kappa_\lambda = 1) = 1$ Asimov dataset, is used to obtain expected constraints on κ_λ when assuming the validity of the SM. The negative natural logarithm of this ratio as a function of κ_λ is shown in Figure 7.5a. Similarly, the ratio of the maximum likelihood value for a given κ_λ hypothesis to the maximum likelihood value for the $\kappa_\lambda = 0$ hypothesis, when performing fits to the $\mu'(\kappa_\lambda = 0) = 1$ Asimov dataset, is used to obtain the expected constraints on κ_λ when assuming that the Higgs boson does not couple to itself.

The negative natural logarithm of this ratio as a function of κ_λ is shown in Figure 7.5b.

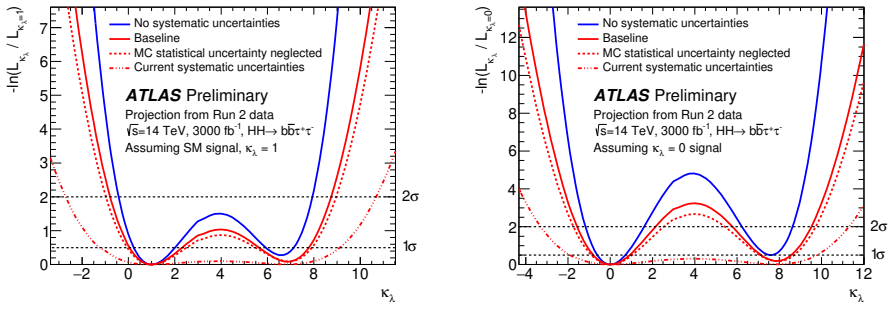

Figure 7.5. Negative natural logarithm of the ratio of the conditional maximum likelihood for κ_λ to the conditional maximum likelihood for (**a**) $\kappa_\lambda = 1$, obtained from fits to the $\mu^{'}(\kappa_\lambda = 1) = 1$ Asimov dataset; and (**b**) $\kappa_\lambda = 0$, obtained from fits to the $\mu^{'}(\kappa_\lambda = 0) = 1$ Asimov dataset [17]. The horizontal lines indicate the expected allowed κ_λ intervals at 1σ and 2σ CL. All four systematic-uncertainty scenarios are shown.

Figure 7.5 indicates that in both cases two minima are obtained. In Figure 7.5a (7.5b), the first minimum is at $\kappa_\lambda = 1$ ($\kappa_\lambda = 0$) by construction (for the unbiased maximum likelihood estimator), given that the conditional fit is performed for the same signal hypothesis as that the Asimov dataset is built upon. The second minimum is obtained for the κ_λ values that correspond to a higher cross-section, but lower acceptance $\times$ efficiency and worse signal-to-background separation, with respect to the $\kappa_\lambda = 1$ ($\kappa_\lambda = 0$) signal. This yields a similar number of expected signal events for the two κ_λ values at which the minima occur, leading to similar maximum likelihood values. For all other κ_λ points, the expected signal yield is either lower or higher, and thus the likelihood ratio, which measures the incompatibility between the fit hypothesis and the dataset to which the fit is performed, is greater. The second minimum is expected to be partially removed if one has the ability to better exploit the signal shape information. The expected constraints on κ_λ are summarised in Table 7.4.

7.3.2 Di-τ_{had} trigger

The extrapolation results shown thus far are based on assuming the same trigger thresholds as in the current analysis. While it is expected that the upgraded detector will allow for triggering on electrons and muons with lower p_T thresholds, it is more difficult to predict the future design of the di-τ_{had} trigger, which is essential for maintaining the high sensitivity to the non-resonant

Table 7.4. *Constraints on κ_λ from the likelihood ratio test performed on the $\mu'(\kappa_\lambda = 1) = 1$ Asimov dataset (upper part of the table) and $\mu'(\kappa_\lambda = 0) = 1$ Asimov dataset (lower part of the table), presented as 1σ and 2σ CL allowed κ_λ intervals, for the four systematic-uncertainty scenarios [17]. The constraints correspond to the results shown in Figure 7.5.*

Scenario	1σ CL interval	2σ CL interval
Assuming the SM signal ($\kappa_\lambda = 1$)		
No systematic uncert.	$[0.2, 2.0] \cup [5.9, 7.2]$	$[-0.4, 7.9]$
Baseline	$[0.1, 2.3] \cup [5.7, 7.8]$	$[-0.8, 8.8]$
MC statistical uncert. neglected	$[-0.1, 2.5] \cup [5.5, 7.9]$	$[-1.0, 9.0]$
Current systematic uncert.	$[-1.2, 9.1]$	$[-2.7, 10.7]$
Assuming $\kappa_\lambda = 0$		
No systematic uncert.	$[-0.6, 0.7]$	$[-1.2, 1.6] \cup [6.2, 8.6]$
Baseline	$[-0.8, 0.9] \cup [7.1, 8.6]$	$[-1.6, 2.2] \cup [5.8, 9.5]$
MC statistical uncert. neglected	$[-0.9, 1.0] \cup [7.1, 8.7]$	$[-1.7, 2.5] \cup [5.4, 9.7]$
Current systematic uncert.	$[-1.9, 9.8]$	$[-3.3, 11.3]$

pair production of Higgs bosons in the $bb\bar{\tau}^+\tau^-$ analysis. As discussed in Section 5.2.1, the DTT requires 2 online-medium τ_{had} candidates of 35 (25) GeV for the leading (sub-leading) candidate. Furthermore, the DTT requires the presence of an additional jet at L1 with $p_T > 25$ GeV. After the full event reconstruction, the offline p_T cuts on the two reconstructed τ_{had} candidates are 40 and 30 GeV, while the leading jet must have a p_T greater than 80 GeV. An illustration of the reduction of the signal acceptance $\times$ efficiency by this jet p_T requirement, after applying a truth-level selection equivalent to the trigger requirements, is shown in Figure 7.6a as a function of κ_λ. Potential gains in $A \times \varepsilon$ with reduced p_T thresholds on the truth-level $\tau_{\text{had-vis}}$ are shown in Figure 7.6b.

The negative impact of a reduced DTT acceptance is studied by repeating the extrapolation of the current analysis, as defined in Section 7.1, for several variations of the τ_{had} p_T thresholds, while maintaining the 80 GeV cut for the leading jet[4]. These studies refer only to the $\tau_{\text{had}}\tau_{\text{had}}$ channel and they are performed without considering any systematic uncertainties. The expected 95% CL upper limits on $\sigma_{HH}/\sigma_{HH}^{\text{SM}}$ at $\sqrt{s} = 14$ TeV and 3000 fb^{-1} are shown in Figure 7.7 for various τ_{had} p_T thresholds and for two different BDT classifiers. In Figure 7.7a, the BDT classifier trained on the SM signal is used, which allows to see the impact of the higher p_T thresholds on the limits on $\sigma_{HH}/\sigma_{HH}^{\text{SM}}$. The sensitivity to the Higgs boson self-coupling (triangle diagram) is affected even more by raising the p_T thresholds given that the m_{HH} spectrum and hence the

[4]Otherwise the extrapolation of the data-driven background estimate would not be valid.

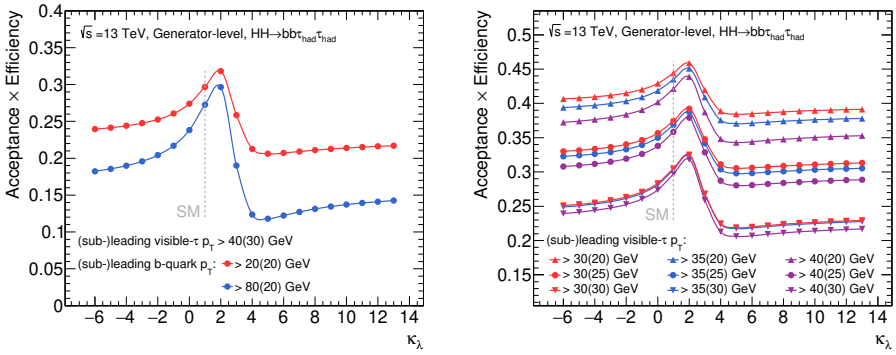

(a) **(b)**

Figure 7.6. (**a**) Truth-level acceptance × efficiency when requiring two $\tau_{\text{had-vis}}$ with p_T greater than 40 (30) GeV for the leading (sub-leading) $\tau_{\text{had-vis}}$ and 2 b-quarks with $p_T > 20$ GeV (red line). The same selection is applied to obtain the results shown by the blue line, but in this case the leading b-quark is required to have a p_T greater than 80 GeV. (**b**) Truth-level acceptance × efficiency when requiring two b-quarks with $p_T > 20$ GeV and two $\tau_{\text{had-vis}}$ objects with varied p_T cuts, as indicated in the legend.

decay products of the Higgs bosons are softer, which is illustrated by repeating the same study using the BDT classifier trained on the $\kappa_\lambda = 20$ signal, as shown in Figure 7.7b.

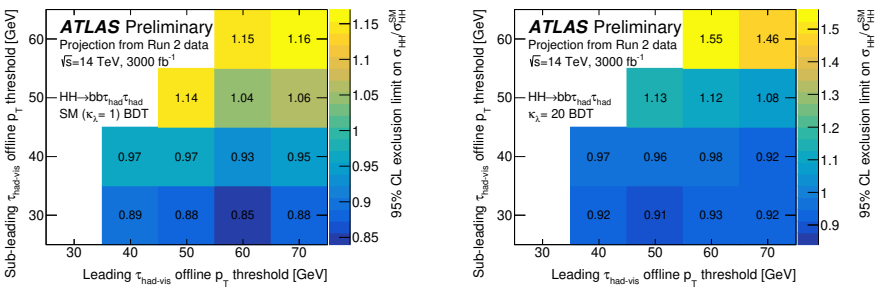

(a) **(b)**

Figure 7.7. Expected 95% CL upper limit on $\sigma_{HH}/\sigma_{HH}^{\text{SM}}$ as a function of the minimum p_T thresholds for the leading and sub-leading τ_{had} candidates [17]. The results are shown for the (**a**) BDT classifier trained on the SM signal and (**b**) BDT classifier trained on the $\kappa_\lambda = 20$ signal. Systematic uncertainties are not included.

The 80 GeV cut on the p_T of the leading jet to a large extent masks the full impact of the reduced acceptance, and thus only a small degradation in limits is seen when raising the p_T cut on the leading τ_{had} candidate. In some cases

even small improvements in the limit are found, but they are not significant and they appear only because the systematic uncertainties are not considered. For a more adequate estimation of the optimal DTT requirements at the HL-LHC, a new analysis needs to be developed for estimating the multijet background below the current trigger thresholds, which is not included in the results presented here.

7.4 Combined ATLAS and CMS results

A statistical combination of the ATLAS projections of the sensitivity to non-resonant Higgs boson pair production at $\sqrt{s} = 14$ TeV and for 3000 fb^{-1} of data was performed for the $b\bar{b}b\bar{b}$, $b\bar{b}\tau^+\tau^-$ and $b\bar{b}\gamma\gamma$ channels. The combination is realised by performing a simultaneous profile likelihood fit across the three channels, both with and without systematic uncertainties. When considering systematic uncertainties, the baseline systematic-uncertainty scenario is assumed in the $b\bar{b}\tau^+\tau^-$ analysis, while the estimated systematic uncertainties in the $b\bar{b}b\bar{b}$ and $b\bar{b}\gamma\gamma$ channels are defined in Ref. [17]. The experimental uncertainties are correlated across the channels, while the theoretical and modelling uncertainties in the background predictions of the different channels are left uncorrelated. Theoretical uncertainties on the signal cross-section are not included, but they are found to have a negligible impact on the result.

The combined 95% CL upper limit on $\sigma_{HH}/\sigma_{HH}^{\mathrm{SM}}$, in the absence of Higgs boson pair production, for $\sqrt{s} = 14$ TeV and 3000 fb^{-1}, is 0.68 if systematic uncertainties are considered and 0.56 if they are not. The combined expected significance for the SM signal reaches 3.0 (3.5) standard deviations over the background-only expectation if systematic uncertainties are (not) considered, as listed in Table 7.5. When performing fits to the $\mu'(\kappa_\lambda = 1) = 1$ Asimov dataset, the uncertainty on the SM signal strength is found to be 40% (30%) when systematic uncertainties are (not) considered, as listed in Table 7.6.

Table 7.5. *Expected significance for the SM HH signal in the three channels and for their combination [17], obtained from fits to the $\mu'(\kappa_\lambda = 1) = 1$ Asimov dataset.*

	Significance [σ]	
Channel	No systematic uncert.	Systematic uncert.
$b\bar{b}b\bar{b}$	1.4	0.61
$b\bar{b}\tau^+\tau^-$	2.5	2.1
$b\bar{b}\gamma\gamma$	2.1	2.0
Combined	3.5	3.0

The combined sensitivity of the three analyses to κ_λ is assessed by performing the same likelihood ratio tests as in the $b\bar{b}\tau^+\tau^-$ channel. The negative

Table 7.6. *The SM HH signal strength with the corresponding relative uncertainty in the three channels and for their combination [17], obtained from fits to the* $\mu'(\kappa_\lambda = 1) = 1$ *Asimov dataset.*

Channel	No systematic uncert.	Systematic uncert.
$b\bar{b}b\bar{b}$	1.0 ± 0.6	1.0 ± 1.6
$b\bar{b}\tau^+\tau^-$	1.0 ± 0.4	1.0 ± 0.5
$b\bar{b}\gamma\gamma$	1.0 ± 0.6	1.0 ± 0.6
Combined	1.0 ± 0.3	1.0 ± 0.4

natural logarithm of the ratio of the conditional maximum likelihood for κ_λ to the conditional maximum likelihood for $\kappa_\lambda = 1$, when performing fits to the $\mu'(\kappa_\lambda = 1) = 1$ Asimov dataset, is shown in Figure 7.8a. Similarly, the negative natural logarithm of the ratio of the conditional maximum likelihood for κ_λ to the conditional maximum likelihood for $\kappa_\lambda = 0$, when performing fits to the $\mu'(\kappa_\lambda = 0) = 1$ Asimov dataset, is shown in Figure 7.8b. The corresponding expected constraints on κ_λ are summarised in Table 7.7. The expected significance with which the Higgs boson pair production would be observed is shown in Figure 7.8c as a function of κ_λ.

Table 7.7. *Constraints on* κ_λ *from the likelihood ratio test performed on the* $\mu'(\kappa_\lambda = 1) = 1$ *Asimov dataset (upper part of the table) and* $\mu'(\kappa_\lambda = 0) = 1$ *Asimov dataset (lower part of the table), presented as* 1σ *and* 2σ *CL allowed* κ_λ *intervals, with and without considering systematic uncertainties [17].*

Scenario	1σ CL interval	2σ CL interval
Assuming the SM signal ($\kappa_\lambda = 1$)		
No systematic uncert.	$[0.4, 1.7]$	$[-0.10, 2.7] \cup [5.5, 6.9]$
Systematic uncert.	$[0.25, 1.9]$	$[-0.4, 7.3]$
Assuming $\kappa_\lambda = 0$		
No systematic uncert.	$[-0.5, 0.5]$	$[-0.9, 1.1]$
Systematic uncert.	$[-0.6, 0.7]$	$[-1.3, 1.5]$

The CMS HL-LHC projections for the $b\bar{b}b\bar{b}$, $b\bar{b}\tau^+\tau^-$, $b\bar{b}\gamma\gamma$, $b\bar{b}VV$ ($\ell\ell\nu\nu$) and $b\bar{b}ZZ$ (4ℓ) channels can be found in Ref. [205]. These are combined with the ATLAS projections discussed above. Systematic uncertainties between the two experiments are left uncorrelated in the combination for simplicity and because their overall impact was found to be very small. The combined expected significance for the SM HH signal reaches 4.0 (4.5) standard deviations over the background-only expectation if systematic uncertainties are (not) considered. The allowed κ_λ interval at 68% CL is $[0.52, 1.5]$ ($[0.57, 1.5]$)

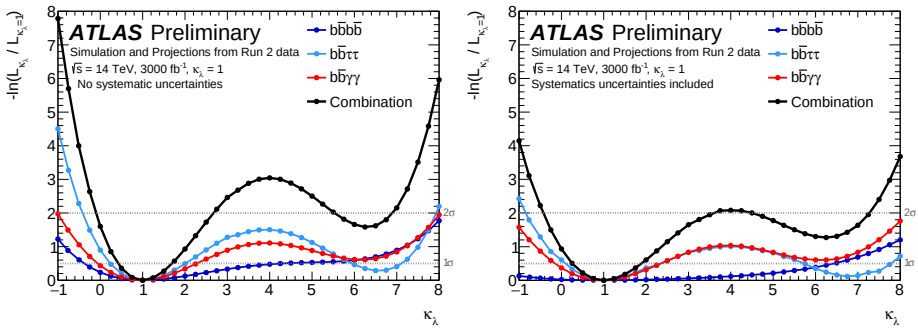

(a)

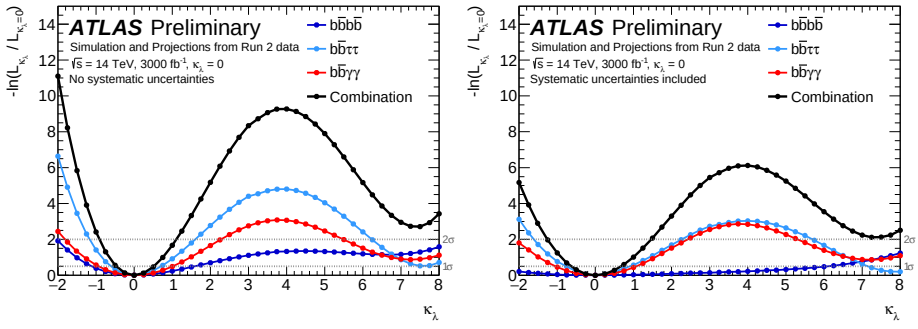

(b)

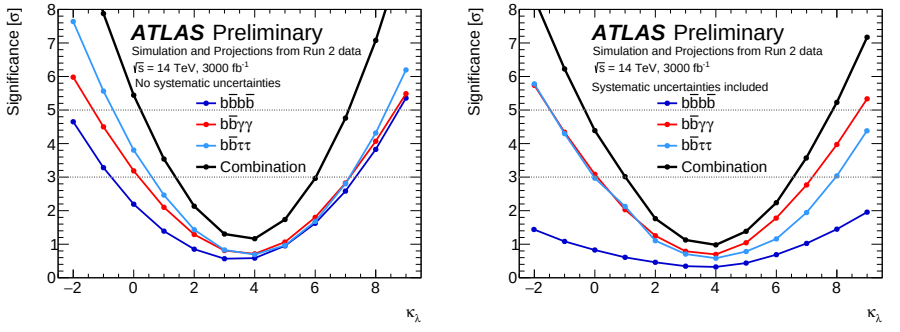

(c)

Figure 7.8. Negative natural logarithm of the ratio of the maximum likelihood for κ_λ to the maximum likelihood for (**a**) $\kappa_\lambda = 1$, obtained from fits to the Asimov dataset that contains the SM signal; and (**b**) $\kappa_\lambda = 0$, obtained from fits to the Asimov dataset that contains the $\kappa_\lambda = 0$ signal [17]. The horizontal lines indicate the expected allowed κ_λ intervals at 1σ and 2σ CL. (**c**) Expected significance of observing Higgs boson pair production, as a function of κ_λ, where two horizontal dashed lines indicate the 3σ and 5σ thresholds, for evidence and discovery, respectively. Plots on the left (right) correspond to the results obtained without (with) considering systematic uncertainties.

with (without) systematic uncertainties when assuming the SM Higgs boson pair production. The likelihood ratio as a function of κ_λ is shown in Figure 7.9 based upon the Asimov dataset with $\mu'(\kappa_\lambda = 1) = 1$.

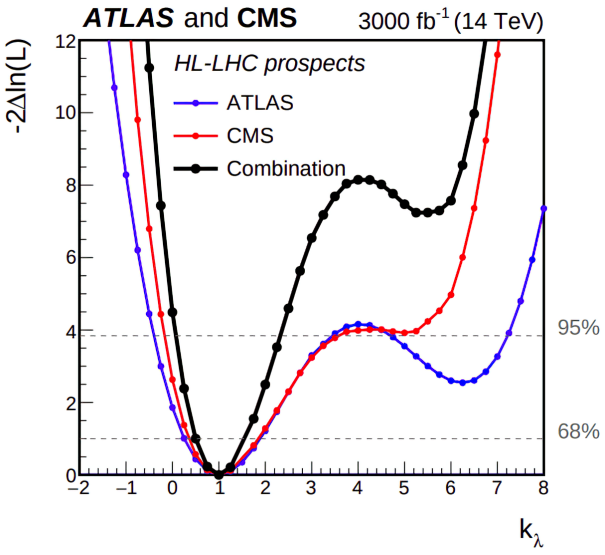

Figure 7.9. Negative natural logarithm of the ratio of the conditional maximum likelihood for κ_λ to the conditional maximum likelihood for $\kappa_\lambda = 1$, obtained from fits to the Asimov dataset that contains the SM signal [203]. The horizontal lines indicate the expected allowed κ_λ intervals at 68% and 95% CL. The black line corresponds to the combined ATLAS and CMS results, while the blue and red lines correspond to the ATLAS and CMS standalone results, respectively.

8. Revised event selection and background estimation in the $\tau_{\text{had}}\tau_{\text{had}}$ channel using the full ATLAS Run 2 dataset

Several attempts to revise the event selection and to improve background estimation techniques presented in Chapter 5 are discussed here, in the context of the ongoing searches for pair production of Higgs bosons in the $bb\tau_{\text{had}}\tau_{\text{had}}$ final state with the full Run 2 ATLAS dataset corresponding to 139 fb^{-1} of 13 TeV pp collision data.

Changes in the configuration used to simulate the signal and background samples, as well as changes in the object and event selections, are summarised in Sections 8.1 and 8.2, respectively. A revised background estimate is discussed in Section 8.3. Results presented in this chapter outline several proposed improvements of the strategy described in Chapter 5; however, these proposed modifications are not final and fully optimised, and they do not include a complete evaluation of the systematic uncertainties.

8.1 Simulation of signal and background processes

The complete set of simulated signal and background samples used to obtain the results presented in this chapter is described in this section. The samples are generated as described in Section 3.3 and they slightly differ in the configuration used to produce them with respect to the samples used for the results presented in Chapters 5–7, which are specified in Table 5.2.

The simulated samples, the MC generators and PDF sets used to calculate the matrix elements (ME), as well as the generators and tunes used to simulate the parton shower (PS) and hadronisation processes, are listed in Table 8.1. For the resonant pair production of Higgs bosons, only the samples corresponding to the scalar resonance are simulated, while spin-2 resonances are not considered. The $t\bar{t}$ sample is produced with the h_{damp} parameter set to 1.5 times the top-quark mass. The assumed production cross-section values used for normalising the simulated samples are kept unchanged with respect to the values specified in Section 5.1, except for the SM HH signal which is normalised to $\sigma_{\text{NNLO FTapprox}} = 31.05$ fb, as specified in Table 1.2.

Signal and background samples used to model the data recorded during (1) 2015 and 2016, (2) 2017 and (3) 2018 are all simulated separately due to different pileup profiles.

Table 8.1. *List of generated MC samples used to model different signal (upper part of the table) and SM-background processes (bottom part of the table) contributing to the $b\bar{b}\tau^+\tau^-$ final state. For each generated sample, the generator and the PDF used for calculating the ME are listed, as well as the generator and the tune used for simulating the PS and hadronisation processes. For processes where the PS generator is not specified, the same generator is used to calculate the ME and to simulate the PS and hadronisation processes. The second column specifies at which order of perturbation theory in QCD the ME are calculated.*

Process	ME Order	Generator	Parton Shower	PDF	Tune
Signal processes:					
SM HH	NLO	MG5_aMC@NLO v2.6.1	HERWIG 7 [108]	CT10	UEEE5
$X \to HH$	LO	MG5_aMC@NLO v2.6.1	HERWIG 7	NNPDF23LO	MMHT2014 [206]
Background processes:					
Single top and $t\bar{t}$	NLO	POWHEG-BOX v2	PYTHIA 8.2	NNPDF23LO	A14
Z+jets, W+jets	NLO	SHERPA 2.2.1		NNPDF30NNLO	
Drell-Yan	NLO	SHERPA 2.2.1		NNPDF30NNLO	
ZZ, WZ, WW	NLO	SHERPA 2.2.1		NNPDF30NNLO	
ZH	NLO	POWHEG-BOX v2	PYTHIA 8.2	NNPDF30	AZNLO
$t\bar{t}H$	NLO	POWHEG-BOX v2	PYTHIA 8.2	NNPDF30	A14

8.2 Object and event selections

The object and event selections applied to the data and simulated samples that correspond to the 2017 and 2018 ATLAS data-taking differ from the $\tau_{\text{had}}\tau_{\text{had}}$-channel selection specified in Chapter 5 due to a different trigger configuration. Furthermore, as outlined in Chapter 4, several new offline reconstruction and identification methods are used for the results presented in this chapter, as will be discussed in the following. The triggers used to select events recorded during the 2017 and 2018 ATLAS data-taking are specified in Section 8.2.1, while novelties in the offline object and event selection are summarised in Section 8.2.2.

8.2.1 Online event selection

The same choice of triggers as that used for the results presented in Chapter 5 is made to select events that correspond to the 2015 and 2016 data-taking periods. The trigger configuration used to select events that correspond to the 2017 and 2018 data-taking is specified below.

*Single-τ_{had} trigger (*2017 *and* 2018 *data-taking)*
In order to pass the single-τ_{had} trigger [192], an event corresponding to the 2017 data-taking is required to have at least one τ_{had} candidate with $p_T >$ 160 GeV that satisfies the online medium BDT-based identification criteria and has 1-3 *fast tracks* [192], similar to the requirements that were used during the 2015 and 2016 data-taking. The STT corresponing to the 2018 data-taking, instead of fast tracks, requires 1-3 *precision tracks* [207]. Additionally, in selecting events recorded towards the end of the 2018 data-taking, a logical OR of two STTs is used, where the first STT is defined as above, while the second one employs the RNN-based online τ_{had}-ID.

*Di-τ_{had} trigger (*2017 *and* 2018 *data-taking)*
Similar to the STT, the di-τ_{had} triggers used for the 2018 data-taking also require 1-3 precision tracks per τ_{had} candidate. Additionally, a logical OR of the DTTs using the BDT- and RNN-based τ_{had}-IDs is used to select events recorded during the last periods of the 2018 data-taking. For the entire 2017 and 2018 dataset, two different versions of the DTT are used, referred to as the "L1Topo" and "4j12" DTTs. In both cases, the online p_T thresholds for the τ_{had} candidates are kept unchanged with respect to the DTT used in the 2015 and 2016 data-taking ($p_T > 35$ (25) GeV for the leading (sub-leading) candidate). The L1Topo version of the DTT requires the presence of an additional jet at L1 with $p_T > 25$ GeV and it also requires that the τ_{had} candidates are within a distance of less than 2.7 in ΔR at L1. The 4j12 version of the DTT requires the presence of two additional jets at L1, each with $p_T > 12$ GeV.

8.2.2 Offline object and event selection

All events that pass the online selection are considered for the analysis. The selection applied offline is to a large extent identical to the one given in Section 5.2, with several changes that are summarised below.

Particle-flow jets
Jets are reconstructed using the particle-flow algorithm, as mentioned in Section 4.4. The number of selected data and simulated events when using the particle-flow jets is found to be consistent with the results obtained when using the jet collection based on topo-clusters. The particle-flow algorithm, on the other hand, has been reported to improve the accuracy of the energy measurement of the charged hadrons [145], hence it is expected that the jet-related systematic uncertainties in the analysis will be smaller.

Deep Learning b-tagging algorithm: DL1r
The MV2c10 b-tagging algorithm is replaced by the DL1r algorithm, as mentioned in Section 4.5. The same working point, corresponding to a 70% efficiency for true b-jets in simulated $t\bar{t}$ events, is used. The DL1r tagger improves the b-tagging performance at high p_T [151]. Parameterised truth-tagging, discussed in Section 5.2.2, is not used for the results presented in this chapter.

Rejection of electrons reconstructed as τ_{had} candidates
As stated in Section 5.2.2, for the results presented in Chapters 5–7, the τ_{had} candidates with one charged track are rejected if they overlap with an identified electron within $\Delta R < 0.4$. This requirement is replaced by the BDT-based electron-veto algorithm, which provides a higher efficiency (95%) for the true-τ_{had} candidates, while maintaining a high rejection of fake-τ_{had} candidates reconstructed from detector signals produced by electrons.

Recurrent neural network (RNN) τ_{had}-ID algorithm
The BDT-based τ_{had}-ID is replaced by the RNN-based algorithm, as mentioned in Section 4.7.2. The comparison of the performance of the two algorithms and the defined working points are shown in Figure 4.11. Due to a significantly better rejection of the quark- and gluon-initiated jets that are misidentified as τ_{had} candidates when using the RNN tagger, looser identification criteria are used for the results presented in this chapter (loose working point) than the τ_{had}-ID criteria used for the results presented in Chapters 5–7 (medium working point). A looser working point allows for increasing the signal selection efficiency while approximately maintaining the level of rejection of events with fake-τ_{had} candidates.

Fail-τ_{had} candidates
In order to define control regions used to estimate important backgrounds containing fake-τ_{had} objects, events containing fail-τ_{had} candidates are also con-

sidered. However, as a consequence of the change of the τ_{had}-ID algorithm, the definition of these objects for the results presented in this chapter differs from the definition given in Section 5.2.2. A fail-τ_{had} candidate is now defined as a candidate that fails the loose but passes the very-loose RNN τ_{had}-ID criteria [157]. The very-loose working point corresponds to a 95% efficiency for the true-τ_{had} candidates.

Step 1 of the overlap removal procedure presented in Section 5.2.3, the (random) fail-τ_{had} selection given in Section 5.2.4, and Step 2 of the overlap removal specified by Equation (5.2) are all kept the same as for the results based on the partial Run 2 dataset, with the exception of the updated detector-object definitions given above. The event selection criteria applied to the data and simulated events that correspond to the 2015 and 2016 data-taking, given by Tables 5.5 and 5.6, are kept unchanged, also with the exception of the updated detector-object definitions given above. The selection criteria applied to the data and simulated events that correspond to the 2017 and 2018 data-taking are kept the same for the STT category, while they are modified for the DTT category, as described in the following.

Selection criteria for the DTT-category events

Events failing the STT are checked if they pass one of the DTTs. If that is the case, events are further required to have two trigger-matched[1] τ_{had} candidates (each can be either loose or fail-τ_{had}) with $p_T > 40\ (30)$ GeV for the leading (sub-leading) candidate. Events that pass these requirements are classified based on the p_T of the sub-leading jet (after the full overlap removal), as illustrated in Figure 8.1, into "4j12" (sub-leading jet $p_T > 45$ GeV) and "L1Topo" (sub-leading jet $p_T < 45$ GeV) categories.

- **DTT 4j12 category:** Events with the sub-leading jet $p_T > 45$ GeV are required to pass the 4j12 version of the DTT, which requires two additional L1 jets with p_T greater than 12 GeV each. Due to the poor jet-p_T resolution at L1, the full trigger efficiency is reached only if the two leading offline jets have $p_T > 45$ GeV, which is thus required.
- **DTT L1Topo category:** Events with the sub-leading jet $p_T < 45$ GeV are required to pass the L1Topo version of the DTT, which requires an additional L1 jet with a p_T greater than 25 GeV. The leading offline jet is required to have a minimum p_T of 80 GeV. At least one more jet with $p_T > 20$ GeV is required due to the event topology of interest. In addition, the L1Topo DTT requires the L1 τ_{had} candidates to be within a distance of less than 2.7 in ΔR, which is translated into requiring the offline τ_{had} candidates to be within $\Delta R < 2.5$.

[1] The $\Delta R < 0.2$ matching criterion is used.

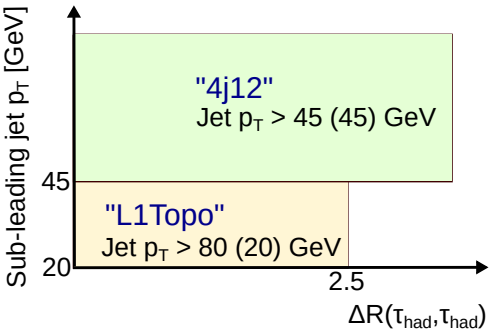

Figure 8.1. Illustration of the selection of events that correspond to the 2017 and 2018 data-taking in the DTT category. Events with the sub-leading jet $p_T > 45$ GeV ($p_T < 45$ GeV) are required to pass the "4j12" ("L1Topo") version of the DTT. In the L1Topo category, events must satisfy $\Delta R(\tau_{\text{had}}, \tau_{\text{had}}) < 2.5$ and they must have two jets with $p_T > 80$ (20) GeV for the leading (sub-leading) jet.

Events are categorised as before, based on the number of b-tagged jets and on whether the visible τ-lepton decay products have opposite-sign, or same-sign electric charges. The SR is defined as the OS 2-b-tag region where both τ_{had} candidates in each event satisfy the loose identification criteria.

8.3 Revised background estimation

This section describes modifications in the methods used to estimate the multijet background and $t\bar{t}$ background with fake-τ_{had} candidates in the $\tau_{\text{had}}\tau_{\text{had}}$ channel. In addition, modifications in the definition of the CR used to determine the normalisation of the Z+hf background are discussed as well.

8.3.1 Revised multijet estimation

The estimation of the multijet background in the $\tau_{\text{had}}\tau_{\text{had}}$ channel presented in Section 5.3.3 is modified in order to simplify the parameterisation of the fake factors shown in Figure 5.6, and thus reduce their statistical uncertainties.

In the modified approach, the DTT-category events from the SS region are used to calculate two sets of fake factors, FF_0 and FF_1, defined as

$$FF_{0,i} = \frac{N^{SS}_{\text{data}-\text{MC(non-multijet)},i}\,\text{(loose, loose)}}{N^{SS}_{\text{data}-\text{MC(non-multijet)},i}\,\text{(fail, loose)}} \text{ in the bin } i \text{ of } p_T^{\text{leading } \tau_{\text{had}}}, \quad (8.1)$$

$$FF_{1,i} = \frac{N^{SS}_{\text{data}-\text{MC(non-multijet)},i}\,\text{(loose, loose)}}{N^{SS}_{\text{data}-\text{MC(non-multijet)},i}\,\text{(loose, fail)}} \text{ in the bin } i \text{ of } p_T^{\text{sub-leading } \tau_{\text{had}}}, \quad (8.2)$$

where N_i^{SS} is the number of events in a bin i in the SS region with defined identification criteria (loose or fail-τ_{had}) for the leading and sub-leading τ_{had} candidates, given in that order. The first set of fake factors, FF_0, are binned in the p_T of the leading τ_{had}, while the second set, FF_1, are binned in the p_T of the sub-leading τ_{had} candidate. Events with two fail-τ_{had} candidates are not considered due to technical reasons[2]. The definitions of the two sets of FFs are schematically shown in Figure 8.2.

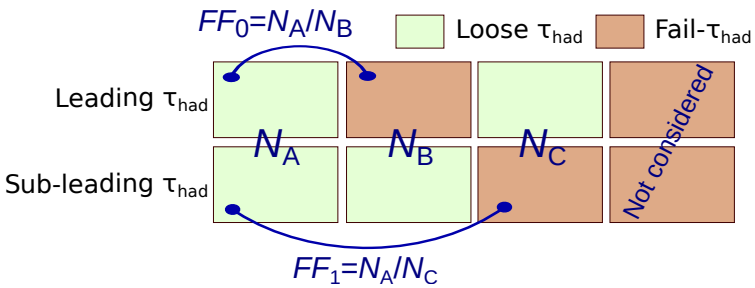

Figure 8.2. Graphical illustration of the calculation of the two independent sets of fake factors, FF_0 and FF_1, where the former (latter) is calculated by taking the ratio of the number of events where both τ_{had} candidates satisfy the loose identification criteria to the number of events where this requirement for the leading (sub-leading) τ_{had} candidate is replaced by the fail-τ_{had} identification criteria, as defined by Equation (8.1) ((8.2)), after subtracting the number of simulated non-multijet events from the number of data events in all regions.

A multijet estimation is obtained by applying the first set of fake factors, FF_0, to the OS events where the leading (sub-leading) τ_{had} candidate satisfies the fail- (loose) τ_{had} identification criteria. Another independent multijet estimation is obtained by applying FF_1 to the OS events where the leading (sub-leading) τ_{had} candidate satisfies the loose (fail-) τ_{had} identification criteria. Averaging the two results reduces the statistical uncertainty of the prediction compared to using only one of them, since more events are available to model the multijet background in the OS region.

This way, instead of four two-dimensional fake factors (binned in p_T of the leading and sub-leading τ_{had} candidates, for the four combinations of the τ_{had} prongness), as defined in Section 5.3.3, four one-dimensional fake factors (FF_0 and FF_1, each separately for the 1- and 3-prong candidates) are used. Given that the statistical uncertainty of FFs is mostly determined by the statistical uncertainty of the numerator in the FF definition, the size of the statistical uncertainty is approximately the same for the p_T-inclusive two-

[2]As part of the centralised production of the majority of the simulated background samples in the ATLAS experiment, in order to reduce their size and the time needed to process all events, the samples are pre-processed and an event selection is applied. For that reason, only events with at least one loose τ_{had} candidate are available for the analysis discussed here.

dimensional and one-dimensional FFs, while finer binning is possible for the latter.

Furthermore, it can be argued that FF_0 and FF_1 are expected to be the same and that they can be combined. Without changing any of the assumptions based on which the FF method used here is defined[3], a set of "inclusive" fake factors can be calculated as

$$FF_{\text{Incl},i} = \frac{1}{2} \frac{N\left[\text{loose } \tau_{\text{had}}\right]^{\text{SS}}_{\text{data}-\text{MC(non}-\text{multijet)},i}(\text{events with 2 loose } \tau_{\text{had}})}{N\left[\text{fail-}\tau_{\text{had}}\right]^{\text{SS}}_{\text{data}-\text{MC(non}-\text{multijet)},i}(\text{events with 1 fail-}\tau_{\text{had}})}, \tag{8.3}$$

where the numerator here represents the number of loose τ_{had} in the p_T range of a bin i in the multijet events where both τ_{had} candidates satisfy the loose identification criteria. Similarly, the denominator represents the number of fail-τ_{had} in the same p_T range in the multijet events that have one loose and one fail-τ_{had} candidate. The number of τ_{had} candidates in the multijet events is obtained by subtracting the number of estimated τ_{had} candidates in the simulated non-multijet background processes from the number of τ_{had} candidates in the data. The definition of $FF_{\text{Incl},i}$ is equivalent to averaging $FF_{0,i}$ and $FF_{1,i}$ weighted by their statistical contribution in the p_T range of the bin i. In order to validate conclusions based on which FF_{Incl} is defined, the dependencies of FF_0, FF_1 and FF_{Incl} on the τ_{had}-candidate p_T are compared in the 0-b-tag and 1-b-tag SS CRs, as shown in Figure 8.3, and they are found to be compatible within statistical uncertainties.

To obtain the final multijet estimation for the DTT-category events, $FF_{\text{Incl},i}$ are applied to the OS events with one loose and one fail-τ_{had}, based on the p_T of the fail-τ_{had} candidate. Fake factors derived in the 1-b-tag region are used in the 2-b-tag region due to the lack of statistics, and thus the STT+DTT $1 \rightarrow 2$-b-tag transfer factors are applied, following the same approach as that defined in Figure 5.5.

The modified approach for estimating the multijet background leads to a nominal prediction that is statistically compatible with the results obtained when using the method defined in Section 5.3.3. This is shown in Appendix A: Figure A.6. However, the statistical uncertainties of the FFs in the DTT category are significantly reduced and a finer binning is possible for the modified approach.

The multijet estimation is validated in the 1-b-tag OS and the 2-b-tag SS validation regions, as shown in Figure 8.4. Additional plots are shown in Appendix A: Figures A.7 and A.8.

[3]The FF method defined in Section 5.3.3, as well as the modified method discussed here, are both based on assuming that the FFs that correspond to quark- and gluon-initiated jets misidentified as τ_{had} candidates in multijet events are the same between the OS and SS regions. This implies assuming that the fractions of jets initiated by light-flavour quarks, heavy-flavour quarks and gluons are the same in the OS and SS regions for the QCD processes, as well as that there are no significant charge correlations between the two fake-τ_{had} candidates.

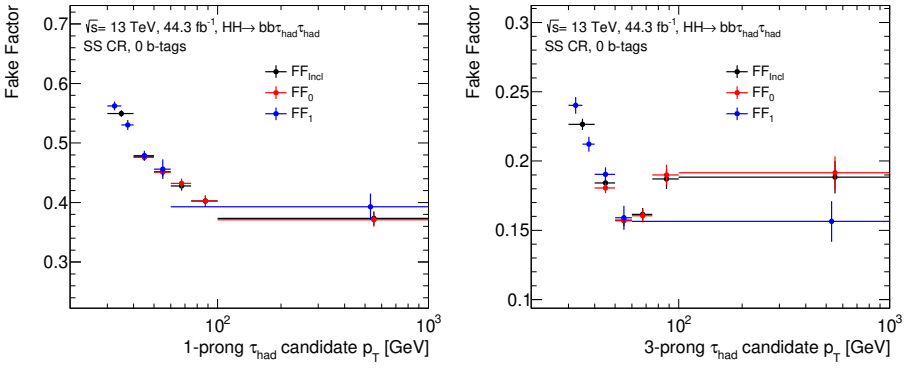

(a) *0-b-tag SS CR*

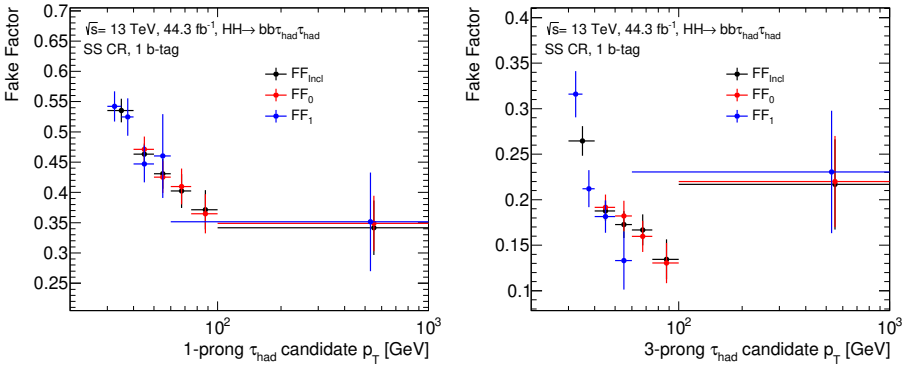

(b) *1-b-tag SS CR*

Figure 8.3. Comparison of the fake factors defined by Equations (8.1), (8.2) and (8.3) for the 1-prong (3-prong) τ_{had} candidates on the left-hand (right-hand) side, obtained from the data and simulated samples that correspond to the 2017 data-taking. The results that correspond to the 2015+2016 and 2018 data-taking periods are given in Appendix A: Figure A.5. The binning used for the three sets of fake factors differs due to different p_T spectra of the leading and sub-leading τ_{had} candidates.

8.3.2 Revised estimation of the $t\bar{t}$ background with fake-τ_{had} candidates

For the results presented in Chapters 5–7, the estimation of the $t\bar{t}$ background where at least one of the selected τ_{had} candidates is a misidentified quark- or gluon jet was based on the Fake Rate (FR) method presented in Section 5.3.4. As discussed in Section 5.5.3, the pre-fit normalisation uncertainty on the obtained prediction in the $\tau_{\text{had}}\tau_{\text{had}}$-channel SR for the 2015+2016 dataset is $\approx \pm 100\%$. Although these uncertainties are constrained in the final fit, a 100% normalisation uncertainty can have an impact on the quality of the fit. Additionally, two approximations were made in developing the method presented in

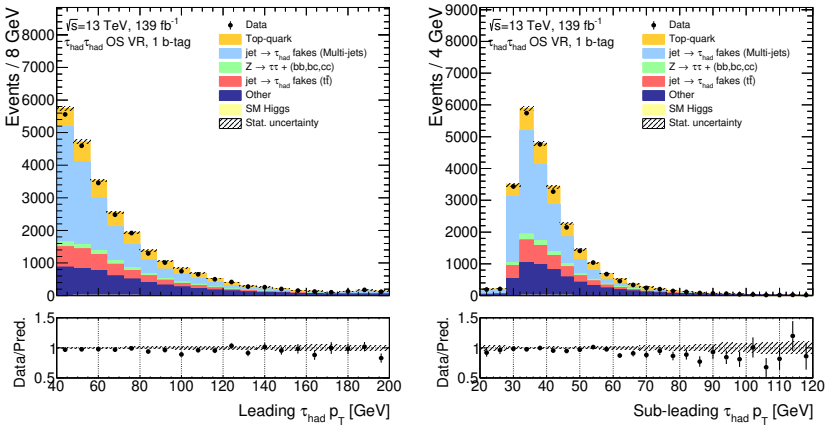

(a) *OS 1-b-tag validation region*

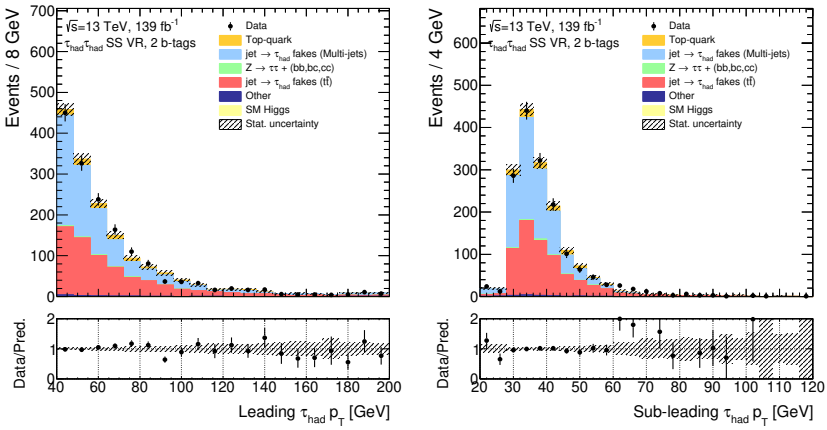

(b) *SS 2-b-tag validation region*

Figure 8.4. Distributions of the leading (sub-leading) τ_{had}-candidate p_T are shown on the left-hand (right-hand) side, in two different regions used to validate the multi-jet background estimation. The multijet background is estimated using the method described in this section, while the $t\bar{t}$ background with fake-τ_{had} candidates is obtained from simulation. The distributions include only the statistical uncertainties in the background estimation.

Section 5.3.4, namely: (1) the DTT-category selection was used for all events in the MC $t\bar{t}$ template to which the fake rates are applied since the fraction of STT-category events is small and (2) fake rates were measured after applying a lower cut on the τ_{had}-ID score, assuming the same efficiency of this cut in simulated and data events.

Modifications to the *FR* method discussed here include removing the two approximations listed above and improving the statistical and shape precision

of the prediction. In addition, an outlook for reducing the total uncertainty on the obtained prediction of this background component is discussed.

Removing the lower cut on the τ_{had}-ID score

In the *FR* method, fake rates are measured in data[4] after which they are applied to simulated events. As already mentioned, if a lower cut on the τ_{had}-ID score is applied when using the *FR* method, it is assumed that this lower cut has the same efficiency in data and simulated events. While the very-loose RNN τ_{had}-ID requirement is optimised to reject only 5% of the true-τ_{had} candidates, the rejection of fake-τ_{had} candidates is already at around 90%, which can be seen from Figure 4.11. In this case, an uncertainty of x% in the efficiency of the very-loose identification requirement on simulated fake-τ_{had} candidates translates into an uncertainty of $\sim 10x$% in the size of the obtained MC template to which the fake rates are applied. For this reason, the definition of a fail-τ_{had} candidate is changed[5] by removing the lower identification requirement. The complete object selection, overlap removal and the event selection are modified to take this change into account, while remaining the same as in the baseline approach in all other aspects.

Measurement of fake rates in the $\tau_{\text{lep}}\tau_{\text{had}}$-channel $t\bar{t}$ control region

Similar to the strategy outlined in Section 5.3.4, fake rates are measured in a dedicated $t\bar{t}$ *FR* CR defined on top of the $\tau_{\text{lep}}\tau_{\text{had}}$ SLT-category selection. The $\tau_{\text{lep}}\tau_{\text{had}}$ SLT selection here is defined as in Tables 5.5 and 5.6, with the exception of the updated detector-object definitions discussed in Section 8.2.2, and the removal of the lower cut on the τ_{had}-ID score discussed above. The $t\bar{t}$ *FR* CR is then defined as the OS 2-*b*-tag region with 50 GeV$< m_T^W <$ 100 GeV.

After removing the lower cut on the τ_{had}-ID score, the composition of fake-τ_{had} candidates in terms of their origin, in the simulated $t\bar{t}$ samples, is checked and found to be the same between the CR and the $\tau_{\text{had}}\tau_{\text{had}}$ OS 2-*b*-tag region in which the fake rates are applied, as shown in Appendix B: Figure B.1, which is necessary given that fake rates depend strongly on the fake-τ_{had} origin, as shown in Appendix B: Figures B.2 and B.3.

Similar to Section 5.3.4, both the offline τ_{had}-ID and τ_{had} trigger requirements are considered when calculating *FR*s. However, in this case two sets of

[4]This is only partly true given that the number of events with fake-τ_{had} candidates in data is usually estimated by subtracting the contribution of events with true-τ_{had} candidates obtained using simulation from the total number of data events.

[5]This change in the definition of the fail-τ_{had} objects is made only for the purpose of the *FR* method given that it increases significantly the size of the simulated and data samples, as well as the running time needed to perform the analysis.

fake rates are measured:

$$FR_i = \frac{N_{\text{data}-\text{MC(all except } t\bar{t} \text{ with fake-}\tau_{\text{had}}),i} \text{ (loose trigger-matched } \tau_{\text{had}})}{N_{\text{data}-\text{MC(all except } t\bar{t} \text{ with fake-}\tau_{\text{had}}),i} \text{ (all } \tau_{\text{had}})}, \quad (8.4)$$

$$FR_i' = \frac{N_{\text{data}-\text{MC(all except } t\bar{t} \text{ with fake-}\tau_{\text{had}}),i} \text{ (loose } \tau_{\text{had}})}{N_{\text{data}-\text{MC(all except } t\bar{t} \text{ with fake-}\tau_{\text{had}}),i} \text{ (all } \tau_{\text{had}})}, \quad (8.5)$$

where the first set of fake rates represents probabilities for a reconstructed fake-τ_{had} candidate to pass the corresponding "resurrected" τ_{had} trigger[6] and the loose offline τ_{had}-ID. The second set of fake rates, denoted FR', represents probabilities for a reconstructed fake-τ_{had} candidate to pass the loose offline τ_{had}-ID, without imposing any τ_{had} trigger requirements. The application of the fake rates is discussed later.

Plots showing simulation-to-data comparisons as a function of the τ_{had} p_T in the $t\bar{t}$ FR CR are given in Figure 8.5. The upper set of plots shows the modelling after applying the loose offline τ_{had}-ID to the τ_{had} candidates and requiring them to be trigger-matched (FR numerator). The middle set of plots shows the modelling after applying only the offline τ_{had}-ID (FR' numerator). Finally, the bottom set of plots shows the modelling before applying any of the τ_{had}-ID and τ_{had} trigger requirements (FR and FR' denominator). The obtained fake rates are shown in Figure 8.6.

Fake rates in the SS region

Fake rates are also measured in the SS $t\bar{t}$ FR CR, which is defined equivalently to the CR discussed above, but with requiring that the selected lepton and the τ_{had} candidate have the same-sign electric charges. The simulation-to-data comparisons in the SS $t\bar{t}$ FR CR are shown in Appendix B: Figure B.4. The obtained fake rates are compared between the OS and SS regions in Figure 8.7. Although fake rates in the SS region can be measured with significantly smaller uncertainties due to the higher fraction of $t\bar{t}$ events with fake-τ_{had} candidates with respect to the OS region, these fake rates cannot be used to obtain the background estimation in the OS region. This is due to strong charge correlations between the visible τ-lepton decay products, which can be

[6]Requiring an offline τ_{had} candidate to be geometrically matched to a trigger-level τ_{had} object implies that the event must pass the trigger requirements. When measuring fake rates for the DTT category, two "resurrected" triggers are used. These triggers require one τ_{had} candidate at trigger level satisfying the online τ_{had}-ID, for the first trigger with $p_T > 25$ GeV (HLT_tau25) and for the second trigger with $p_T > 35$ GeV (HLT_tau35), representing the "two legs" of the nominal di-τ_{had} trigger at HLT. These two triggers have extremely high rates and thus they were pre-scaled during the data-taking, but the corresponding trigger decision is resurrected for all recorded events (in this case for all events satisfying the $t\bar{t}$ FR CR selection) and used to measure the fake rates per fake-τ_{had} candidate. When measuring fake rates for the STT category, HLT_tau35 trigger is used instead of triggers with higher p_T thresholds for simplicity, but the corresponding STT-category p_T requirements are applied offline (as in the baseline selection: 20 GeV above the corresponding online STT p_T threshold).

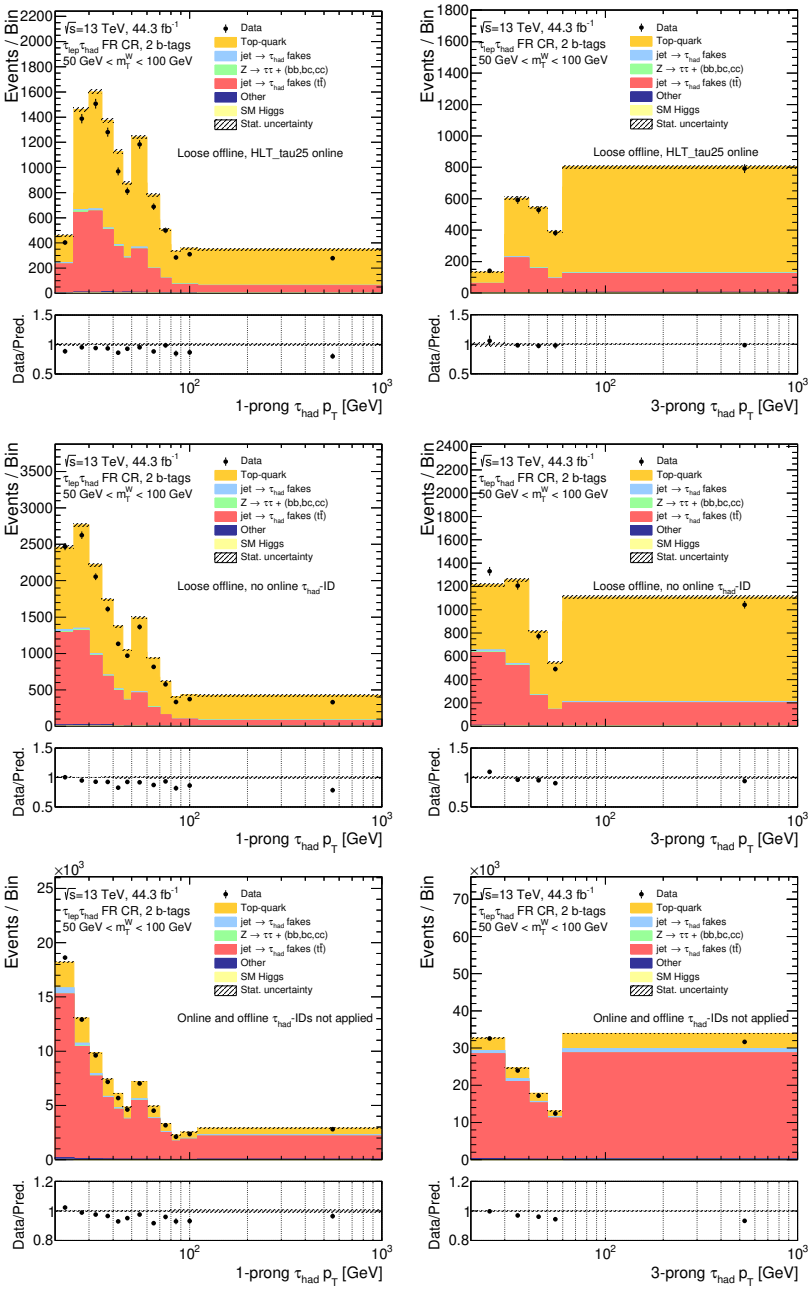

Figure 8.5. Distributions of the τ_{had}-candidate p_T in the OS $t\bar{t}$ *FR* CR, corresponding to the 2017 data-taking period, used to derive fake rates given by Equations (8.4) and (8.5) for 1-prong (left-hand side) and 3-prong (right-hand side) τ_{had} candidates. All backgrounds but the simulated $t\bar{t}$ background with fake-τ_{had} objects (red) are subtracted from data before the set of fake rates FR (FR') are calculated by taking the ratios of the top and bottom (middle and bottom) histograms. The distributions include only the statistical uncertainties.

seen from Figure 5.2: a jet produced in a hadronic $W^{\pm}$ decay is more likely to fake a $\tau_{\text{had}}^{\pm}$ than a $\tau_{\text{had}}^{\mp}$.

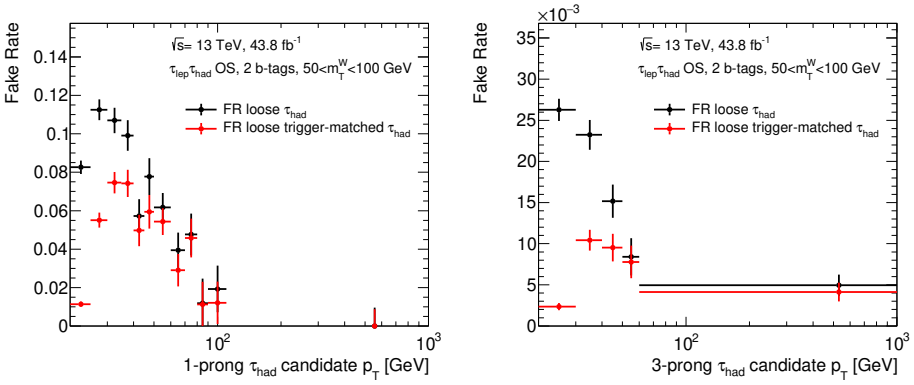

(a) *1-prong* **(b)** *3-prong*

Figure 8.6. Fake rates corresponding to the 2017 data-taking period, measured as a function of the τ_{had}-candidate p_T in the OS $t\bar{t}$ *FR* CR, as defined by Equations (8.4) and (8.5) when accounting for only the offline τ_{had}-ID (FR' – black) and when accounting for offline τ_{had}-ID and requiring the τ_{had} candidate to be trigger-matched (FR – red), separately for (**a**) 1-prong and (**b**) 3-prong τ_{had} candidates.

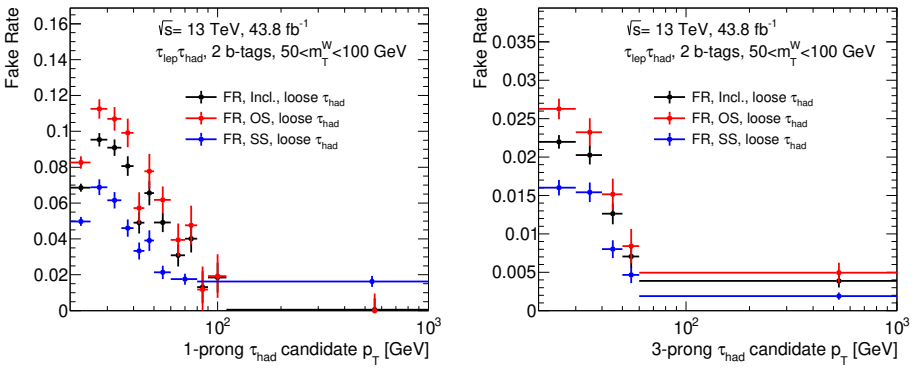

(a) *1-prong* **(b)** *3-prong*

Figure 8.7. Fake rates corresponding to the 2017 data-taking period, measured as a function of the τ_{had}-candidate p_T in the OS (red), SS (blue) and OS+SS $t\bar{t}$ *FR* CR (black), as defined by Equation (8.5), i.e. when accounting for only the offline τ_{had}-ID, separately for (**a**) 1-prong and (**b**) 3-prong τ_{had} candidates.

Modelling of the $t\bar{t}$ background

The largest uncertainty in the measured fake rates comes from the subtraction of simulated $t\bar{t}$ events with true-τ_{had} candidates and other simulated non-$t\bar{t}$ backgrounds. The fraction of the $t\bar{t}$ background with true-τ_{had} candidates accounts for more than 80% of the total expected background at high p_T in the OS $t\bar{t}$ *FR* CR after applying the loose offline τ_{had}-ID and trigger matching requirements, as shown in Figure 8.5. Additionally, as it can be seen from Figure 8.5 (bottom plots), the $t\bar{t}$ background is mismodelled even prior to applying offline and trigger matching τ_{had}-ID requirements, which leads to mismodelling of fake rates, in particular to an underestimate of fake rates at high p_T. One of the prospects for improving the measurement of fake rates is to constrain the normalisation and shape of the $t\bar{t}$ background containing true-τ_{had} candidates from data: e.g. by re-weighting the simulated $t\bar{t}$ background to the data after subtracting the non-$t\bar{t}$ backgrounds, prior to applying offline and trigger matching τ_{had}-ID requirements; or by performing a template fit to the data after applying the offline and trigger matching τ_{had}-ID requirements. Both of these proposed methods come with certain caveats and thus they must be carefully tested. The results of these studies are however not finalised at the time of writing this thesis.

Application of the fake rates in the $\tau_{\text{had}}\tau_{\text{had}}$ channel

The measured fake rates are applied per fake-τ_{had} candidate in the simulated $t\bar{t}$ MC template, which is obtained using a similar selection to that described in Section 5.3.4. The trigger requirements are removed from the object and event selections given that they are modelled by the fake rates themselves. The event selection is performed by choosing events with exactly two loose τ_{had} candidates or exactly one loose τ_{had} candidate. For the latter, following the nominal selection, one fail-τ_{had} candidate is selected in addition, chosen randomly if more fail-τ_{had} candidates are found in the event. Events with two fail-τ_{had} candidates are not considered due to technical reasons, as explained in Section 8.3.1.

Mimicking the DTT- and STT-category selection criteria

Given that the trigger requirements are removed from the event and object selections, the trigger information cannot be used to decide to which category an event should be assigned to. For that reason, the categorisation of events is approximated by the following criteria. Prior to selecting two τ_{had} candidates, an event is assigned to the STT category if there is a loose or fail-τ_{had} candidate with a p_T greater than the STT threshold, otherwise the event is assigned to the DTT category. For the DTT-category events corresponding to the 2017 and 2018 data-taking, an event is assigned to the 4j12 category if the sub-leading jet p_T is greater than 45 GeV, otherwise the L1Topo DTT category selection is applied.

Events are further divided into 3 categories:

- **TF**: Events where the leading (sub-leading) τ_{had} is true (fake).
- **FT**: Events where the leading (sub-leading) τ_{had} is fake (true).
- **FF**: Events with two fake-τ_{had} candidates.

While it is straightforward to apply the fake rates to the TF and FT events, the estimation in the FF category cannot be obtained by simply applying the product of two fake rates given that the events with two fail-τ_{had} candidates are not included in the $t\bar{t}$ MC template, as mentioned above. For that reason, a set of scale factors (SFs) are derived in addition to fake rates. The scale factors are derived as ratios of the fake rates measured in data, as discussed above, to the "MC fake rates", i.e. fake rates obtained directly from the simulated samples as

$$FR_i^{\text{MC}} = \frac{N_{\text{MC}(t\bar{t}\text{ with fake-}\tau_{\text{had}}),i}\text{ (loose trigger-matched }\tau_{\text{had}})}{N_{\text{MC}(t\bar{t}\text{ with fake-}\tau_{\text{had}}),i}\text{ (all }\tau_{\text{had}})}, \tag{8.6}$$

$$FR_i^{\prime\text{MC}} = \frac{N_{\text{MC}(t\bar{t}\text{ with fake-}\tau_{\text{had}}),i}\text{ (loose }\tau_{\text{had}})}{N_{\text{MC}(t\bar{t}\text{ with fake-}\tau_{\text{had}}),i}\text{ (all }\tau_{\text{had}})}, \tag{8.7}$$

The obtained scale factors ($SF_i = FR_i/FR_i^{\text{MC}}$ and $SF_i^{\prime} = FR_i^{\prime}/FR_i^{\prime\text{MC}}$) are applied to loose fake-τ_{had} candidates in the FF category to correct the efficiency of the loose τ_{had}-ID and the trigger matching requirements, where the latter is included only if required. The corresponding fake rate is then applied to the other fake-τ_{had} candidate. If both fake-τ_{had} candidates satisfy the loose τ_{had}-ID and the trigger matching criteria, a random choice is made to which one the SF is applied. The corresponding fake rate in that case is applied to the remaining τ_{had} candidate. Additionally, given that the charge correlations between the two fake-τ_{had} candidates in the FF category are smeared out[7], the fake rates and scale factors used in this case are calculated inclusively in the OS+SS $t\bar{t}$ FR CR. The application of the FR method in all three categories of the $t\bar{t}$ events with fake-τ_{had} (TF, FT and FF) and for both the DTT and STT categories separately is schematically depicted in Figure 8.8.

The background modelling plots in the $\tau_{\text{had}}\tau_{\text{had}}$-channel $t\bar{t}$ VR, in this case defined as the OS 2-b-tag region with $m_{bb} > 150$ GeV and $m_{\tau\tau}^{\text{MMC}} > 130$ GeV, are shown in Figure 8.9. The plots on the left-hand side show the $t\bar{t}$ background with fake-τ_{had} obtained directly from simulation. As a comparison, in the plots on the right-hand side, the $t\bar{t}$ background with fake-τ_{had} is obtained using the FR method. A slightly better agreement between the background prediction and the data is obtained when using the FR method. In addition, the statistical uncertainty of the prediction when using the FR method is smaller by construction and the systematic uncertainties are well defined. The main challenge in improving the method presented here resides in the modelling of

[7] This is because the two jets misidentified as τ_{had} candidates can come from the same W boson.

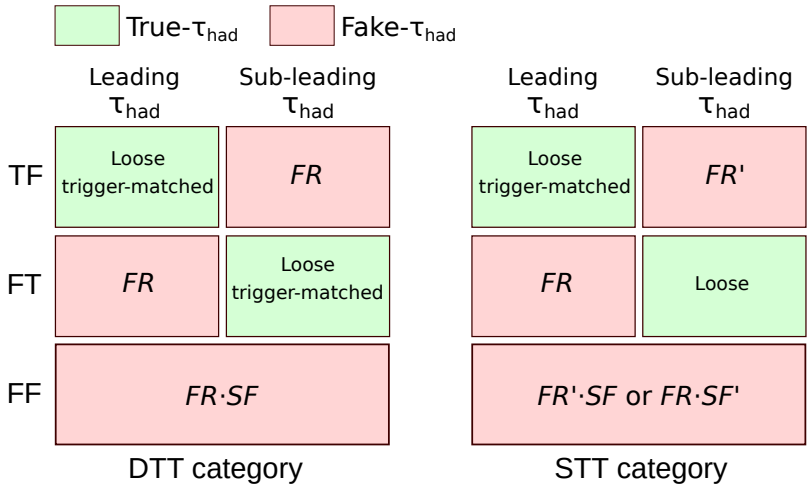

Figure 8.8. Schematic depiction of the application of the measured fake rates to the simulated $t\bar{t}$ events with fake-τ_{had} candidates in the dedicated MC $t\bar{t}$ template. Fake rates are applied to fake-τ_{had} based on their p_T, while taking into account if the selected τ_{had} candidate would have been required to be trigger-matched in order to pass the $\tau_{\text{had}}\tau_{\text{had}}$-channel SR selection ($FR$), or not ($FR'$). True-$\tau_{\text{had}}$ candidates corresponding to the DTT category, or to the leading τ_{had} candidate in the STT category, are required to be trigger-matched to the HLT_tau25 trigger (sub-leading τ_{had} in the DTT category) or HLT_tau35 (leading τ_{had}) and to pass the offline loose τ_{had}-ID. For the events where both selected τ_{had} candidates are fake (FF), the product of a fake rate and a scale factor is applied given that events with two fail-τ_{had} candidates are not available in the $t\bar{t}$ MC template. Scale factors are always applied to loose fail-τ_{had} candidates, while in events where both τ_{had} candidates satisfy the loose τ_{had}-ID, a random choice is made to which one the SF is applied. The corresponding fake rate in that case is applied to the remaining τ_{had} candidate.

the $t\bar{t}$ background with true-τ_{had} candidates to reduce the systematic uncertainties coming from the subtraction of this background from the data.

8.3.3 Modified Z+heavy flavour jets CR

The Z+heavy flavour jets CR is used to constrain the normalisation of the $Z \to \tau\tau$+hf background from data, as discussed in Section 5.3.5. While the motivation for defining the CR remains the same as that discussed in Chapter 5, the definition of the CR is changed.

To increase the statistical precision, both $Z \to \mu\mu$ and $Z \to ee$ decay channels are now included. Furthermore, the definition of the CR is harmonised with the $HH \to b\bar{b}\ell^+\ell^-$ analysis for the purpose of a future statistical combination of the results.

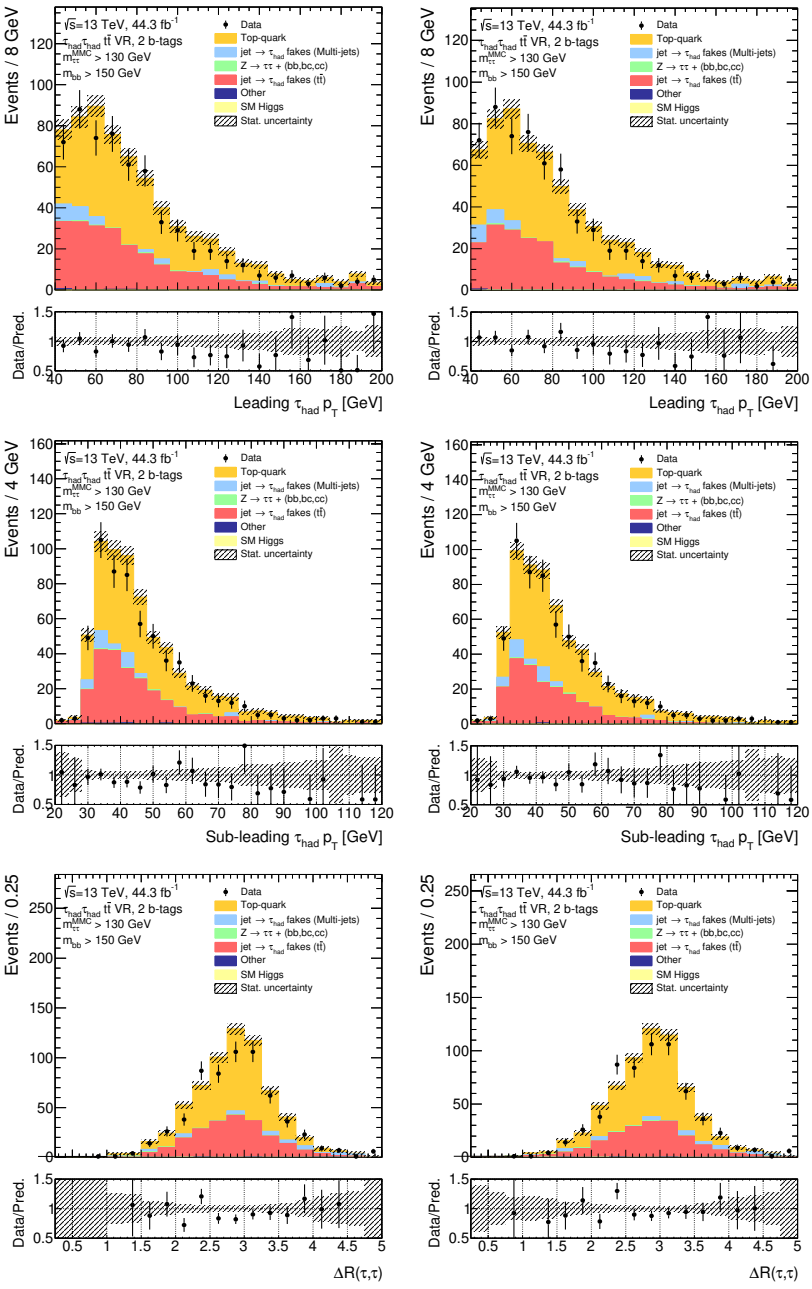

Figure 8.9. Distributions of the leading and sub-leading τ_{had}-candidate p_T and the $\Delta R(\tau,\tau)$ in the $\tau_{\text{had}}\tau_{\text{had}}$-channel $t\bar{t}$ VR, corresponding to the 2017 data-taking period. Plots on the left-hand (right-hand) side show the background modelling when using the estimation of the $t\bar{t}$ background with fake-τ_{had} candidates directly from simulation (using the FR method, as described above). The distributions include only the statistical uncertainties.

Events are required to pass a single-lepton trigger or a dilepton trigger, to have exactly two electrons or muons with $p_T > 9$ GeV (and a p_T that is 1 GeV greater than the corresponding trigger threshold for the trigger-matched leptons) and to have exactly two b-tagged jets with $p_T > 20$ GeV. The leptons are required to have opposite-sign electric charges. The object reconstruction and identification techniques used match those listed in Section 8.2.2. Furthermore, the invariant mass of the two selected leptons, $m_{\ell\ell}$, is required to be between 75 GeV and 110 GeV, while the m_{bb} mass is required to be greater than 210 GeV, or less than 40 GeV.

The prediction-to-data comparison of the dilepton invariant mass is shown in Figure 8.10. As already discussed in Section 5.3.5, the normalisation of the Z+hf background obtained from simulation is underestimated. After applying a normalisation factor of 1.29 the overall background modelling is significantly improved. This normalisation factor is obtained from the background-only-hypothesis profile likelihood fit to data when searching for the SM HH signal using the $m_{\ell\ell}$ distribution in the CR and the BDT score distribution in the $\tau_{\text{had}}\tau_{\text{had}}$ SR, and when considering only the statistical uncertainties in data. Systematic uncertainties have not yet been evaluated for this method. The normalisation factor is found to be compatible between the $Z \to ee$ and $Z \to \mu\mu$ channels.

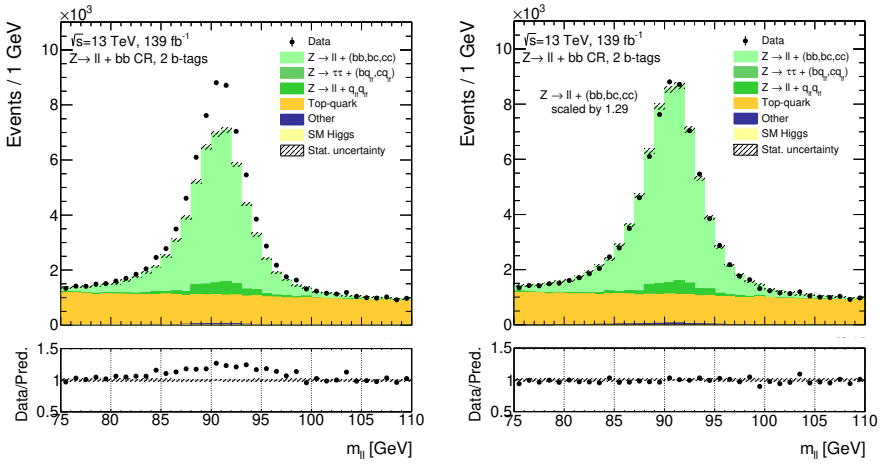

(a) *No scaling applied* **(b)** *Scaling applied*

Figure 8.10. Dilepton invariant mass in the $Z \to \ell\ell$+hf CR. The distributions are pre-fit and they include only the statistical uncertainties. The post-fit normalisation factor of 1.29 is applied to the pre-fit Z+hf background yield in subfigure (**b**).

8.4 Conclusion and outlook

This chapter presents the object and event selections applied in the $\tau_{\text{had}}\tau_{\text{had}}$ channel when considering the full Run 2 ATLAS dataset. Additionally, several studies aimed at revising the background estimation techniques presented in Chapter 5 are discussed. These mostly refer to the estimation of the multijet background and the $t\bar{t}$ background with fake-τ_{had} candidates in the $\tau_{\text{had}}\tau_{\text{had}}$ channel. However, the methods developed are yet to be fully optimised and finalised, after evaluating all potential systematic uncertainties.

Other means of improving the analysis strategy (e.g. optimising the signal and control regions, testing new multivariate-analysis approaches, revising the fit strategy, etc.) are explored as well in order to improve the sensitivity to the signal processes. These studies are however still ongoing and they are not presented in this thesis.

Conclusion

This thesis discusses the pair production of Higgs bosons in the final state with two bottom quarks and two τ leptons in the ATLAS experiment at the LHC. As stated throughout the thesis, non-resonant pair production of Higgs bosons is directly related to the shape of the Higgs potential, and therefore it is essential for probing the exact nature of electroweak symmetry breaking. Resonant pair production is searched for as an attempt to establish physics beyond the SM at the LHC.

Searches for pair production of Higgs bosons in the $b\bar{b}\tau^+\tau^-$ final state based on 36.1 fb^{-1} of 13 TeV pp collision ATLAS data recorded in 2015 and 2016, originally reported in Ref. [15], are presented first. Non-resonant pair production is searched for assuming the SM Higgs boson couplings, while generic narrow-width spin-0 resonances, X, and spin-2 Kaluza-Klein excitations of the graviton in the bulk Randall-Sundrum model, G_{KK}, decaying into pairs of Higgs bosons, are searched for in the mass range between 260 GeV and 1 TeV. Important contributions from background processes in which quark- or gluon-initiated jets are misidentified as hadronically-decaying τ leptons are estimated using data-driven techniques, while other backgrounds are estimated using simulation. Boosted Decision Tree classification is used to maximise the sensitivity of the analysis to the signal processes.

Given that no statistically significant excess over the expected background is found in any of the searches, upper limits on the production cross-section are set for each of the assumed signals. The observed (expected) 95% CL upper limit on the non-resonant Higgs boson pair production cross-section times the $b\bar{b}\tau^+\tau^-$ branching ratio, when assuming the SM Higgs boson couplings, is 12.7 (14.8) times the SM expectation, representing the most stringent limit set by an individual channel based on the 2015 and 2016 LHC data, in both the ATLAS and CMS experiments. The scalar resonance, when interpreted as a CP-even heavy Higgs boson in the hMSSM benchmark scenario with $\tan\beta = 2$, is excluded at 95% CL for the mass range of 305 GeV $< m_X <$ 402 GeV. The spin-2 G_{KK}, assuming $k/\bar{M}_{\text{pl}} = 1$ ($k/\bar{M}_{\text{pl}} = 2$), is excluded for 325 GeV $< m_{G_{\text{KK}}} <$ 885 GeV (the entire mass range of the search, 260 GeV $< m_{G_{\text{KK}}} <$ 1000 GeV).

A similar analysis strategy, originally reported in Ref. [16], is used to probe the anomalous Higgs boson self-coupling and to set constraints on the coupling modifier $\kappa_\lambda = \lambda_{HHH}/\lambda_{HHH}^{\text{SM}}$ when assuming all other couplings to be equal to their SM values. The possibility of performing a linear combination of three samples with different κ_λ values to obtain a signal prediction

for an arbitrary κ_λ hypothesis is used to perform searches for non-resonant pair production of Higgs bosons in the $b\bar{b}\tau^+\tau^-$ final state as a function of this parameter. The observed (expected) allowed κ_λ interval is $\kappa_\lambda \in [-7.4, 15.7]$ ($[-8.9, 16.8]$) at 95% CL.

Observing the self-coupling of the Higgs boson is one of the primary physics goals of the HL-LHC, and thus the obtained results are extrapolated to estimate the sensitivity to this process, as well as to estimate the sensitivity to measuring the overall SM Higgs boson pair production cross-section, when assuming 3000 fb^{-1} of 14 TeV pp collision data, which originally was reported in Ref. [17]. These projections assume the same triggers and the performance of the ATLAS detector as in Run 2, while in reality the detector will be upgraded to cope with a significantly busier LHC environment with approximately 200 pp collisions per bunch crossing, which might impact the performance in various ways. The estimated expected signal significance for the SM Higgs boson pair production in the $b\bar{b}\tau^+\tau^-$ final state, assuming the SM Higgs boson couplings, reaches 2.1 standard deviations, while the expected allowed κ_λ interval is $\kappa_\lambda \in [-0.8, 8.8]$, in the scenario of reduced systematic uncertainties. In the same scenario, the combined sensitivity of the $b\bar{b}\tau^+\tau^-$, $b\bar{b}b\bar{b}$ and $b\bar{b}\gamma\gamma$ analyses reaches 3.0 standard deviations. Including additional channels in the combination could potentially further boost the sensitivity. Furthermore, additional constraints on κ_λ can be obtained from searches for single Higgs boson production, for which electroweak NLO corrections depend on λ_{HHH} [208].

Finally, several proposals for improving background estimation techniques when searching for pair production of Higgs bosons using the full Run 2 ATLAS dataset, corresponding to 139 fb^{-1} of 13 TeV pp collision data, are presented. The suggested improvements aim to improve the statistical precision of the background prediction and to reduce the corresponding systematic uncertainties, and they include a revised estimate of the $t\bar{t}$ background with quark- or gluon-initiated jets misidentified as hadronically decaying τ leptons and a revised estimate of the multijet background.

***

The Higgs sector represents the central part of our understanding of the world of elementary particles and as such it potentially connects the Standard Model with what might exist beyond. Higgs physics is still not fully explored, but the LHC and its future upgrades offer unprecedented possibilities for shedding light upon it. Probing the Higgs boson self-coupling remains a crucial step towards this goal.

Summary in Swedish

Alla elementarpartiklar som standardmodellen (SM) har förutsagt har observerats experimentellt. Till dessa hör: Fermioner med spinn 1/2 – materiepartiklar, indelade i kvarkar och leptoner; gaugebosoner med spinn 1 – kraftförmedlarna; och till sist Higgsbosonen med spinn 0.

Higgsbosonen är den elementarpartikel i SM som upptäcktes sist. Upptäckten av Higgsbosonen tillkännagavs 2012 av ATLAS- och CMS-experimenten, men dess existens förutsades redan ett halvt århundrade tidigare, som en del av ett teoretiskt koncept som förklarar hur elementarpartiklar får sina massor, Higgsmekanismen. Higgsmekanismen är den del av SM som förklarar hur W- och Z-bosonerna får sina massor genom ett symmetribrott av den elektrosvaga kraften. Standardmodellen förutsäger en speciell egenskap hos Higgsbosonen, nämligen att den växelverkar med sig själv, självkopplar, något som ännu inte har bekräftats experimentellt. Självkopplingens styrka är direkt relaterad till Higgspotentialens form och därmed grundläggande för att förstå detaljerna i det elektrosvaga symmetribrottet.

Higgsbosonens självkoppling förväntas kunna observeras i parproduktion av Higgsbosoner, till exempel i ATLAS-experimentet vid LHC, vilket är ämnet för denna avhandling. Det förutsagda tvärsnittet för denna process är dock mycket litet och det är osannolikt att processen kan observeras med de data som LHC för närvarande har att tillgå. Å andra sidan kan tvärsnittet bli signifikant större om självkopplingens styrka är annan än vad SM förutsäger. Dessutom kan argument för att söka efter par av Higgsbosoner återfinnas i många bortom-SM-teorier som förutsäger nya tunga resonanser som kan sönderfalla till Higgsbosoner.

Resultaten och studierna som presenteras i denna avhandling har tagits fram inom ATLAS-experimentet vid LHC. LHC är en 27 kilometer lång cirkulär partikelaccelerator, byggd och underhållen av CERN, som accelererar två partikelstrålar av hadroner, framför allt protoner, i motsatta riktningar. Under LHC:s andra aktiva period, Run-2 (2015-2018), nådde protonstrålarna en energi på 6,5 TeV vardera. LHC har fyra interaktionspunkter, utrustade med varsitt experiment, där strålarna möts. ATLAS-experimentet, som är det största av de fyra på CERN, är designat för att testa giltigheten hos SM, genom högprecisionsmätningar av dess parametrar, samt sökandet efter ny fysik. ATLAS-detektorn består av: Innerdetektorn, där laddade partiklars banor rekonstrueras; de elektromagnetiska och hadroniska kalorimetrarna, där energi och rörelsemängd hos fotoner, elektroner och hadroner mäts; och myonspektrometern som används för att identifiera myoner. Förutom detta innefattar ATLAS

ett specialgjort magnetsystem som används för att böja de laddade partiklarnas banor så att man kan mäta förhållandet mellan deras rörelsemängd och laddning.

Resonant och icke-resonant parproduktion av Higgsbosoner i ett sluttillstånd som består av två bottenkvarkar och två τ-leptoner ($b\bar{b}\tau^+\tau^-$) har sökts efter i en datamängd som motsvarar 36,1 fb^{-1} av proton-proton-kollisioner insamlade av ATLAS vid en masscentrumsenergi $\sqrt{s} = 13$ TeV. När kvarkar och gluoner produceras genomgår de omedelbart en process som kallas hadronisering, som producerar en kollimerad skur av hadroner - en hadronskur (på eng. jet). Hadronskurar som startats av en bottenkvark (på eng. b-jets) har distinkta egenskaper som gör att man kan identifiera dem med en teknik som kallas b-tagging. τ-leptoner som sönderfaller hadroniskt producerar också speciella hadronskurar, här kallade τ_{had}, medan τ-leptoner som sönderfaller leptoniskt är omöjliga att särskilja från elektroner och myoner. Det finns flera SM-processer som kan producera eller imitera sluttillståndet $b\bar{b}\tau^+\tau^-$. Med anledning av detta måste bakgrundsprocesserna noggrant uppskattas.

Den största andelen av bakgrunden vid sökandet efter parproduktion av Higgsbosoner kommer från toppkvarkar, QCD-inducerade multi-hadronskurshändelser och händelser av $Z \to \tau^+\tau^-$ + hadronskurar. Bakgrundsprocesser som innehåller två sanna τ_{had} uppskattas genom simulering, medan processer där minst ett av de utvalda τ_{had}-objekten är en felidentifierad kvark- eller gluon-initierad hadronskur uppskattas genom datadrivna metoder speciellt designade för ändamålet. En beslutsträdsalgoritm, Boosted Decision Tree (BDT), används för att separera signal och bakgrundsprocesser och således sätta en övre gräns för tvärsnittets storlek för resonant och icke-resonant parproduktion av Higgsbosoner. Den observerade (förväntade) 95% övre konfidensgraden (CL, av engelskans confidence level) för tvärsnittet av icke-resonant parproduktion av Higgsbosoner gånger förgreningsförhållandet hos $b\bar{b}\tau^+\tau^-$ är 12,7 (14,8) gånger det förutsagda från SM, under förutsättning att Higgsbosonens kopplingar följer SM.

Med en liknande analysmetod har även en sökning efter parproduktion av Higgsbosoner utförts i samband med den onormala självkopplingen av Higgsbosonen (λ_{HHH}) och övre gränser på kopplingen $\kappa_\lambda = \lambda_{HHH}/\lambda_{HHH}^{\text{SM}}$ har satts. Det observerade (förväntade) tillåtna intervallet vid 95% CL är $\kappa_\lambda \in [-7{,}4, 15{,}7]$ ($[-8{,}9, 16{,}8]$).

Resultaten som presenteras här har även extrapolerats till $\sqrt{s} = 14$ TeV och 3000 fb^{-1} så att känsligheten för icke-resonant parproduktion av Higgsbosoner vid High-Luminosity Large Hadron Collider (HL-LHC) har kunnat uppskattas, under olika antaganden vad gäller utvecklingen av de systematiska osäkerheterna. Den uppskattade upptäcktssignifikansen för parproducerade SM-Higgsbosoner i sluttillståndet $b\bar{b}\tau^+\tau^-$ når 2,1 standardavvikelser i ett scenario med reducerad systematisk osäkerhet. I samma scenario når den kombinerade känsligheten från $b\bar{b}\tau^+\tau^-$, $b\bar{b}b\bar{b}$ och $b\bar{b}\gamma\gamma$ 3,0 standardavvikelser.

Slutligen innehåller avhandlingen flera förslag på förbättringar som kan göras i metoderna som används för att uppskatta bakgrundsprocesser i sökandet efter par av Higgsbosoner, när sökandet kommer att ske i all data från Run-2 i ATLAS, motsvarande 139 fb^{-1} med en energi på 13 TeV. De föreslagna förbättringarna innehåller en reviderad uppskattning av $t\bar{t}$-bakgrunden med hadronskurar av antingen kvarkar eller gluoner felidentifierade som τ_{had}-objekt samt en reviderad uppskattning av multi-hadronskursbakgrunden.

Acknowledgements

My biggest thanks go to my supervisors, Arnaud Ferrari and Stan Lai, for their guidance and patience during the four years of my PhD-studies. Thank you for making work enjoyable, for all the research chats and discussions, amazing wine (not at work though), and for your unfailing support. I am sorry about all the missing articles, too many hyphens and for rejecting the nicknames you proposed. I feel I have learned much less than you two have to offer, yet a lot compared to what I hoped for.

I would also like to say thank you to Pedro Sales de Bruin and Michel Janus. The work I have done over the last four years is due in no small part to your support and encouragement. My gratitude also goes to those professors and supervisors who introduced me to the world of particle physics, especially to Marija Dimitrijević Ćirić, Lidija Živković and Victor Coco. Richard Brenner, thank you for the trip to Helsinki, and for making me laugh even when you talk in Swedish. Elin Bergeås Kuutmann, thanks for being the one to welcome me and for all the interesting lunch discussions. Doña Rebeca Gonzalez Suarez, thank you for stopping me from starting a prank war with Stan.

Tack to Olga Sunneborn Gudnadottir, Thomas Mathisen and Elin for their gigantic help with writing the thesis summary in Swedish. Thank you also to my other colleagues, Myrto Asimakopoulou (you still owe me a road trip to Greece), Max (not Mæx) Isacson, Mikael Mårtensson (in the office at 7 a.m.), Christina Dimitriadi, Joakim Gradin, Mattias Ellert, Timo Dreyer, Andrés Melo, Joshua The Dictator Beirer and Jason Veatch. Kira Abeling, thanks for all the chats, ice cream, and I am really sorry about eating your cookies – and even worse, for giving some to Lino. Over the last couple of years, I tried something much more difficult than earning a PhD-degree in physics – I attended an intensive course in coolness given by Serhat Ördek and Lino Gerlach. I have failed massively, but thanks guys for trying. Finally, my gratitude goes to everyone else at the II. Institute of Physics in Göttingen and the Department of Physics and Astronomy in Uppsala.

My thanks also go to everyone I have had the opportunity to work with in the ATLAS collaboration. I am particularly grateful to Carl Gwilliam for providing immense support when I started. Chris Deutsch, thanks for the countless productive discussions and all your help. Thanks also to Alessandra Betti, Adam Parker, Katharine Leney and the rest of the $bb\tau\tau$ team.

I am thankful to the German Academic Exchange Service (DAAD) for awarding me a scholarship through the "Research Grants - Cotutelle Doctoral Programmes" to support my studies in Göttingen.

Aleksandra Dimitrievska, Marija Marjanović and Danijela Bogavac, I very much appreciate all your huge help and advice. Michael Wright, thanks for your support and I am sorry for making fun of your taste in movies. Lucie Hamdi, thank you for allowing me to build the best desk ever (I was tempted to include a picture) and for a lot more.

Hvala mami što me je uvek bodrila da mogu visoko da letim, i tati što me je savetovao da mama nije uvek u pravu i da moram sam da znam. Hvala Mili, Igoru i Slađi, Ivanu, Jeleni, Ivani, Tamari, Tomi i Mariću, Nori, i mnogima drugima, jer sve čega ste vi deo meni više znači.

References

[1] ATLAS Collaboration, *Observation of a new particle in the search for the Standard Model Higgs boson with the ATLAS detector at the LHC*, *Phys. Lett. B* **716**, 1 (2012), arXiv: 1207.7214[hep-ex]. (Cited on pages 11, 15, 25, 29, 31, and 45.)

[2] CMS Collaboration, *Observation of a new boson at a mass of 125 GeV with the CMS experiment at the LHC*, *Phys. Lett. B* **716**, 30 (2012), arXiv: 1207.7235[hep-ex]. (Cited on pages 11, 15, 25, 29, 31, and 45.)

[3] F. Englert and R. Brout, *Broken Symmetry and the Mass of Gauge Vector Mesons*, *Phys. Rev. Lett.* **13**, 321 (1964). (Cited on pages 11, 15, and 22.)

[4] P. W. Higgs, *Broken Symmetries and the Masses of Gauge Bosons*, *Phys. Rev. Lett.* **13**, 508 (1964). (Cited on pages 11, 15, and 22.)

[5] P. W. Higgs, *Spontaneous Symmetry Breakdown without Massless Bosons*, *Phys. Rev.* **145**, 1156 (1966). (Cited on pages 11, 15, and 22.)

[6] G. S. Guralnik, C. R. Hagen and T. W. B. Kibble, *Global Conservation Laws and Massless Particles*, *Phys. Rev. Lett.* **13**, 585 (1964). (Cited on pages 11 and 22.)

[7] S. L. Glashow, *Partial-symmetries of weak interactions*, *Nucl. Phys.* **22**, 579 (1961). (Cited on pages 11 and 15.)

[8] S. Weinberg, *A Model of Leptons*, *Phys. Rev. Lett.* **19**, 1264 (1967). (Cited on pages 11 and 15.)

[9] A. Salam, *Weak and electromagnetic interactions*, *Conf. Proc. C* **680519**, 367 (1968). (Cited on pages 11 and 15.)

[10] S. L. Glashow, J. Iliopoulos and L. Maiani, *Weak Interactions with Lepton-Hadron Symmetry*, *Phys. Rev. D* **2**, 1285 (1970). (Cited on pages 11 and 15.)

[11] G. C. Branco, P. M. Ferreira, L. Lavoura, M. N. Rebelo, M. Sher and J. P. Silva, *Theory and phenomenology of two-Higgs-doublet models*, *Physics Reports* **516**, 1 (2012), arXiv: 1106.0034[hep-ph]. (Cited on pages 11, 34, and 37.)

[12] L. Randall and R. Sundrum, *Large Mass Hierarchy from a Small Extra Dimension*, *Phys. Rev. Lett.* **83**, 3370 (1999), arXiv: hep-ph/9905221. (Cited on pages 11, 35, 37, 39, and 40.)

[13] K. Agashe, H. Davoudiasl, G. Perez and A. Soni, *Warped gravitons at the CERN LHC and beyond*, *Phys. Rev. D* **76**, 036006 (2007), arXiv: hep-ph/0701186. (Cited on pages 11, 35, and 37.)

[14] L. Fitzpatrick, J. Kaplan, L. Randall and L.T. Wang, *Searching for the Kaluza-Klein graviton in bulk RS models*, *JHEP* **09**, 013 (2007), arXiv: hep-ph/0701150. (Cited on pages 11, 35, and 37.)

[15] ATLAS Collaboration, *Search for Resonant and Nonresonant Higgs Boson Pair Production in the $b\bar{b}\tau^+\tau^-$ Decay Channel in pp Collisions at $\sqrt{s} = 13$ TeV with the ATLAS Detector*, *Phys. Rev. Lett.* **121**, 191801 (2018), URL `https://atlas.web.cern.ch/Atlas/GROUPS/PHYSICS/PAPERS/HIGG-2016-16/`, [Erratum: *Phys. Rev. Lett.* **122**, 089901 (2019)], arXiv: `1808.00336[hep-ex]`. (Cited on pages 12, 79, 96, 108, 128, 129, 130, 132, 133, and 187.)

[16] ATLAS Collaboration, *Combination of searches for Higgs boson pairs in pp collisions at $\sqrt{s} = 13$ TeV with the ATLAS detector*, *Phys. Lett. B* **800**, 135103 (2020), URL `https://atlas.web.cern.ch/Atlas/GROUPS/PHYSICS/PAPERS/HDBS-2018-58/`, arXiv: `1906.02025[hep-ex]`. (Cited on pages 12, 43, 130, 131, 134, 135, 137, 145, 146, 147, and 187.)

[17] ATLAS Collaboration, *Measurement prospects of the pair production and self-coupling of the Higgs boson with the ATLAS experiment at the HL-LHC*, *ATL-PHYS-PUB-2018-053* (2018), URL `https://atlas.web.cern.ch/Atlas/GROUPS/PHYSICS/PUBNOTES/ATL-PHYS-PUB-2018-053/`. (Cited on pages 12, 13, 149, 153, 154, 156, 157, 158, 159, 160, 161, 162, 163, 164, 165, and 188.)

[18] ATLAS Collaboration, *Reconstruction and identification of boosted di-τ systems in a search for Higgs boson pairs using 13 TeV proton–proton collision data in ATLAS*, *Submitted to JHEP* (2020), arXiv: `2007.14811[hep-ex]`. (Cited on page 13.)

[19] M. D. Schwartz, *Quantum Field Theory and the Standard Model*, Cambridge University Press, ISBN 978-1-107-03473-0 (2014). (Cited on pages 15, 28, and 50.)

[20] M. E. Peskin and D. V. Schroeder, *An Introduction to quantum field theory*, Addison-Wesley, ISBN 978-0-201-50397-5 (1995). (Cited on page 15.)

[21] M. Thomson, *Modern Particle Physics*, Cambridge University Press, ISBN 978-1-139-52536-7, doi:10.1017/CBO9781139525367 (2013). (Cited on pages 15, 20, 26, and 38.)

[22] V. Radovanović, *Problem Book in Quantum Field Theory*, Springer-Verlag Berlin Heidelberg, ISBN 978-3-540-29063-6, doi:10.1007/3-540-29063-X (2006). (Cited on page 15.)

[23] Super-Kamiokande Collaboration, *Evidence for Oscillation of Atmospheric Neutrinos*, *Phys. Rev. Lett.* **81**, 1562 (1998). (Cited on pages 16 and 27.)

[24] SNO Collaboration, *Direct Evidence for Neutrino Flavor Transformation from Neutral-Current Interactions in the Sudbury Neutrino Observatory*, *Phys. Rev. Lett.* **89**, 011301 (2002), arXiv: `nucl-ex/0204008v2`. (Cited on pages 16 and 27.)

[25] M. Tanabashi et al., *Particle Data Group*, *Phys. Rev. D* **98**, 030001 (2018). (Cited on pages 16, 22, 25, 33, 73, 74, and 92.)

[26] C. S. Wu, E. Ambler, R. W. Hayward, D. D. Hoppes and R. P. Hudson, *Experimental Test of Parity Conservation in Beta Decay*, *Phys. Rev.* **105**, 1413 (1957). (Cited on page 17.)

[27] E. Noether, *Invariante variationsprobleme*, *Nachrichten von der Gesellschaft der Wissenschaften zu Göttingen, Mathematisch-Physikalische Klasse* **1918**, 235 (1918). (Cited on page 17.)

[28] LHCb Collaboration, *Observation of $J/\psi p$ Resonances Consistent with Pentaquark States in $\Lambda_b^0 \to J/\psi K^- p$ Decays*, *Phys. Rev. Lett.* **115**, 072001 (2015). (Cited on page 20.)

[29] G. K. Wilson, *Confinement of quarks*, *Phys. Rev. D* **10**, 2445 (1974). (Cited on page 20.)

[30] H. D. Politzer, *Reliable Perturbative Results for Strong Interactions?*, *Phys. Rev. Lett.* **30**, 1346 (1973). (Cited on page 20.)

[31] D. J. Gross and F. Wilczek, *Ultraviolet Behavior of Non-Abelian Gauge Theories*, *Phys. Rev. Lett.* **30**, 1343 (1973). (Cited on page 20.)

[32] P. Achard et al. (L3 Collaboration), *Measurement of the running of the electromagnetic coupling at large momentum-transfer at LEP*, *Phys. Lett. B* **623**, 26 (2005), arXiv: hep-ex/0507078. (Cited on page 20.)

[33] C. H. Albright, *y and ν distributions for neutral current reactions of the Weinberg-type*, *Nucl. Phys. B* **70**, 486 (1974). (Cited on page 22.)

[34] J. Ellis, M. K. Gaillard and D. V. Nanopoulos, *An Updated Historical Profile of the Higgs Boson*, *KCL-PH-TH/2015-20, LCTS/2015-10, CERN-PH-TH/2015-098* (2015). (Cited on page 24.)

[35] D. M. Webber et al. (MuLan Collaboration), *Measurement of the Positive Muon Lifetime and Determination of the Fermi Constant to Part-per-Million Precision*, *Phys. Rev. Lett.* **106**, 041803 (2011), arXiv: 1010.0991[hep-ex]. (Cited on page 25.)

[36] T2K Collaboration, *Constraint on the matter-antimatter symmetry-violating phase in neutrino oscillations*, *Nature* **580**, 339 (2020). (Cited on page 28.)

[37] D. de Florian et al., *Handbook of LHC Higgs Cross Sections: 4. Deciphering the Nature of the Higgs Sector* (2016), arXiv: 1610.07922[hep-ph]. (Cited on pages 28, 30, 33, 81, 82, and 139.)

[38] LHC Higgs Cross Section Working Group, *Web page*, URL https://twiki.cern.ch/twiki/bin/view/LHCPhysics/LHCHXSWG, Public plots (2016). (Cited on pages 29, 150, and 152.)

[39] ATLAS Collaboration, *Study of the spin and parity of the Higgs boson in diboson decays with the ATLAS detector*, *Eur. Phys. J. C* **75**, 476 (2015), arXiv: 1506.05669[hep-ex]. (Cited on pages 30 and 38.)

[40] CMS Collaboration, *Study of the Mass and Spin-Parity of the Higgs Boson Candidate via Its Decays to Z Boson Pairs*, *Phys. Rev. Lett.* **110**, 081803 (2013), arXiv: 1212.6639[hep-ex]. (Cited on pages 30 and 38.)

[41] ATLAS Collaboration, *Combined measurements of Higgs boson production and decay using up to 80 fb^{-1} of proton-proton collision data at $\sqrt{s} = 13$ TeV collected with the ATLAS experiment*, *Phys. Rev. D* **101**, 012002 (2020), arXiv: 1909.02845[hep-ex]. (Cited on page 30.)

[42] CMS Collaboration, *Combined measurements of Higgs boson couplings in proton-proton collisions at $\sqrt{s} = 13$ TeV*, *Eur. Phys. J. C* **79**, 421 (2019), arXiv: 1809.10733[hep-ex]. (Cited on page 30.)

[43] LHC Higgs Cross Section HH Sub-group, *Web page*, URL https://twiki.cern.ch/twiki/bin/view/LHCPhysics/LHCHXSWGHH (2019). (Cited on pages 31, 32, and 80.)

[44] S. Dawson, S. Dittmaier and M. Spira, *Neutral Higgs-boson pair production at hadron colliders: QCD corrections*, *Phys. Rev. D* **58**, 115012 (1998), arXiv: hep-ph/9805244. (Cited on pages 31, 32, and 80.)

[45] S. Borowka et al., *Higgs Boson Pair Production in Gluon Fusion at Next-to-Leading Order with Full Top-Quark Mass Dependence*, *Phys. Rev. Lett.* **117**, 012001 (2016), [Erratum: *Phys. Rev. Lett.* **117**, 079901 (2016)], arXiv: 1604.06447v2[hep-ph]. (Cited on pages 31, 32, 80, and 140.)

[46] J. Baglio at al., *Gluon fusion into Higgs pairs at NLO QCD and the top mass scheme*, *Eur. Phys. J. C* **79**, 459 (2019), arXiv: 1811.05692[hep-ph]. (Cited on pages 31, 32, and 80.)

[47] D. de Florian and J. Mazzitelli, *Higgs Boson Pair Production at Next-to-Next-to-Leading Order in QCD*, *Phys. Rev. Lett.* **111**, 201801 (2013), arXiv: 1309.6594[hep-ph]. (Cited on pages 31, 32, and 80.)

[48] D. Y. Shao, C. S. Li, H. T. Li and J. Wang, *Threshold resummation effects in Higgs boson pair production at the LHC*, *JHEP* **07**, 169 (2013), arXiv: 1301.1245v2[hep-ph]. (Cited on pages 31, 32, and 80.)

[49] D. de Florian and J. Mazzitelli, *Higgs pair production at next-to-next-to-leading logarithmic accuracy at the LHC*, *JHEP* **09**, 053 (2015), arXiv: 1505.07122[hep-ph]. (Cited on pages 31, 32, and 80.)

[50] M. Grazzini et al., *Higgs boson pair production at NNLO with top quark mass effects*, *JHEP* **05**, 059 (2018), arXiv: 1803.02463[hep-ph]. (Cited on pages 31 and 32.)

[51] ATLAS Collaboration, *Search for the $HH \to b\bar{b}b\bar{b}$ process via vector-boson fusion production using proton-proton collisions at $\sqrt{s} = 13$ TeV with the ATLAS detector*, *JHEP* **07**, 108 (2020), arXiv: 2001.05178[hep-ex]. (Cited on page 31.)

[52] J. Baglio, A. Djouadi, R. Gröber, M. M. Mühlleitner, J. Quevillon, M. Spira, *The measurement of the Higgs self-coupling at the LHC: theoretical status*, *JHEP* **04**, 151 (2013), arXiv: 1212.5581[hep-ph]. (Cited on page 32.)

[53] G. W. Bennett et al. (Muon g-2 Collaboration), *Final report of the E821 muon anomalous magnetic moment measurement at BNL*, *Phys. Rev. D* **73**, 072003 (2006). (Cited on page 34.)

[54] BaBar Collaboration, *Evidence for an Excess of $\overline{B} \to D^{(*)}\tau^-\overline{\nu}_\tau$ Decays*, *Phys. Rev. Lett.* **109**, 101802 (2012), arXiv: 1205.5442v2[hep-ex]. (Cited on page 34.)

[55] BaBar Collaboration, *Measurement of an excess of $\overline{B} \to D^{(*)}\tau^-\overline{\nu}_\tau$ decays and implications for charged Higgs bosons*, *Phys. Rev. D* **88**, 072012 (2013), arXiv: 1303.0571v1[hep-ex]. (Cited on page 34.)

[56] Belle Collaboration, *Measurement of the branching ratio of $\overline{B} \to D^{(*)}\tau^-\overline{\nu}_\tau$ relative to $\overline{B} \to D^{(*)}\ell^-\overline{\nu}_\ell$ decays with hadronic tagging at Belle*, *Phys. Rev. D* **92**, 072014 (2015), arXiv: 1507.03233v3[hep-ex]. (Cited on page 34.)

[57] Belle Collaboration, *Measurement of the branching ratio of $\overline{B}^0 \to D^{*+}\tau^-\overline{\nu}_\tau$ relative to $\overline{B}^0 \to D^{*+}\ell^-\overline{\nu}_\ell$ decays with a semileptonic tagging method*, *Phys. Rev. D* **94**, 072007 (2016), arXiv: 1607.07923v3[hep-ex]. (Cited on page 34.)

[58] LHCb Collaboration, *Measurement of the Ratio of Branching Fractions $\mathscr{B}(\overline{B}^0 \to D^{*+}\tau^-\overline{\nu}_\tau)/\mathscr{B}(\overline{B}^0 \to D^{*+}\mu^-\overline{\nu}_\mu)$*, *Phys. Rev. Lett.* **115**, 111803 (2015), arXiv: 1506.08614v2[hep-ex]. (Cited on page 34.)

[59] LHCb Collaboration, *Search for lepton-universality violation in $B^+ \to K^+\ell^+\ell^-$ decays*, *Phys. Rev. Lett.* **122**, 191801 (2019), arXiv: 1903.09252v2[hep-ex]. (Cited on page 34.)

[60] LHCb Collaboration, *Measurement of CP-Averaged Observables in the $B^0 \to K^{*0}\mu^+\mu^-$ Decay*, *Phys. Rev. Lett.* **125**, 011802 (2020), arXiv: 2003.04831v2[hep-ex]. (Cited on page 34.)

[61] C. Bambi and A. D. Dolgov, *Introduction to Particle Cosmology – The Standard Model of Cosmology and its Open Problems*, Springer-Verlag Berlin Heidelberg, ISBN 978-3-662-48078-6 (2016). (Cited on page 34.)

[62] S. P. Martin, *A Supersymmetry Primer*, *Perspectives on supersymmetry. Vol.2* (2016), arXiv: hep-ph/9709356v7. (Cited on page 38.)

[63] C. Csaki, *The Minimal Supersymmetric Standard Model (MSSM)*, *Modern Phys. Lett. A* **11**, 599 (1996), arXiv: hep-ph/9606414. (Cited on page 38.)

[64] A. Djouadi, L. Maiani, G. Moreau, A. Polosa, J. Quevillon and V. Riquer, *The post-Higgs MSSM scenario: habemus MSSM?*, *Eur. Phys. J. C* **73**, 2650 (2013), arXiv: 1307.5205[hep-ph]. (Cited on page 38.)

[65] A. Djouadi and J. Quevillon, *The MSSM Higgs sector at a high MSUSY: reopening the low tanβ regime and heavy Higgs searches*, *JHEP* **10**, 028 (2013), arXiv: 1304.1787[hep-ph]. (Cited on page 39.)

[66] Y. Liu, *Introduction to Extra Dimensions and Thick Braneworlds* (2017), arXiv: 1707.08541[hep-th]. (Cited on page 39.)

[67] A. Oliveira, *Gravity particles from Warped Extra Dimensions, predictions for LHC* (2014), arXiv: 1404.0102[hep-ph]. (Cited on pages 40 and 81.)

[68] P. Traczyk and G. Wrochna, *Search for Randall-Sundrum Graviton Excitations in the CMS Experiment* (2002), arXiv: hep-ex/0207061. (Cited on page 41.)

[69] A. Efrati and Y. Nir, *What if $\lambda_{hhh} \neq 3m_h^2/v$* (2014), arXiv: 1401.0935[hep-ph]. (Cited on page 41.)

[70] F. Goertz, A. Papaefstathiou, L Yang and J. Zurita, *Higgs boson pair production in the D = 6 extension of the SM*, *JHEP* **04**, 167 (2015), arXiv: 1410.3471[hep-ph]. (Cited on page 44.)

[71] Gargamelle Neutrino Collaboration, *Observation of Neutrino Like Interactions Without Muon Or Electron in the Gargamelle Neutrino Experiment*, *Phys. Lett. B* **46**, 138 (1973). (Cited on page 45.)

[72] UA1 Collaboration, *Experimental observation of isolated large transverse energy electrons with associated missing energy at* $\sqrt{s} = 540$ *GeV*, *Phys. Lett. B* **122**, 103 (1983). (Cited on page 45.)

[73] UA1 Collaboration, *Experimental Observation of Lepton Pairs of Invariant Mass Around 95 GeV*$/c^2$ *at the CERN SPS Collider*, *Phys. Lett. B* **126**, 398 (1983). (Cited on page 45.)

[74] UA2 Collaboration, *Observation of single isolated electrons of high transverse momentum in events with missing transverse energy at the CERN* pp *collider*, *Phys. Lett. B* **122**, 476 (1983). (Cited on page 45.)

[75] UA2 Collaboration, *Evidence for* $Z^0 \to e^+e^-$ *at the CERN* pp *collider*, *Phys. Lett. B* **129**, 130 (1983). (Cited on page 45.)

[76] NA31 Collaboration, *First Evidence for Direct CP Violation*, *Phys. Lett. B* **206**, 169 (1988). (Cited on page 45.)

[77] NA48 Collaboration, *A new measurement of direct CP violation in two pion decays of the neutral kaon*, *Phys. Lett. B* **465**, 335 (1999), arXiv: hep-ex/9909022. (Cited on page 45.)

[78] L. Evans and P. Bryant, *LHC Machine*, *JINST* **3**, S08001 (2008). (Cited on pages 45 and 47.)

[79] F. K. J. L. Feng, I. Galon and S. Trojanowski, *ForwArd Search ExpeRiment at the LHC*, *Phys. Rev. D* **97**, 035001 (2018), arXiv: 1708.09389[hep-ph]. (Cited on page 46.)

[80] ATLAS Collaboration, *The ATLAS Experiment at the CERN Large Hadron Collider*, *JINST* **3**, S08003 (2008). (Cited on pages 46, 51, 52, 53, 54, 57, and 58.)

[81] CMS Collaboration, *The CMS experiment at the CERN LHC*, *JINST* **3**, S08004 (2008). (Cited on page 46.)

[82] ALICE Collaboration, *The ALICE experiment at the CERN LHC*, *JINST* **3**, S08002 (2008). (Cited on page 46.)

[83] LHCb Collaboration, *The LHCb Detector at the LHC*, *JINST* **3**, S08005 (2008). (Cited on page 46.)

[84] TOTEM Collaboration, *The TOTEM Experiment at the CERN Large Hadron Collider*, *JINST* **3**, S08007 (2008). (Cited on page 46.)

[85] LHCf Collaboration, *The LHCf detector at the CERN Large Hadron Collider*, *JINST* **3**, S08006 (2008). (Cited on page 46.)

[86] MoEDAL Collaboration, *Technical Design Report of the MoEDAL Experiment*, *CERN-LHCC-2009-006; MoEDAL-TDR-001* (2009), URL https://cds.cern.ch/record/1181486. (Cited on page 46.)

[87] ATLAS Collaboration, *Luminosity determination in pp collisions at $\sqrt{s} = 13$ TeV using the ATLAS detector at the LHC*, *ATLAS-CONF-2019-021* (2019), URL https://cds.cern.ch/record/2677054. (Cited on pages 47 and 110.)

[88] ATLAS Collaboration, *Web page: ATLAS Luminosity Public Results Run 2*, URL https://twiki.cern.ch/twiki/bin/view/AtlasPublic/LuminosityPublicResultsRun2, Public plots (2019). (Cited on pages 47 and 48.)

[89] High-Luminosity LHC Project, *Web page*, URL https://hilumilhc.web.cern.ch/content/hl-lhc-project, Public plots (2020). (Cited on page 49.)

[90] A. D. Martin, W. J. Stirling, R. S. Thorne and G. Watt, *Parton distributions for the LHC*, *Eur. Phys. J. C* **63**, 189 (2009), arXiv: 0901.0002[hep-ph]. (Cited on pages 50 and 51.)

[91] J. D. Bjorken, *Asymptotic Sum Rules at Infinite Momentum*, *Phys. Rev.* **179**, 1547 (1969). (Cited on page 50.)

[92] Y. L. Dokshitzer, *Calculation of the Structure Functions for Deep Inelastic Scattering and e^+e^- Annihilation by Perturbation Theory in Quantum Chromodynamics*, *Sov. Phys. JETP* **46**, 641 (1977). (Cited on page 51.)

[93] V. N. Gribov and L. N. Lipatov, *Deep inelastic ep scattering in perturbation theory*, *Sov. J. Nucl. Phys.* **15**, 438 (1972). (Cited on page 51.)

[94] G. Altarelli and G. Parisi, *Asymptotic freedom in parton language*, *Nucl. Phys. B* **126**, 298 (1977). (Cited on page 51.)

[95] ATLAS Collaboration, *ATLAS Insertable B-Layer Technical Design Report*, *CERN-LHCC-2010-013, ATLAS-TDR-19* (2010), URL https://cds.cern.ch/record/1291633. (Cited on page 54.)

[96] ATLAS Collaboration, *Web page: Computer generated image of the ATLAS inner detector*, URL https://cds.cern.ch/record/1095926, Public plots (2018). (Cited on page 55.)

[97] ATLAS Collaboration, *2015 start-up trigger menu and initial performance assessment of the ATLAS trigger using Run-2 data*, *ATL-DAQ-PUB-2016-001* (2016), URL https://cds.cern.ch/record/2136007. (Cited on page 59.)

[98] ATLAS Collaboration, *Web page: ATLAS Trigger and Data Acquisition*, URL https://twiki.cern.ch/twiki/bin/view/AtlasPublic/ApprovedPlotsDAQ, Public plots (2019). (Cited on page 59.)

[99] ATLAS Collaboration, *The ATLAS Simulation Infrastructure*, *Eur. Phys. J. C* **70**, 823 (2010), arXiv: 1005.4568[physics.ins-det]. (Cited on pages 60 and 62.)

[100] J. Alwall et al., *Comparative study of various algorithms for the merging of parton showers and matrix elements in hadronic collisions*, *Eur. Phys. J. C* **53**, 473 (2008), arXiv: 0706.2569v2[hep-ph]. (Cited on page 60.)

[101] J. Alwall et al., *The automated computation of tree-level and next-to-leading order differential cross sections, and their matching to parton shower simulations*, *JHEP* **07**, 079 (2014), arXiv: 1405.0301v2[hep-ph]. (Cited on pages 61, 80, and 83.)

[102] S. Alioli, P. Nason, C. Oleari and E. Re, *A general framework for implementing NLO calculations in shower Monte Carlo programs: the POWHEG BOX*, *JHEP* **06**, 043 (2010), arXiv: 1002.2581[hep-ph]. (Cited on pages 61, 81, and 83.)

[103] T. Gleisberg, S. Höche, F. Krauss, M. Schönherr, S. Schumann, F. Siegert and J. Winter, *Event generation with SHERPA 1.1*, *JHEP* **02**, 007 (2009), arXiv: 0811.4622[hep-ph]. (Cited on pages 61, 82, and 83.)

[104] T. Sjöstrand, S. Mrenna and P. Skands, *PYTHIA 6.4 physics and manual*, *JHEP* **05**, 026 (2006), arXiv: hep-ph/0603175. (Cited on pages 61, 81, and 83.)

[105] T. Sjöstrand, S. Mrenna and P. Skands, *A brief introduction to PYTHIA 8.1*, *Comput. Phys. Commun.* **178**, 852 (2008), arXiv: 0710.3820v1[hep-ph]. (Cited on pages 61, 81, and 83.)

[106] T. Sjöstrand et al., *An introduction to PYTHIA 8.2*, *Comput. Phys. Commun.* **191**, 159 (2015), arXiv: 1410.3012[hep-ph]. (Cited on pages 61, 81, and 83.)

[107] M. Bähr et al., *Herwig++ physics and manual*, *Eur. Phys. J. C* **58**, 639 (2008), arXiv: 0803.0883v3[hep-ph]. (Cited on pages 61, 80, and 83.)

[108] J. Bellm et al., *Herwig* 7.0/*Herwig++* 3.0 *release note*, *Eur. Phys. J. C* **76**, 196 (2016), arXiv: 1512.01178[hep-ph]. (Cited on pages 61 and 168.)

[109] S. Gieseke, P. Stephens and B. Webber, *New formalism for QCD parton showers*, *JHEP* **12**, 045 (2003), arXiv: hep-ph/0310083. (Cited on page 61.)

[110] T. Sjöstrand and P. Z. Skands, *Transverse-momentum-ordered showers and interleaved multiple interactions*, *Eur. Phys. J. C* **39**, 129 (2005), arXiv: hep-ph/0408302. (Cited on page 61.)

[111] S. Schumann and F. Krauss, *A parton shower algorithm based on Catani-Seymour dipole factorisation*, *JHEP* **03**, 038 (2008), arXiv: 0709.1027[hep-ph]. (Cited on pages 61, 82, and 83.)

[112] B. Andersson, G. Gustafson, G. Ingelman and T. Sjöstrand, *Parton fragmentation and string dynamics*, *Physics Reports* **97**, 31 (1983). (Cited on page 61.)

[113] B. R. Webber, *A QCD Model for Jet Fragmentation Including Soft Gluon Interference*, *Nucl. Phys. B* **238**, 492 (1984). (Cited on page 61.)

[114] T. Sjöstrand and P. Skands, *Multiple Interactions and the Structure of Beam Remnants*, *JHEP* **03**, 053 (2004), arXiv: hep-ph/0402078. (Cited on page 61.)

[115] M. Bähr, S. Gieseke and M. H. Seymour, *Simulation of multiple partonic interactions in Herwig++*, *JHEP* **07**, 076 (2008), arXiv: 0803.3633[hep-ph]. (Cited on page 61.)

[116] A. Buckley, H. Hoeth, H. Lacker, H. Schulz and J. E. von Seggern, *Systematic event generator tuning for the LHC*, *Eur. Phys. J. C* **65**, 331 (2010), arXiv: 0907.2973[hep-ph]. (Cited on page 61.)

[117] P. Z. Skands, *Tuning Monte Carlo generators: The Perugia tunes*, *Phys. Rev. D* **82**, 074018 (2010), arXiv: 1005.3457[hep-ph]. (Cited on pages 61 and 83.)

[118] D. J. Lange, *The EvtGen particle decay simulation package*, *Nucl. Instrum. Meth. A* **462**, 152 (2001). (Cited on page 61.)

[119] S. Jadach, Z. Wąs, R. Decker and J. H. Kühn, *The τ decay library TAUOLA, version 2.4*, *Comput. Phys. Commun.* **76**, 361 (1993). (Cited on page 61.)

[120] Z. Marshall, *Simulation of Pile-up in the ATLAS Experiment*, *J. Phys.: Conf. Ser.* **513**, 022024 (2014). (Cited on page 62.)

[121] Geant4 Collaboration, *Geant4–a simulation toolkit*, *Nucl. Instrum. Meth. A* **506**, 250 (2003). (Cited on page 62.)

[122] B. Nachman, *Investigating the Quantum Properties of Jets and the Search for a Supersymmetric Top Quark Partner with the ATLAS Detector*, *CERN-THESIS-2016-083* (2016), URL https://cds.cern.ch/record/2204912, PhD Thesis, arXiv: 1609.03242[hep-ex]. (Cited on page 63.)

[123] M. Cacciari, G. P. Salam and G. Soyez, *The catchment area of jets*, *JHEP* **04**, 005 (2008), arXiv: 0802.1188v2[hep-ph]. (Cited on page 64.)

[124] ATLAS Collaboration, *Performance of the ATLAS track reconstruction algorithms in dense environments in LHC Run 2*, *Eur. Phys. J. C* **77**, 673 (2017), arXiv: 1704.07983v2[hep-ex]. (Cited on page 64.)

[125] E. Belau et al., *Charge collection in silicon strip detectors*, *Nucl. Instrum. Meth.* **214**, 253 (1983). (Cited on page 64.)

[126] R. Fröhwirth, *Application of Kalman filtering to track and vertex fitting*, *Nucl. Instrum. Meth. A* **262**, 444 (1987). (Cited on page 64.)

[127] T. Cornelissen, M. Elsing, I. Gavrilenko, W. Liebig, E. Moyse and A. Salzburger, *The new ATLAS track reconstruction (NEWT)*, *J. Phys.: Conf. Ser.* **119**, 032014 (2008). (Cited on page 64.)

[128] ATLAS Collaboration, *Performance of primary vertex reconstruction in proton-proton collisions at $\sqrt{s} = 7$ TeV in the ATLAS experiment*, *ATLAS-CONF-2010-069* (2010), URL https://cds.cern.ch/record/1281344. (Cited on page 64.)

[129] ATLAS Collaboration, *Reconstruction of primary vertices at the ATLAS experiment in Run 1 proton-proton collisions at the LHC*, *Eur. Phys. J. C* **77**, 332 (2017). (Cited on page 64.)

[130] ATLAS Collaboration, *Electron reconstruction and identification in the ATLAS experiment using the 2015 and 2016 LHC proton-proton collision data at $\sqrt{s} = 13$ TeV*, *Eur. Phys. J. C* **79**, 639 (2019), arXiv: 1902.04655[physics.ins-det]. (Cited on pages 65, 66, 86, and 111.)

[131] ATLAS Collaboration, *Calorimeter Clustering Algorithms : Description and Performance*, *ATL-LARG-PUB-2008-002* (2008), URL https://cds.cern.ch/record/1099735. (Cited on page 65.)

[132] ATLAS Collaboration, *Electron and photon energy calibration with the ATLAS detector using LHC Run 1 data*, *Eur. Phys. J. C* **74**, 3071 (2014), arXiv: 1407.5063[hep-ex]. (Cited on page 66.)

[133] ATLAS Collaboration, *Electron and photon energy calibration with the ATLAS detector using 2015-2016 LHC proton-proton collision data*, *JINST* **14**, 3017 (2019), arXiv: 1812.03848[hep-ex]. (Cited on page 66.)

[134] ATLAS Collaboration, *Muon reconstruction performance of the ATLAS detector in proton-proton collision data at $\sqrt{s} = 13$ TeV*, *Eur. Phys. J. C* **76**, 292 (2016), arXiv: 1603.05598v2[hep-ex]. (Cited on pages 66, 67, 86, and 111.)

[135] ATLAS Collaboration, *Measurement of the muon reconstruction performance of the ATLAS detector using 2011 and 2012 LHC proton-proton collision data*, *Eur. Phys. J. C* **74**, 3130 (2014), arXiv: 1407.3935[hep-ex]. (Cited on page 67.)

[136] G. P. Salam, *Towards jetography*, *Eur. Phys. J. C* **67**, 637 (2010), arXiv: 0906.1833v2[hep-ph]. (Cited on page 68.)

[137] T. Carli, K. Rabbertz and S. Schumann, *Studies of Quantum Chromodynamics at the LHC*, Springer, Cham, ISBN 978-3-319-15001-7, doi:10.1007/978-3-319-15001-7_5 (2015), arXiv: 1506.03239[hep-ex]. (Cited on page 68.)

[138] ATLAS Collaboration, *Topological cell clustering in the ATLAS calorimeters and its performance in LHC Run 1*, *Eur. Phys. J. C* **77**, 490 (2017), arXiv: 1603.02934v3[hep-ex]. (Cited on pages 68 and 75.)

[139] M. Cacciari, G. P. Salam and G. Soyez, *The anti-kt jet clustering algorithm*, *JHEP* **04**, 063 (2008), arXiv: 0802.1189v2[hep-ph]. (Cited on page 68.)

[140] M. Cacciari, G. P. Salam and G. Soyez, *FastJet User Manual*, *Eur. Phys. J. C* **72**, 1896 (2012), arXiv: 1111.6097[hep-ph]. (Cited on page 68.)

[141] ATLAS Collaboration, *Determination of jet calibration and energy resolution in proton-proton collisions at $\sqrt{s} = 8$ TeV using the ATLAS detector*, *Submitted to Eur. Phys. J. C* (2019), URL https://cds.cern.ch/record/2693121, arXiv: 1910.04482[hep-ex]. (Cited on pages 69 and 111.)

[142] ATLAS Collaboration, *Jet energy scale measurements and their systematic uncertainties in proton-proton collisions at $\sqrt{s} = 13$ TeV with the ATLAS detector*, *Phys. Rev. D* **96**, 072002 (2017), arXiv: 1703.09665v2[hep-ex]. (Cited on pages 69 and 111.)

[143] M. Cacciari and G. P. Salam, *Pileup subtraction using jet areas*, *Phys. Lett. B* **659**, 119 (2008), arXiv: 0707.1378v2[hep-ph]. (Cited on page 69.)

[144] ATLAS Collaboration, *Tagging and suppression of pileup jets with the ATLAS detector*, *ATLAS-CONF-2014-018* (2014), URL https://cds.cern.ch/record/1700870. (Cited on pages 69 and 86.)

[145] ATLAS Collaboration, *Jet reconstruction and performance using particle flow with the ATLAS Detector*, *Eur. Phys. J. C* **77**, 466 (2017), arXiv: 1703.10485v2[hep-ex]. (Cited on pages 69 and 170.)

[146] ATLAS Collaboration, *Optimisation of the ATLAS b-tagging performance for the 2016 LHC Run*, *ATL-PHYS-PUB-2016-012* (2016), URL https://cds.cern.ch/record/2160731. (Cited on pages 70, 71, and 86.)

[147] ATLAS Collaboration, *Commissioning of the ATLAS high-performance b-tagging algorithms in the 7 TeV collision data*, *ATLAS-CONF-2011-102* (2011), URL https://cds.cern.ch/record/1369219. (Cited on page 70.)

[148] ATLAS Collaboration, *Optimisation and performance studies of the ATLAS b-tagging algorithms for the 2017-18 LHC run*, *ATL-PHYS-PUB-2017-013* (2017), URL http://cds.cern.ch/record/2273281. (Cited on page 70.)

[149] G. Piacquadio and C. Weiser, *A new inclusive secondary vertex algorithm for b-jet tagging in ATLAS*, *J. Phys.: Conf. Ser.* **119**, 032032 (2008). (Cited on page 70.)

[150] ATLAS Collaboration, *Measurements of b-jet tagging efficiency with the ATLAS detector using $t\bar{t}$ events at $\sqrt{s} = 13$ TeV*, *JHEP* **08**, 089 (2018), arXiv: 1805.01845[hep-ex]. (Cited on pages 71 and 86.)

[151] ATLAS Collaboration, *Search for new resonances in mass distributions of jet pairs using 139 fb^{-1} of pp collisions at $\sqrt{s} = 13$ TeV with the ATLAS detector*, *JHEP* **03**, 145 (2020), arXiv: 1910.08447[hep-ex]. (Cited on pages 71 and 170.)

[152] ATLAS Collaboration, *Identification of Jets Containing b-Hadrons with Recurrent Neural Networks at the ATLAS Experiment*, *ATL-PHYS-PUB-2017-003* (2017), URL https://cds.cern.ch/record/2255226. (Cited on page 72.)

[153] ATLAS Collaboration, *Evidence for the $H \to b\bar{b}$ decay with the ATLAS detector*, *JHEP* **12**, 024 (2017), arXiv: 1708.03299v2[hep-ex]. (Cited on pages 72, 87, 117, and 118.)

[154] ATLAS Collaboration, *Performance of missing transverse momentum reconstruction with the ATLAS detector using proton-proton collisions at $\sqrt{s} = 13$ TeV*, *Eur. Phys. J. C* **78**, 903 (2018), arXiv: 1802.08168[hep-ex]. (Cited on pages 73 and 111.)

[155] ATLAS Collaboration, *Reconstruction, Energy Calibration, and Identification of Hadronically Decaying Tau Leptons in the ATLAS Experiment for Run-2 of the LHC*, *ATL-PHYS-PUB-2015-045* (2015), URL https://cds.cern.ch/record/2064383. (Cited on pages 75, 76, 77, and 86.)

[156] ATLAS Collaboration, *Measurement of the tau lepton reconstruction and identification performance in the ATLAS experiment using pp collisions at* $\sqrt{s} = 13$ *TeV*, *ATLAS-CONF-2017-029* (2017), URL `http://cds.cern.ch/record/2261772`. (Cited on pages 75, 86, and 111.)

[157] ATLAS Collaboration, *Identification of hadronic tau lepton decays using neural networks in the ATLAS experiment*, *ATL-PHYS-PUB-2019-033* (2019), URL `https://cds.cern.ch/record/2688062`. (Cited on pages 75, 78, and 171.)

[158] A. Elagin, P. Murat, A. Pranko and A. Safonov, *A new mass reconstruction technique for resonances decaying to* $\tau\tau$, *Nucl. Instrum. Meth. A* **654**, 481 (2011), arXiv: `1012.4686v2[hep-ph]`. (Cited on page 77.)

[159] R. Frederix et al., *Higgs pair production at the LHC with NLO and parton-shower effects*, *Phys. Lett. B* **732**, 142 (2014), arXiv: `1401.7340v2[hep-ph]`. (Cited on page 80.)

[160] R. Gröber at al., *NLO QCD corrections to Higgs pair production including dimension-6 operators*, *JHEP* **09**, 092 (2015), arXiv: `1504.06577[hep-ph]`. (Cited on page 80.)

[161] S. Borowka, N. Greiner, G. Heinrich, S. P. Jones, M. Kerner, J. Schlenk and T. Zirke, *Full top quark mass dependence in Higgs boson pair production at NLO*, *JHEP* **10**, 107 (2016), arXiv: `1608.04798[hep-ph]`. (Cited on pages 80 and 140.)

[162] P. Artoisenet, R. Frederix, O. Mattelaer and R. Rietkerk, *Automatic spin-entangled decays of heavy resonances in Monte Carlo simulations*, *JHEP* **03**, 015 (2013), arXiv: `1212.3460v2[hep-ph]`. (Cited on page 81.)

[163] M. Czakon, M. L. Mangano, A. Mitov and J. Rojo, *Constraints on the gluon PDF from top quark pair production at hadron colliders*, *JHEP* **07**, 167 (2013), arXiv: `1303.7215v3[hep-ph]`. (Cited on page 82.)

[164] M. Aliev, H. Lacker, U. Langenfeld, S. Moch, P. Uwer and M. Wiedermann, *HATHOR – HAdronic Top and Heavy quarks crOss section calculatoR*, *Comput. Phys. Commun.* **182**, 1034 (2011), arXiv: `1007.1327[hep-ph]`. (Cited on page 82.)

[165] P. Kant at al., *HATHOR for single top-quark production: Updated predictions and uncertainty estimates for single top-quark production in hadronic collisions*, *Comput. Phys. Commun.* **191**, 74 (2015), arXiv: `1406.4403[hep-ph]`. (Cited on page 82.)

[166] N. Kidonakis, *Two-loop soft anomalous dimensions for single top quark associated production with a* W^- *or* H^-, *Phys. Rev. D* **82**, 054018 (2010), arXiv: `1005.4451[hep-ph]`. (Cited on page 82.)

[167] T. Gleisberg and S. Höche, *Comix, a new matrix element generator*, *JHEP* **12**, 039 (2008), arXiv: `0808.3674v2[hep-ph]`. (Cited on pages 82 and 83.)

[168] F. Cascioli, P. Maierhöfer and S. Pozzorini, *Scattering Amplitudes with Open Loops*, *Phys. Rev. Lett.* **108**, 111601 (2012), arXiv: `1111.5206v2[hep-ph]`. (Cited on pages 82 and 83.)

[169] S. Höche et al., *QCD matrix elements + parton showers*, *JHEP* **04**, 027 (2013), arXiv: 1207.5030[hep-ph]. (Cited on pages 82 and 83.)

[170] C. Anastasiou, L. Dixon, K. Melnikov and F. Petriello, *High-precision QCD at hadron colliders: Electroweak gauge boson rapidity distributions at next-to-next-to leading order*, *Phys. Rev. D* **69**, 094008 (2004), arXiv: hep-ph/0312266. (Cited on page 82.)

[171] M. L. Ciccolini, S. Dittmaier and M. Krämer, *Electroweak radiative corrections to associated WH and ZH production at hadron colliders*, *Phys. Rev. D* **68**, 073003 (2003), arXiv: hep-ph/0306234. (Cited on page 82.)

[172] O. Brein, A. Djouadi and R. Harlander, *NNLO QCD corrections to the Higgs-strahlung processes at hadron colliders*, *Phys. Lett. B* **579**, 149 (2004), arXiv: hep-ph/0307206. (Cited on page 82.)

[173] G. Ferrera, M. Grazzini and F. Tramontano, *Associated Higgs-W-Boson Production at Hadron Colliders: A Fully Exclusive QCD Calculation at NNLO*, *Phys. Rev. Lett.* **107**, 152003 (2011), arXiv: 1107.1164[hep-ph]. (Cited on page 82.)

[174] O. Brein, R. Harlander, M. Wiesemann and T. Zirke, *Top-quark mediated effects in hadronic Higgs-Strahlung*, *Eur. Phys. J. C* **72**, 1868 (2012), arXiv: 1111.0761[hep-ph]. (Cited on page 82.)

[175] G. Ferrera, M. Grazzini and F. Tramontano, *Higher-order QCD effects for associated WH production and decay at the LHC*, *JHEP* **04**, 039 (2014), arXiv: 1312.1669[hep-ph]. (Cited on page 82.)

[176] G. Ferrera, M. Grazzini and F. Tramontano, *Associated ZH production at hadron colliders: The fully differential NNLO QCD calculation*, *Phys. Lett. B* **740**, 51 (2015), arXiv: 1407.4747[hep-ph]. (Cited on page 82.)

[177] J. M. Campbell, R. Keith Ellis and C. Williams, *Associated production of a Higgs boson at NNLO*, *JHEP* **06**, 179 (2016), arXiv: 1601.00658[hep-ph]. (Cited on page 82.)

[178] C. O. S. Alioli, P. Nason and E. Re, *NLO Higgs boson production via gluon fusion matched with shower in POWHEG*, *JHEP* **04**, 002 (2009), arXiv: 0812.0578v2[hep-ph]. (Cited on pages 82 and 83.)

[179] L. Altenkamp, S. Dittmaier, R. V. Harlander, H. Rzehak and T. J. E. Zirke, *Gluon-induced Higgs-strahlung at next-to-leading order QCD*, *JHEP* **02**, 078 (2013), arXiv: 1211.5015[hep-ph]. (Cited on page 82.)

[180] B. Hespel, F. Maltoni and E. Vryonidou, *Higgs and Z boson associated production via gluon fusion in the SM and the 2HDM*, *JHEP* **06**, 065 (2015), arXiv: 1503.01656[hep-ph]. (Cited on page 82.)

[181] R. V. Harlander, A. Kulesza, V. Theeuwes and T. Zirke, *Soft gluon resummation for gluon-induced Higgs Strahlung*, *JHEP* **11**, 082 (2014), arXiv: 1410.0217[hep-ph]. (Cited on page 82.)

[182] R. V. Harlander, S. Liebler and T. Zirke, *Higgs Strahlung at the Large Hadron Collider in the 2-Higgs-doublet model*, *JHEP* **02**, 023 (2014), arXiv: 1307.8122v2[hep-ph]. (Cited on page 82.)

[183] O. Brein, R. V. Harlander and T. J. E. Zirke, *vh@nnlo–Higgs Strahlung at hadron colliders*, *Comput. Phys. Commun.* **184**, 998 (2013), arXiv: 1210.5347v2[hep-ph]. (Cited on page 82.)

[184] H.-L Lai, M. Guzzi, J. Huston, Z. Li, P. M. Nadolsky, J. Pumplin and C.-P. Yuan, *New parton distributions for collider physics*, *Phys. Rev. D* **82**, 074024 (2010), arXiv: 1007.2241v3[hep-ex]. (Cited on page 83.)

[185] S. Gieseke, C. Röhr and A. Siódmok, *Colour reconnections in Herwig++*, *Eur. Phys. J. C* **72**, 2225 (2012), arXiv: 1206.0041v2[hep-ph]. (Cited on page 83.)

[186] R. D. Ball at al., *Parton distributions with LHC data*, *Nucl. Phys. B* **867**, 244 (2013), arXiv: 1207.1303v2[hep-ph]. (Cited on page 83.)

[187] ATLAS Collaboration, *ATLAS Pythia 8 tunes to 7 TeV datas*, *ATL-PHYS-PUB-2014-021* (2014), URL https://cds.cern.ch/record/1966419. (Cited on page 83.)

[188] R. D. Ball et al., *Parton distributions for the LHC run II*, *JHEP* **04**, 040 (2015), arXiv: 1410.8849v4[hep-ph]. (Cited on page 83.)

[189] ATLAS Collaboration, *Measurement of the Z/γ^* boson transverse momentum distribution in pp collisions at $\sqrt{s} = 7$ TeV with the ATLAS detector*, *JHEP* **09**, 145 (2014), arXiv: 1406.3660v2[hep-ph]. (Cited on page 83.)

[190] ATLAS Collaboration, *Web page: Public Egamma Trigger Plots for Collision Data*, URL https://twiki.cern.ch/twiki/bin/view/AtlasPublic/EgammaTriggerPublicResults, Public plots (2019). (Cited on pages 84 and 111.)

[191] ATLAS Collaboration, *Web page: Muon Trigger Public Results*, URL https://twiki.cern.ch/twiki/bin/view/AtlasPublic/MuonTriggerPublicResults, Public plots (2018). (Cited on pages 84 and 111.)

[192] ATLAS Collaboration, *The ATLAS Tau Trigger in Run 2*, *ATLAS-CONF-2017-061* (2017), URL https://cds.cern.ch/record/2274201. (Cited on pages 85, 111, and 169.)

[193] A. Hoecker et al., *TMVA - Toolkit for Multivariate Data Analysis*, *CERN-OPEN-2007-007* (2007), arXiv: physics/0703039[physics.data-an]. (Cited on page 104.)

[194] O. Behnke, K. Kröninger, G. Schott and T. Schörner-Sadenius, *Data Analysis in High Energy Physics: A Practical Guide to Statistical Methods*, WILEY-VCH, ISBN 9783527653416, doi:10.1002/9783527653416 (2013). (Cited on pages 104 and 123.)

[195] ATLAS Collaboration, *Measurement of the Inelastic Proton-Proton Cross Section at $\sqrt{s} = 13$ TeV with the ATLAS Detector at the LHC*, *Phys. Rev. Lett.* **117**, 182002 (2016), arXiv: 1606.02625[hep-ex]. (Cited on page 111.)

[196] J. Butterworth et al., *PDF4LHC recommendations for LHC Run II*, *Journal of Phys. G: Nucl. and Part. Phys.* **43**, 023001 (2016), arXiv: 1510.03865v2[hep-ph]. (Cited on pages 114 and 116.)

[197] ATLAS Collaboration, *Evidence for the associated production of the Higgs boson and a top quark pair with the ATLAS detector*, *Phys. Rev. D* **97**, 072003 (2018), arXiv: 1712.08891v2[hep-ex]. (Cited on pages 117 and 118.)

[198] K. Cranmer, G. Lewis, L. Moneta, A. Shibata and W. Verkerke, *HistFactory: A tool for creating statistical models for use with RooFit and RooStats*, *CERN-OPEN-2012-016* (2012), URL https://cds.cern.ch/record/1456844. (Cited on pages 121, 122, and 123.)

[199] G. Cowan, K. Cranmer, E. Gross and O. Vitells, *Asymptotic formulae for likelihood-based tests of new physics.*, *Eur. Phys. J. C* **71**, 1554 (2011), [Erratum: *Eur.Phys.J.C* **73**, 2501 (2013)], arXiv: 1007.1727v3[physics.data-an]. (Cited on pages 123 and 125.)

[200] A. L. Read, *Presentation of search results: the CLs technique*, *Journal of Phys. G: Nucl. and Part. Phys.* **28**, 2693 (2002). (Cited on pages 125 and 126.)

[201] CMS Collaboration, *Combination of Searches for Higgs Boson Pair Production in Proton-Proton Collisions at* $\sqrt{s} = 13$ TeV, *Phys. Rev. Lett.* **122**, 121803 (2019), arXiv: 1811.09689v2[hep-ex]. (Cited on page 130.)

[202] G. Degrassi, P. P. Giardino, F. Maltoni and D. Pagani, *Probing the Higgs self coupling via single Higgs production at the LHC*, *JHEP* **12**, 080 (2016), arXiv: 1607.04251v3[hep-ph]. (Cited on page 146.)

[203] M. Cepeda et al., *Higgs Physics at the HL-LHC and HE-LHC* (2019), arXiv: 1902.00134v2[hep-ph]. (Cited on pages 149 and 166.)

[204] ATLAS Collaboration, *Technical Design Report for the ATLAS Inner Tracker Pixel Detector*, *CERN-LHCC-2017-021, ATLAS-TDR-030* (2017), URL https://cds.cern.ch/record/2285585. (Cited on page 150.)

[205] CMS Collaboration, *Prospects for HH measurements at the HL-LHC*, *CMS-PAS-FTR-18-019* (2019), URL https://cds.cern.ch/record/2652549. (Cited on page 164.)

[206] L. A. Harland-Lang, A. D. Martin, P. Motylinski and R.S. Thorne, *Parton distributions in the LHC era: MMHT 2014 PDFs*, *Eur. Phys. J. C* **75**, 204 (2015), arXiv: 1412.3989v2[hep-ph]. (Cited on page 168.)

[207] ATLAS Collaboration, *Web page: Public Tau Trigger Plots for Collision Data*, URL https://twiki.cern.ch/twiki/bin/view/AtlasPublic/TauTriggerPublicResults, Public plots (2019). (Cited on page 169.)

[208] ATLAS Collaboration, *Constraints on the Higgs boson self-coupling from the combination of single-Higgs and double-Higgs production analyses performed with the ATLAS experiment*, *ATLAS-CONF-2019-049* (2019), URL https://cds.cern.ch/record/2693958. (Cited on page 188.)

Appendix A.
Additional figures

This appendix contains additional figures for the results presented in Chapters 5, 7 and 8.

Figures A.1 and A.2 show the pre-fit distributions of the BDT input variables in the $\tau_{\text{had}}\tau_{\text{had}}$ channel in the 1-b-tag OS validation region and the 2-b-tag SS validation region, respectively. These distributions validate the data-driven multijet estimation in the $\tau_{\text{had}}\tau_{\text{had}}$ channel defined in Section 5.3.3.

Figure A.3 shows the pre-fit distributions of the BDT input variables in the $\tau_{\text{had}}\tau_{\text{had}}$ channel in the 2-b-tag OS $t\bar{t}$ validation region. These distributions show background-to-data agreement in the region dominated by the $t\bar{t}$ background with true-τ_{had} candidates estimated using simulation, and $t\bar{t}$ background with fake-τ_{had} candidates estimated using the Fake Rate method, as discussed in Section 5.3.4.

Figure A.4 shows a comparison of truth-level distributions between the SM HH signal samples generated at $\sqrt{s}$ =13 TeV and 14 TeV. The agreement between the two samples justifies using the 13 TeV samples and the BDT classifiers trained on these samples to obtain the sensitivity projections to the non-resonant HH production at the HL-LHC, as discussed in Section 7.1.

Figure A.5 shows a comparison of the fake factors defined by Equations (8.1), (8.2) and (8.3) for the 2015+2016 and 2018 data-taking periods, complementary to the results shown in Figure 8.3 for the 2017 data-taking period.

Figure A.6 shows a comparison of the multijet background predictions obtained using the method described in Section 5.3.3 and the modified method described in Section 8.3 using the full Run 2 dataset.

Figures A.7 and A.8 show the pre-fit distributions of the BDT input variables in the $\tau_{\text{had}}\tau_{\text{had}}$ channel in the 1-b-tag OS validation region and the 2-b-tag SS validation region, respectively. These distributions validate the data-driven multijet estimation in the $\tau_{\text{had}}\tau_{\text{had}}$ channel defined in Section 8.3.

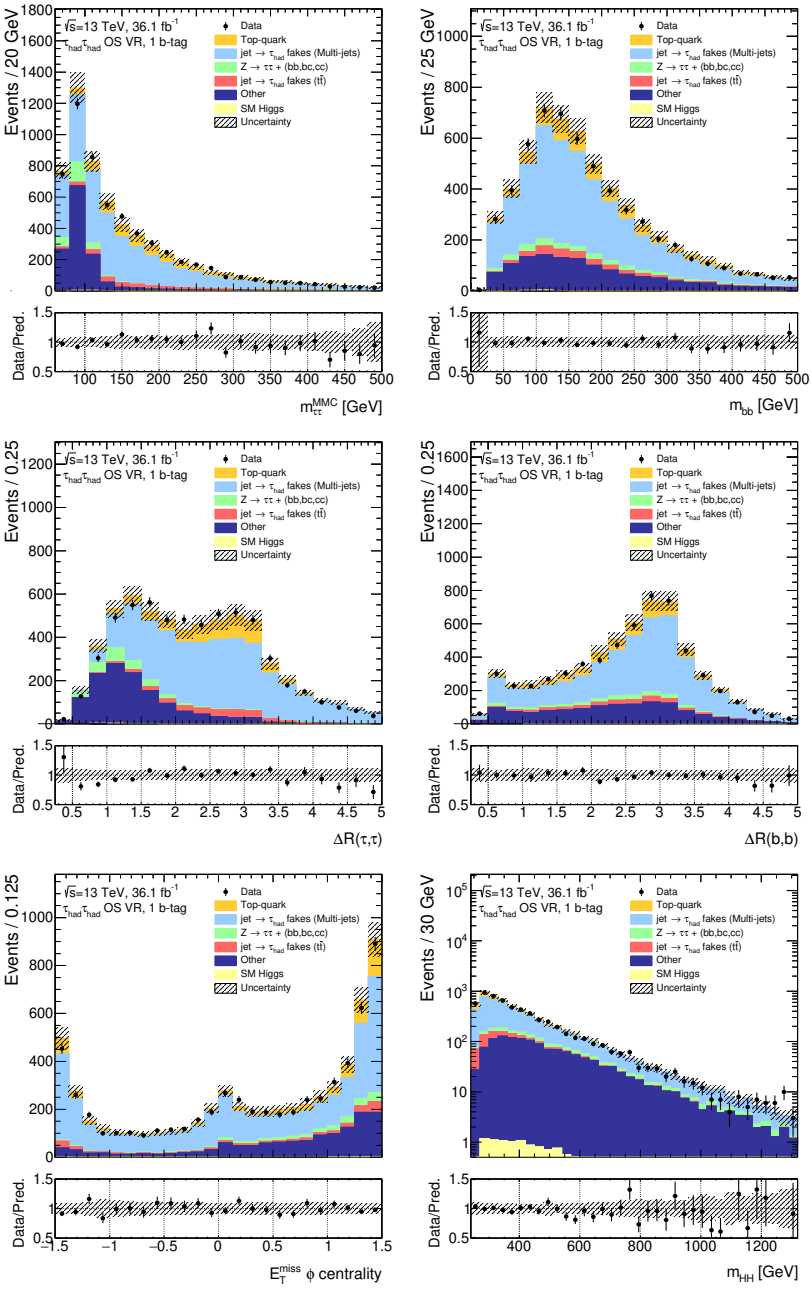

Figure A.1. Pre-fit distributions of $\Delta R(\tau,\tau)$, $\Delta R(b,b)$, $m_{\tau\tau}^{\mathrm{MMC}}$, m_{bb}, E_T^{miss} ϕ centrality and m_{HH} (defined in Section 5.4.2) in the $\tau_{\mathrm{had}}\tau_{\mathrm{had}}$ channel in the 1-b-tag OS validation region. The distributions include statistical and systematic uncertainties in the background estimation.

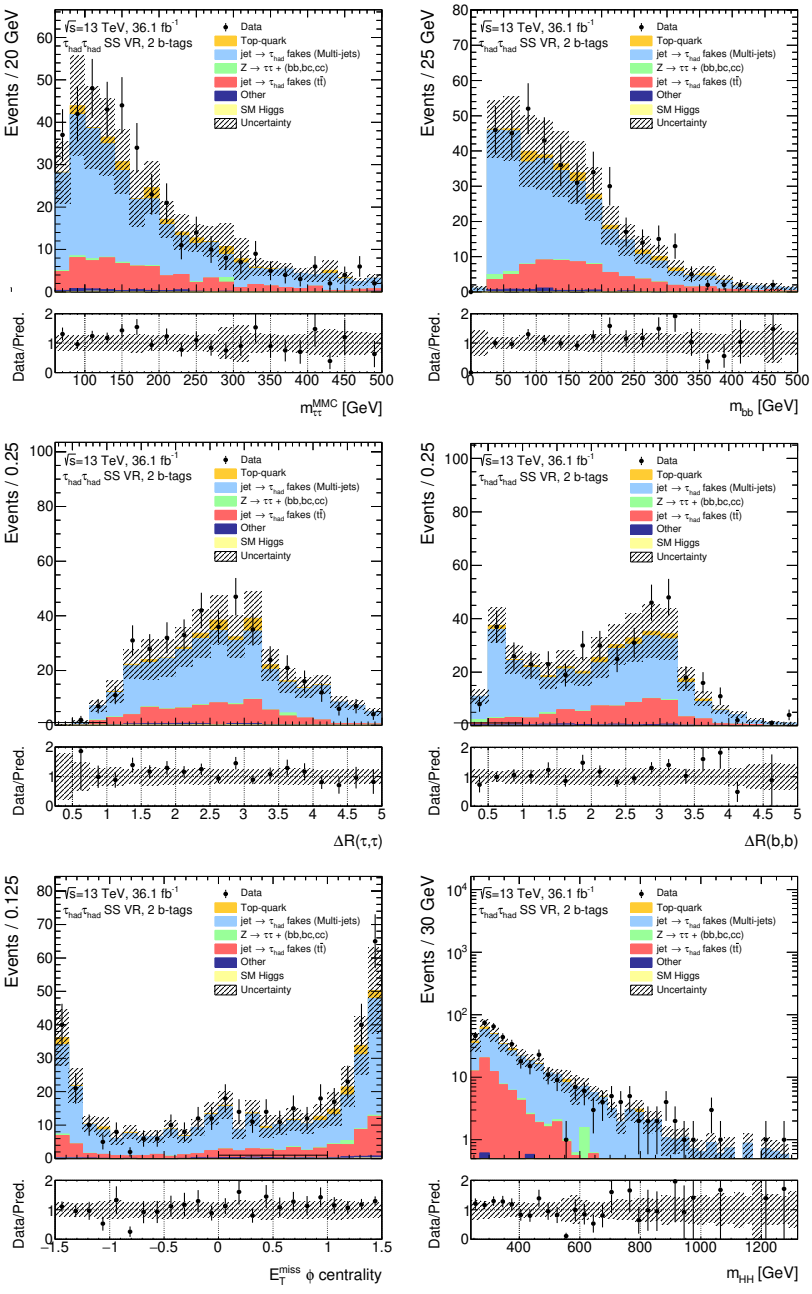

Figure A.2. Pre-fit distributions of $\Delta R(\tau,\tau)$, $\Delta R(b,b)$, $m_{\tau\tau}^{\mathrm{MMC}}$, m_{bb}, E_T^{miss} ϕ centrality and m_{HH} (defined in Section 5.4.2) in the $\tau_{\mathrm{had}}\tau_{\mathrm{had}}$ channel in the 2-b-tag SS validation region. The distributions include statistical and systematic uncertainties in the background estimation.

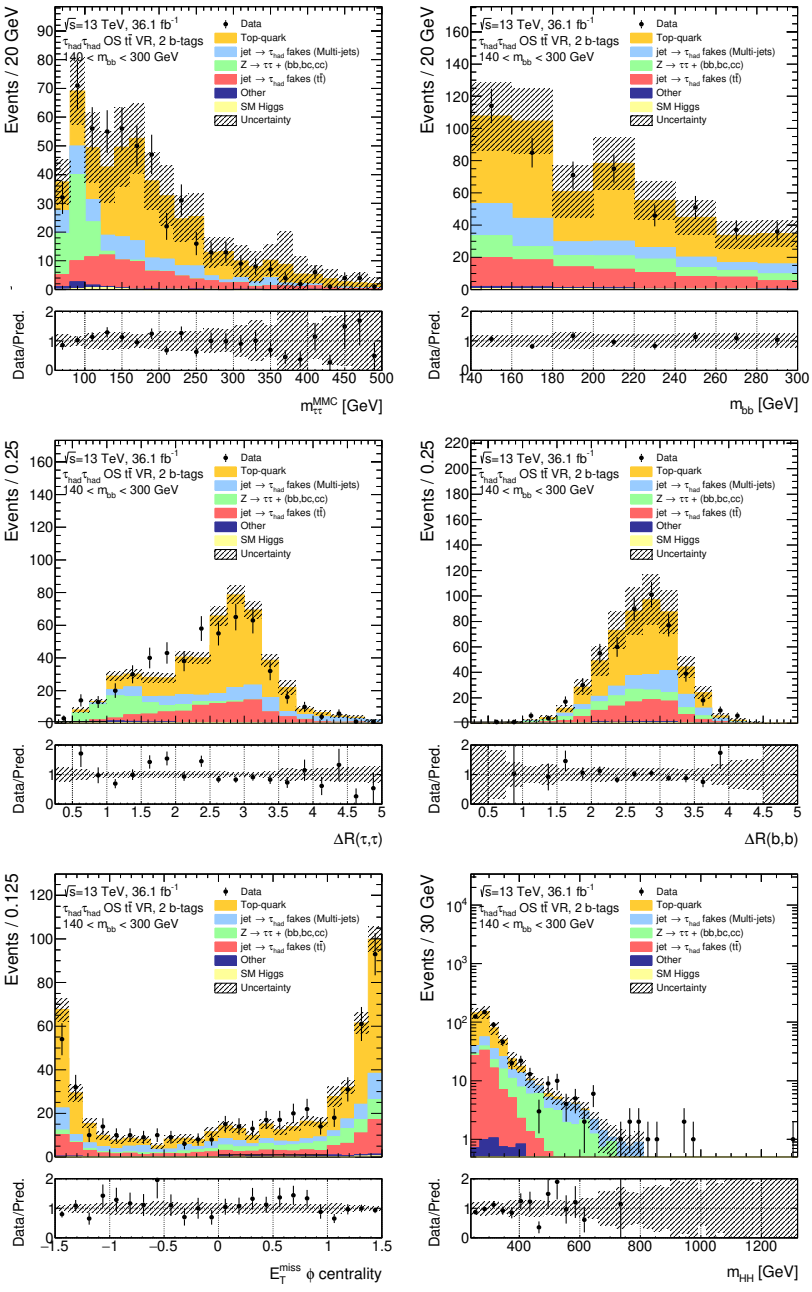

Figure A.3. Pre-fit distributions of $\Delta R(\tau,\tau)$, $\Delta R(b,b)$, $m_{\tau\tau}^{\mathrm{MMC}}$, m_{bb}, E_T^{miss} ϕ centrality and m_{HH} (defined in Section 5.4.2) in the $\tau_{\mathrm{had}}\tau_{\mathrm{had}}$ channel in the 2-b-tag OS $t\bar{t}$ validation region. The distributions include statistical and systematic uncertainties in the background estimation.

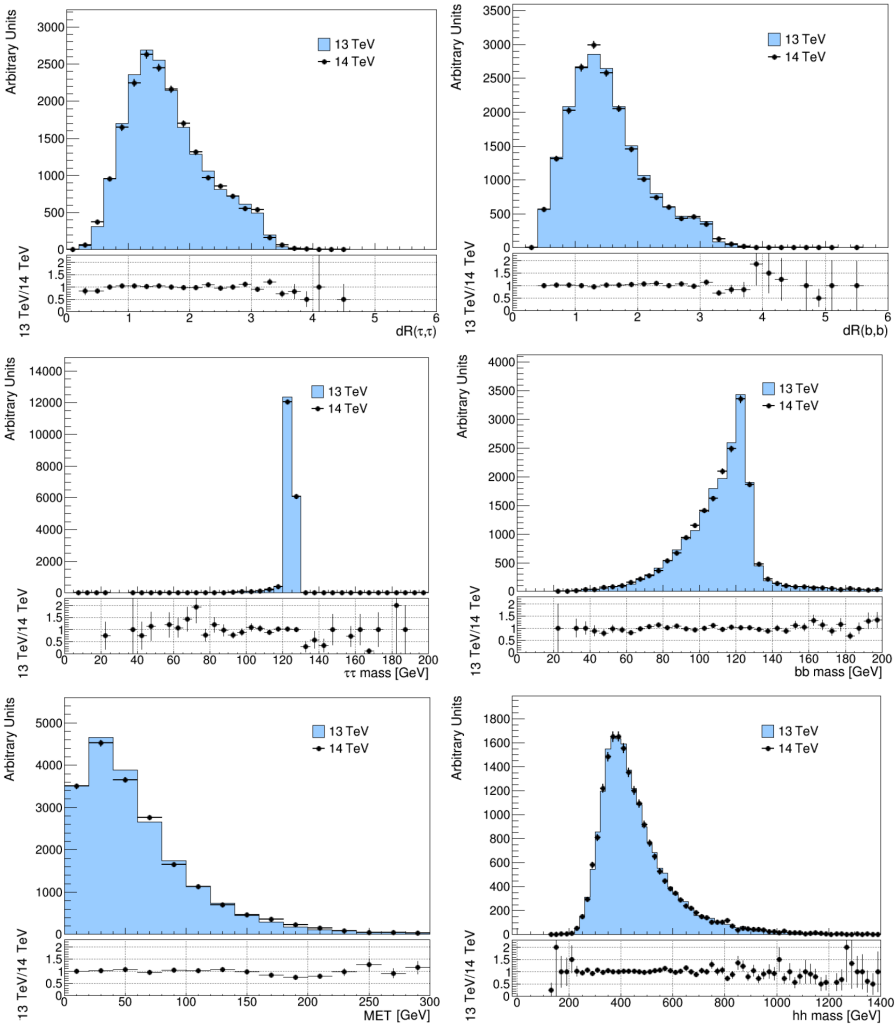

Figure A.4. Truth-level distributions of $\Delta R(\tau,\tau)$, $\Delta R(b,b)$, $m_{\tau\tau}$ ($\tau\tau$ mass), m_{bb} (bb mass), E_T^{miss} (MET) and m_{HH} (hh mass) compared between 13 TeV and 14 TeV SM HH signal samples. The compared distributions are normalised to the same area.

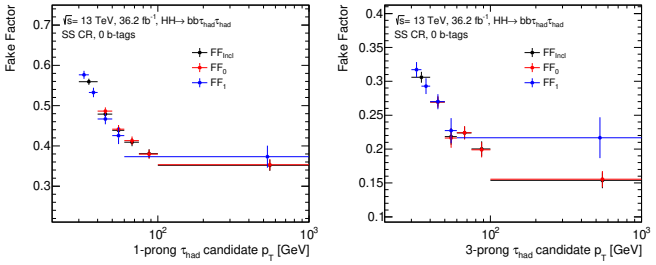

(a) *0-b-tag SS CR, 2015+2016 data-taking period*

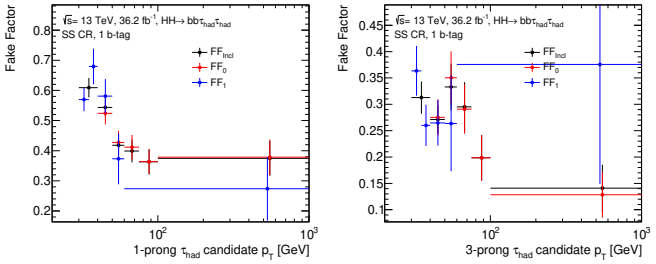

(b) *1-b-tag SS CR, 2015+2016 data-taking period*

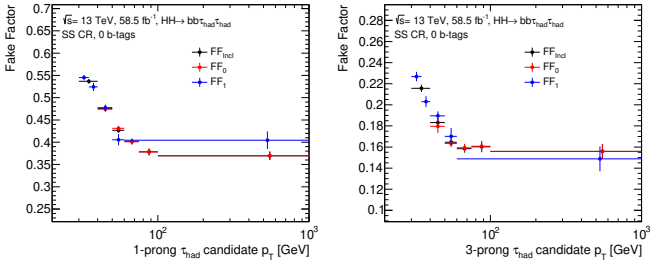

(c) *0-b-tag SS CR, 2018 data-taking period*

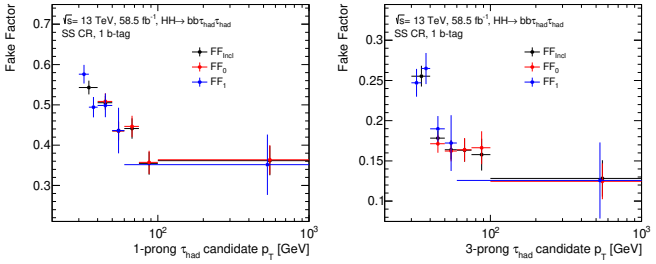

(d) *1-b-tag SS CR, 2018 data-taking period*

Figure A.5. Comparison of the fake factors defined by Equations (8.1), (8.2) and (8.3) for the 1-prong (3-prong) τ_{had} candidates on the left-hand (right-hand) side, obtained from the data and simulated samples that correspond to the 2015+2016 and 2018 data-taking periods.

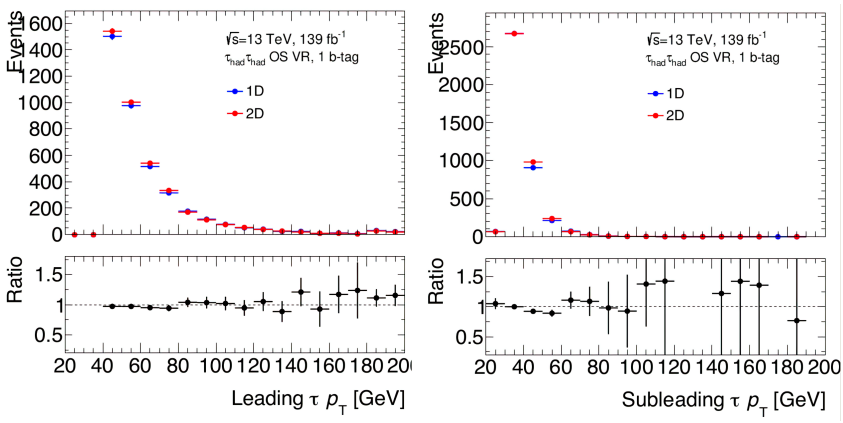

(a) *1-b-tag OS CR*

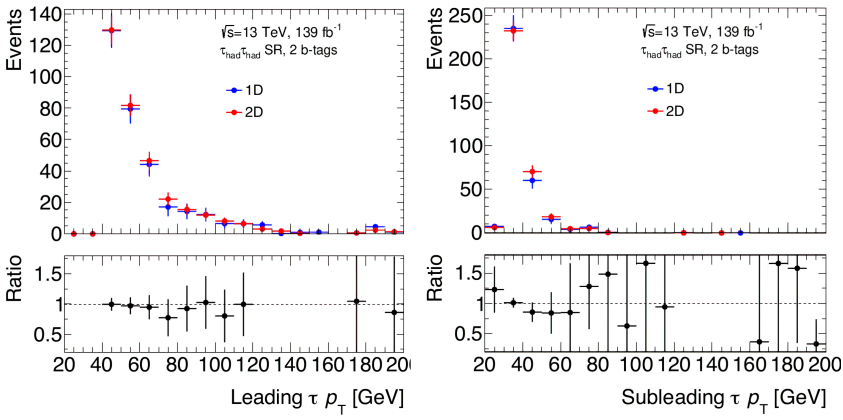

(b) *SR*

Figure A.6. Comparison of the multijet background predictions obtained using the data-driven method described in Section 5.3.3 (labelled "2D") and the modified method described in Section 8.3 (labelled "1D"), in the $\tau_{\text{had}}\tau_{\text{had}}$ channel using the full Run 2 dataset.

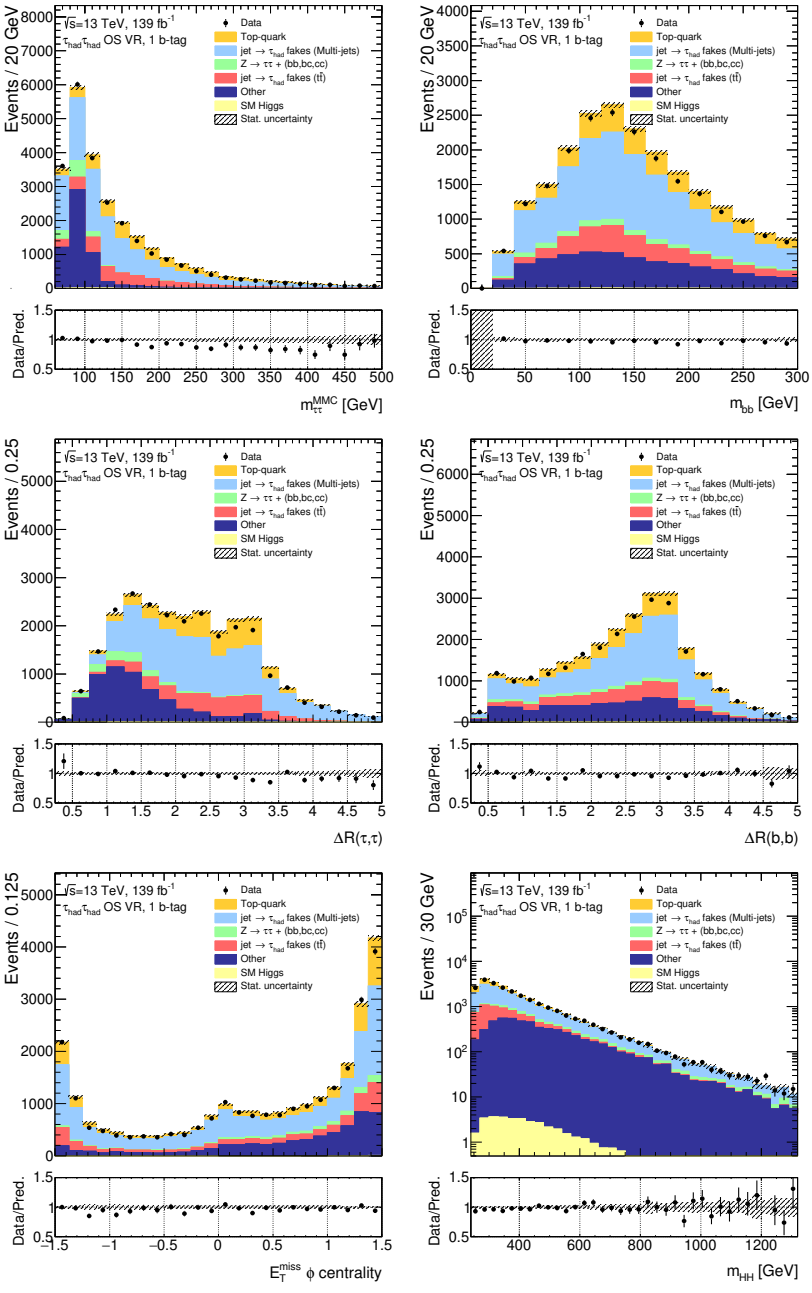

Figure A.7. Pre-fit distributions of $\Delta R(\tau,\tau)$, $\Delta R(b,b)$, $m_{\tau\tau}^{\text{MMC}}$, m_{bb}, E_T^{miss} ϕ centrality and m_{HH} (defined in Section 5.4.2) in the $\tau_{\text{had}}\tau_{\text{had}}$ channel in the 1-b-tag OS validation region. The multijet background is estimated using the method described in Section 8.3, while the $t\bar{t}$ background with fake-τ_{had} candidates is obtained from simulation. The distributions include only the statistical uncertainty in the background estimation.

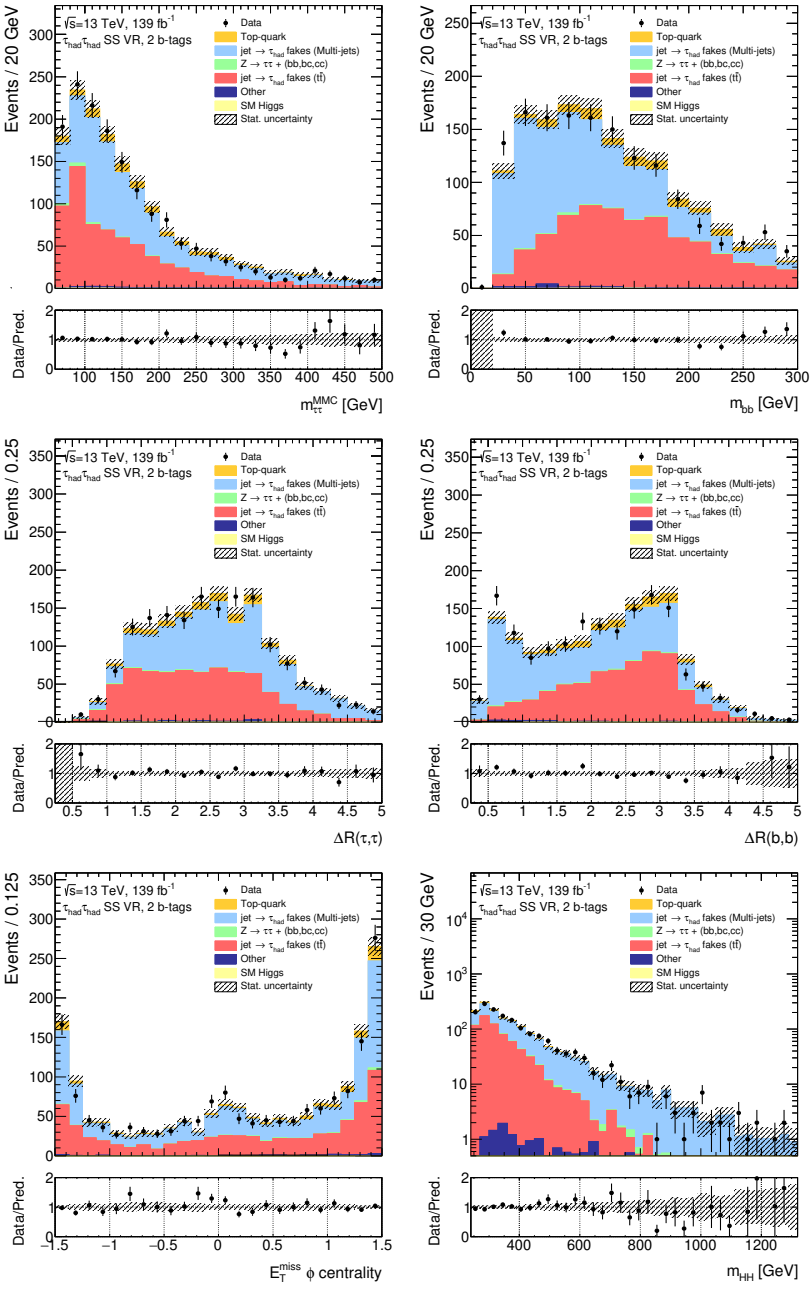

Figure A.8. Pre-fit distributions of $\Delta R(\tau,\tau)$, $\Delta R(b,b)$, $m_{\tau\tau}^{\mathrm{MMC}}$, m_{bb}, E_T^{miss} ϕ centrality and m_{HH} (defined in Section 5.4.2) in the $\tau_{\mathrm{had}}\tau_{\mathrm{had}}$ channel in the 2-b-tag SS validation region. The multijet background is estimated using the method described in Section 8.3, while the $t\bar{t}$ background with fake-τ_{had} candidates is obtained from simulation. The distributions include only the statistical uncertainty in the background estimation.

Appendix B.
Revised Fake Rate method – Additional figures

This appendix contains additional figures for the results presented in Section 8.3.2.

Figure B.1 shows the comparison of the fake-τ_{had} origin between the OS $t\bar{t}$ *FR* CR and the $\tau_{\text{had}}\tau_{\text{had}}$ OS 2-*b*-tag region.

Figures B.2 and B.3 show the comparison of the fake rates obtained directly from the simulation for different origins of the fake-τ_{had}.

Figure B.4 shows the distributions of the τ_{had}-candidate p_T in the SS $t\bar{t}$ *FR* CR that are used to derive fake rates shown in Figure 8.7.

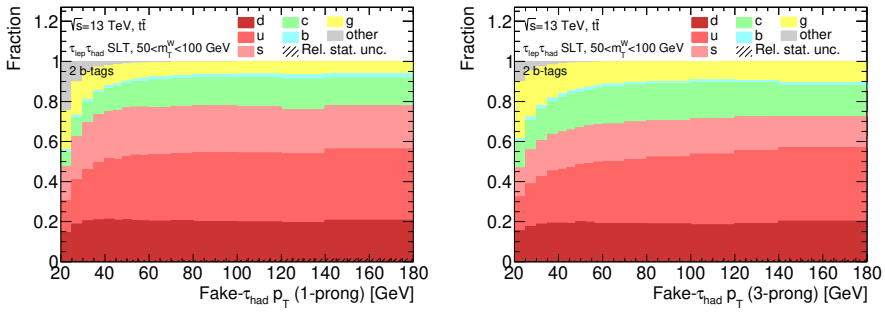

(a) $\tau_{\text{lep}}\tau_{\text{had}}$ *SLT-category* $t\bar{t}$ *CR*

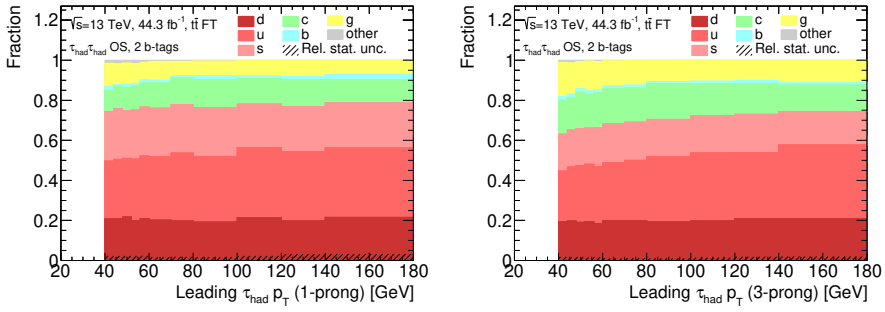

(b) $\tau_{\text{had}}\tau_{\text{had}}$ *OS 2-b-tag region, (fake-*τ_{had}*, true-*τ_{had}*) events*

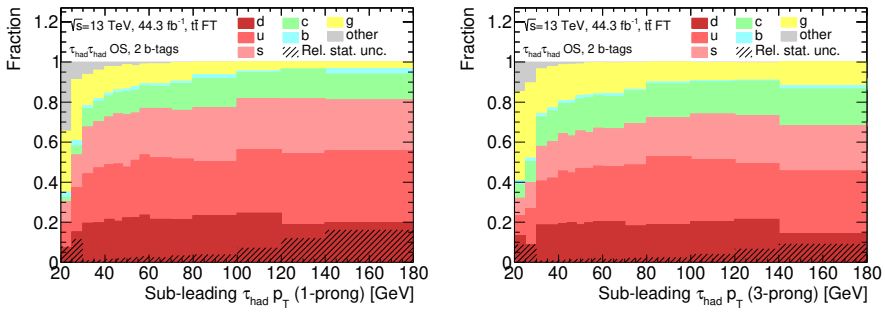

(c) $\tau_{\text{had}}\tau_{\text{had}}$ *OS 2-b-tag region, (true-*τ_{had}*, fake-*τ_{had}*) events*

Figure B.1. Composition of the fake-τ_{had} origin between the $t\bar{t}$ *FR* CR ($\tau_{\text{lep}}\tau_{\text{had}}$ SLT OS 2-*b*-tag region with 50 GeV$< m_T^W <$ 100 GeV) (top) and the $\tau_{\text{had}}\tau_{\text{had}}$ OS 2-*b*-tag region for the events where the leading τ_{had} candidate is fake (middle) and for the events where the sub-leading τ_{had} candidate is fake (bottom), shown separately for 1-prong (3-prong) on the left-hand (right-hand) side.

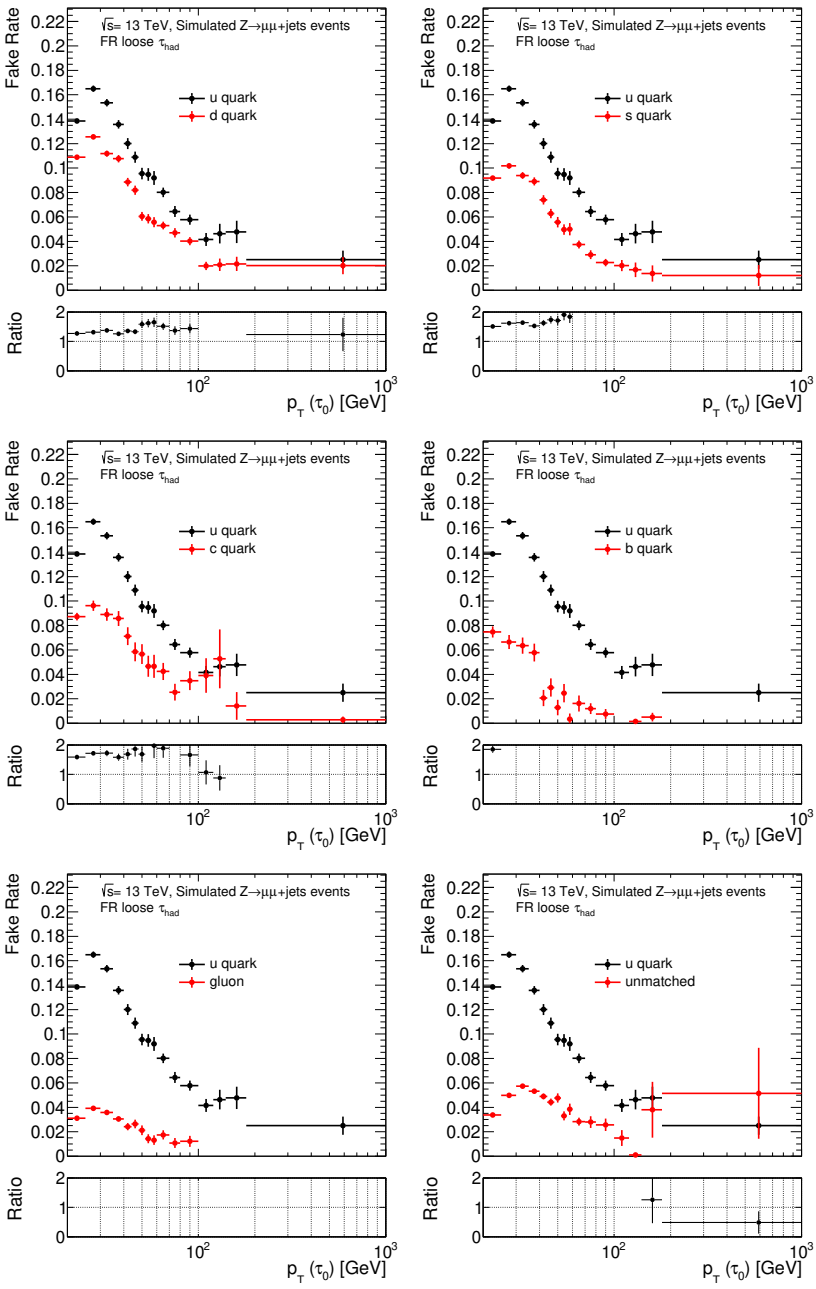

Figure B.2. Fake rates measured in simulated events as a function of the 1-prong fake-τ_{had} p_T for jets initiated by up quarks and their comparison to the fake rates corresponding to jets initiated by down, strange, charm, and bottom quarks, as well as to gluon-initiated jets and to jets for which the truth record is not available ("Unmatched" – likely pileup jets).

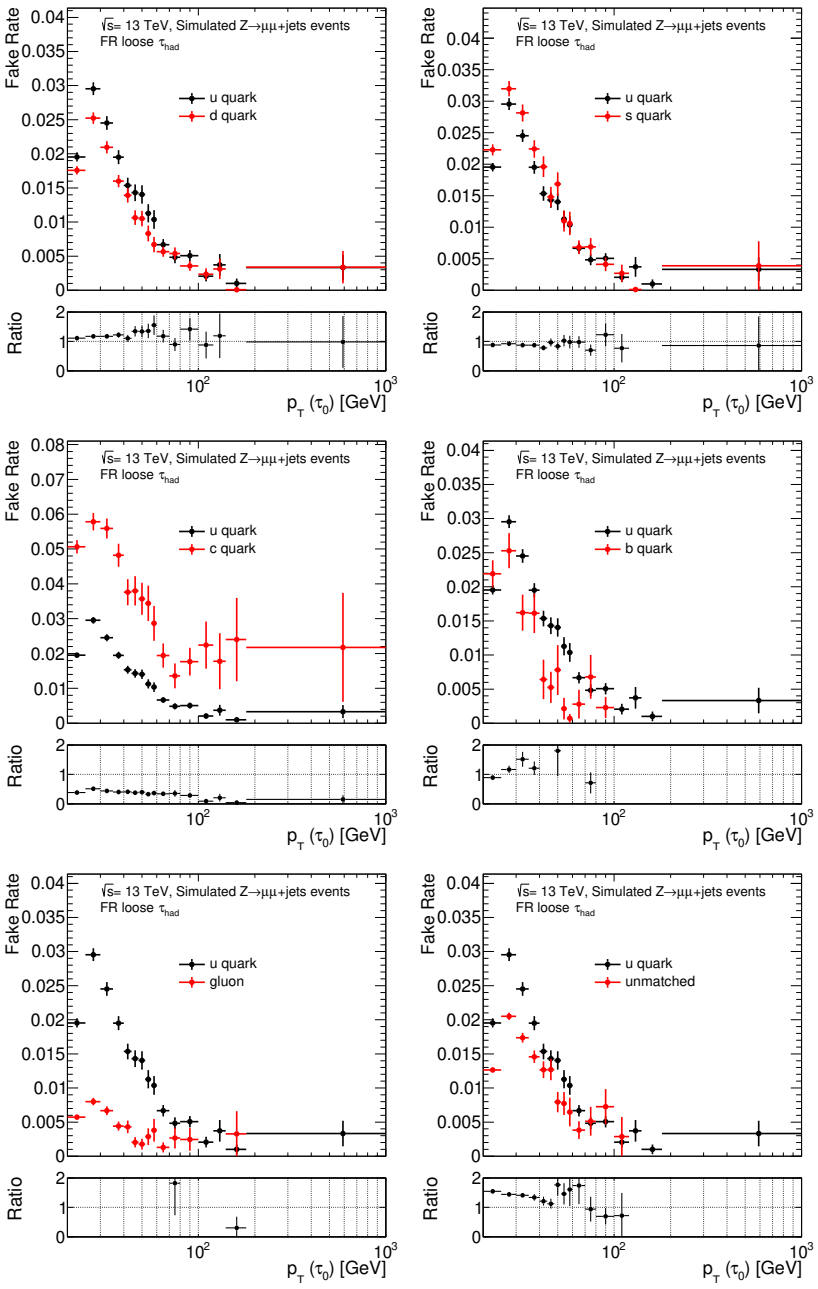

Figure B.3. Fake rates measured in simulated events as a function of the 3-prong fake-τ_{had} p_T for jets initiated by up quarks and their comparison to the fake rates corresponding to jets initiated by down, strange, charm, and bottom quarks, as well as to gluon-initiated jets and to jets for which the truth record is not available ("Unmatched" – likely pileup jets).

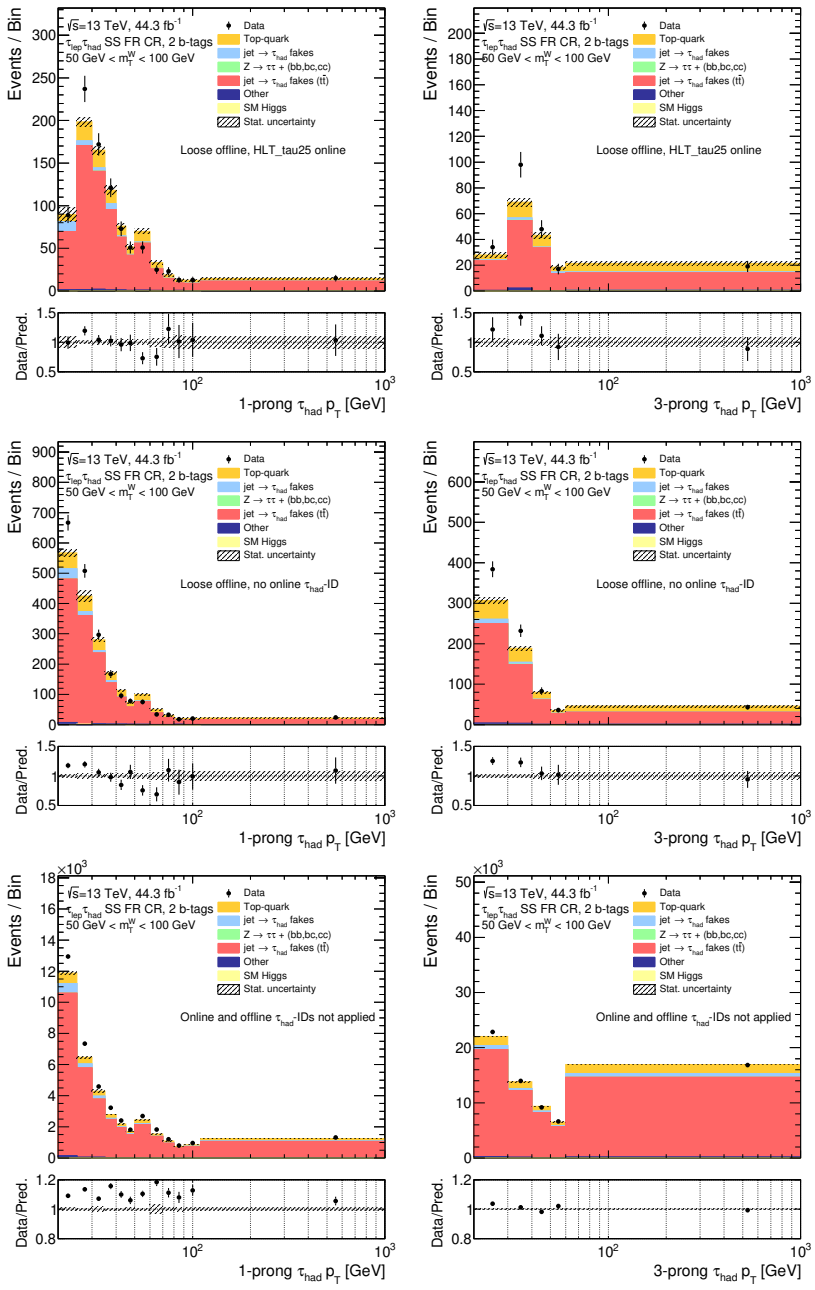

Figure B.4. Distributions of the τ_{had}-candidate p_T in the SS $t\bar{t}$ *FR* CR, corresponding to the 2017 data-taking period, used to derive fake rates given by Equations (8.4) and (8.5) for 1-prong (left-hand) and 3-prong τ_{had} candidates (right-hand side). All backgrounds but the simulated $t\bar{t}$ background with fake-τ_{had} objects (red) are subtracted from data before the set of fake rates FR (FR') are calculated by taking the ratios of the top and bottom (middle and bottom) histograms. The distributions include only the statistical uncertainties.